Recherche de discriminants polarimétriques dans la diffraction par des objets situés à proximité de l'interface plan entre deux milieux diélectriques à pertes.

Nicolas Marquart

N° d'ordre : 3345

THESE

présentée

DEVANT L'UNIVERSITE DE RENNES 1

pour obtenir le grade de

DOCTEUR DE L'UNIVERSITE DE RENNES 1

Mention : Traitement du signal et Télécommunications

par

Nicolas Pascal MARQUART

Equipe d'accueil : Institut d'Electronique et de Télécommunications de Rennes
UMR CNRS 6164

Ecole doctorale : MATISSE

Composante universitaire : Structure et Propriétés de la Matière

Recherche de Discriminants Polarimétriques dans la Diffraction par des Objets situés à proximité de l'Interface Plan entre deux Milieux Diélectriques à Pertes

Soutenue le 17 janvier 2006 devant la commission d'examen

COMPOSITION DU JURY

Président	Gerd WANIELIK	Professeur – Chemnitz University of Technology, Allemagne
Rapporteurs	Daniel BOUCHE	Directeur de Recherche – E.N.S. Cachan
	Walid TABBARA	Professeur – Université Pierre et Marie Curie, Paris VI
Examinateur	Laurent FERRO-FAMIL	Maître de Conférences – IETR, Université de Rennes 1
Directeur de thèse	Frédéric MOLINET	Docteur es Sciences – Directeur de MOTHESIM, Le Plessis Robinson
Directeur de thèse	Eric POTTIER	Professeur – IETR, Université de Rennes 1

The known is finite, the unknown infinite.
Intellectually we stand on an islet in the midst of an illimitable ocean of inexplicability.
Our business in every generation is to reclaim a little more land.

T.H. Huxley, 1887

To my parents

Contents

Introduction

The general process of identifying, observing and obtaining information about an area without coming into direct physically contact with it, is commonly referred as Remote Sensing. In terms of geoscience it is also mentioned as Earth Monitoring. The state-of-the-art of Radar Remote Sensing technique is the Synthetic Aperture Radar (SAR). Here the high spatial resolution is created using a small antenna in a synthetic way, which is analogous to a real antenna of a much larger size. The method consists of a physically small antenna that moves along a track and sends successive coherent Radar signals, and this simulates a virtual physically large antenna. After a data processing procedure (range and azimuth compression) from the backscattered signals of the illuminated area, a high spatial resolution is obtained, independent from the range and wavelength. The resolution in azimuth for a side looking Radar is given here by half the size of the real physical antenna. Using a well defined polarized Radar signal typically one speaks of SAR polarimetry which has become an important contributor to the advancement of Radar in the last decades. One advantage of using Radar detection compared to the optical detection in earth monitoring is its robustness to weather conditions. For example in the case where rain clouds or hazy weather conditions are present the use of optical sensors is very difficult. In the case of infrared sensors e.g. the night and daytime alternation of the earth limits its application innately. Additionally, Radar signals in general can measure energy at wavelengths which are beyond the response of optical sensors and so improve the detection range. Considering the development and set-up of full SAR polarimetric systems either airborne or spaceborne in the past, SAR polarimetry will certainly gain in importance in the near future. SAR polarimetry has diverse applications in the field of geoscience and global economy. Apart from the pure scientific point of view, the observation and prediction of crop failures, pollution control and climate change will be become more important. Subsequently, the main application areas in earth monitoring could be classified as followed:

- Agriculture (crop type and extent, health of plants)
- Cartography (urban mapping, land use, land waste)
- Forestry (biomass, areas of different vegetation types, deforestation)
- Geology (structure mapping, exploration, mineral exploration)
- Hydrology (drainage patterns, soil moisture, flood mapping)
- Meteorology (weather forecasting, climate investigations)

- Oceanography (monitoring ocean currents, monitoring ocean waves → wind speed)
- Target detection (man made objects e.g. nuclear facilities)

The physical principle of Remote Sensing consists in transmitting a well defined electromagnetic wave from an antenna in an area of interest. In the illuminated area the electromagnetic field interacts with the given objects from where the field is again scattered back into the space. The purpose of Radar polarimetry is to investigate these interactions and so to get information about the objects where the objects may be e.g. man-made targets or vegetation. The interactions depend on the geometrical and electromagnetic properties of the objects and from the transmitted field. The experimental setup of a Radar measurement is divided in the way from the transmitter antenna to the lighted spot and in the way to the receiver antenna. The spatial alignment of the transmitting and receiving antenna can be either monostatic or bistatic. In the first case the two antennas coincide, where in the second case both are positioned at different locations. In this work the monostatic alignment is considered.
In the classical Radar detection the temporal information (Range) and the power (Reflectivity) of the scattered field are measured. Additionally to it, Radar polarimetry takes the vectorial properties of the scattered field into account. Thus, the dynamic of the field is investigated. This polarimetric behavior is directly related to the interaction mechanisms that occurs at the scattering process. Due to the excess of information, one can extract more information about the targets. Depending of the objects which are present at the illuminated area the interactions are superposed in a coherent or incoherent way. For example the superposition of the waves reflected from an urban area is coherent, where in contrast the backscattered field of a forested area is incoherent. Here, complex interactions are given e.g. between the single branches and leaves. Further, a reflected field of a time invariant target like plants in the wind or a undulating plane is also incoherent.
The scattering process at an illuminated area is mathematically described through a linear mapping. It relates the incident and back scattered field from the considered area via a matrix. Due to the possible coherent or incoherent superposition of the interactions, two different quantities are measured. In the case that a coherent scattering process is given, the received voltage of the field is measured over time. Here, the incident and scattered fields are related through the complex (2×2) scattering matrix $[S]$. The Sinclair matrix $[S]$ contains all the information about the scattering process. In contrast, if a incoherent scattering process is given the measured voltage would be equal to zero due to the statistical averaging. In this case the received power must be considered at the antenna. A power measurement averages the incoming energy over time. In consequence the relative phase between the elements of $[S]$ is lost compared to the exact voltage measurement. Therefore, the voltage measurement represents a scattering process of statistical first order, where a power measurement is a statistical second order description of the process. The relation between the incident and reflected power are in general described by the Müller matrix $[M]$, Kennaugh matrix $[K]$, Graves matrix $[G]$, Covariance $[C]$ or Coherency matrix $[T]$. In Earth Monitoring one wants to correlate the data from an illuminated region to the corresponding scatterer types. This leads at the end to the so-called inversion problem or classification problem. Hence, the interpretation and analysis of the scattering matrix either in the voltage or power domain is a focal point in Radar polarimetry. The classification problem may be divided

into the two areas:

- **The Inversion Problem**
  Determination of the shape and the physical properties of the scatterers from measurements.
- **The Forward Modeling**
  From the knowledge of the incident field and the scattering obstacle the radiated field is computed and compared with measurements.

The interpretation of polarimetric data is either based on the Geometrical Optic (GO) ray tracing approach or statistical models. Ray tracing is a resourceful method of analyzing wave fields to get more physical insight into the entire scattering process.

Scope and Objective

Synthetic generated data sets represent an important tool in Radar polarimetry since by forward calculations of single mechanisms the entire scattering process can be better understood. Hence, a better classification of the measured data can be carried out. The diffraction of a plane wave by an object situated close to an interface of a two-layer media has been investigated by many authors and an extensive literature exists on this subject e.g. Butler [14], Chen[13], Geng [24] or Michalski [49]. However, only a few publications have been devoted to the analysis of the polarimetric behavior of the diffracted field. Generally very simple ray models based on the GO are used involving single and double bounce effects for explaining some experimental results. The objective of this thesis is to investigate again this problem by using more refined ray models following the Geometrical Theory of Diffraction (GTD) or étalon method. The étalon method[1] is based on the principle that similar ray geometry leads to similar asymptotic formulas for wave fields. For a smooth convex target in front of an air-soil interface, the simplest étalon problem is here a sphere or cylinder. The polarimetric behavior of the solution of the étalon problem gives the main features of the polarimetric behavior of an arbitrary convex target. The scattered field is investigated for an incident field varying from perpendicular to grazing incidence. In order to check the accuracy of the implemented ray model, a full wave solution based on the result of the scattering problem by the integral equation method is developed for the case where the object is situated in the air. The effect of the soil is introduced by the modified Green dyad for a two-layer media. Michalski's method [49] for transforming the electric field integral equation in the less singular Mixed Potential Integral Equation (MPIE) is used together with the Discrete Complex Image Method (DCIM) for calculating the related Sommerfeld integrals. Here an existing program code solving the Electrical Field Integral Equation (EFIE) for the free space has been adapted according to the MPIE.

Depending from the geometrical properties of the model, lit and shadow regions are given in the GTD field. The dividing line of such a lit and shadow region is the so-called Surface Shadow

[1] The étalon problem is the simplest problem in which the field of rays has the same singularities as in the original problem (caustics, shadow boundaries). It is based on the principle that similar ray geometry leads to similar asymptotic formulas for wave fields e.g. that geometric principles characterize the asymptotic behavior as $k \to \infty$

Boundary (SSB). A special emphasis is attributed to the transition regions, near the shadow boundaries, where the reflected spatial waves disappear and transform into creeping waves at the target which are strongly attenuated on the shadowed side. The implemented GTD ray system takes into account not only all types of multiple reflections between the target and the ground but also the effects of creeping waves near the shadow boundaries. Here the transition of the related spatial waves implies similar ray path close to these geometrical boundaries which modify the polarimetric behavior of the target significantly. In order to have a continuous field at the transition from the lit into the shadow region, the Uniform Theory of Diffraction (UTD) is applied.

The polarimetric behavior is represented on the Poincaré sphere in a first step for the target situated once in the air and once embedded in a lossy soil. Furthermore, the ray system and the polarimetric behavior near the transition zones are validated with measurements performed at the European Microwave Signature Laboratory (EMSL) at the Joint Research Centre (JRC) of the European Commission in Ispra - Italy. Where the backscattered field of a sphere above a perfect conducting plate was measured in the anechoic chamber for different heights. The resulting scattering matrix $[S]$ was investigated with the common coherent and incoherent decomposition theorems used in Radar polarimetry (Huynen, Krogager, Cameron and Cloude-Pottier).

The thesis is divided into seven chapters and an appendix. In view of the legibility and to make the thesis self-contained the derivations and common formulas are enclosed in the appendix.

CHAPTER 1

Theoretical Fundamentals

This chapter gives a brief introduction of the theoretical fundamentals on which this work is based. The purpose is to appoint the notation of the canonical equations used along the thesis. In general, the electromagnetic problems in remote sensing may be divided into two fields of activity, namely the radiation and scattering scope. The radiation problem belongs more to the engineering sector and involves materials such as conductors and dielectrics near a radiating source as given in the antenna design and development (near field). In contrast, the scattering problem is of particular interest in Geosciences respectively Earth Monitoring. Here, the scattered field from an illuminated region or object is investigated and local plane waves are considered (far field). The total measured field E_T at the antenna is shown in fig. 1.1 given by the sum of the scattered E_S and incident field E_I at the receiver. Where the Maxwell equations form the basis of electromagnetism and frame therefore the solutions of the scattering problem. The scattering problem can be grouped as follows:

- **The Helmholtz Equation**
  This elliptic partial differential equation describes the propagation of the electromagnetic wave to the target and back to the receiver.
- **The Boundary Conditions**
  The boundary conditions at the surface of the target must be satisfied.
- **Coherent or Incoherent Superposition**
  The superposition of diffracted waves due to different scattering mechanisms can be coherent or incoherent. For deterministic scattering mechanisms the backscattered waves interfere in a coherent way. Here, statistics of first order describe the whole scattering process. Nevertheless, if a large number of deterministic diffraction points is given, a statistical description of second order has to be applied e.g. different phase centers (Speckle). The same holds for time invariant scattering mechanisms, where the superposition of the scattered waves is incoherent.

- **The Roughness-Smoothness**
  For the general case where the surface is not perfectly smooth, the incident field is reflected in different directions. Depending from the ratio of the wave number k and the surface parameter σ, a smooth $k\sigma < 1$ or a rough surface $k\sigma > 2$ is defined. Where σ is the height standard deviation relative to the average curvature plane.

- **The Sommerfeld's Radiation Condition**
  According to Sommerfeld, the electromagnetic field must vanish in the unbounded space at infinity ($r \to \infty$). E.g. for a line source stated with the Landau symbol as:

$$\left(\frac{\partial}{\partial r} - ik\right) E \;=\; \mathrm{o}\left(\frac{1}{\sqrt{r}}\right) \qquad r \to \infty \tag{1.1}$$

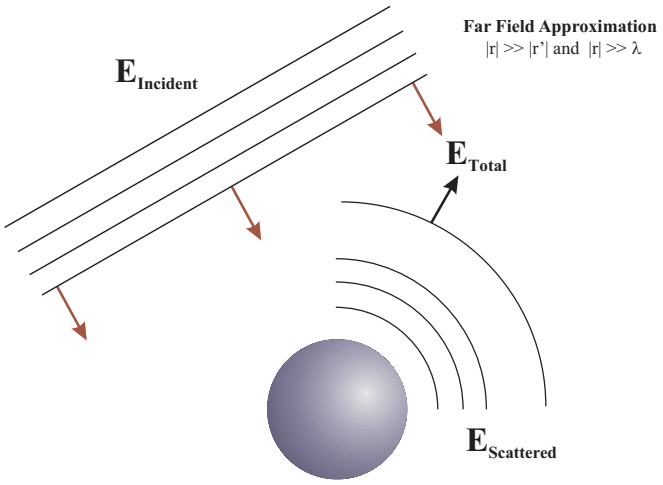

Figure 1.1: The total field at the receiver [$E_T = E_I + E_S$]

1.1 Maxwell Equations

The behavior of electromagnetic fields given by a set, consisting of four canonical equations which were written down in their final form by J. C. Maxwell (1831-1879). Here, Maxwell added the displacement current term to the steady-state form known as the law of A. M. Ampère (1775-1836). The spatial-and-temporal dependence of a monochromatic wave is described in the following by its phase term $exp(ikr - i\omega t)$.[1] Considering a driving oscillating source of the form $\vec{J}_{0\,(\omega)}$, the four Maxwell equations are given by:

[1] The angular frequency ω describes the phase change within one second and wave-number k the phase change within one meter. With that sign convention the wave is regressing toward the origin. If signs in the exponential term are swapped to $exp(-ikr + i\omega t)$, then the matter of studied phenomena does not change (all the laws stay valid). For latter convention the wave is traveling forward, away from the origin.

$$
\begin{aligned}
\nabla \times \vec{H}_{(\vec{r},\omega)} &= -i\,k\,\eta\,\vec{E}_{(\vec{r},\omega)} + \vec{J}_{0\,(\vec{r},\omega)} && \text{(1) Ampère-Maxwell} \\
\nabla \times \vec{E}_{(\vec{r},\omega)} &= i\,k\,\zeta\,\vec{H}_{(\vec{r},\omega)} && \text{(2) Faraday-Maxwell} \\
\nabla \cdot \vec{E}_{(\vec{r},\omega)} &= \frac{\nabla \cdot \vec{J}_{0\,(\vec{r},\omega)}}{i\,k\,\eta} && \text{(3) Electric Gauss law} \\
\nabla \cdot \vec{H}_{(\vec{r},\omega)} &= 0 && \text{(4) Magnetic Gauss law}
\end{aligned}
\tag{1.2}
$$

According to the set (1.2) it follows that for Radar measurements it is not possible to distinguish between a radiated field due to a induced conductive or permittivity current distribution. Therefore, it is of advantage if homogeneous soil properties are introduced. Such a substitutive homogeneous quantity is denoted e.g. for a dielectric soil as an effective permittivity. Also, in the sense of structure analysis which may consist of several dielectric layers, an approximate homogenous description of of the media is easier to handle for numerical purposes.
The case may be where either a displacement current $\vec{D}$ or an electric conductance σ dominates in the media. Thus, both material parameters can be combined into the effective quantities σ_{eff} or ϵ_{eff}. The admittance η from the set (1.2) is now in terms of the effective quantities by:

$$
\begin{aligned}
k\,\eta &= \omega\,\epsilon_0\,\epsilon + i\,\sigma \\
&= \omega\,\epsilon_0\,\epsilon_{eff} \\
&= i\,\sigma_{eff}
\end{aligned}
\tag{1.3}
$$

Where the effective permittivity ϵ_{eff} is defined by:

$$
\begin{aligned}
\epsilon_{eff}(\omega) &= \epsilon(\omega) + i\,\frac{\sigma(\omega)}{\omega\epsilon_0} \\
&= \epsilon'_{eff} + i\epsilon''_{eff}
\end{aligned}
\tag{1.4}
$$

in the case that an effective conductance σ_{eff} is considered, it turns out:

$$
\begin{aligned}
\sigma_{eff}(\omega) &= \sigma(,\omega) - i\,\omega\epsilon_0\epsilon(\omega) \\
&= \sigma'_{eff} + i\sigma''_{eff}
\end{aligned}
\tag{1.5}
$$

Here, the impedance ζ in the Maxwell equations is related with the magnetic susceptibility by:

$$k\,\zeta = \omega\,\mu_0\,\mu$$

Attenuation and Dispersion

The dispersion describes the attenuation of a wave on its propagation through a lossy medium. Also, it relates the angular frequency ω and the wave number k which defines the phase velocity v_{Ph} of the wave. Taking the curl of the second equation of the set (1.2) and assuming that no other electrical sources are present $\nabla \cdot \vec{E}_{(\vec{r},\omega)} = 0$, it turns out:

$$k^2 \;=\; \mu\omega^2 \left(\epsilon \;+\; i\frac{\sigma}{\omega}\right) \tag{1.6}$$

The propagation takes only place in the $+\hat{z}$-direction, yielding:

$$k = |\vec{k}| = \sqrt{k_x^2 + k_y^2 + k_z^2} \qquad k_y = k_x = 0$$

$$\Longrightarrow \quad k = k_z$$

The complex wave number component k_z is introduced as follows:

$$k_z = \beta + i\alpha \tag{1.7}$$

Then, squaring (1.7) and comparing it with (1.6) and using the definition of the effective permittivity ϵ_{eff}, the real and imaginary part of the k_z component are given by:

$$\beta = \pm\,\omega \left[\frac{\mu_0\mu\epsilon_0\,\epsilon'_{eff}(\omega)}{2}\left(\sqrt{1+\left[\frac{\epsilon''_{eff}(\omega)}{\epsilon'_{eff}(\omega)}\right]^2}\;+1\right)\right]^{\frac{1}{2}} \tag{1.8}$$

$$\alpha = \pm\,\omega \left[\frac{\mu_0\mu\epsilon_0\,\epsilon'_{eff}(\omega)}{2}\left(\sqrt{1+\left[\frac{\epsilon''_{eff}(\omega)}{\epsilon'_{eff}(\omega)}\right]^2}\;-1\right)\right]^{\frac{1}{2}} \tag{1.9}$$

Referring to a ray fixed system, the propagation direction is set equal to the z, the attenuation factor α in a lossy soil is finally determined as:

$$\vec{E}_{(\vec{r},\omega)} = E_{0Z}\, e^{-\alpha z}\, e^{i(\beta z - \omega t)} \tag{1.10}$$

The latter expression points out that e.g. a clayey soil or a general soil with a high loss $\epsilon''_{eff} \gg$ lead to a strong attenuation of the field. In consequence, no deep penetration into the soil is possible and the penetration depth $\delta = \frac{1}{\alpha}$ describes the damping of the amplitude to the loss value $\frac{1}{e}$. For a high conductive material this represents a penetration depth around μm. With $C_0 = 0,3m/ns$, as the speed in vacuum, it yields for the phase velocity $v_{Ph,z}$:

$$v_{Ph,z} = \frac{\omega}{\beta} = \frac{C_0}{\left[\frac{\mu\epsilon'_{eff}(\omega)}{2}\left(\sqrt{1+\left[\frac{\epsilon''_{eff}(\omega)}{\epsilon'_{eff}(\omega)}\right]^2}\;+1\right)\right]^{\frac{1}{2}}} \tag{1.11}$$

Hence, for a high lossy medium the phase velocity converge to zero and no propagation is on hand.

1.2 Sommerfeld Identity

The problem of a dipole radiation in the presence of a dissipative half-space dates back to the work of Sommerfeld [60] who uses the Hertzian vector or polarization potentials to describe the field of a vertical electric dipole located at the interface separating the two half-spaces. Sommerfeld formulated this problem by expanding the polarization potentials in terms of cylindric waves. In this work the radiation from an illuminated object close to the interface air-soil is considered. Here, the incident field at the target induces surface currents having horizontal and vertical components. According to the Maxwell equations (1.2), these induced currents scatter again an electromagnetic field back into the space. The current distribution represents an assembly of Hertz dipoles. Therefore, the formulation for an elementary Hertz dipole for the radiation in a bounded space is first derived. In this case the boundary condition at the interface must be fulfilled. First of all, a suitable integral representation in Cartesian coordinates for the free Green function is presented for an elementary dipole. When, a transformation to cylindric coordinates in the configuration space as well as in the fourier space will lead to the final Sommerfeld integral representation or Sommerfeld identity. The final expressions will form the basis of the so called Sommerfeld integrals discussed in chapter 2. The Green function for an electric dipole in the free space is known to be of the form:

$$G_0 \;=\; \frac{e^{ikR}}{R} \tag{1.12}$$

Where the R describes the distance from the dipole to the point of observation and the Green function G_0 represents a spherically-symmetric wave function. Next, a suitable spectral representation of G is introduced. In accordance to Baños [3], the free Green function G_0 is decomposed in the Fourier domain as follows:

$$G(\vec{R}) \;=\; \frac{1}{2\pi^2} \int_{-\infty}^{\infty}\int_{-\infty}^{\infty}\int_{-\infty}^{\infty} \frac{e^{i(k_x\hat{x}\,+\,k_y\hat{y}\,+\,k_z\hat{z})}}{K^2 \;-\; k^2}\, dk_x\, dk_y\, dk_z \tag{1.13}$$

Where the wave number K is given by the three components k_x, k_y and k_z:

$$K^2 \;=\; k_x^2 \;+\; k_y^2 \;+\; k_z^2 \tag{1.14}$$

Referring to the work of Baños the derivation of expression (1.13) is only valid if the variable k_x is reel. In (1.13) the $\hat{z}$ direction corresponds to the axis of symmetry. Rewriting next the variable k_z in the following way:

$$k_z \;=\; \pm i\sqrt{k_x^2 \;+\; k_y^2 \;-\; K^2} \;\;\Rightarrow\;\; k_z \;=\; \pm i\gamma \tag{1.15}$$

and substituting k_z by γ, the denominator of (1.13) is rewritten as follows:

$$G(\vec{R}) \;=\; \frac{e^{i\,k\,R}}{R} \;=\; \frac{1}{2\pi^2} \int_{-\infty}^{\infty}\int_{-\infty}^{\infty}\int_{-\infty}^{\infty} \frac{e^{i(k_x\hat{x}\,+\,k_y\hat{y}\,+\,k_z\hat{z})}}{[k_z \;+\; i\gamma]\,[k_z \;-\; i\gamma]}\, dk_x\, dk_y\, dk_z \tag{1.16}$$

The integration of (1.13) or (1.16) is performed using either the residuals given in the complex k-plane or in the γ-plane. This implies that the medium has a finite conductivity. Setting the wave number k of the medium equal to $k = \beta + i\alpha$, it yields for the integration path a so-called strip of analyticity, defined by:

$$-\alpha < \Im(K) < \alpha \tag{1.17}$$

The corresponding strips and residuals in the K and γ plane are outlined in fig 1.2 and 1.3. Here, the two residuals $\pm i\gamma$ were applied in referring to the denominator of (1.16). Introducing the attenuation as follows:

$$\gamma \; = \; \gamma^{'} \; + \; i\gamma^{''}$$

the two residuals $\pm i\gamma$ are now given by:

$$\begin{aligned} \gamma^{+} \; &= \; +i\gamma \quad &= \quad -\gamma^{''} \; + \; i\gamma^{'} \\ \gamma^{-} \; &= \; -i\gamma \quad &= \quad +\gamma^{''} \; - \; i\gamma^{'} \end{aligned}$$

Due to the uniqueness both residuals must lead to the same result. Substituting the above mentioned definition of γ^{+} and γ^{-} in (1.16), yielding:

$$\gamma^{+} \; \Rightarrow \; G(R) \quad = \quad \frac{1}{2\pi} \int_{-\infty}^{\infty} \int_{-\infty}^{\infty} \frac{1}{\gamma} \, e^{-\gamma^{'} z \, - \, i\gamma^{''} z \, + \, i\left(\vec{k}_x \hat{x} + \vec{k}_y \hat{y}\right)} \, dk_x \, dk_y \tag{1.18}$$

$$\gamma^{-} \; \Rightarrow \; G(R) \quad = \quad \frac{1}{2\pi} \int_{-\infty}^{\infty} \int_{-\infty}^{\infty} \frac{1}{\gamma} \, e^{-\gamma^{'} z \, - \, i\gamma^{''} z \, + \, i\left(\vec{k}_x \hat{x} + \vec{k}_y \hat{y}\right)} \, dk_x \, dk_y \tag{1.19}$$

As outlined in fig. 1.2 and 1.3 the integration path C_1 or C_2 and their related residual can be applied. Here, the upper half-space ($i > 0$) is chosen which implies the following restriction for γ:

$$\Re(\gamma) \; > \; 0 \tag{1.20}$$

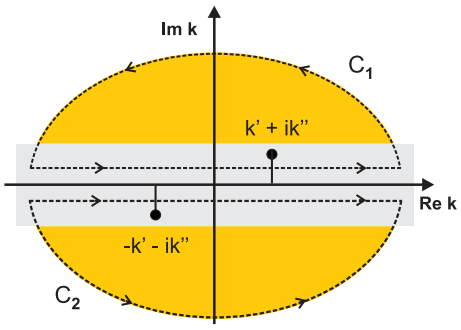

Figure 1.2: Residuals in the complex k-plane

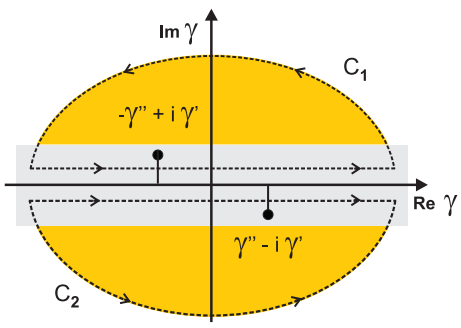

Figure 1.3: Residuals in the complex γ-plane

Furthermore, the Sommerfeld radiation condition (1.1) must be fulfilled for the far field. Therefore, the absolute value of the variable z must be taken in the equivalent expression (1.18) and

(1.19). This leads to the Sommerfeld identity of the form:

$$\frac{e^{i\,k\,R}}{R} \;=\; \frac{1}{2\pi} \int\limits_{-\infty}^{\infty} \int\limits_{-\infty}^{\infty} \frac{1}{\gamma}\, e^{-\gamma\,|z| \,+\, i(k_x \hat{x} \,+\, k_y \hat{y})}\, dk_x\, dk_y \tag{1.21}$$

The integral (1.21) describes the superposition of elementary harmonic plane waves propagating in the $\hat{x}$- $\hat{y}$ plane with an exponential attenuation away from the surface $z = 0$. The dipole is located at the origin and so combined through the attenuation factor $1/\gamma$ and with the double integral over all real values of k_x and k_y. This yields to the elementary spherical wave description as given on the left hand of (1.21).

Cylindric Coordinates (ρ, β, z)
Due to the symmetry around the $\hat{z}$ axis, cylindric co-ordinates are introduced in configuration space and Fourier space. Per definition:

$$\begin{aligned} x \;&=\; r\cos\phi \;\;\Longleftrightarrow\;\; k_x \;=\; \rho\cos\beta \\ y \;&=\; r\sin\phi \;\;\Longleftrightarrow\;\; k_y \;=\; \rho\sin\beta \\ r \;&=\; \sqrt{x^2 \,+\, y^2} \;\;\Longleftrightarrow\;\; \xi \;=\; \sqrt{k_x^2 \,+\, k_y^2} \end{aligned}$$

Next, substituting the Cartesian coordinates by its corresponding cylindric coordinates and using the identity $J_(z) \;=\; \frac{1}{2}\left[H_0^1(z) \;-\; H_0^1(-z)\right]$, the Sommerfeld identity is defined [3]:

$$\boxed{\frac{e^{i\,k\,R}}{R} \;=\; \frac{1}{2} \int\limits_{-\infty}^{\infty} \frac{1}{\gamma}\, H_0^1\left[\rho\,\xi\right]\; e^{-\gamma|z|}\; \xi\; d\xi} \tag{1.22}$$

In (1.22) the term H_0^1 signifies the Hankel function of first kind of order zero. Considering in the following a radiation in air, the wave number is referred as k_0. In consequence, for a given propagation in free space the attenuation factor γ in $\hat{z}$ is therefore:

$$\gamma \;=\; \sqrt{k_0^2 \;-\; k_x^2 \;-\; k_y^2} \tag{1.23}$$

1.3 Wave Polarimetry

Radar polarimetry investigates the vectorial nature of the backscattered EM-field from an area illuminated by a well defined incident field. Here, the polarization of the backscattered field describes the tip of the electric field vector in space over time. Depending on its position and orientation, a linear, circular or a general elliptical polarization may be present. The wave is called linear polarized if the vector $\vec{E}$ is oriented in the same direction during the whole time period. If an arrow represents the instantaneous intensity vector, then its length changes from zero to maximum and back during the half-period. During the second half-period, the described phenomenon is repeated with opposite sign. So, a linear polarization characterizes the movement of the arrowhead along a straight line. For the more general case, where an elliptical polarized wave is given, the vector apex moves along an ellipse during one period (fig. 1.4). A

special case is on hand where the trajectory of the apex runs onto a circle, referred as circular polarization. The elliptical or circular rotation can here be clock-or anticlockwise according to the IEEE (Std. 211-1997) definition for right[2] and circular[3] polarization state. An elliptical polarized wave can be understood as a superposition of two coherent linearly polarized waves, which vectors $\vec{E}$ oscillate in different directions and a have non-zero mutual shift [32].
The propagation of a monochromatic wave may be described by a ray fixed coordinate system given by the axes $\hat{x}$, $\hat{y}$ and $\hat{z}$. One is free by setting the $\hat{z}$-axis equal to the wave propagation direction $\vec{k}$. In consequence the $\hat{x}$- and $\hat{y}$-axes lie in a plane perpendicular to the direction of propagation. Here, for diffraction problems, the two orthogonal polarization planes are defined by the plane of incidence. Where the parallel and perpendicular plane corresponds to the horizontal (h) and vertical (v) polarization basis. (Appendix ($A.1$)).
In Earth Monitoring, two alignments for the transmitting and receiving antenna are in general considered, the monostatic and the bistatic alignment. For last mentioned, the source and receiver antenna are situated at different locations, whereas in the monostatic case both coincide. The monostatic case is solely treated in the following. Due to the opposite propagation direction for the way back of the wave on its round trip, the $\hat{z}$-axis must be clearly defined. Two conventions are regarded in polarimetry: the *F*orward *S*catter *A*lignment (FSA) and the *B*ack *S*catter *A*lignment (BSA). The $\hat{z}$-axis points in the FSA convention in the propagation direction for the way to as well as for the way back to the antenna. In contrast, the $\hat{z}$-axis in the BSA convention points towards the target for both ways.

1.3.1 Jones Vector

The Jones vector is an alternative descriptor for the wave polarimetry apart of e.g. the classical polarization ellipse. The propagation of a monochromatic plane wave away from the source is shown in fig. 1.4. The apex of the field vector $\vec{E}$ describes a helix in space over the time. Rename the ray fixed orthogonal basis $\hat{x}$ and $\hat{y}$ with $\perp$ and $\parallel$ the wave propagation is given on the form:

$$\vec{E}_{(\vec{r},t)} = \begin{bmatrix} E_{\perp}(\vec{r},t) \\ E_{\parallel}(\vec{r},t) \end{bmatrix} = \begin{bmatrix} |E_{\perp}| \; e^{i\left(\vec{k}\cdot\vec{z}-\omega t+\Phi_{\perp}\right)} \\ |E_{\parallel}| \; e^{i\left(\vec{k}\cdot\vec{z}-\omega t+\Phi_{\parallel}\right)} \end{bmatrix}$$

One note that the absolute phase of the two components $E_{\perp}$ and $E_{\parallel}$ are defined through their initial phase $\Phi_{\perp}$ and $\Phi_{\parallel}$ at the source. All points in space have the same harmonic temporal dependence of the form $exp(-i\,\omega\,t)$. Hence, the temporal term can be dropped and the phasor notation is introduced. One gets:

$$\vec{E}_{(\vec{r})} = \begin{bmatrix} |E_{\perp}| \; e^{i\,\Phi_{\perp}} \\ |E_{\parallel}| \; e^{i\,\Phi_{\parallel}} \end{bmatrix} e^{i\,\vec{k}\cdot\vec{z}} \tag{1.24}$$

[2]right-hand polarized wave: A circularly or an elliptically polarized EM-wave for which the electric field vector, when viewed with the wave approaching the observer, rotates counter-clockwise in space. Notes: 1. This definition is consistent with observing a clockwise rotation when the electric field vector is viewed in the direction of propagation. 2. A right-handed helical antenna radiates a right-hand polarized wave.

[3]left-hand polarized wave: A circularly or an elliptically polarized EM-wave for which the electric field vector, when viewed with the wave approaching the observer, rotates clockwise in space. Notes: 1. This definition is consistent with observing a counterclockwise rotation when the electric field vector is viewed in the direction of propagation. 2. A left-handed helical antenna radiates a left-hand polarized wave.

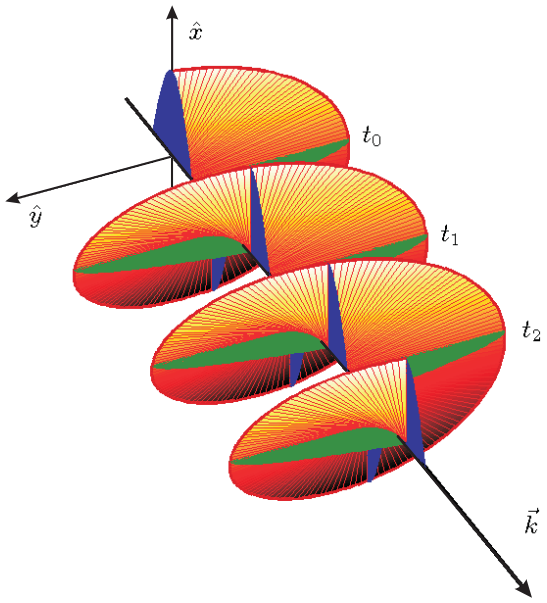

Figure 1.4: The propagation helix $[t_0 < t_2 < \cdots < t_n]$

Observing the wave over time at a constant location e.g. $z = 0$, the Jones vector is introduced as follows:

$$\vec{E}_{(0)} = \begin{bmatrix} |E_\perp| \; e^{i\,\Phi_\perp} \\ |E_\parallel| \; e^{i\,\Phi_\parallel} \end{bmatrix} \tag{1.25}$$

Subtracting the phase $\Phi_\perp$ of the perpendicular component from the parallel component, it yields:

$$\vec{E}_{(0)} = \begin{bmatrix} |E_\perp| \\ |E_\parallel| \; e^{i\,\Phi} \end{bmatrix} = |E_\perp| \; \hat{e}_\perp + |E_\parallel| \; \hat{e}_\parallel \; e^{i\,\Phi} \tag{1.26}$$

Where the phase difference Φ is defined as:

$$\Phi = \Phi_\parallel - \Phi_\perp \tag{1.27}$$

In order to investigate (1.26) in the complex plane the Jones vector is rewritten in the following manner:

$$\vec{E}_{(0)} = \left[\, |E_\perp| \; \hat{e}_\perp + |E_\parallel| \; \hat{e}_\parallel \; \cos(\Phi) \, \right] + i \, |E_\parallel| \; \hat{e}_\parallel \; \sin(\Phi) \tag{1.28}$$

The different possible polarization states can now be discussed by taking the lateral view in propagation direction (fig. 1.5). The sense of rotation is defined through the sign of (1.28) as the temporal dependance is of the form $\pm i\,(\omega t + \Phi)$. Considering next the simplest case where no phase difference occurs $\Phi = 0$. Between the two field components the maximum, minimum and

the zero crossing is at the same time. Hence, this corresponds to a linear polarization where the arrowhead runs along a line. Here, the tilt angle ϕ relative to the horizontal plane is determined through the amplitude of the two components $|E_\perp|\ \hat{e}_\perp\ +\ \left|E_{||}\right|\ \hat{e}_{||}$.

Next, in the case that both components have the same amplitude and the phase difference is $\pm\frac{\pi}{2}$ it follows from (1.28):

$$\vec{E}_{(0)}\ =\ |E_\perp|\ \hat{e}_\perp\quad \pm\quad i\ \left|E_{||}\right|\ \hat{e}_{||} \tag{1.29}$$

The plus sign corresponds to a *L*eft *H*anded *C*irculation (LHC) and the minus sign to a *R*ight *H*anded *C*irculation (RHC). As both amplitudes are equal, the field vector apex will describe a circle over time. In general, the field vector will move along an ellipse. The rotation direction is given here by:

$$\begin{aligned} \sin(\Phi)\ &\geq\ 0 \qquad 0 \leq \Phi \leq \pi \qquad \Rightarrow\quad RHC \\ \sin(\Phi)\ &\leq\ 0 \qquad \pi \leq \Phi \leq 2\pi \qquad \Rightarrow\quad LHC \end{aligned}$$

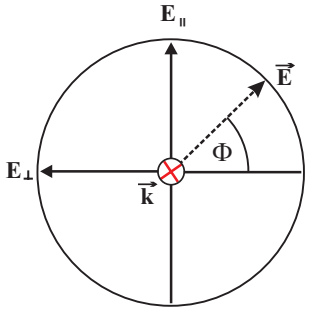

Figure 1.5: Snapshot at the location z = const.

1.3.2 Voltage Scattering Matrix

The scattered field $\vec{E}^S$ from an object is related to the incident field $\vec{E}^I$ via a linear mapping. The mapping is done by means of the complex 2 × 2 Sinclair matrix $[S]$ as follows:

$$\vec{E}^S\ =\ [S]\ \vec{E}^I \tag{1.30}$$

Where the four elements of the scattering matrix are complex quantities and (1.30) is strictly spoken only valid for a single frequency. As a short Radar pulse in the time domain corresponds to a large frequency range it is assumed that the dielectric property of the scatterer constant within the frequency range. The backscattering properties of the object are completely constrained by the four elements of the scattering matrix $[S]$, written out as:

$$\begin{pmatrix} E^S_\perp \\ E^S_{||} \end{pmatrix}\ =\ \begin{bmatrix} S_{11} & S_{12} \\ S_{21} & S_{22} \end{bmatrix}\ \begin{pmatrix} E^I_\perp \\ E^I_{||} \end{pmatrix} \tag{1.31}$$

Further, due to the reciprocity theorem, where the same intensity is measured if the emitter and receiver antenna are interchanged, it follows that the scattering matrix is symmetric, yielding:

$$S_{12} \;=\; S_{21} \tag{1.32}$$

As the phase difference between the elements of $[S]$ is of interest, the phase of S_{11} is taken as reference phase, one gets:

$$[S] = e^{i\phi} \begin{bmatrix} |S_{11}| & |S_{12}|e^{-i(\phi-\phi_{12})} \\ |S_{12}|e^{-i(\phi-\phi_{12})} & |S_{22}|e^{-i(\phi-\phi_{22})} \end{bmatrix} \tag{1.33}$$

Thus, the voltage reflection matrix $[S]$ yields finally five independent parameters, where three parameters describe the amplitudes and two parameters the relative phase of the matrix . Referring to (1.30), the columns of $[S]$ represents the new basis in the measured system $\vec{E}^S$. The components of the new basis are given by the coefficients of the transmitting system $\vec{E}^I$. Hence, by changing the basis, the values of the scattering matrix $[S]$ will also change. The scattering matrix $[S]$ is therefore not base invariant.

In Radar polarimetry the relative phase between the single terms is investigated and not the absolute phase. The absolute phase is at the end of the day determined through the installed electronic components in the receive and transmit path of the whole Radar system. Additionally, due to the volumetric expansion of the antenna the positioning of the phase origin in the middle of the antenna is finally an approximation.

1.3.3 Stokes Vector

Based on power measurements, Stokes introduced a power vector in order to describe partially polarized waves. The four components of the Stokes vector $\vec{g}$ are determined by the quadratic of the field strength as follows:

$$\vec{g} = \begin{bmatrix} g_0 \;=\; |E_\perp|^2 \;+\; |E_{||}|^2 \\ g_1 \;=\; |E_\perp|^2 \;-\; |E_{||}|^2 \\ g_2 \;=\; 2Re\left(E_\perp\, E_{||}^*\right) \\ g_3 \;=\; -2Im\left(E_\perp\, E_{||}^*\right) \end{bmatrix} \tag{1.34}$$

The Stokes component g_0 expresses the total field intensity, g_1 points out the linear polarization and the quantities g_2 and g_3 mutually describe the phase difference of the two scattered polarization. The g_2 and g_3 components describe therefore either a left or right handed circulation. For the general case, where a total or a partially polarized wave is received at the antenna,

the returned power is equal or less than g_0, yielding to the relation:

$$g_0^2 \geq g_1^2 + g_2^2 + g_3^2 \tag{1.35}$$

The scattered power $\vec{g}^S$ of the target is related with the incident power $\vec{g}^I$ by 4×4 Müller matrix $[M]$ as follows:

$$\vec{g}^S = [M]\, \vec{g}^I \tag{1.36}$$

CHAPTER 2

Integral Field Equation

At that time an existing program at the company MOTHESIM[1] was developed in order to calculate the scattered field from an illuminated object in free space by using the Electric Field Integral Equation (EFIE) and the equivalence principle. Here, the program with the name DIFFRA uses a vector and scalar potential twosome for solving the EFIE. In the present case, where the radiation of a sphere situated above the interface of two dielectric half-spaces is investigated, the existing DIFFRA program according to the Green dyad for the free space had to be adapted. In order to keep the structure of a vector and scalar potentials twosome, the Mixed Potential Integral Equation (MPIE) is applied for the case of a bounded space. The corresponding Green dyad was modified by using the Michalski method [49]. The method comprises of adding a correction term to the general Lorenz gauge, relating the vector and scalar potential. Additionally, the Sommerfeld integrals occurring in the modified Green dyad were calculated by the more rapid and robust Discrete Complex Image Method (DCIM). The modified Green dyad was implemented in the original DIFFRA code and the exact numerical method was used to validate the ray system according to the Geometrical Theory of Diffraction (GTD). Furthermore, the implemented ray system is checked via measurements made in an anechoic chamber. The following chapter outlines the derivation of the MPIE for a two layer media. In a first step, the radiation of an elementary dipole situated near an interface is described by the Hertz vector potential based on the work of Baños [3]. The Hertz vector will be defined through a set of essential Sommerfeld integrals and discussed in section 2.2.3.

2.1 Hertz Vector Potential

The Hertz vector potential comprises the advantage that the field can be described by a single potential term. It is therefore sometimes considered to act as a "super-potential". First, the Hertz vector of an elementary dipole is presented for free space. Afterwards the expressions for a

[1] Société MOTHESIM: Modelisation-Optimisation-Theorie-Simulation Mathematique
Centre d'Affaires La Boursidire, Rn 186 - BP 182, 92357 Le Plessis-Robinson Cedex, France

location near an interface of a two-layer media is pointed out, fulfilling the boundary conditions at the interface.

2.1.1 Free Space

A homogeneous and isotropic media of infinite extent is considered in the following. According to the magnetic Gauss law of the set (1.2), where the divergence of the magnetic field $\vec{H}$ is equal zero, one may represent $\vec{H}$ as the curl of some other vector, yielding:

$$\boxed{\vec{H}_S \;=\; -i\,k\,\eta\,\nabla\times\vec{\Pi}} \tag{2.1}$$

Inserting (2.1) in the Faraday-Maxwell relation of (1.2) it follows with $\eta\,\zeta \;=\; 1$:

$$\nabla\times\Big[\,\vec{E}_{S\,(\vec{r})} \;-\; k^2\vec{\Pi}_{(\vec{r})}\,\Big] \;=\; 0 \tag{2.2}$$

Further, any curl-free vector is the gradient of some scalar. Hence, it follows the definition:

$$\vec{E}_{S\,(\vec{r})} \;-\; k^2\vec{\Pi}_{(\vec{r})} \;=\; \nabla\Phi_{(\vec{r})} \tag{2.3}$$

The scalar function Φ can be restricted through the divergence of the vector field $\vec{\Pi}$ as follows:

$$\Phi_{(\vec{r})} \;=\; \nabla\cdot\vec{\Pi}_{(\vec{r})} \tag{2.4}$$

Providing finally the equation describing the radiation of an elementary dipole in a homogenous media as follows:

$$\boxed{\vec{E}_{S\,(\vec{r})} \;=\; \nabla\Big[\nabla\cdot\vec{\Pi}_{(\vec{r})}\Big] \;+\; k^2\vec{\Pi}_{(\vec{r})}} \tag{2.5}$$

Inserting (2.1 and (2.5) in the Ampère-Maxwell relation of (1.2), using the identity $\nabla\times(\nabla\times\vec{\Pi}) \;=\; \nabla\,(\nabla\cdot\vec{\Pi}) \;-\; \nabla^2\,\vec{\Pi}$ the inhomogeneous Helmholtz equation is given by:

$$\boxed{(\nabla^2 \;+\; k^2)\,\vec{\Pi} \;=\; -i\,\frac{\vec{J}_0}{k\,\eta}} \tag{2.6}$$

A particular solution of the inhomogeneous Helmholtz equation is given as:

$$\vec{\Pi} \;=\; i\,\frac{\vec{P}_0}{k\eta}\;\frac{e^{ik\,R}}{4\Pi R} \Rightarrow i\,\frac{\vec{P}_0}{k\eta}\;\;G_{0(R)} \tag{2.7}$$

Where the scalar function $G_{0(R)}$ is the so-called Green function of the free space. Here, the distance from the dipole to the point of observation is given by R. The bottom line of this derivation is that the radiated field is expressed exclusively with the single term $\vec{\Pi}$.

2.1.2 Two-Layer Media

Considering next a two layer-media, the Green function G_0 and the corresponding Hertz vector potential for free space are not valid any more. Therefore, the Green dyad and Hertz vector potential for the radiation of a dipole near the interface is derived in the following. Depending in which half-space the dipole and the point of observation are located, the homogeneous or inhomogeneous Helmholtz equation has to be satisfied. Further, the boundary conditions at the interface must be fulfilled (see appendix A). In the following notation the first suffix signifies the layer in which the dipole is located. Whereas, the second suffix refers to the layer in which the observation point lies. In the case of imparity this corresponds to the geometrical mirrored image of the dipole at the interface as shown in fig. 2.13. Note, that the notation of the two half-spaces after Baños [3] is opposite to that commonly used in literature. If the dipole and the point of observation lie in the same half-space the scalar functions G_{11} and G_{22} are solutions of the related inhomogeneous Helmholtz equation.

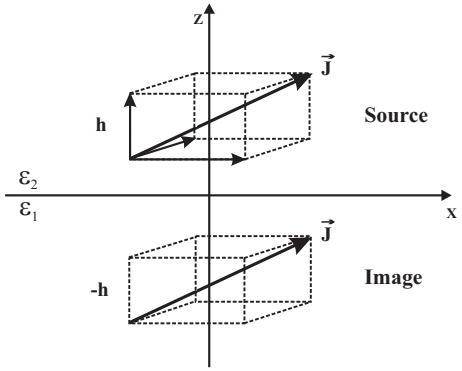

Figure 2.1: Source and Image

According to this, the functions G_{12} and G_{21} have to fulfill the corresponding homogeneous Helmholtz equation. For the special case where the dipole is situated on the ground $z = 0$ the source and its image coincide (e.g. $G_{11} + G_{12} = 0$). For the dipole embedded in the lower half-space (1) the following relations must be accomplished:

$$\begin{aligned}(\nabla^2 + k^2)\, G_{11} &= -\delta(\vec{r}) \\ (\nabla^2 + k^2)\, G_{12} &= 0\end{aligned}$$

Hence, if the dipole is placed in the upper medium (2), it turns out:

$$\begin{aligned}(\nabla^2 + k^2)\, G_{22} &= -\delta(\vec{r}) \\ (\nabla^2 + k^2)\, G_{21} &= 0\end{aligned}$$

The source and the image function must fit the boundary condition at the interface $z = 0$. This signifies that the tangential electric components of the field $(\hat{z} \times \vec{E})$ must be continuous at the interface. According to the continuity for the dipole situated in the lower half-space it yields the commensurate and sufficient condition in the following form:

$$G_{11} = G_{12} \qquad \frac{\partial G_{11}}{\partial z} = -\frac{\partial G_{12}}{\partial z} \tag{2.8}$$

In the case where the dipole is situated in the upper half-space, the corresponding boundary condition is given by:

$$G_{22} = G_{21} \qquad \frac{\partial G_{22}}{\partial z} = -\frac{\partial G_{21}}{\partial z} \tag{2.9}$$

The magnetic field $\vec{H}$ is defined as:

$$\vec{H} = -i\,k\,\eta\left(\nabla \times \vec{\Pi}\right) \tag{2.10}$$

Regarding the vertical and horizontal component of an arbitrary aligned Hertz vector, it follows from the boundary conditions the following relations.

Vertical Hertz Vector

The $\hat{z}$-component for a vertical aligned dipole is given by:

$$\begin{aligned} \vec{\Pi}_1 &= \vec{\Pi}_{1z}\hat{e}_z \\ \vec{\Pi}_2 &= \vec{\Pi}_{2z}\hat{e}_z \end{aligned}$$

Hence, with the tangential components $\hat{z} \times \vec{E}$ and $\hat{z} \times \vec{H}$ the following commensurate conditions are valid:

$$\begin{aligned} \epsilon_2 \frac{\partial \vec{\Pi}_{2z}}{\partial x} &= \epsilon_1 \frac{\partial \vec{\Pi}_{1z}}{\partial x} \\ \epsilon_2 \frac{\partial \vec{\Pi}_{2z}}{\partial y} &= \epsilon_1 \frac{\partial \vec{\Pi}_{1z}}{\partial y} \\ \epsilon_2 \frac{\partial \vec{\Pi}_{2z}}{\partial z} &= \epsilon_1 \frac{\partial \vec{\Pi}_{1z}}{\partial z} \end{aligned} \tag{2.11}$$

As a sufficient condition, it turns out for the Hertz vector:

$$\epsilon_2 \vec{\Pi}_{2z} = \epsilon_1 \vec{\Pi}_{1z} \tag{2.12}$$

Horizontal Hertz Vector

Next, a horizontal aligned dipole in the $\hat{x}\hat{y}$-plane is discussed. For a given distance from the interface, the Hertz vector is defined as:

$$\begin{aligned} \vec{\Pi}_1 &= \vec{\Pi}_{1x}\hat{e}_x + \vec{\Pi}_{1z}\hat{e}_z \\ \vec{\Pi}_2 &= \vec{\Pi}_{2x}\hat{e}_x + \vec{\Pi}_{2z}\hat{e}_z \end{aligned}$$

$$\begin{aligned} \vec{\Pi}_1 &= \vec{\Pi}_{1y}\hat{e}_y + \vec{\Pi}_{1z}\hat{e}_z \\ \vec{\Pi}_2 &= \vec{\Pi}_{2y}\hat{e}_y + \vec{\Pi}_{2z}\hat{e}_z \end{aligned}$$

Similar to the vertical aligned dipole it follows from the boundary condition the commensurate conditions:

$$k_1^2 \frac{\partial \vec{\Pi}_{1x}}{\partial z} = k_2^2 \frac{\partial \vec{\Pi}_{2x}}{\partial z} \tag{2.13}$$

$$\frac{\partial \vec{\Pi}_{1x}}{\partial x} + \frac{\partial \vec{\Pi}_{1z}}{\partial z} = \frac{\partial \vec{\Pi}_{2x}}{\partial x} + \frac{\partial \vec{\Pi}_{2z}}{\partial z} \tag{2.14}$$

The sufficient condition for the Hertz vector are given by:

$$\epsilon_2 \vec{\Pi}_{1x} = \epsilon_1 \vec{\Pi}_{2x} \tag{2.15}$$

$$\epsilon_2 \vec{\Pi}_{1z} = \epsilon_1 \vec{\Pi}_{2z} \tag{2.16}$$

2.1.3 Definition of the Hertz Vector Potential

Next, two different Hertz vectors are presented in accordance to the case where the dipole is situated either in the upper or lower half-space. The two Hertz vectors $\vec{\Pi}$ are defined by a set of essential integrals [3]. Considering a dipole in the upper half-space (2), it follows after some manipulation:

$$\begin{aligned} \vec{\Pi}_{(\vec{r},\vec{r}\prime)} = C_0 \Bigg\{ & \left[(G_{22} - G_{21} + U_{22})\hat{x} + \frac{\partial W_{22}}{\partial x}\hat{z} \right] I_x \\ & + \left[(G_{22} - G_{21} + U_{22})\hat{y} + \frac{\partial W_{22}}{\partial y}\hat{z} \right] I_y \\ & + \left[(G_{22} - G_{21} + \frac{k_1^2}{k_2^2}(U_{22} + \frac{\partial W_{22}}{\partial z}) \right] \hat{z} I_z \Bigg\} \end{aligned} \tag{2.17}$$

In contrast for the case where the dipole is situated in the soil (1), it follows:

$$\begin{aligned} \vec{\Pi}_{(\vec{r},\vec{r}\prime)} = C_0 \Bigg\{ & \left[U_{12}\hat{x} + \frac{\partial W_{12}}{\partial x}\hat{z} \right] I_x \\ & + \left[U_{12}\hat{x} + \frac{\partial W_{12}}{\partial y}\hat{z} \right] I_y \\ & + \left[U_{12} + \frac{\partial W_{12}}{\partial z} \right] \hat{z} I_z \Bigg\} \end{aligned} \tag{2.18}$$

Where the constant C_0 is defined by:

$$C_0 = \frac{i\omega}{4\pi} \frac{\mu_2}{k_2^2} p$$

The set of essential Sommerfeld integrals is defined as follows:

$$G_{22} = \frac{1}{2\pi} \int_{-\infty}^{+\infty}\int \frac{1}{\gamma_2}\, e^{-\gamma_2|z'-z|}\, e^{i[\xi(x-x')+\eta(y-y')]}\, d\xi\, d\eta \tag{2.19}$$

$$G_{21} = \frac{1}{2\pi} \int_{-\infty}^{+\infty}\int \frac{1}{\gamma_2}\, e^{-\gamma_2(z'+z)}\, e^{i[\xi(x-x')+\eta(y-y')]}\, d\xi\, d\eta \tag{2.20}$$

$$G_{11} = \frac{1}{2\pi} \int_{-\infty}^{+\infty}\int \frac{1}{\gamma_1}\, e^{-\gamma_1|z'+z|}\, e^{i[\xi(x-x')+\eta(y-y')]}\, d\xi\, d\eta \tag{2.21}$$

$$G_{12} = \frac{1}{2\pi} \int_{-\infty}^{+\infty}\int \frac{1}{\gamma_1}\, e^{-\gamma_1(z'-z)}\, e^{i[\xi(x-x')+\eta(y-y')]}\, d\xi\, d\eta \tag{2.22}$$

The attenuation in the considered layer is given by the factors γ_1 and γ_2 in the following way:

$$\begin{aligned} \gamma_1 &= \sqrt{\xi^2 + \eta^2 - k_1^2} \quad \mathcal{R}e\,\gamma_1 \geq 0 \\ \gamma_2 &= \sqrt{\xi^2 + \eta^2 - k_2^2} \quad \mathcal{R}e\,\gamma_2 \geq 0 \end{aligned}$$

Here, the first subscript refers to the layer in which the source is located , and the second subscript refers to the distance from the point of observation to the point source or to its image as outlined in fig. 2.13. The set of U_{ij} is defined by:

$$U_{22} = \frac{1}{2\pi} \int_{-\infty}^{+\infty}\int \frac{2}{M}\, e^{-\gamma_2(z'+z)}\, e^{i[\xi(x-x')+\eta(y-y')]}\, d\xi\, d\eta \tag{2.23}$$

$$U_{21} = \frac{1}{2\pi} \int_{-\infty}^{+\infty}\int \frac{2}{M}\, e^{\gamma_1 z - \gamma_2 z'}\, e^{i[\xi(x-x')+\eta(y-y')]}\, d\xi\, d\eta \tag{2.24}$$

$$U_{11} = \frac{1}{2\pi} \int_{-\infty}^{+\infty}\int \frac{2}{M}\, e^{-\gamma_1(z'-z)}\, e^{i[\xi(x-x')+\eta(y-y')]}\, d\xi\, d\eta \tag{2.25}$$

$$U_{12} = \frac{1}{2\pi} \int_{-\infty}^{+\infty}\int \frac{2}{M}\, e^{-\gamma_1 z' - \gamma_2 z}\, e^{i[\xi(x-x')+\eta(y-y')]}\, d\xi\, d\eta \tag{2.26}$$

Finally, the set of W_{ij} is given by:

$$W_{22} = \frac{1}{2\pi} \iint_{-\infty}^{+\infty} g\, e^{-\gamma_2(z'+z)}\, e^{i[\xi(x-x')+\eta(y-y')]}\, d\xi\, d\eta \tag{2.27}$$

$$W_{21} = \frac{1}{2\pi} \iint_{-\infty}^{+\infty} g\, e^{\gamma_1 z - \gamma_2 z'}\, e^{i[\xi(x-x')+\eta(y-y')]}\, d\xi\, d\eta \tag{2.28}$$

$$W_{11} = \frac{1}{2\pi} \iint_{-\infty}^{+\infty} g\, e^{-\gamma_1(z'-z)}\, e^{i[\xi(x-x')+\eta(y-y')]}\, d\xi\, d\eta \tag{2.29}$$

$$W_{12} = \frac{1}{2\pi} \iint_{-\infty}^{+\infty} g\, e^{-\gamma_1 z' - \gamma_2 z}\, e^{i[\xi(x-x')+\eta(y-y')]}\, d\xi\, d\eta \tag{2.30}$$

The quantities M, N, and g are the Sommerfeld denominators determined as follows:

$$M = \gamma_1 + \gamma_2, \quad N = k_2^2\,\gamma_1 + k_1^2\,\gamma_2, \quad g = \frac{2(\gamma_1 - \gamma_2)}{N} \tag{2.31}$$

2.2 Discrete Complex Image Method

The radiation of a single elementary dipole near the interface of two dielectric half-spaces was discussed in the previous section. Where the Hertz vector potential $\vec{\Pi}$ was described by the Sommerfeld integrals G, U and W having highly oscillating kernels. In section 2.5, the radiation from a given surface current distribution of an object is approximated by an assembly of such elementary dipoles. Therefore, the calculation of the corresponding functions G, U and W by classical integration techniques would be much time consuming and not robust due to the integral kernels. It exists some approximations more or less accurate for calculating these integrals. In this work, the more efficient and robust DCIM technique is considered and was implemented in the existing DIFFRA code. The complex image method is reported in the article of Michalski and Mosig [50] and has gained importance in the past. The method was developed right from the start to compute the Sommerfeld integrals. Recently, a direct numerical method was published by Fang [22] and written down in its final form by Chow and al. [15]. Here, the innovation consists in the approximation of the Sommerfeld integral by a series of exponential functions each weighted by a complex coefficient.

2.2.1 Sommerfeld Identity

The DCIM is based on the Sommerfeld identity (IS) introduced in section 1.2. According to (1.22) the Sommerfeld identity is rewritten in the form:

$$IS(\xi) = \frac{e^{i\,k_0\,R}}{R} = \frac{i}{2} \int_{\infty e^{i\pi}}^{\infty} \frac{1}{\sqrt{k_0^2 - \xi^2}}\, H_0^1[\rho\,\xi]\; e^{i\sqrt{k_0^2-\xi^2}\,|z|}\; \xi\, d\xi \tag{2.32}$$

Where the definitions used in the report of MOTHESIM [51] are considered for the variables ζ, and ξ:

$$\zeta = \gamma = \sqrt{k_0 - \xi^2} \tag{2.33}$$

$$\xi = \sqrt{k_x^2 + k_y^2} \tag{2.34}$$

$$R = \sqrt{\rho^2 + z^2} \tag{2.35}$$

In the above mentioned expressions the variables ζ and ξ correspond to the wave numbers k_z and k_ρ in the $\hat{x} - \hat{y}$ plane. The co-domain of the Hankel function H_0^1 in (2.32) is not defined for negative real arguments. Therefore, the negative reel axis represents a branch cut and the integration path of (2.32) is chosen along C_0 as shown in fig. 2.2 .

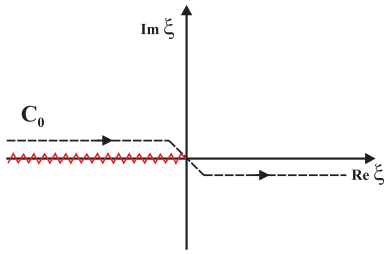

Figure 2.2: Brunch cut for the Hankel function

Regarding (2.33) it follows that the variable ζ may have two possible determinations satisfying the relation. Hence, the Sommerfeld identity (2.32) is not clearly defined and cannot be integrated. This problem is solved if the co-domain of the variable ξ is precised in such a manner, so that ζ is clearly defined. The radiation condition (1.1) implies that the field must vanish at infinity. Substituting (2.33) in (2.32) it follows that for the limit $\mid z \mid \rightarrow \infty$ the imaginary part of ζ is fixed through:

$$Im\,\zeta > 0 \tag{2.36}$$

The restriction (2.36) defines the top of a Riemann sheet. Hence, it follows for the bottom Riemann sheet and for the cut between both sheets:

$$Im\,\zeta < 0 \quad Bottom\ Riemann\ sheet$$

$$Im\,\zeta = 0 \quad Brunch\ cut \tag{2.37}$$

Next, the co-domain of the variable ξ is defined in accordance to the radiation condition (2.36), leading to the substitutions:

$$k_0 = k_0' + ik_0''$$

$$\xi = \xi' + i\xi''$$

in (2.33), yielding:

$$\zeta \;=\; \sqrt{k_0'^2 - k_0''^2 \;-\; \left[\,\xi'^2 - \xi''^2\,\right] \;+\; 2i\,\left[\,k_0' k_0'' \;-\; \xi'\xi''\,\right]} \tag{2.38}$$

The brunch cut $Im\,\zeta \;=\; 0$ is given by (2.38) as follows:

$$\xi'\xi'' \;=\; k_0' k_0'' \tag{2.39}$$

$$k_0'^2 - k_0''^2 \;>\; \xi'^2 - \xi''^2 \tag{2.40}$$

According to (2.39) the brunch cut corresponds to a hyperbola in the first and third quadrant in the complex ξ plane. Further, the condition $Re\,\zeta \;=\; 0$ leads to:

$$k_0'^2 - k_0''^2 \;=\; \xi'^2 - \xi''^2 \tag{2.41}$$

$$\xi'\xi'' \;=\; k_0' k_0'' \tag{2.42}$$

and corresponds to an extension of the two hyperbolas. In accordance with the two possible values of the wave number $\pm k_0$ the co-domain of the variable ξ is finally pointed out in fig. 2.3 as the grey area.

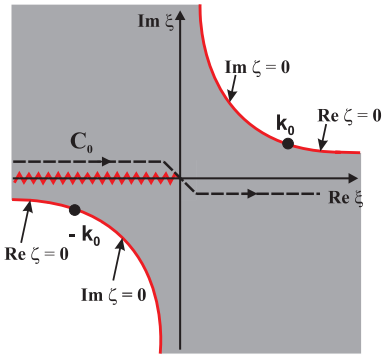

Figure 2.3: Co-domain ξ for the condition $Im\zeta > 0$

In order to derive the DCIM procedure the Sommerfeld integrals G, U and W are rewritten in the general form:

$$I_{(\xi)} \;=\; \frac{i}{2} \int\limits_{\infty e^{i\pi}}^{\infty} F_{1(\xi)}\; \frac{H_0^1\,[\rho\,\xi]}{\sqrt{k_0^2 \;-\; \xi^2}}\;\; e^{i\sqrt{k_0^2 - \xi^2}\,|z|}\;\, \xi\; d\xi \tag{2.43}$$

The kernel $F_{1(\xi)}$ in (2.43) is decomposed in a series of complex coefficient a_n and b_n as follows

$$F_{1(\xi)} \;=\; \sum_{n=1}^{N} \; a_n\; e^{-b_n \sqrt{k_0^2 - \xi^2}} \qquad\qquad a_n, b_n \in \mathbb{C} \tag{2.44}$$

Note, that by setting the kernel $F_{1(\xi)}$ equal to one, the classical Sommerfeld identity is again obtained, expressed by:

$$F_{1(\xi)} \;=\; 1 \Longrightarrow IS \;=\; \frac{2}{i}\,\frac{e^{i\,k_0\,R}}{R} \tag{2.45}$$

The basic idea of the DCIM consists in replacing the integration of the single terms of the series (2.45) by its corresponding Sommerfeld identity (2.32). In the following this will be done in the complex ζ plane because here a more suitable linear integration path is given.
First of all, the problems occurring at the numerical calculation of the Sommerfeld integrals are discussed. The soil may be considered as an assembly of dielectric layers, as pointed out in fig. 2.4. According to Felsen and Marcuvitz [23], the kernel $F_{1(\xi)}$ in (2.43) has branch point singularities in the case where the source is embedded in the soil or on the interface. In this case surface waves are generated.

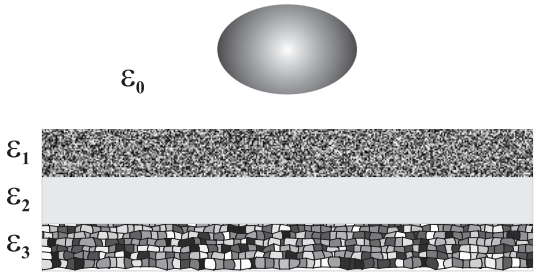

Figure 2.4: Dielectric layers

The related singularities and the integration path C_0 are shown in fig 2.5. In view of the numerical stability one should not pass too close at the singularities. Therefore, the path C_0 is spread into the path C_1 as shown in fig. 2.7. In accordance with Chow [15] the distance between the two points A and B is set equal to $5k_0$.

$$T_0 \;=\; 5k_0 \tag{2.46}$$

Another more smarter solution for calculating the Sommerfeld integrals would consists in folding the integration path C_1 in such a manner, that it circles around the residual point k_0.

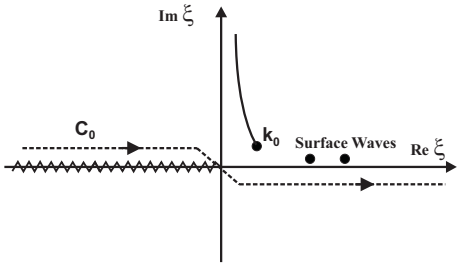

Figure 2.5: Path C_0 in the ξ plane

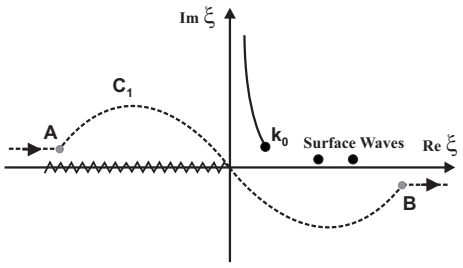

Figure 2.6: Modified path C_1 in the ξ plane

The folding of the integration path around the point k_0 can be realized applying a transformation into the complex ζ plane. In the next section this transformation is discussed.

2.2.2 Transformation to the ζ plane

The integration of the Sommerfeld integrals is performed after the variable ζ which corresponds to the wave number k_z. In contrast ξ describes the wave number k_ρ in the horizontal $\hat{x} - \hat{y}$ plane. According to (2.33) both components ζ and ξ are related by:

$$\xi = \sqrt{k^2 - \zeta^2} \tag{2.47}$$

$$d\xi = -\frac{\zeta}{\sqrt{k^2 - \zeta^2}}\, d\zeta \tag{2.48}$$

Substituting (2.47) and (2.48) in (2.32), the Sommerfeld identity attributed to the ζ plane is given as follows :

$$IS(\zeta) = \frac{e^{i\,k\,R}}{R} = \frac{i}{2} \int\limits_{C_1(\zeta)} H_0^1 \left[\rho \sqrt{k^2 - \zeta^2}\right]\, e^{i\,\zeta|z|}\, d\zeta \tag{2.49}$$

The important step consists herein that the integration path $C_0(\xi)$ respectively the path $C_1(\xi)$ is transformed in the ζ plane into the paths $C_0(\zeta)$ and $C_1(\zeta)$ as shown in the fig. 2.7 and fig. 2.8. The transformation into the $C_1(\zeta)$ path can be performed as no other singularities are given in the first quadrant.

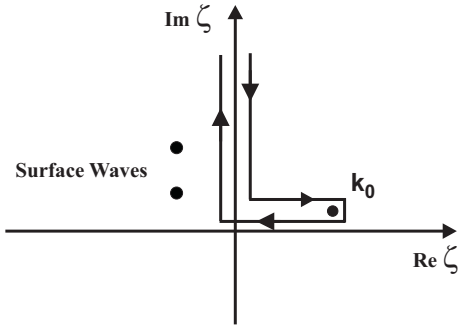

Figure 2.7: Path C_0 in the ζ plane

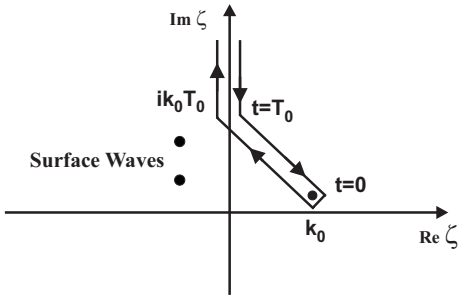

Figure 2.8: Path C_1 in the ζ plane

According to fig. 2.8, the integration path $C_1(\zeta)$ starts from $\infty e^{\frac{i}{2}}$, circles around k_0 and goes back again to $\infty e^{i\frac{1}{2}}$. The two gradients along the way to and back from k_0 are of opposite sign. One may think that due to this circumstance the integral is equal to zero. Indeed, this is not the case as the Hankel function has different values for negative and positive arguments. Hence, the two integration sections don't annul each other. After the relation (9.1.39) in [1], it holds:

$$H_\nu^1 \left[z e^{i\pi}\right] = -e^{-i\nu\pi} H_\nu^2 [z]$$

In the same manner as (2.43) the general Sommerfeld integral representation according to the ζ plane is given by:

$$I(\zeta) = \frac{i}{2} \int\limits_{C_1(\zeta)} F_1(\zeta)\, H_0^1 \left[\rho \sqrt{k^2 - \zeta^2}\right]\, e^{i\,\zeta|z|}\, d\zeta \tag{2.50}$$

Substituting (2.47) in (2.44) it yields for the kernel $F_{1(\zeta)}$:

$$F_{1(\zeta)} \;=\; \sum_{n=1}^{N} \; a_n \; e^{-b_n \, \zeta} \qquad\qquad a_n, b_n \in \mathbb{C} \tag{2.51}$$

Now, the integration of the Sommerfeld integrals given in (2.49) can be easily performed using the straight integration path $C_{1(\zeta)}$ enclosing the residual k_0. Considering fig. 2.8, the parametrization $\zeta_{(t)} \;=\; m \cdot t \;+\; b$ is introduced for the line $C_{1(\zeta)}$, where t is a reel variable. The quantities m and b of the straight integration path are determined by the two points:

$$\begin{aligned} t \;&=\; 0 \Longrightarrow b \;=\; k \\ t \;&=\; T_0 \Longrightarrow m \;=\; k(i \;-\; \frac{1}{T_0}) \end{aligned}$$

At the end of the day the parametrization of $C_{1[\zeta(t)]}$ is given in the form:

$$\zeta_{(t)} \;=\; k \left[it \;+\; \left(1 \;-\; \frac{t}{T_0} \right) \right] \qquad t \in \mathbb{R} \tag{2.52}$$

It exists numerical algorithms like the Method of Prony [63] or the Pencil of Function Method which decompose a complex function $\tilde{F}_{(t)}$ into a series of complex exponentials, where t is a reel variable, given as follows:

$$f_{(t)} \;=\; \sum_{n=1}^{N} \; A_n \; e^{B_n \, t} \qquad t \in \mathbb{N} \quad A_n \cap B_n \in \mathbb{C} \tag{2.53}$$

Substituting the parametrization form (2.52) in (2.51) and comparing with (2.53), the complex coefficient a_n and b_n of the series (2.44) are fixed by:

$$a_n \;=\; A_n \; e^{b_n \, k} \tag{2.54}$$

$$b_n \;=\; \frac{B_n \, T_0}{k \, (1 \;-\; i T_0)} \tag{2.55}$$

Thus, by substituting the coefficient a_n and b_n in the series (2.51) it follows the decomposition of the general Sommerfeld integral (2.49) in the form:

$$I_{(\zeta)} \;=\; \frac{i}{2} \sum_{n=1}^{N} \; a_n \int\limits_{C_1(\zeta)} \; H_0^1 \left[\rho \, \sqrt{k^2 - \zeta^2} \right] \; e^{i \, \zeta(|z| \, + \, i b_n)} \; d\zeta \tag{2.56}$$

Applying the Sommerfeld identity (2.49) for every single term in the series, the CPU time consuming integral calculation is replaced now by a series of discrete complex images:

$$\boxed{I_{(\zeta)} \;=\; \frac{2}{i} \left[a_1 \, \frac{e^{i \, k \, R_1}}{R_1} \;+\; a_2 \, \frac{e^{i \, k \, R_2}}{R_2} \;+\; \cdots \;+\; a_n \, \frac{e^{i \, k \, R_n}}{R_n} \right]} \tag{2.57}$$

In (2.56) the variable z has been modified, thus the distance R_n between source and observation point in (2.57) is defined as:

$$R_n^2 \;=\; \rho^2 \;+\; (z \;+\; ib_n)^2 \tag{2.58}$$

Up to now the problem accorded to the surface waves has been solved. Another problem is given for the case where the kernel $F(\zeta)$ has a finite value F_{QS} at the limit $\zeta \to \infty$. The integral cannot be computed without using appropriate and time consuming integration techniques. Moreover, the direct application of the DCIM procedure does not converge with an upper limit of integration T_0 defined by (2.46). Here, in the configuration space the limit $\zeta \to \infty$ corresponds to a location at the source $|\vec{r} - \vec{r}'| \;=\; 0$. Therefore, F_{QS} is called "Quasi Static" (QS). Thus, in order to compute the integral, F_{QS} must first be subtracted from the kernel $F(\zeta)$. After the calculation the value of the integral $I_{QS(\zeta)}$ is again added. Where the integral value must be finite. Hence, one decompose the integral in two parts as follows:

$$I_{[\zeta(t)]} \;=\; I_{I(\zeta)} \;+\; I_{QS(\zeta)} \tag{2.59}$$

$$I_{[\zeta(t)]} \;=\; \int\limits_{C_1(t)} [F \;-\; F_{QS}]\; H_0^1\; e^{i\,\zeta(t)\,|z|}\; dt \;+\; I_{QS} \tag{2.60}$$

The value of the Sommerfeld integral for the quasi static kernel F_{QS} is defined by:

$$I_{QS(\zeta)} \;=\; \int\limits_{C_1(\zeta)} F_{QS}\; H_0^1\; e^{i\,\zeta\,|z|}\; d\zeta \tag{2.61}$$

One important property of the complex image method is that the complex coefficients a_n and b_n are independent of the location source-observation point. Hence, they have to be calculated only once in the Method of Moments (MoM) program, which will be introduced in the next section. Thus, the numerical CPU time consuming calculation of the integrals is significantly slashed. Additionally, the computing accuracy is increased using the robust DCIM technique.

2.2.3 Essential Sommerfeld Integrals

According to section 2.1.3, the Hertz vector for an elementary dipole located near the interface of a two-layer media was described by a set of essential Sommerfeld integrals in the complex ξ plane. Due to the transformation into the ζ plane, the set and the corresponding integral kernels are rewritten in terms of ζ as follows:

$$\begin{aligned}
G_{11}(\zeta) &= \frac{i}{2}\int_C H_0^1\left[\rho\sqrt{k_0^2-\zeta^2}\right] e^{i\,\zeta_1(|h|-z)}\,d\zeta \qquad z\le 0\\
G_{12}(\zeta) &= \frac{i}{2}\int_C H_0^1\left[\rho\sqrt{k_0^2-\zeta^2}\right] e^{i\,\zeta_1|h|\,+\,i\,\zeta_2 z}\,d\zeta \qquad z\ge 0\\
G_{22}(\zeta) &= \frac{i}{2}\int_C H_0^1\left[\rho\sqrt{k_0^2-\zeta^2}\right] e^{i\;\zeta_2(|h|+z)}\,d\zeta \qquad z\ge 0\\
G_{21}(\zeta) &= \frac{i}{2}\int_C H_0^1\left[\rho\sqrt{k_0^2-\zeta^2}\right] e^{i\,\zeta_2|h|\,-\,i\,\zeta_1 z}\,d\zeta \qquad z\le 0
\end{aligned} \tag{2.62}$$

$$\begin{aligned}
U_{11}(\zeta) &= \frac{i}{2}\int_C F_U(\zeta)\;\; H_0^1\left[\rho\sqrt{k_0^2-\zeta^2}\right] e^{i\,\zeta_1(|h|-z)}\,d\zeta \qquad z\le 0\\
U_{12}(\zeta) &= \frac{i}{2}\int_C F_U(\zeta)\;\; H_0^1\left[\rho\sqrt{k_0^2-\zeta^2}\right] e^{i\,\zeta_1|h|\,+\,i\,\zeta_2 z}\,d\zeta \qquad z\ge 0\\
U_{22}(\zeta) &= \frac{i}{2}\int_C F_U(\zeta)\;\; H_0^1\left[\rho\sqrt{k_0^2-\zeta^2}\right] e^{i\;\zeta_2(|h|+z)}\,d\zeta \qquad z\ge 0\\
U_{21}(\zeta) &= \frac{i}{2}\int_C F_U(\zeta)\;\; H_0^1\left[\rho\sqrt{k_0^2-\zeta^2}\right] e^{i\,\zeta_2|h|\,-\,i\,\zeta_1 z}\,d\zeta \qquad z\le 0
\end{aligned} \tag{2.63}$$

Where the kernels of the Sommerfeld integrals U are given by:

$$F_U(\zeta) = -i\,\frac{\zeta}{\zeta + \sqrt{k_1^2 - k_0^2 + \zeta^2}} \tag{2.64}$$

$$
\begin{aligned}
W_{11}(\zeta) &= \int_C F_W(\zeta)\, H_0^1\left[\rho\sqrt{k_0^2-\zeta^2}\right]\, e^{i\,\zeta_1(|h|-z)}\, d\zeta \qquad z \le 0 \\
W_{12}(\zeta) &= \int_C F_W(\zeta)\, H_0^1\left[\rho\sqrt{k_0^2-\zeta^2}\right]\, e^{i\,\zeta_1|h|\,+\,i\,\zeta_2 z}\, d\zeta \qquad z \ge 0 \\
W_{22}(\zeta) &= \int_C F_W(\zeta)\, H_0^1\left[\rho\sqrt{k_0^2-\zeta^2}\right]\, e^{i\ \zeta_2(|h|+z)}\, d\zeta \qquad z \ge 0 \\
W_{21}(\zeta) &= \int_C F_W(\zeta)\, H_0^1\left[\rho\sqrt{k_0^2-\zeta^2}\right]\, e^{i\,\zeta_2|h|\,-\,i\,\zeta_1 z}\, d\zeta \qquad z \le 0
\end{aligned}
\tag{2.65}
$$

The kernel of W is defined by:

$$
\begin{aligned}
F_W(\zeta) &= -\frac{\zeta\left[\sqrt{k_1^2\,-\,k_0^2\,+\,\zeta^2}\,-\,\zeta\right]}{k_1^2\zeta\,+\,k_0^2\sqrt{k_1^2\,-\,k_0^2\,+\,\zeta^2}} \\
&= -\left(\frac{1\,-\,\epsilon_r\mu_r}{\epsilon_r\mu_r}\right)\frac{\zeta}{[\zeta\,+\,\sqrt{k_1^2-k_0^2+\zeta^2}]\,[\zeta\,+\,\frac{1}{\epsilon_r\mu_r}\sqrt{k_1^2-k_0^2+\zeta^2}]}
\end{aligned}
\tag{2.66}
$$

Where $\frac{k_1}{k_0}$ was substituted by $\sqrt{\epsilon_r\mu_r}$. The derivation of $W(\zeta)$ after the $\hat{z}$ co-ordinate yields:

$$
\begin{aligned}
\tfrac{\partial W_{11}(\zeta)}{\partial z} &= \int_C F_{W_z}(\zeta)\, H_0^1\left[\rho\sqrt{k_0^2-\zeta^2}\right]\, e^{i\,\zeta_1(|h|-z)}\, d\zeta \qquad z \le 0 \\
\tfrac{\partial W_{12}(\zeta)}{\partial z} &= \int_C F_{W_z}(\zeta)\, H_0^1\left[\rho\sqrt{k_0^2-\zeta^2}\right]\, e^{i\,\zeta_1|h|\,+\,i\,\zeta_2 z)}\, d\zeta \qquad z \ge 0 \\
\tfrac{\partial W_{22}(\zeta)}{\partial z} &= \int_C F_{W_z}(\zeta)\, H_0^1\left[\rho\sqrt{k_0^2-\zeta^2}\right]\, e^{i\ \zeta_2(|h|+z)}\, d\zeta \qquad z \ge 0 \\
\tfrac{\partial W_{21}(\zeta)}{\partial z} &= \int_C F_{W_z}(\zeta)\, H_0^1\left[\rho\sqrt{k_0^2-\zeta^2}\right]\, e^{i\,\zeta_2|h|\,-\,i\,\zeta_1 z)}\, d\zeta \qquad z \le 0
\end{aligned}
\tag{2.67}
$$

Where $F_{W_z}(\zeta)$ is set to:

$$
F_{W_z}(\zeta) = -\,i\left(\frac{1-\epsilon_r\mu_r}{\epsilon_r\mu_r}\right)\frac{\zeta^2}{\left[\zeta\,+\,\sqrt{k_1^2\,-\,k_0^2\,+\,\zeta^2}\right]\left[\zeta\,+\,\frac{1}{\epsilon_r\mu_r}\sqrt{k_1^2\,-\,k_0^2\,+\,\zeta^2}\right]}
\tag{2.68}
$$

According to section 2.2.2, the quasi-static approximation of the kernels F_U, F_W and $\frac{dF_W(\zeta)}{dz}$ are given by:

$$F_{UQS(\zeta)} = \lim_{\zeta\to\infty} F_{U(\zeta)} = \frac{1}{2} \tag{2.69}$$

$$F_{WQS(\zeta)} = \lim_{\zeta\to\infty} F_{W(\zeta)} = 0 \tag{2.70}$$

$$\frac{dF_{WQS(\zeta)}}{dz} = \lim_{\zeta\to\infty} \frac{dF_{W(\zeta)}}{dz} = -\frac{i}{2}\left(\frac{1-\epsilon_r\mu_r}{\epsilon_r\mu_r}\right)\left(\frac{1}{1+\frac{1}{\epsilon_r\mu_r}}\right) \tag{2.71}$$

2.2.4 Numerical Results of the DCIM

The results obtained after the DCIM and the direct calculation of the Sommerfeld integrals for the complex Green functions U and W are confronted next. Whereas, 10 discrete complex images were calculated according to U and 9 discrete images according to W. A precision of 10^{-5} is achieved in the numerical results. This efficient analogy is pointed out in fig. 2.9 to fig. 2.12 for the reel and imaginary parts. The discrete complex image method is on one hand a precise method but more import represents a robust and fast numerical algorithm. In view of the Method of Moments based calculation the decomposition into a series of complex exponentials is independent of the location of the source and the observation point. Hence, it has to be computed only once in the program which decreases the CPU time significantly. The remaining CPU time is similar to the quasi-static calculation.

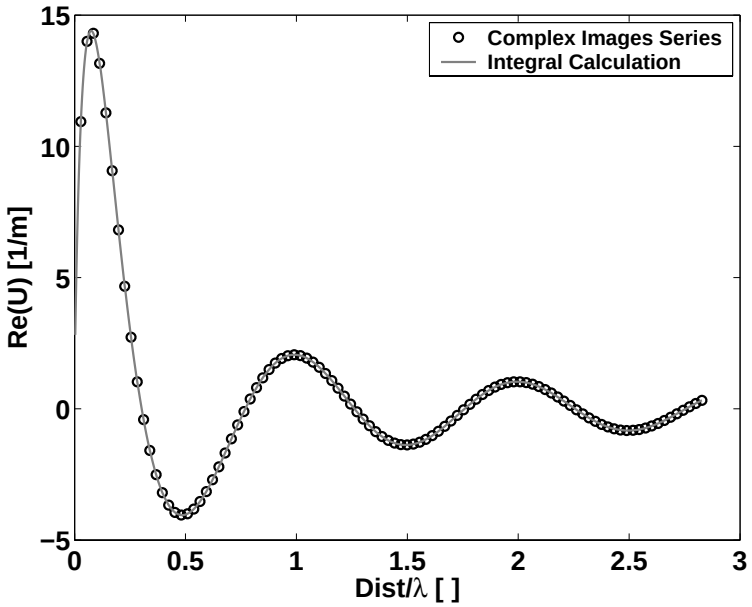

Figure 2.9: $\Re(U)$: DCIM versus the integral calculation [$\epsilon_1 = 9.6,\ f = 1GHz$]

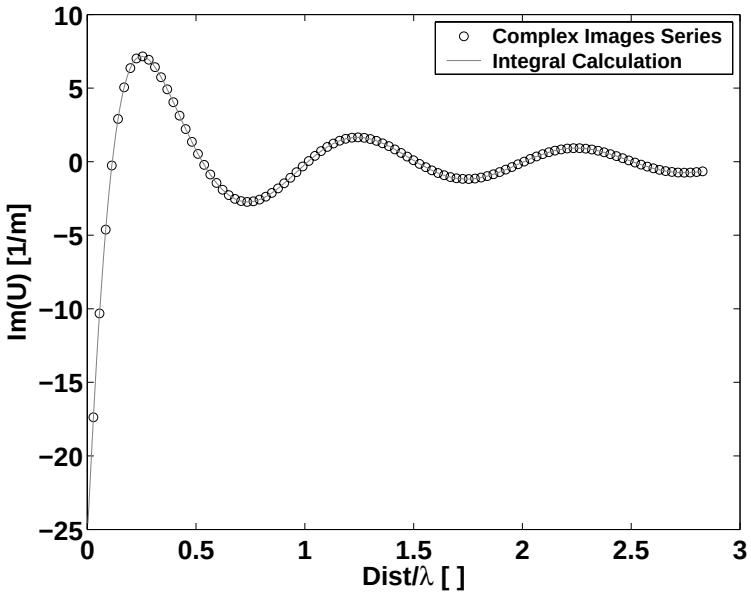

Figure 2.10: $\Im(U)$: DCIM versus the integral calculation $[\epsilon_1 = 9.6,\ f = 1GHz]$

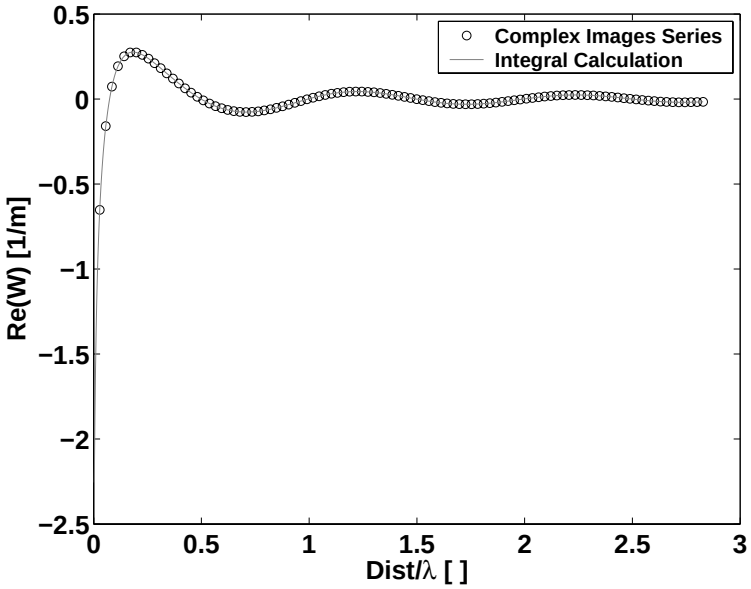

Figure 2.11: $\Re(W)$: DCIM versus the integral calculation $[\epsilon_1 = 9.6,\ f = 1GHz]$

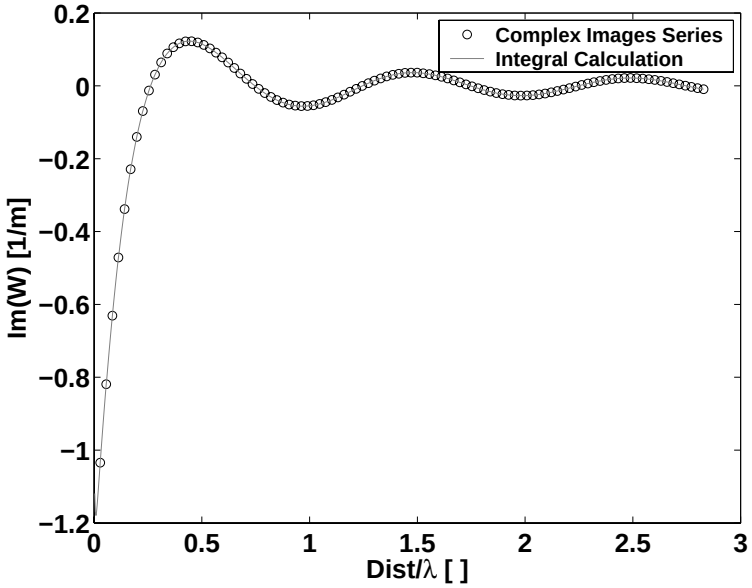

Figure 2.12: $\Im(W)$: DCIM versus the integral calculation [$\epsilon_1 = 9.6,\ f = 1GHz$]

2.3 Scalar and Vector Potential

The two first Maxwell equations of the set (1.2) are rewritten first in terms of the effective dielectric properties as follows:

$$\nabla \times \vec{H}_{(\vec{r},\omega)} = -i\omega\epsilon_0\epsilon_{eff}(\omega)\vec{E}_{(\vec{r},\omega)} + \vec{J}_{0(\vec{r}\,')} \tag{2.72}$$

$$\nabla \times \vec{E}_{(\vec{r},\omega)} = i\omega\mu_0\mu\vec{H}_{(\vec{r},\omega)} \tag{2.73}$$

2.3.1 Green Dyad for Free Space

The radiation of an elementary dipole in free space can also be expressed in terms of a vector and scalar potential. In comparison to the equivalent Hertz vector potential, both potential terms are related via the Lorentz gauge presented in section 2.4. In the same manner as the Hertz vector potential, the magnetic field, as its divergence is equal to zero, may be expressed as the curl of another vector. Hence, for a homogenous media the magnetic field $\vec{H}$ is defined according to the magnetic vector potential $\vec{A}$ in the following way:

$$\vec{H}_{(\vec{r})} = \frac{1}{\mu_0\mu}\nabla \times \vec{A}_{(\vec{r})} \tag{2.74}$$

Comparing with definition (2.1) one gets the relation:

$$\vec{A}_{(\vec{r})} = \frac{k^2}{i\,\omega}\,\vec{\Pi}_{(\vec{r})} \tag{2.75}$$

Substituting next (2.74) in (2.73), it yields:

$$\nabla \times \left(\vec{E}_{s\,(\vec{r})} - i\omega\vec{A}_{(\vec{r})}\right) = 0 \tag{2.76}$$

Any curl-free vector is the gradient of some scalar. Hence, for the radiated field $\vec{E}_s$ of a dipole, one may set:

$$\vec{E}_{s(\vec{r})} - i\omega\vec{A}_{(\vec{r})} = -\nabla\Phi_{(\vec{r})} \tag{2.77}$$

Going on by substituting (2.77) and (2.74) in (2.72), considering further a non magnetic media $\mu = 1$, it turns out:

$$\nabla \times \nabla \times \vec{A}_{(\vec{r})} - k^2\,\vec{A}_{(\vec{r})} = \vec{J}_{0\,(\vec{r}\,)} + i\omega\epsilon_0\mu_0\epsilon_{eff}(\omega)\nabla\Phi_{(\vec{r})} \tag{2.78}$$

Using the identity $\nabla \times (\nabla \times \vec{A}) = \nabla\,(\nabla \cdot \vec{A}) - \nabla^2\,\vec{A}$ one gets in a first step:

$$\nabla\left(\nabla \cdot \vec{A}_{(\vec{r})}\right) - \nabla^2\vec{A}_{(\vec{r})} - k^2\vec{A}_{(\vec{r})} = \vec{J}_{0\,(\vec{r}\,')} + i\omega\epsilon_0\mu_0\,\epsilon_{eff}\,\nabla\Phi_{(\vec{r})} \tag{2.79}$$

No restriction has been made yet on the magnetic potential $\vec{A}_{(\vec{r})}$. Only $\nabla \times \vec{A}$ was specified in (2.74). Thus, one is free in the choice of the scalar quantity $\nabla \cdot \vec{A}$ as the curl freeness still remains by adding a scalar field to the vector field $\vec{A}$. Defining the scalar potential with the divergence of the vector potential as follows:

$$\Phi_{(\vec{r})} = -\frac{i\,\omega}{k^2}\,\nabla \cdot \vec{A}_{(\vec{r})} \tag{2.80}$$

Expression (2.79) is simplified to the Helmholtz equation:

$$\left(\nabla^2 + k^2\right)\vec{A}_{(\vec{r})} = -\vec{J}_{0\,(\vec{r}\,')} \tag{2.81}$$

Generally, the above mentioned vector potential $\vec{A}$ is given by the Green dyad in the form:

$$\vec{A}_{(\vec{r})} = \overline{\overline{G}}_{A(\vec{r},\vec{r}\,')} \cdot \vec{J}_{0\,(\vec{r}\,')} \tag{2.82}$$

Hence, the scalar potential Φ is given by:

$$\Phi_{(\vec{r})} = -\frac{i\omega}{k^2}\,\nabla \cdot \left[\overline{\overline{G}}_{A(\vec{r},\vec{r}\,')} \cdot \vec{J}_{0\,(\vec{r}\,')}\right] \tag{2.83}$$

Where the vector $\vec{r}$ describes the point of observation and $\vec{r}\,\prime$ the location of the elementary dipole.

2.3.2 Modified dyadic Green function

In this section, the modified dyadic Green function $\overline{\overline{G}}_A$ for the magnetic vector potential $\vec{A}_{(\vec{r})}$ is derived for the case where the object and the antenna are located in the upper half-space. Starting from the general dyad formulation introduced in (2.82), the vector potential $\vec{A}_{(\vec{r})}$ is

rewritten in the following form:

$$\begin{aligned}\vec{A}_{(\vec{r})} \;=\; & G^A_{xx}\,J_x\,\hat{x} \;+\; G^A_{yx}\,J_x\,\hat{y} \;+\; G^A_{zx}\,J_x\,\hat{z} \\ & +\; G^A_{xy}\,J_y\,\hat{x} \;+\; G^A_{yy}\,J_y\,\hat{y} \;+\; G^A_{zy}\,J_y\,\hat{z} \\ & +\; G^A_{xz}\,J_z\,\hat{x} \;+\; G^A_{yz}\,J_z\,\hat{y} \;+\; G^A_{zz}\,J_z\,\hat{z}\end{aligned} \tag{2.84}$$

Substituting the Hertz vector definition related to the upper half-space (2.17) in the relation (2.75) and applying the three elementary dipole components simply given by:

$$\begin{aligned} J_x &= 1,\; J_y = 0,\; J_z = 0 \\ J_x &= 0,\; J_y = 1,\; J_z = 0 \\ J_x &= 0,\; J_y = 0,\; J_z = 1 \end{aligned} \tag{2.85}$$

It follows for the dyadic Green function $\overline{\overline{G}}_A$:

$$\overline{\overline{G}}_A \;=\; G^A_{xx}(\hat{x}\hat{x} \;+\; \hat{y}\hat{y}) \;+\; G^A_{zx}\hat{z}\hat{x} \;+\; G^A_{zy}\hat{z}\hat{y} \;+\; G^A_{zz}\hat{z}\hat{z} \tag{2.86}$$

Where the elements G^A_{ij} are given by:

$$\begin{aligned} G^A_{xx} &= G^A_{yy} \;=\; \frac{\mu_2}{4\pi}\,(G_{22} - G_{21} + U_{22}) \\ G^A_{zx} &= \frac{\mu_2}{4\pi}\frac{\partial W_{22}}{\partial x} \\ G^A_{zy} &= \frac{\mu_2}{4\pi}\frac{\partial W_{22}}{\partial y} \\ G^A_{zz} &= \frac{\mu_2}{4\pi}\left[G_{22} - G_{21} + \frac{k_1^2}{k_2^2}\left(U_{22} + \frac{\partial W_{22}}{\partial z}\right)\right] \end{aligned} \tag{2.87}$$

The general dyad will form the basis of Mixed Potential Integral Equation (MPIE) introduced in section 2.5. Further, due to the anisotropy in the $\hat{x}\hat{y}$-plane it follows from (2.88):

$$G^A_{zx} \;=\; G^A_{zy} \tag{2.88}$$

The scalar potential Φ is formally defined by (2.83) for the potential twosome structure.

2.3.3 Electric Field Integral Equation

A monochromatic local plane wave is considered as incident field $\vec{E}_{i(\vec{r}\,')}$ and defined in the absence of the scatterer. The field induces surface currents that in turn radiate again a field into the space. According to the equivalence principle after Harrington [29], the current distribution represents an assembly of elementary dipoles, leading finally to an integration over the entire

surface. The surface of the object is considered to be perfect conducting and closed. The boundary conditions impose for the tangential component of the total field: $\vec{E}_{t(\vec{r}\,')}$:

$$\vec{E}_{t(\vec{r}\,')} \times \hat{n} \;=\; 0$$

Furthermore, as the total field $\vec{E}_{t(\vec{r}\,')}$ is the sum of the incident $\vec{E}_{i(\vec{r}\,')}$ and scattered field $\vec{E}_{s(\vec{r}\,')}$, it yields on the surface:

$$\left[\vec{E}_{i(\vec{r}\,')} \;+\; \vec{E}_{s(\vec{r}\,')}\right] \times \hat{n} \;=\; 0 \tag{2.89}$$

Considering an induced current distribution at the point $\vec{r}\,'$ at the target and observing the scattered field at the location $\vec{r}$ and by substituting (2.77) in (2.89) the following relation is derived:

$$\hat{n} \times \left(-i\omega\ \vec{A}_{(\vec{r},\vec{r}\,')} \;+\; \nabla\Phi_{(\vec{r},\vec{r}\,')}\right) \;=\; \hat{n} \times \vec{E}_{i(\vec{r}\,')} \tag{2.90}$$

The next step consists in performing the summation of the entire elementary dipoles assembly.

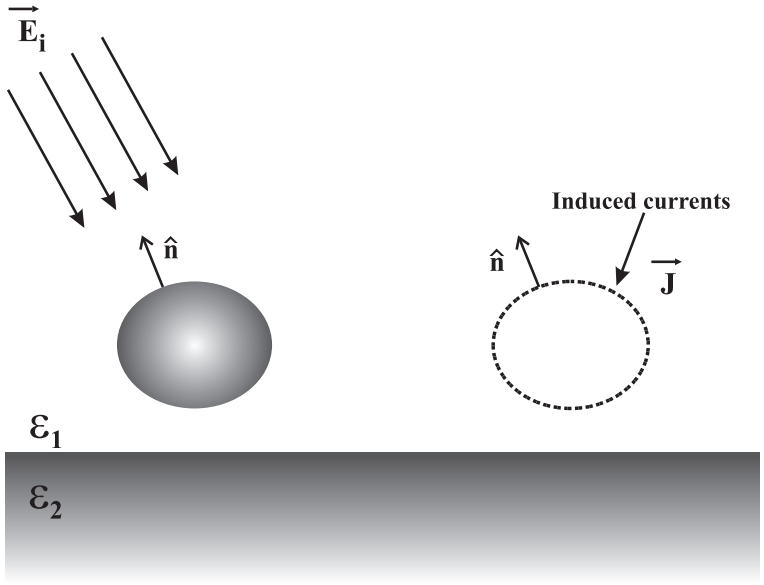

Figure 2.13: The equivalence principle

Leading finally to the Electric Field Integral Equation (EFIE):

$$-\frac{i\omega}{k^2}\ \hat{n} \times \left(\nabla\,\nabla\cdot\ + k^2\right) \iint\limits_{S\,'} \overline{\overline{G}}_{A(\vec{r},\vec{r}\,')} \cdot \vec{J}_{(\vec{r}\,')}\ dS' \;=\; \hat{n} \times \vec{E}_{i(\vec{r}\,')} \tag{2.91}$$

Some remarks concerning the integration of the EFIE and the MPIE presented in the next section. The free space scalar Green function G_0 mentioned in section 2.3 and the functions G, U and W of the essential Sommerfeld integrals in the MPIE (see appendix 2.2.3) have an singularity of the form:

$$G,\ U\ and\ W \;\propto\; \frac{1}{R} \tag{2.92}$$

Where R is the distance between the source and observation points. The second derivatives of the functions have $\frac{1}{R^3}$ singularities, which are not generally integrable. The integrals have therefor hypersingular kernels for the limit $R \to 0$. The integration is done by the Hadamard finite part integral [27] [28].

2.4 Lorenz Gauge

In the original DIFFRA program the mixed structure of a scalar potential Φ and vector potential $\vec{A}$ is considered according to the EIFE. In order to keep this mixed potential structure for a two-layer media considered, the Green dyad is modified after the MPIE. In earth monitoring the case is considered where the point of observation and the object are located in the upper layer (2) air. First of all, the general Lorenz gauge is introduced linking the scalar Φ and vector $\vec{A}$ potentials. According to the definition of the scalar potential in (2.83) it follows for a current distribution on a closed surface:

$$\begin{aligned}
\Phi_{(\vec{r})} &= -\frac{i\omega}{k_2^2} \iint\limits_{S'} \nabla \cdot \left[\overline{\overline{G}}_{A(\vec{r},\vec{r}\,')} \cdot \vec{J}_{0(\vec{r}\,')} \right] \, dS' \\
&= -\frac{i\omega}{k_2^2} \iint\limits_{S'} [\, \nabla_r \cdot \overline{\overline{G}}_{A(\vec{r},\vec{r}\,\prime)} \, \vec{J}_{(\vec{r}\,\prime)} \; + \; \overline{\overline{G}}_{A(\vec{r},\vec{r}\,\prime)} \, \underbrace{\nabla_r \cdot \vec{J}_{(\vec{r}\,\prime)}}_{0} \,] \, dS' \\
&= -\frac{i\omega}{k_2^2} \iint\limits_{S'} \nabla_r \cdot \overline{\overline{G}}_{A(\vec{r},\vec{r}\,\prime)} \, \vec{J}_{(\vec{r}\,\prime)} \, dS' \qquad (2.93)
\end{aligned}$$

For a given charge density $q_{(\vec{r}\,')}$ the potential $\Phi_{(\vec{r})}$ is defined as:

$$\Phi_{(\vec{r})} = \iint\limits_{S'} G_{\phi(\vec{r},\vec{r}\,')} \, q_{(\vec{r}\,')} \, dS' \qquad (2.94)$$

Further, the current continuity on the surface holds:

$$q = \frac{1}{i\omega} \nabla' \cdot \vec{J}_{(\vec{r}\,')} \qquad (2.95)$$

Substituting the charge density in (2.94) by (2.95), it yields:

$$\begin{aligned}
\Phi_{(\vec{r})} &= \frac{1}{i\omega} \iint\limits_{S'} [\, \underbrace{\nabla_{r'} \cdot \left(G_\phi \, \vec{J}_{(\vec{r}')} \right)}_{0} - \nabla_{r'} \, G_\phi \, \cdot \vec{J}_{(\vec{r}')} \,] \, dS' \\
&= -\frac{1}{i\omega} \iint\limits_{S'} \nabla_{r'} \, G_\phi \, \cdot \vec{J}_{(\vec{r}')} \, dS' \qquad (2.96)
\end{aligned}$$

Finally, comparing (2.93) and (2.96) the general Lorenz gauge for the vector and scalar potential is given as follows:

$$\boxed{\frac{i\omega}{k_2^2} \, \nabla_r \cdot \overline{\overline{G}}_{A(\vec{r},\vec{r}\,')} = \frac{1}{i\omega} \, \nabla_{r'} \, G_{\Phi\,(\vec{r},\vec{r}\,')}} \qquad (2.97)$$

2.5 Mixed Potential Integral Equation

In general, such a scalar function G_Φ satisfying the Lorenz gauge for a two-layer media does not exists. This is due to the fact that the horizontal and vertical components of the vector potential $\vec{A}$ are not of the same form. But as both sides in the Lorenz gauge represents vector quantities, a correction vector $\vec{P}_{(\vec{r})}$ may be introduced in accordance to the Michalski [49] as follows:

$$\frac{i\omega}{k^2}\,\nabla\cdot\overline{\overline{G}}_{A(\vec{r},\vec{r}\,')} \;=\; \frac{1}{i\omega}\,\nabla\,'K_{\Phi\,(\vec{r},\vec{r}\,')} \;+\; i\omega\vec{P}_{(\vec{r})} \tag{2.98}$$

Hence, the correction vector $\vec{P}_{(\vec{r})}$ and the scalar function K_Φ have to be determined. Afterwards, by adding the correction vector $\vec{P}_{(\vec{r})}$ to the vector potential $\nabla_r\cdot\overline{\overline{G}}_{A(\vec{r},\vec{r}\,\prime)}$, the mixed structure of a vector and scalar potential is kept as implemented in DIFFRA program. The equation system (2.98) is solved in the wave number domain. By definition the Fourier transformation is given as follows:

$$\tilde{f}_{(\xi,\eta,z,z')} \;=\; \frac{1}{2\pi}\iint_{-\infty}^{\infty} F_{(x-x',y-y',z,z')}e^{-i[\xi(x-x')+\eta(y-y')]}\,dx\,dy$$

Substituting the corresponding Fourier transformation in (2.98) it yields:

$$-\frac{i\omega}{k_2^2}\left(i\xi\,\tilde{G}_{xx} \;+\; \frac{\partial}{\partial z}\,\tilde{G}_{zx}\right) \;=\; \frac{\xi}{\omega}\,\tilde{K}_\Phi \;-\; i\omega\,\tilde{P}_x \tag{2.99}$$

$$-\frac{i\omega}{k_2^2}\left(i\eta\,\tilde{G}_{xx} \;+\; \frac{\partial}{\partial z}\,\tilde{G}_{zy}\right) \;=\; \frac{\eta}{\omega}\,\tilde{K}_\Phi \;-\; i\omega\,\tilde{P}_y \tag{2.100}$$

$$-\frac{i\omega}{k_2^2}\,\frac{\partial}{\partial z}\,\tilde{G}_{zz} \;=\; -\frac{1}{i\omega}\,\frac{\partial}{\partial z'}\,\tilde{K}_\Phi \;-\; i\omega\,\tilde{P}_z \tag{2.101}$$

Referring to (2.99), (2.100) and (2.101) the four unknowns $\tilde{P}_x$, $\tilde{P}_y$, $\tilde{P}_z$ and $\tilde{K}_\Phi$ have to be calculated. In order to reduce the unknowns one set $\tilde{P}_x = 0$. According to (2.88) and $\eta = \xi$ due to the homogenous anisotropic half-space, it holds:

$$\eta\frac{\partial}{\partial z}\,\tilde{G}_{zx} \;=\; \xi\frac{\partial}{\partial z}\,\tilde{G}_{zy}\;, \tag{2.102}$$

From (2.99) and (2.100) also follows $\tilde{P}_y = 0$. In this case both equations are identical and $\tilde{P}_z$ and $\tilde{K}_\Phi$ remain as unknowns. The Sommerfeld integrals introduced in section 2.1.3 are immediately given in the frequency domain as:

$$\begin{aligned}
\tilde{G}_{22} &= \tfrac{1}{\gamma_2}\,e^{-\gamma_2|z'-z|} & \qquad \tilde{G}_{21} &= \tfrac{1}{\gamma_2}\,e^{-\gamma_2|z'+z|}\\
\tilde{U}_{22} &= \tfrac{2}{M}\,e^{-\gamma_2|z'+z|} & \qquad \tilde{W}_{22} &= g\,e^{-\gamma_2|z'+z|}
\end{aligned} \tag{2.103}$$

According to (2.88), (2.99) - (2.101) and (2.103), the function $\tilde{K}_\Phi$ and the component $\tilde{P}_z$ are

given in the form as follows:

$$\tilde{K}_\Phi = \frac{\mu_2}{4\pi}\frac{\omega^2}{k_2^2}\left[\frac{1}{\gamma_2}\left(e^{-\gamma_2|z-z'|} - e^{-\gamma_2(z+z')}\right) + \left(\frac{2}{M} - \gamma_2\, g\right) e^{-\gamma_2(z+z')}\right] \quad (2.104)$$

$$\tilde{P}_z = \frac{\mu_2}{4\pi k_2^2}\left[2 + \gamma_2\left(1 + \frac{k_1^2}{k_2^2}\right)\left(\gamma_2\, g - \frac{2}{M}\right) e^{-\gamma_2(z+z')}\right] \quad (2.105)$$

The modified scalar potential $\Phi_{(\vec{r})}$

Inserting the Sommerfeld denominators in (2.104) and comparing with the definition of the Sommerfeld integrals presented in the section 2.2.3, the scalar quantity K_Φ is finally given by:

$$K_\Phi = \frac{1}{4\pi\epsilon_2}\left[G_{22} - G_{21} + U_{22} + \frac{\partial W_{22}}{\partial z}\right] \quad (2.106)$$

For the whole surface it yields:

$$\Phi_{(\vec{r})} = -\iint_{S'} K_\Phi\, q_{(\vec{r}\,')}\, dS' \quad (2.107)$$

The modified vector potential $\vec{A}_{(\vec{r})}$

In order to keep a purely decomposition into a vector and scalar potential, the correction vector $\vec{P}_{(\vec{r})}$ is added to the vector potential $\overline{\overline{K}}_{A(\vec{r},\vec{r}\,')}$ in the following manner:

$$\overline{\overline{K}}_{A(\vec{r},\vec{r}\,\prime)} = \overline{\overline{G}}_{A(\vec{r},\vec{r}\,\prime)} + \nabla\vec{P}_{(\vec{r})} \quad (2.108)$$

The modified Green dyad $\overline{\overline{K}}_A$ for a two-layer media is finally given by:

$$\begin{aligned}\overline{\overline{K}}_{A(\vec{r},\vec{r}\,\prime)} = {} & (\hat{x}\hat{x} + \hat{y}\hat{y})\,K_{xx} + \hat{x}\hat{z}\,K_{xz} + \hat{y}\hat{z}\,K_{yz} \\ & + \hat{z}\hat{x}\,K_{zx} + \hat{z}\hat{y}\,K_{zy} + \hat{z}\hat{z}\,K_{zz}\end{aligned} \quad (2.109)$$

Where the single elements of $\overline{\overline{K}}_{A(\vec{r},\vec{r}\,\prime)}$ are determined by:

$$K_{xx(\vec{r},\vec{r}\,\prime)} = G_{xx} = \frac{\mu_2}{4\pi}\left[G_{22} - G_{21} + U_{22}\right]$$

$$K_{xz(\vec{r},\vec{r}\,\prime)} = \frac{\partial P_z}{\partial x}, \quad K_{yz(\vec{r},\vec{r}\,\prime)} = \frac{\partial P_z}{\partial y}$$

$$K_{zx(\vec{r},\vec{r}\,\prime)} = G_{zx} = \frac{\mu_2}{4\pi}\frac{\partial W_{22}}{\partial x}$$

$$K_{zy(\vec{r},\vec{r}\,\prime)} = G_{zy} = \frac{\mu_2}{4\pi}\frac{\partial W_{22}}{\partial y}$$

$$K_{zz(\vec{r},\vec{r}\,\prime)} = G_{zz} + \frac{\partial P_z}{\partial z} = \frac{\mu_2}{4\pi}\left[G_{22} - G_{21} + \frac{k_1^2}{k_2^2}\left(U_{22} + \frac{\partial W_{22}}{\partial z}\right)\right] + \frac{\partial P_z}{\partial z}$$

The vector potential $\vec{A}_{(\vec{r})}$ for the entire current distribution on the surface S' is given by:

$$\vec{A}_{(\vec{r})} \;=\; \iint\limits_{S'} \overline{\overline{K}}_A \cdot \vec{J}_{(\vec{r}\,')}\, dS' \tag{2.110}$$

Substituting (2.108) in (2.110), it yields:

$$\begin{aligned} \vec{A}_{(\vec{r})} = & \iint\limits_{S'} \Big[\; \hat{x}(\vec{J}\cdot\hat{x}) \;+\; \hat{y}(\vec{J}\cdot\hat{y})\Big]\; K_A^1\, dS' \\ & + \iint\limits_{S'} \hat{z}\left[(\nabla'\cdot\vec{J})K_A^{2a} \;+\; (\vec{J}\cdot\hat{z})K_A^{2b}\right]\; dS' \\ & + \nabla_r \frac{\partial}{\partial z} \iint\limits_{S'} (\vec{J}\cdot\hat{z})K_A^3 \;\; dS' \end{aligned} \tag{2.111}$$

Where the single functions of the dyad $\overline{\overline{K}}_A$ are specified as follows:

$$\begin{aligned} K_A^1(\vec{r},\vec{r}') &= \frac{\mu_2}{4\pi}\left[\, G_{22} \;-\; G_{21} \;+\; U_{22}\right] \\ K_A^{2a}(\vec{r},\vec{r}') &= \frac{\mu_2}{4\pi}\, W_{22} \\ K_A^{2b}(\vec{r},\vec{r}') &= \frac{\mu_2}{4\pi}\left[\, G_{22} \;-\; G_{21} \;+\; \frac{k_1^2}{k_2^2}U_{22} \;+\; \left(\frac{k_1^2}{k_2^2} \;+\; 1\right)\frac{\partial W_{22}}{\partial z}\right] \\ K_A^3(\vec{r},\vec{r}') &= \frac{\mu_2}{4\pi k_2^2}\left[-2G_{21} \;+\; \left(\frac{k_1^2}{k_2^2} \;+\; 1\right)\left(U_{22} \;+\; \frac{\partial W_{22}}{\partial z}\right)\right] \end{aligned}$$

The tangential component of the scattered and incident field are related through the boundary condition $\hat{n}\times\left[\vec{E}_i \;+\; \vec{E}_s\right] \;=\; 0$ for a perfect conducting surface. At the end of the day the integral equation after MPIE is given in its final form:

$$\hat{n}\times\left\{-i\omega \iint\limits_{S'} \overline{\overline{K}}_{A(\vec{r},\,\vec{r}')}\cdot\vec{J}_{(\vec{r}\,')}\, dS' \;+\; \nabla \iint\limits_{S'} K_{\Phi(\vec{r},\,\vec{r}')}\,\vec{q}_{(\vec{r}\,')}\, dS'\right\} \;=\; \hat{n}\times\vec{E}_{i(\vec{r})} \tag{2.112}$$

2.6 Method of Moments

Two numerical methods were compared in this work, namely the *M*ethod *o*f *M*oments (MoM) for solving the presented MPIE and the asymptotic method represented by the *G*eometrical *T*heory of *D*iffraction (GTD), respectively the *U*niform *T*heory of *D*iffraction (UTD) introduced next. A special emphasis was given to the backscattered field at look angles near transition zones due to geometrical *S*urface *S*hadow *B*oundaries (SSB). In such transition region the GTD was replaced by the UTD which removes the shortcomings of the GTD at transition zones. The exact integral equation method after the MoM was used here in order to validate the GTD-UTD ray system. Details concerning the implementation of the MoM for computing the MPIE are given in appendix *B*. In order to class the MoM in the area of the computational electromagnetic, a short overview over the different ways for solving the radiation problem is presented below.

In a nutshell, besides the analytical methods to solve electromagnetic problems, the computational numerical methods has gain in importance in the recent decades, staying abreast of hardware improvements. The application of numerical methods to electromagnetic problems is named the area of *C*omputational *E*lectro-*M*magnetic CEM. Where four main categories of numerical methods are used in general in electromagnetic, classified in the following way:

- **Differential Equation Methods**
  *F*inite *D*ifference frequency domain method (FD)
  *F*inite *D*ifference *T*ime *D*omain method (FDTD)
- **Integral Equation Methods**
  MoM technique
- **Mode Matching**
  In general this method relies on piecing together solutions of differential equations in different regions
- **Numerical Methods Based on Asymptotic Approximations**
  Ray tracing like the GTD or its further development the UTD.

CHAPTER 3

Target situated in the Air

A ray system after the Geometrical and Uniform Theory of Diffraction for calculating the backscattered field of an illuminated object placed above the soil in the half-space air is introduced in this chapter. The geometrical diffraction theories are asymptotic expansions solving the Helmholtz equation describing waves propagation. The asymptotic method [2] is based on the principle that similar ray geometry leads to similar asymptotic formulas for wave fields. Hence, the asymptotic behavior $k \to \infty$ characterizes the propagation of waves by rays obeying a set of geometrical rules. In this connection one deals with a high frequency field HF and the asymptotic method implies that the dimensions of the illuminated objects are much greater than the incoming wavelength. The solution of such an asymptotic method has the form of a series of inverse powers of the wave number k. Where, the first term of the series is usually retained according to Bouche and Molinet [8]. Therefore, a brief historical overview of the asymptotic approximations used in the area of computational electromagnetic CEM and their shortcuts mentioned in the literature is given first.

Geometrical Optics (GO)

The GO is the simplest ray tracing techniques that have been used for centuries at optical frequencies. The basic postulates of the GO are:

- Wavefronts are locally plane and em-waves are of transversal electromagnetical nature TEM
- The wave's propagation direction is specified by the normal to the equiphase planes (Eikonal $\to$ Rays)
- Rays travel in straight lines in a homogeneous medium
- Polarization is constant along a ray in an isotropic medium
- Power in a flux tube is conserved

- Reflection and transmission obey Snell's law
- The reflected field is linearly related to the incident field via the Fresnel coefficients

One disadvantage of the GO is that it does not predict the field in occurring geometrical shadows. Another important handicap is that it cannot handle the radiation from flat or singly curved surfaces.

Geometrical Theory of Diffraction (GTD)
The GTD eliminates many of the problems associated with the GO technique. In real world, the field distribution is continuous in the section of shade and the intensity of an em-field is non-zero in shadowed regions. Keller [41] proposed a specific correction of the GO in order to eliminate field discontinuities in the surrounding of objects. That way, the basics of the GTD was developed. The total field at an observation point is decomposed into GO and diffracted components. In comparison with the GO the GTD postulates:

- As the GO the incident wavefronts have to be locally plane
- Diffracted rays are determined by a generalisation of the Fermat principle
- The diffracted field strength is inversely proportional to the cross sectional area of the flux tube (spatial spreading)
- The diffracted field is linearly related to the incident field at the diffraction point by a diffraction coefficient
- The diffraction coefficients are determined by an appropriate canonical problem whose solution is known

However, the GTD has singularities at the shadow and reflection boundaries (transition zones) and the field is not continuous crossing such a surface shadow boundary (SSB)

Uniform Theory of Diffraction (UTD)
As mentioned before, the GTD has some shortcomings near the transition zones surrounding an obstacle. The discontinuity of the field at such a SSB is removed by introducing a transition function. The introduced transition function approaches zero at the same rate as the diffraction coefficients become singular at the SSB angle. Thus, UTD expressions describe the behavior of the wave field in the lit, transition and shadow region and is therefore called the uniform theory. Far away from such a SSB, the GTD and the UTD fall in turn together. Hence, the UTD closes the gap of the GTD at the SSB [48] [8]. Details concerning the transition function, reflection and diffraction coefficients as used along this work can be looked up in the appendices *C*.1 and *C*.4.

3.1 Energy Spread

The incident wave vector $\vec{k}$ and the local normal vector $\hat{n}$ of the object define the plane of incident at the point of reflection. Here the orthogonal ray fixed coordinate system is determined by the parallel basis $\hat{n}_{||}$, lying in the plane of incidence, where the other basis is aligned

perpendicular $\hat{n}_\perp$ to the plane. The incoming wave front at the reflection point is described by the Differential Geometry introduced by Gauss[1]. The two principal radii of curvature are given as follows:

$$\perp: \quad \frac{1}{\rho_1} = \frac{1}{\rho_1^i} + \frac{2\cos(\theta_i)}{a_1} \tag{3.1}$$

$$\|: \quad \frac{1}{\rho_2} = \frac{1}{\rho_2^i} + \frac{2}{a_2\cos(\theta_i)} \tag{3.2}$$

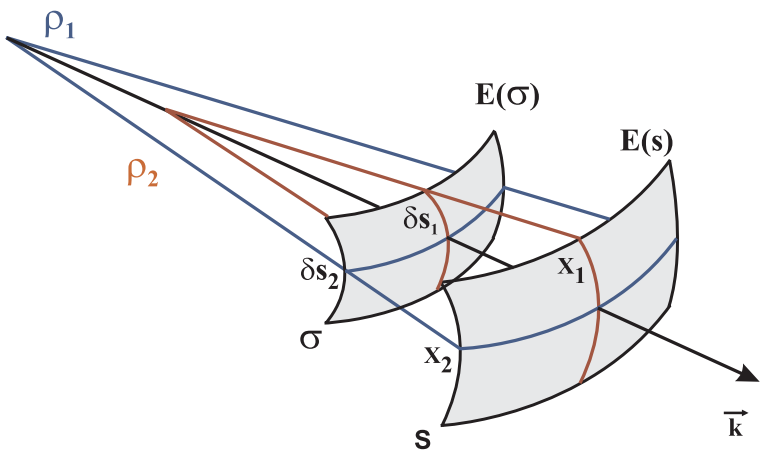

Figure 3.1: Tube of rays

Which describe a tube of rays where the conservation of energy holds for the spatial propagation along the tube. According to fig. 3.1 it yields for the simultaneous triangles:

$$\frac{\rho_1}{\rho_1 + \overline{\sigma\, s}} = \frac{\delta s_1}{x_1}$$
$$\frac{\rho_2}{\rho_2 + \overline{\sigma\, s}} = \frac{\delta s_2}{x_2}$$

The differential surface elements at the points σ and s are defined by:

$$\delta A(\sigma) = \delta s_1\, \delta s_2$$
$$\delta A(s) = x_1\, x_2$$

As a result of the conservation of energy inside a ray tube it yields:

$$\iint_A E^2(\sigma) dA(\sigma)\hat{n} = \iint_A E^2(s) dA(s)\hat{n}$$

The location of the origin $\sigma = 0$ is arbitrary. Hence, after a propagation distance s the spatial

[1] Disquisitiones generales circa superficies curvas (1823)

energy divergence within a tube is finally given by:

$$E(s) \; = \mid E(0) \mid \; \sqrt{\frac{\rho_1 \, \rho_2}{(\rho_1 \, + \, s) \; (\rho_2 \, + \, s)}} \tag{3.3}$$

A couple of interactions are introduced in the following. In view of the legibility the remaining divergence of a wave on its way back to the antenna is described by a single spreading factor term (SF). Nevertheless, where of particular interest, the implemented spreading factor is explicit discussed as the GTD presents a corner-stone in this work. In accordance to the introduced cylinder model (fig. 3.2) the perpendicular radius of curvature at the cylinder has the limit $\rho_1 \; \rightarrow \; \infty$. Hence, expression (3.3) simplifies to:

$$E(s) \; = \mid E(0) \mid \; \sqrt{\frac{\rho_2}{\rho_2 \, + \, s}} \tag{3.4}$$

3.2 Ray System

For the half-space air the étalon problem consists in a general elliptical cylinder with its principle axis a and b located at the height h above the soil. Here a is parallel to the interface. The surface of the cylinder is considered to be perfect conducting (PC). The polarization of the incoming em-field at the incident angle φ_L (look angle) is shown in fig. 3.2. One notes that in the considered setup the component $\vec{E}_{||}$ lies in the plane of incidence respectively the component $\vec{E}_{\perp}$ perpendicular to it. Whereas, the notation $\vec{E}_{||}$ and $\vec{E}_{\perp}$ corresponds to the $\vec{E}_h$ and $\vec{E}_v$ polarization by looking along the line of sight. The range of the look angle φ_L is set to $0° - 90°$. A monostatic alignment is regarded and a monochromatic unitary plane wave $|\vec{E}_0| \; = 1$ is assumed as incident em-field at the object in the following. The phase origin is placed in the center of the ellipsis. The numerical calculation is done by extracting the phase propagation term $exp(-2\,i\,k_1\,0M)$ and the divergence term $1\,/\,\sqrt{0M}$ for every single wave in the ray system. Hence, the resulting phase differences of the single waves are due to their various interactions respectively different paths between the cylinder and the ground. At the beginning the various rays of the system are introduced.

Also, the corresponding numerical implemented UTD/GTD expressions are presented. Where a UTD/GTD wave is calculated after the "brick building method" for the wave propagation. That means a simple multiplication of the following building blocks:

1. Amplitude term
2. Spreading factor
3. Phase term

One note that a propagation term of the form $exp(-ik_1r \; + \; i\omega t)^2$ were implemented in the GTD/UTD algorithm. In the electromagnetic literature e.g. [8] and [48], the parallel h polarization and the perpendicular polarization v are also mentioned as the hard respectively the soft polarization. Where the synonyms hard and soft arise from acoustics and correspond to

[2] If a time dependence of the form $exp(-i\omega t)$ is present, the complex conjugate of the field has to be considered.

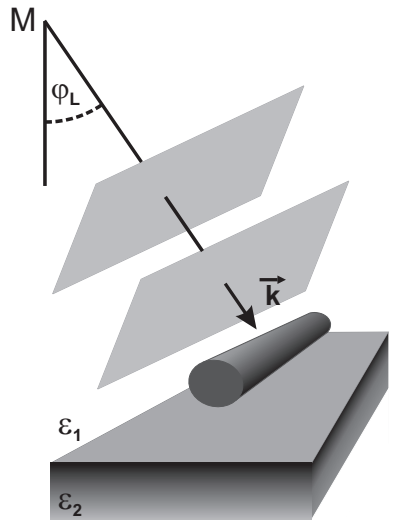

Figure 3.2: The étalon problem

the Neuman boundary condition (hard object) and to the Dirichlet boundary condition (soft object). On a perfect conducting surface, in electromagnetism, the soft $\perp$ field component is stronger attenuated compared to the hard $\parallel$ one. Some remarks concerning the notation in the following. The quantities $\underline{f}$, $\underline{D}$ and $\underline{R}$ signify the Fresnel coefficients, the UTD diffraction and UTD reflection dyads. For the way back to the observation point M, the same Fresnel coefficients as for the way to the cylinder are calculated. That represents an approximation due to the fact that the Fresnel coefficients are in the strict sense only valid for plane waves. The Fresnel coefficients for the normal incidence are abbreviated with $\underline{f}^0$ notation.

3.2.1 List of the Waves

According to the étalon problem method, analog ray types have similar asymptotic formulas. A ray system composed of 13 different waves was implemented in this thesis. The different ray geometries respectively their interactions for the object situated above the soil are given below in the fig. 3.3 to fig. 3.15. Concerning the implementation of the ray system every single wave is related to a subprogram where the geometrical points are calculated in dependence of the incidence angle φ_L. From fig. 3.3 and fig. 3.9 one finds that the specular wave 1 and the creeping wave 7 have no interaction with the soil. Note that the phase origin $\vec{0}$ is set in the middle of the object. Wave 2 and 10 have a transition region for the vertical incidence $\varphi_L = 0$. In our analysis, the shadow boundary transition region of waves 2 and 10 at $\varphi_L = 0$ will not be treated since, in the case of a three-dimensional object, this direction is also a caustic direction for these waves and needs therefore a different approach. The waves 3 and 8 have a common shadow boundary where both disappear and are replaced by wave 4 which creeps on a part of the surface. A special UTD procedure has been developed for treating the continuity of these waves at the surface shadow boundary (SSB1). A similar situation arises at the shadow boundary of

wave 5 and 9 (SSB2) where the continuity of the field in the shadow is taken over by wave 6. The same situation at the shadow boundary of wave 11 and 12 which are associated with wave 13. Outside the shadow boundary transition region, the GTD applies again. Hence, in the following section we present the GTD formulas for the waves 1, 2, 7 and 10. All other types of waves (3, 4, 8, 5, 6, 9, 11, 12 and 13) will be treated by an extended UTD procedure and presented exemplarily for the two transition zones corresponding to the waves 3, 4 and 8 and the waves 5, 6 and 9. Since wave 11, 12 and 13 have three interactions with the soil, their contributions is normally for a dielectric soil small. In view of the measurements in the anechoic chamber where a perfect conducting interface is given, their contributions cannot be neglected. Therefore, they were also considered and calculated after the UTD formalism near their corresponding transition zone.

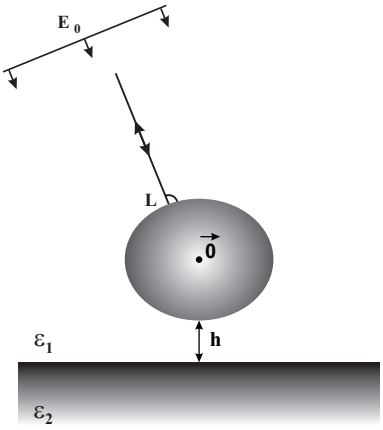

Figure 3.3: Wave 1 and phase origin

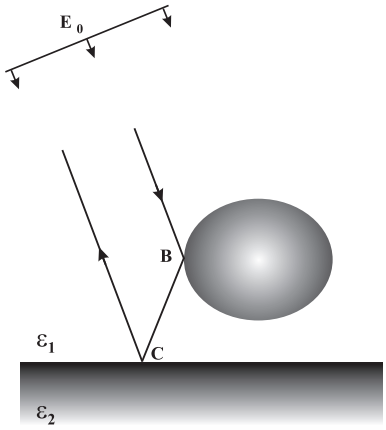

Figure 3.4: Wave 2 (Double Bounce)

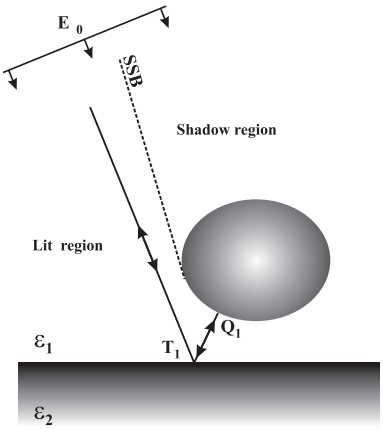

Figure 3.5: Wave 3

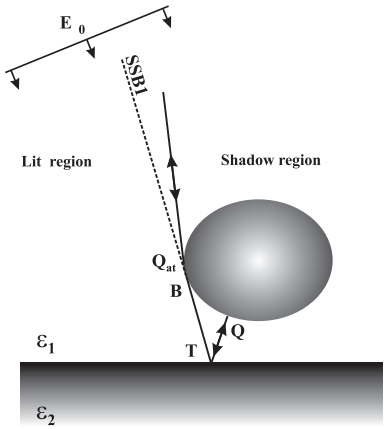

Figure 3.6: Wave 4

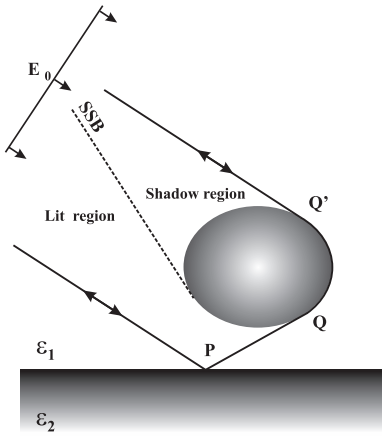

Figure 3.7: Wave 5

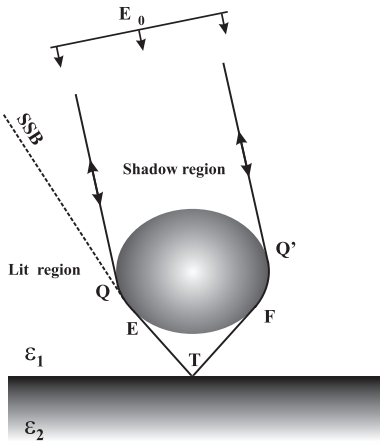

Figure 3.8: Wave 6

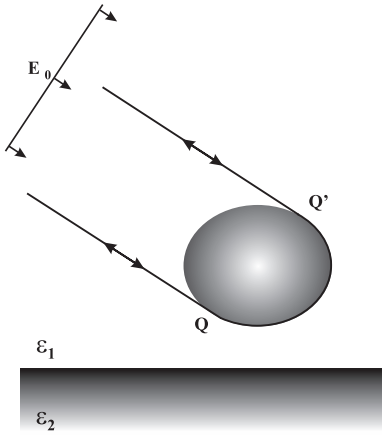

Figure 3.9: Wave 7 (Creeping wave)

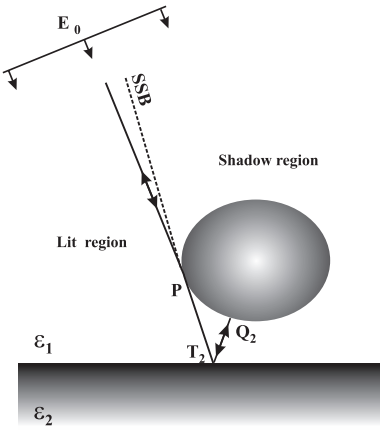

Figure 3.10: Wave 8

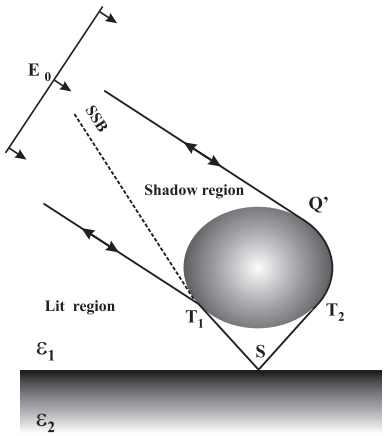

Figure 3.11: Wave 9

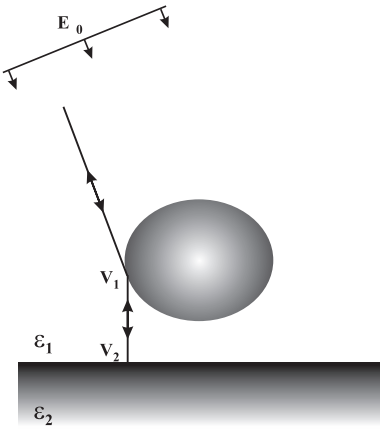

Figure 3.12: Wave 10

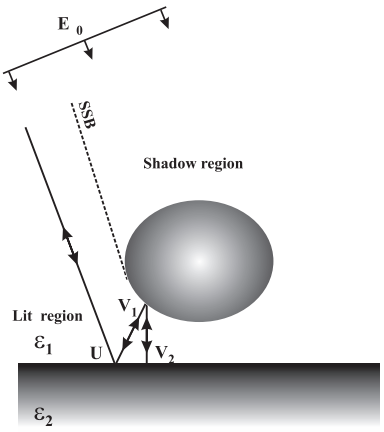

Figure 3.13: Wave 11

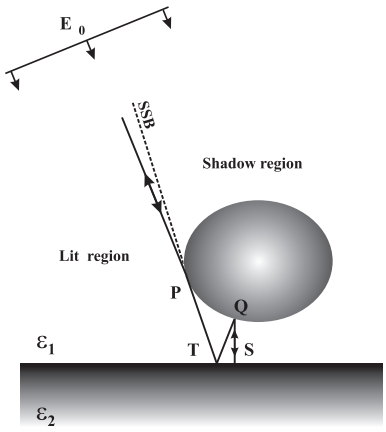

Figure 3.14: Wave 12

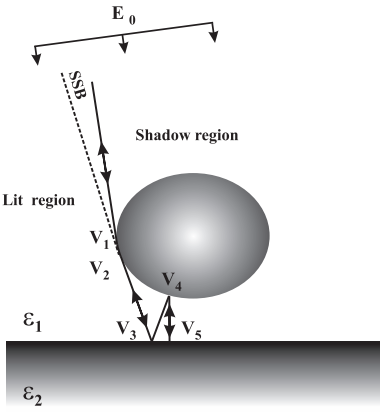

Figure 3.15: Wave 13

3.2.2 Numerical Implementation of the Ray System

The introduced ray system of the previous section 3.2.1 was numerically implemented as a Fortran code. The main computing time is used for calculating the corresponding geometrical points for a varying incident angle φ_L. The location of the antenna for the monostatic case as considered here is mentioned by M. Further, the phase origin is set in the middle of the cylinder along this thesis. The divergence term $1 \,/\, \sqrt{0M}$ and the phase term $e^{-2i\vec{k}_1^i \cdot \overrightarrow{0M}}$ are extracted for numerical purpose for every single wave.

3.3 GO-GTD Field

3.3.1 Wave 1

The first interaction between the field and the object is the one reflected from the object at normal incident at point L. The way to the cylinder and back are identical and represents the shortest path in the ray system. Further, as no reflection occurs with the interface the single wave 1 is the first receipted signal and besides the double bounced wave 2 one of the strongest. It will therefore be called the specular wave along this thesis. The field at the observation point M is expressed using the dyadic notation. According to fig. 3.3 the GO field of the specular

reflection is given by:

$$\vec{E}(M) \;=\; \vec{E}_0 \cdot \underline{R}_{0(L)} \;\; SF_{W1} \;\; e^{-2i\,\vec{k}_1^{\,i}\,\overrightarrow{0L}} \tag{3.5}$$

Where $\vec{E}_0$, $\underline{R}_{0(L)}$, SF_{W1} and $-2i\,\vec{k}_1^{\,i}\,\overrightarrow{0L}$ signify the incident field amplitude, the reflection dyad at the point L, the spreading factor and the phase term of the wave. Here, the general reflection dyad $\underline{R}$ describe the reflection coefficients of the parallel and perpendicular field component relative to the plane of incidence, given in the form:

$$\underline{R} \;=\; R_H\;\hat{e}^{\,i}_{\parallel} \cdot \hat{e}^{\,r}_{\parallel} \;+\; R_S\;\hat{e}^{\,i}_{\perp} \cdot \hat{e}^{\,r}_{\perp} \tag{3.6}$$

The reflection dyad $\underline{R}_{0(L)}$ reduces for a perfect conducting surface according to the hard $\parallel$ and soft $\perp$ polarization to $R_H = 1 \;\; R_S = -1$. In (3.5), the wave vector $\vec{k}_1^{\,i}$ describes the the phase of the incident field at the reflection point L. As a local plane wave ($\rho_{i2} \;\rightarrow\; \infty$) is given at L, it follows from (3.2) the radius of curvature $\rho_{2(L)}$ of the reflected wave as follows:

$$\rho_{2(L)} \;=\; \frac{a_{2(L)}}{2} \tag{3.7}$$

Where $a_{2(L)}$ describes the local radius of curvature at L. In consequence, as a symmetric cylinder is considered, $a_{2(L)}$ is constant over the look angle range. The spatial divergence loss of wave 1 is finally given in accordance to (3.4) by:

$$SF_{W1} \;=\; \sqrt{\rho_{2(L)}} \tag{3.8}$$

In (3.8) the term $1\,/\,\sqrt{\rho_2 \;+\; LM}$ is set equal to the extracted term $1\,/\,\sqrt{0M}$ as mentioned in section 3.2.2.

3.3.2 Wave 2 (Double Bounce)

The second considered ray in the system is the so-called double bounced wave (fig. 3.4). Here, the round trip of the wave can be performed on two paths respectively the way to the cylinder and back are interchangeable. Hence, two double bounced waves exists. Due to the fact that an identical geometry is on hand for the two double bounced waves, the two waves superpose in a constructive way. Thus, only one double bounce wave has to be computed and its double field value has to be taken. This is also a result of the reciprocity theorem verified by the GO and GTD fields. The wave 2 is computed a priori in the following way:

$$\vec{E}_{2(M)} \;=\; 2\vec{E}_0 \cdot \underline{R}_{0(B)} \cdot \underline{f}_{(C)} \;\; SF_{W2} \;\; e^{-i\left[\vec{k}_1^{\,i}\cdot(\overrightarrow{0B}\;+\;\overrightarrow{0C})\;+\;k_1\,BC\right]} \tag{3.9}$$

Similar to wave 1, $\vec{E}_0$, $\underline{R}_{0(B)}$, SF_{W2} and $-i\;\left[\vec{k}_1^{\,i}\cdot(\overrightarrow{0B}\;+\;\overrightarrow{0C})\;+\;k_1\,BC\right]$ signify the incident field amplitude, the reflection dyad at the point B, the spreading factor and the phase term of the double bounced wave. According to appendix $A.1$ the Fresnel dyad $\underline{f}_{(C)}$ for computing the

reflection at the interface at point C is given by:

$$\underline{f} \;=\; f_H\;\hat{e}^i_{\parallel}\cdot\hat{e}^r_{\parallel} \;+\; f_S\;\hat{e}^i_{\perp}\cdot\hat{e}^r_{\perp} \tag{3.10}$$

Analog to wave 1, the reflection dyad $\underline{R}_{0(B)}$ is reduced for a perfect conducting surface to $R_H = 1 \quad R_S = -1$. Referring to (3.2), the radius of curvature after the reflection at B is calculated with the local incident angle θ_i as follows:

$$\rho_{2(B)} \;=\; \frac{a_{2(B)}\cos(\theta_i)}{2} \tag{3.11}$$

According to the plane interface ($a_{2(C)} \to \infty$), the reflection at C doesn't modify the radius of curvature. Hence, the spreading factor of wave 2 is immediately given by:

$$SF_{W2} \;=\; \sqrt{\rho_{2(B)}} \tag{3.12}$$

In the same manner as wave 1, the approximation $1\,/\,\sqrt{\rho_2 \,+\, BM} \;\approx\; 1\,/\,\sqrt{0M}$ is considered in (3.30) for the numerical calculation. Next, the phase term mentioned in (3.9) is exemplarily discussed in details. The entire phase term $e^{i\phi}$ from the antenna to the cylinder and back is given as follows:

$$\phi \;=\; \vec{k}^i_1\cdot\vec{MB} \;+\; k_1\,BC \;+\; \vec{k}^r_1\cdot\vec{CM} \tag{3.13}$$

Where $\vec{k}^r_1$ signifies the wave vector for the way back, thus $\vec{k}^r_1 = -\vec{k}^i_1$. Rewriting the phase term (3.13) in the form:

$$\phi \;=\; \vec{k}^i_1\cdot\left(\vec{M0}+\vec{0B}\right) \;+\; k_1\,BC \;+\; \vec{k}^r_1\cdot\left(\vec{C0}+\vec{0M}\right) \tag{3.14}$$

Yielding immediately the final phase expression to be computed:

$$\phi \;=\; -2\vec{k}^i_1\cdot\vec{0M} \;+\; \vec{k}^i_1\cdot\left(\vec{0B} \;+\; \vec{0C}\right) \;+\; k_1\,BC \tag{3.15}$$

Again the term $-2\vec{k}^i_1\cdot\vec{0M}$ is neglected for the numerical calculation.

3.3.3 Wave 7 (Creeping Wave)

As outlined in fig 3.9, the incoming wave 7 propagates around the cylinder as a creeping wave. Here, wave 7 has no interaction with the interface. As a long arc length is given on the cylinder for the wave, the asymptotic approximation of the attachment and detachment coefficients $\underline{D}^*_{(Q,Q')}$ are considered according to Bouche and Molinet [8]. Their definition is discussed in appendix C.4.2. Hence, the creeping wave 7 is given by:

$$\vec{E}_{7(M)} \;=\; 2\vec{E}_0(Q)\cdot\underline{D}^*(Q,Q')\;\; e^{-i\gamma^h_s(QQ')}\;\; e^{-i\,k_1\,QQ'} \tag{3.16}$$

Where $\vec{E}_{0(Q)}$ and $-i\,k_1\,QQ'$ signify the incident field amplitude at point Q and the phase along the arc QQ'. The term $e^{-i\gamma_s^h(QQ')}$ describes the attenuation between the attachment and detachment point Q and Q'. Here, the asterisk $(*)$ signifies that the complex conjugate has to be considered as a harmonic temporal dependency $e^{-i\omega t}$ is chosen in [8]. Further, as the direction around the object is also interchangeable, the double value of the wave 7 has to be considered. The spatial spreading from Q' is given by $1\,/\,\sqrt{Q'M}$ and approximated by $1\,/\,\sqrt{0M}$.

3.3.4 Wave 10

Next, wave 10 is introduced which is reflected from the cylinder in such a way that it falls perpendicular on the interface at the point V_2. Afterwards the wave propagates on the same path, back to the antenna. Unfortunately this wave is mostly neglected in literature. According to fig. 3.12 the diffracted wave 10 is given at the antenna as follows:

$$\vec{E}_{10(M)} \;=\; \vec{E}_0 \cdot \underline{R}_{0(V_1)} \cdot \underline{f}_{(V_2)} \cdot \underline{R}_{0(V_1)} \;\; SF_{W10} \;\; e^{-2i\left[\,\vec{k}_1^{\,i}\cdot\overrightarrow{0V_1} + k_1\,V_1V_2\,\right]} \tag{3.17}$$

Where, $\vec{E}_0$, $\underline{R}_{0(V_1)}$, $\underline{f}_{(V_2)}$, SF_{W10} and $-2i\left[\,\vec{k}_1^{\,i}\cdot\overrightarrow{0V_1} + \,k_1\,V_1V_2\,\right]$ signify the incident field amplitude, the reflection dyad at the point V_1, the Fresnel dyad at the point V_2, the spreading factor and the phase term. Refer to (3.2) the radius of curvature after the first interaction at V_1 is given by:

$$\rho_{2(V_1)} \;=\; \frac{a_2\cos(\theta_i)}{2} \tag{3.18}$$

The curvature is not modified at V_2 due to the plane interface. Hence, the radius $\rho_{2(V_1)}$ for the propagation from V_1 to V_2 and back is defined by the distance V_1V_2 as follows:

$$\rho'_{2(V_1)} \;=\; \rho_{2(V_1)} + 2V_1V_2 \tag{3.19}$$

On the way back, the radius given in (3.19) is the incident radius of curvature for calculating the spreading factor at V_1 of the diffracted wave. The reflection at V_1 modifies the wave front curvature as follows:

$$\rho''_{2(V_1)} \;=\; \frac{1}{\frac{1}{\rho'_{2(V_1)}} \;+\; \frac{2}{a_2\cos(\theta_i)}} \tag{3.20}$$

Setting $1\,/\,\sqrt{\rho''_{2(V_1)} \,+\, V_1M} \;\approx\; 1\,/\,\sqrt{0M}$, the final spreading factor takes the final form:

$$SF_{W10} \;=\; \sqrt{\rho''_{2(V_1)}} \tag{3.21}$$

3.4 UTD Field

A serious shortcoming arises in GTD where the diffracted field doesn't remain continuous across a Surface Shadow Boundary (SSB). Away from such a SSB, the GTD and UTD field coincide. In the ray system, three transition regions are present for the backscattered field(fig. 3.16 - 3.18). The three transition zones are indicated as SSB 1, SSB 2 and SSB 3. The first shadow boundary (SSB 1) refers to the waves 3, 8 and 4. As outlined in fig. 3.16, with decreasing look angle φ_L, the waves 3 and 8 will approach the shadow boundary (SSB1) on their way back to the receiver and finally are replaced by the wave 4 at the transition. Here the corresponding look angle is given by φ_{SSB1}. The wave 4 propagates on a small arc length along the cylinder and compared to the spatial waves 3 and 8 the creeping wave 4 is powerless. Hence, a special emphasis is attributed in the following to the transition zones as near shadow boundaries a significant polarimetric behavior is expected. The same comments hold for the second considered transition zone at the boundary SSB 2 (fig. 3.17). Where by crossing the boundary, the creeping wave 13 replaces the spatial waves 11 and 12. In comparison to the first shadow boundary the two waves have here one additional interaction with the cylinder and the interface. Finally, according to fig. 3.18 a third shadow boundary SSB3 is investigated in the ray system. In this case, wave 6 replaces the waves 5 and 9 in the shadow region. The arc length of the creeping wave 6 along the cylinder is compared to the one of wave 4 much longer. Thus, the backscattered field is not of great power compared to those related to the first and second shadow boundaries. The UTD formulas in the work of McNamara [48] are valid for incident fields of GO type where the wave is locally plane. Thus, according to the introduced list of rays the single field values up to the points $\vec{E}_{W3(Q_1)}$, $\vec{E}_{W8(Q_2)}$, $\vec{E}_{W11(V_1)}$, $\vec{E}_{W12(Q)}$, $\vec{E}_{W5(Q)}$ and $\vec{E}_{W9(T_2)}$ can be calculated according to the classical UTD. In order to investigate the polarimetric behavior at such transition zones the continuity of the total field at the shadow boundary must be estimated. Note that the continuity is given by the wave twosomes 3+8, 11+12 and 5+9 where according to [48] the waves 3, 11 and 5 correspond to the incident field and the waves 8, 12 and 9 to the reflected field. The problem consists here that after the reflection on the cylinder the single spatial waves W3+W8, W11+W12 and W5+W9 have different radii of curvature.

Hence, the superposition of the incident and reflected wave represents no local plane wave front any more. Thus, for the way back the field cannot be calculated in the transition zones accurately by the UTD. The exact method to solve this problem would consists in a spectral decomposition of the wave front in elementary plane waves. Where for each single component the UTD would again be applicable. On the other hand, the field has to be continuous through the boundary as in nature no jumps occur at the transition from the lit into the shadow region. With that on mind, an Approximate Method is introduced for the field near the shadow boundary. Thus, the field over the entire range $0 \leq \varphi \leq 90°$ is split up in three segments: in the deep lit region away from the shadow boundaries the classical UTD formalism for the single waves 3, 5, 8, 9, 11 and 12 is accurate, in the vicinity of the boundaries the UTD field is calculated after the Approximate Method and finally in the shadow region the waves 4, 6 and 13 are computed without restriction.

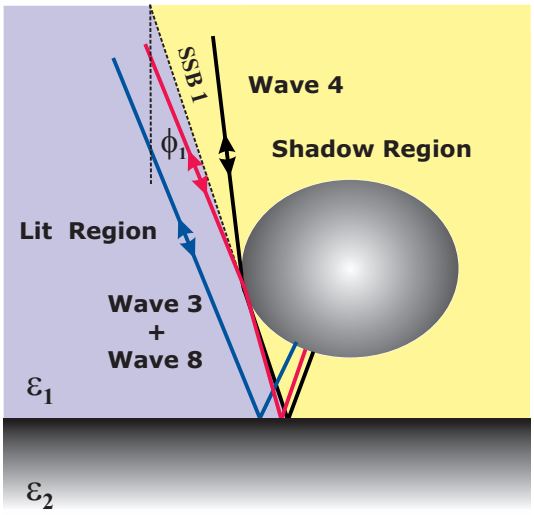

Figure 3.16: Transition Zone 1 (SSB1)

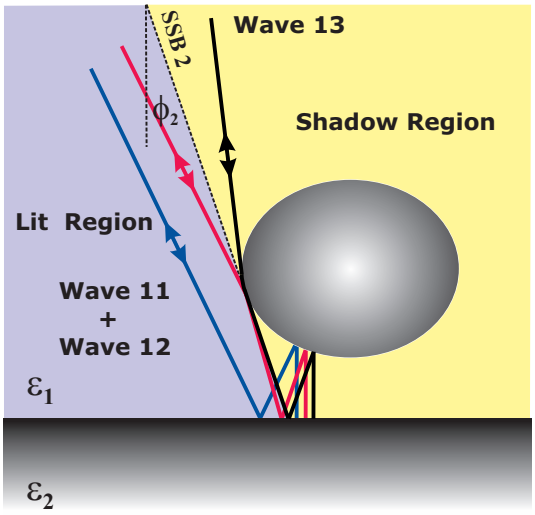

Figure 3.17: Transition Zone 2 (SSB2)

The exact and Approximate Method are summarized as follows:

- **Fourier Decomposition**
  The exact method consists in a Fourier spectral decomposition of the non plane wave front into elementary plane waves. In consequence every single plane wave can be calculated using the Fresnel coefficients, Pekeris and Fresnel function in the transition region.

- **Approximate Method**
  The total field is continues on the boundary approaching from lit and shadow region. Hence, on the boundary which correspond to the grazing case, it holds:

$$\vec{E}_3^i(M) + \vec{E}_8^r(M) = \vec{E}_4^D(M) \tag{3.22}$$

$$\vec{E}_{11}^i(M) + \vec{E}_{12}^r(M) = \vec{E}_{13}^D(M) \tag{3.23}$$

$$\vec{E}_5^i(M) + \vec{E}_9^r(M) = \vec{E}_6^D(M) \tag{3.24}$$

As the incidence field $\vec{E}^i(M)$ is plane for the grazing incidence, the above mentioned relations (3.22), (3.23) and (3.24) are only valid if the other two spatial waves are plane at the same time. This means that for the grazing incidence the Fourier components have a preferential contribution in this direction. Considering the boundary SSB 1 this means that the incident waves 3 + 8 at their reflection points Q_1 and Q_2 on the cylinder can be approximated by a local plane wave. Thus, both waves have the same radius of curvature after the reflection and the UTD is again valid. The same reasoning for the shadow boundaries SSB 2 and SSB 3. Note that this assumption is only valid close to the shadow boundaries. Here the Approximate Method is applied for the look angle range $\varphi_{SSB} < \varphi_L < \varphi_{SSB} + 5°$. Therefore, the three segments are determined by $0° < \varphi_L < \varphi_{SSB}$, $\varphi_{SSB} < \varphi_L < \varphi_{SSB} + 5°$ and $\varphi_{SSB} + 5° < \varphi_L < 90°$ corresponding to the shadow region, a small stripe at the boundary and finally to the lit region. The combination of the three segments is done by a polynomial fit, presented in section 3.5.

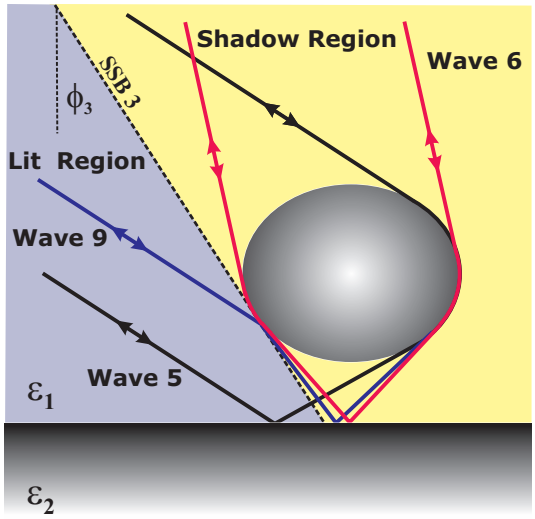

Figure 3.18: Transition Zone 3 (SSB3)

3.4.1 Surface Shadow Boundary 1

The introduced Approximate Method represents an innovation in the general UTD field calculation, so that the field transition at the shadow boundary SSB1 is discussed exemplary in detail next. The calculation at the second and third shadow boundary is performed in the same manner.

Lit Region

In a first step the waves 3 and 8 in the lit region are calculated up to the their reflection points Q_1 and Q_2 as outlined in fig. 3.5 and 3.10 in accordance to the classical UTD formalism. Approaching the boundary and finally at grazing incidence, the two points Q_1 and Q_2 coincide. This point is referred as Q (fig. 3.6). According to McNamara [48] the single fields of the waves 3 and 8 are given at Q_1 and Q_2 by:

$$\begin{aligned}\vec{E}_{3,8}(Q_1,Q_2) = &\underbrace{\vec{E}_0 \cdot \underline{f}(T_1)\ e^{-i\left[\vec{k}_1^{\,i}\cdot 0\vec{T}_1 + k_1\, T_1 Q_1\right]}}_{\vec{E}_3(Q_1)} \\ &+ \underbrace{\vec{E}_0 \cdot \underline{R}^a(P) \cdot \underline{f}(T_2)\ SF_{W8}(Q_2)\ e^{-i\left[\vec{k}_1^{\,i}\cdot 0\vec{P} + k_1(PT_2 + T_2Q_2)\right]}}_{\vec{E}_8(Q_2)}\end{aligned} \tag{3.25}$$

Where the first term on the right side in (3.25) corresponds to wave 3 and the second term is related to wave 8. Here the waves 3 and 8 correspond to the incident and reflected field [48]. The reflection dyad $\underline{R}^a(P)$ at the point P is described in appendix C.3.The scripting $\underline{R}^b(P)$ will describe the reflection at P for the way back to the antenna. The numerical computation of the two waves mentioned in (3.25) is outlined in the following.

- $\vec{E}_{3(Q_1)}$
  According to fig.3.5, it follows that no spatial divergence is given for wave 3 on its way to point Q_1. At T_1 the flat interface doesn't modify the wave front. Up to Q_1 field is simply computed by the Fresnel coefficients $\underline{f}_{(T_1)}$ and the phase term given in the exponent.

- $\vec{E}_{8(Q_2)}$
  From fig.3.10 it follows that with decreasing look angle φ_L a grazing incidence ($\theta_i = 0$) is given at point P. The related look angle is indicated as φ_{lim} and marks the boundary. Approaching the boundary, the radius of curvature at P tends to the limit $1/\rho_{2(P)} \to \infty$. Hence, the corresponding spreading factor gets equal to zero. Thus, in order to get a continuous field at the transition, the uniform reflection coefficients $\underline{R}^a$ are considered in (3.25). For the sake of legibility the general reflection dyad $\underline{R}$ expressions are put in appendix $C.3$. The related parameters of $\underline{R}^a$ are estimated as follows:

$$\begin{aligned} m_{(P)} &= \left[\frac{k_1\, a_{2(P)}}{2}\right]^{\frac{1}{3}} \\ \xi_p &= -2\; m_{(P)}\, cos_{(\theta^i)} \\ L_p &= PT_2 \;+\; T_2Q_2 \\ X_p &= 2\, k_1\, L_p\, cos^2{}_{(\theta^i)} \end{aligned} \tag{3.26}$$

  The quantity $\underline{f}_{(T_2)}$ describe the reflection at the interface and $SF_{W8(Q_2)}$ the spatial divergence. Here the radius of curvature $\rho_{2(P)}$ of the incident field $\vec{E}_0$ is changed at P due to the reflection on the cylinder. According to (3.2) it follows for a plane incident wave at P, the curvature by:

$$\rho_{2(P)} = \frac{a_{2(P)}\cos(\theta_i)}{2} \tag{3.27}$$

  The spatial divergence of the wave 8 up to Q_2 is given after (3.3) by:

$$SF_{W8(Q_2)} = \sqrt{\frac{\rho_{2(P)}}{\rho_{2(P)} \;+\; PT_2 \;+\; T_2Q_2}} \tag{3.28}$$

After the reflection at Q_1 and Q_2, the superposition of wave 3 and 8 doesn't yield a local plane front as both waves have different radii of curvature. Hence, the calculation of the waves W3+W8 for the way back according to the UTD formalism fails. In accordance to the Approximate Method, the incident waves 3 and 8 at their reflection points Q_1 and Q_2 are considered now as plane waves. Thus, both waves have approximately the same radius of curvature after their interactions with the target. Away from the boundary, in the lit region, the field is given accurately according to the classical UTD formulas. In general, the diffracted field is calculated for the way back as follows:

$$\begin{aligned} \vec{E}_{3,8(M)} = \vec{E}_{3(Q_1)} \cdot \underline{f}_{(T_1)} \;\; SF_{W3(Q_1)} \;\; e^{-i\left[\vec{k}_1^r \cdot 0\vec{T}_1 \,+\, k_1\, Q_1T_1\right]} \\ +\; \vec{E}_{8(Q_2)} \cdot \underline{f}_{(T_2)} \cdot \underline{R}^b_{(P)} \;\; SF_{W8(P)} \;\; e^{-i\left[\vec{k}_1^r \cdot 0\vec{P} \,+\, k_1(Q_2T_2 \,+\, T_2P)\right]} \end{aligned} \tag{3.29}$$

Wave 3

At Q_1 a plane incident field is always on hand, so that the divergence factor $SF_{W3(Q_1)}$ of wave 3 for the way back is given by:

$$SF_{W3(Q_1)} = \sqrt{\rho_{2(Q_1)}} \tag{3.30}$$

Where:

$$\rho_{2(Q_1)} = \frac{a_{2(Q1)}}{2} \tag{3.31}$$

Straightforward the term $1 / \sqrt{\rho_{2(Q_1)} + Q_1T_1 + T_1M}$ is set equal to $1 / \sqrt{0M}$ in (3.30) and neglected in the computation.

Wave 8

The Approximate Method is applied near the surface boundary in the look angle range $\varphi_{SSB1} < \varphi_L < \varphi_{SSB1} + 5°$. This region is noted as Segment 1. Away from the surface shadow boundary, in the range $\varphi_{SSB1} + 5° < 90°$, the classical UTD is applied for calculating the field. The field in the lit region is marked here as Segment 2. Hence, according to the two segments, the superposition (3.29) is computed in two different manners and discussed next.

- **Segment 1**

  Here the incident wave 8 at the point Q_2 is considered to be local plane. Hence, the radius of curvature of wave 8 is determined after the reflection at Q_2 by:

$$\rho_{2(Q_2)} = \frac{a_{2(Q_2)}}{2} \tag{3.32}$$

  The propagation from Q_2 back to P increases the radius in (3.32) in the following way:

$$\rho_{2(P)} = \rho_{2(Q_2)} + Q_2T_2 + T_2P \tag{3.33}$$

  After the reflection at P the curvature takes the form:

$$\rho'_{2(P)} = \frac{1}{\frac{1}{\rho_{2(P)}} + \frac{2}{a_{2(P)}\cos(\theta_i)}} \tag{3.34}$$

  In the same manner, substituting $1 / \sqrt{\rho'_{2(P)} + PM}$ by $1 / \sqrt{0M}$, it follows the divergence term of wave 8 as:

$$SF_{W8(P)} = \sqrt{\rho'_{2(P)}} \tag{3.35}$$

  For the way back the parameter L_p will be modified due to the adapted curvature expressed

in (3.33). The reflection dyad $\underline{\underline{R}}^b$ at P for the way back is here defined through:

$$\begin{aligned} m_{(P)} &= \left[\frac{k\, a_{2(P)}}{2}\right]^{\frac{1}{3}} \\ \xi_p &= -2\, m_{(P)}\, cos(\theta^i) \\ L_p &= \rho_{2(Q_2)} + Q_2T_2 + T_2P \\ X_p &= 2\, k\, L_p\, cos^2(\theta^i) \end{aligned}$$

- **Segment 2**

  In the lit region, the field of wave 8 is calculated after the classical UTD. Hence, no incident plane wave is considered at Q_2. Therefore, the radius of curvature of former interactions along its propagation must be considered. In consequence considering the first reflection at P, the incident plane wave 8 is modified by:

$$\rho_{2(P)} = \frac{a_{2(P)}\cos(\theta_i)}{2} \tag{3.36}$$

The radius of curvature of the incident wave at Q_2 is therefore due to its propagation up to Q_2 defined as:

$$\rho_{2(Q_2)} = \rho_{2(P)} + PT_2 + T_2Q_2 \tag{3.37}$$

Then, after the perpendicular reflection at Q_2 the radius becomes:

$$\rho'_{2(Q_2)} = \frac{1}{\frac{1}{\rho_{2(Q_2)}} + \frac{2}{a_{2(Q_2)}}} \tag{3.38}$$

In turn, the propagation back to the reflection point P yields:

$$\rho''_{2(Q_2)} = \rho'_{2(Q_2)} + Q_2T_2 + T_2P \tag{3.39}$$

Finally, after the way to the point of return Q_2 and back, the curvature of the wave front is given after the reflection at P in the way:

$$\rho'_{2(P)} = \frac{1}{\frac{1}{\rho''_{2(Q_2)}} + \frac{2}{a_{2(P)}\cos(\theta_i)}} \tag{3.40}$$

For numerical purpose the approximation $1\,/\,\sqrt{\rho'_{2(P)} + PM} = 1\,/\,\sqrt{0M}$ is set. At the end of the day the spreading factor $SF_{W8(P)}$ of wave 8 is given by:

$$SF_{W8(P)} = \sqrt{\rho'_{2(P)}} \tag{3.41}$$

Shadow Region

The spatial waves 3 and 8 are replaced by the creeping wave 4 in the shadow region. The latter propagates on a small arc length along the cylinder as shown in fig 3.6 and leaves the surface tangentially at the detachment point B again as a spatial wave towards the point T. In the shadow region the points B, T and F are fixed points and therefore must be computed only once. Here only the attachment point Q_{at} varies on the cylinder. Referring to the UTD diffraction dyad $\underline{T}$ introduced in appendix $C.4$ the field of wave 4 is given up to the point Q in a first step by:

$$\vec{E}_4(Q) \;=\; \vec{E}_0 \cdot \underline{T}^a(Q_{at},B)\;\; SF^a_{W4}(Q)\;\; e^{-i\left[\vec{k}^i_1 \cdot 0\vec{Q}_{at} + k_1\,(BT+TQ)\right]} \tag{3.42}$$

The detachment of all the points B along the cylinder describes the radiation of a line source. Hence, the radius of curvature $\rho_2(Q)$ and the divergence $SF^a_{W4}(Q)$ in (3.42) is immediately given by:

$$\rho_2(Q) \;=\; BT \;+\; TQ \tag{3.43}$$

$$SF^a_{W4}(Q) \;=\; \frac{1}{\sqrt{\rho_2(Q)}} \tag{3.44}$$

The general diffraction coefficients $\underline{T}^a$ is defined for the propagation up to the point of return Q as follows [48]:

$$\begin{aligned} m(Q_{at}) \;&=\; m(B) \;=\; \left[\frac{k\,a_2(Q_{at})}{2}\right]^{\frac{1}{3}} \\ \xi_d \;&=\; \int\limits_{\tau(Q_{at})}^{B} \frac{m(\tau)}{a_2(\tau)}\,d\tau \end{aligned} \tag{3.45}$$

$$L_d \;=\; BT \;+\; TQ \tag{3.46}$$

$$X_d \;=\; \frac{kL_d\,\xi_d^2}{2m(Q_{at})\,m(B)}$$

In order to calculate the way back of wave 4, the values $\vec{E}_4(Q)$ at Q and the radius of curvature mentioned in (3.46) are taken as input quantities. The received field at M is therefore computed as:

$$\vec{E}_4(M) \;=\; \vec{E}_4(Q) \cdot \underline{T}^b(B,Q_{at})\;\; SF^b_{W4}(B)\;\; e^{-i\left[-\vec{k}^r_1 \cdot 0\vec{Q}_{at} + k_1\,(QT+TB)\right]} \tag{3.47}$$

In this case, the numerical computation of the divergence term SF^b_{W4} and the diffraction dyad $\underline{T}^b(B,Q_{at})$ is of particular interest. Considering the curvature of the incoming wave 4 at Q given by (3.43), it follows after its reflection at Q the radius of curvature $\rho_2'(Q)$ as:

$$\rho_2'(Q) \;=\; \frac{1}{\frac{1}{\rho_2(Q)} \;+\; \frac{2}{a_2(Q)}}$$

Refer to (3.3) the propagation back from Q to B, yields:

$$SF^{b}_{W4(B)} \;=\; \sqrt{\frac{\rho_2'(Q)}{\rho_2'(Q) \;+\; BT \;+\; TQ}}$$

The spatial radiation at Q_{at} back to M corresponds again to a line source. Therefore one set the divergence term $1\,/\,\sqrt{Q_{at}M}$ equal to $1\,/\,\sqrt{0M}$. In (3.47) the creeping wave described by $\underline{T}^{b}{}_{(B,\,Q_{at})}$ is determined by:

$$\begin{aligned} L_d &= \rho_2'(Q) \;+\; BT \;+\; TQ \\ \xi_d &= \int\limits_{\tau(B)}^{\tau(Q_{at})} \frac{m(\tau)}{a_2(\tau)}\, d\tau \\ X_p &= \frac{k\, L_d\, \xi_d^2}{2m_{(Q_{at})} m_{(B)}} \end{aligned} \tag{3.48}$$

The shadow boundary of the wave 3 and 8 is determined through the geometrical setup. In the case that the general ellipsis with its major and minor axis a and b is degenerated into a circle, the shadow boundary (SSB1) considered here, is determined through the radius of the sphere $R = a = b$ and its height h above the ground. The boundary angle φ_{lim} is here given by:

$$\frac{R}{b+h} \;=\; \frac{\sin(2\varphi_{lim})}{\cos(\varphi_{lim})} \tag{3.49}$$

Wave 3, 4 and 8 on the boundary

The UTD implies the continuity of the field at the transition at a boundary. According to McNamara [48], the total field on the boundary (SSB1) is given here by the sum of the incident wave 3 and the reflected field wave 8. Hence, the total field $\vec{E}_{38}^{SSB1}$ at the reflection point Q_1 on the boundary takes at first the form:

$$\begin{aligned} \vec{E}_{3,8}^{SSB1}{}_{(Q_1=Q_2)} = \vec{E}_0 \cdot \Bigg[& \underline{f}_{(T_1)}\; e^{-i\left(\vec{k}_1^{\,i}\cdot 0\vec{T}_1 \,+\, k_1\, T_1 Q_1\right)} \;-\; \frac{1}{2}\, \underline{f}_{(T_2)}\, e^{-i\left(\vec{k}_1^{\,i}\cdot 0\vec{T}_2 \,+\, k_1\, T_2 Q_2\right)} \\ & -\; \underline{f}_{(T_2)}\, m_{(P)}\; \sqrt{\frac{2}{k_1}}\; e^{-i\frac{\pi}{4}}\; SF_{W8(Q_2)}\; e^{-i\left(\vec{k}_1^{\,i}\cdot 0\vec{T}_2 \,+\, k_1\, T_2 Q_2\right)} \left\{ \begin{array}{c} p^*{}_{(0)} \\ \\ q^*{}_{(0)} \end{array} \right\} \Bigg] \end{aligned} \tag{3.50}$$

Where the first term on the right side of (3.50) corresponds to the direct wave 3 and the last two terms are related to the indirect wave 8. In 3.50 the quantities p^* and q^* are the complex Fock scattering functions. The asterisk signifies that the complex conjugate has to be taken in

the case of a time-dependance $\exp(-i\omega t)$. Further, the quantity $m_{(P)}$ is given in appendix C.4. The divergence from the point P to Q_2 is calculated as follows:

$$SF_{W8(Q_2)} \;=\; \frac{1}{\sqrt{PT_2 \;+\; T_2Q_2}} \tag{3.51}$$

Again using $\vec{E}_{3,8}^{SSB1}{}_{(Q_1=Q_2)}$ as start value for the way back the total field at the antenna is calculated by:

$$\begin{aligned}\vec{E}_{3,8}^{SSB}{}_{(M)} = \vec{E}_{3,8\,(Q_1=Q_2)} \cdot \Bigg[& \underline{f}_{(T_1)} \cdot \underline{R}_{0\,(Q_1)} \;\; SF_{W3(Q_1)} \;\; e^{-i\left(\vec{k}_1^{\,r}{}_0\vec{T}_1 \,-\, k_1\, Q_1T_1\right)} \\ & - \frac{1}{2}\, \underline{f}_{(T_2)} \cdot \underline{R}_{0\,(Q_2)} \;\; SF_{W8(Q_2)} \;\; e^{-i\left(\vec{k}_1^{\,r}{}_0\vec{T}_2 \,-\, k_1\, Q_2T_2\right)} \;\; - \;\; m_{(P)} \sqrt{\frac{2}{k_1}}\, \underline{R}_{0\,(Q_2)} \\ & \cdot \underline{f}_{(T_2)} \;\; e^{-i\frac{\pi}{4}} \;\; SF_{W8(P)} \;\; e^{-i\left(\vec{k}_1^{\,r}{}_0\vec{T}_2 \,-\, k_1\, Q_2T_2\right)} \left\{ \begin{array}{c} p^*{}_{(0)} \\ \\ q^*{}_{(0)} \end{array} \right\} \Bigg]\end{aligned} \tag{3.52}$$

Where the spreading factor $SF_{W3(Q_1)}$ and $SF_{W8(Q_2)}$ in (3.52) are given by the reflection of a plane incident wave at the cylinder. The divergence related to Q_1 is therefore given by:

$$\rho_{2(Q_1)} \;=\; \rho_{2(Q_2)} \;=\; \frac{a_{2(Q_1)}}{2} \tag{3.53}$$

$$SF_{W3(Q_1)} \;=\; SF_{W8(Q_2)} \;=\; \sqrt{\rho_{2(Q_1)}} \tag{3.54}$$

Where $1\,/\,\sqrt{\rho_{2(Q_1)} \;+\; Q_1T_1 \;+\; T_1M}$ is set equal to $1\,/\,\sqrt{0M}$.
In addition, the spreading factor of wave 8 yields:

$$SF_{W8(P)} \;=\; \sqrt{\frac{\rho_{2(Q_2)}}{\rho_{2(Q_2)} \;+\; Q_2T_2 \;+\; T_2P}} \tag{3.55}$$

For the way back the spatial divergence terms $1\,/\,\sqrt{PM}$ is approximately equal to $1\,/\,\sqrt{0M}$.

3.4.2 Surface Shadow Boundary 2

Lit Region

According to fig. 3.17, the waves 11 and 12 related to the lit region are replaced by the wave 13 in the shadow region. In accordance to [48], the sum of the direct incident wave 11 and the reflected wave 12 assures the continuity of the field at the second shadow boundary (SSB2). In comparison to the first investigated transition zone, one additional interaction between the object and the interface is given. The structure of the field expressions is kept in the same manner as for the first transition zone. An additional reflection coefficient must be added respecting the interaction with the soil at the points V_2 and S and the corresponding radii of curvature are arranged. Similar to the first transition zone, the superposition of the wave 11 and 12 is calculated in a first step up to the points of return V_2 and S. The field at the points V_2 and S yields:

$$\begin{aligned}\vec{E}_{11,12(V_2,S)} = &\underbrace{\vec{E}_0 \cdot \underline{f}_{(U)} \cdot \underline{R}_{0(V_1)} \;\; SF_{W11(V_2)} \;\; e^{-i\left[\vec{k}_1^i \cdot 0\vec{U} + k_1(UV_1+V_1V_2)\right]}}_{\vec{E}_{11(V_2)}} \\ &+ \underbrace{\vec{E}_0 \cdot \underline{R}^a_{(P)} \cdot \underline{f}_{(T)} \cdot \underline{R}_{0(Q)} \;\; SF_{W12(S)} \;\; e^{-i\left[\vec{k}_1^i \cdot 0\vec{P} + k_1(PT+TQ+QS)\right]}}_{\vec{E}_{12(S)}}\end{aligned} \tag{3.56}$$

Where the first term on the right side in (3.56) describes the direct field (wave 11) and the second one the reflected field (wave 12). The UTD reflection dyad $\underline{R}^a$ describes the reflection at P for the way to the point of return S. The reflection dyad $\underline{R}_0$ for the perfect conducting cylinder reduces, according to the hard $\parallel$ and soft $\perp$ polarization, to $R_H = 1 \;\; R_S = -1$.
Next, the spatial divergence of the two waves is discussed. Considering first the reflection of the incident wave 11 at V_1. Straightforward its curvature is modified after the reflection as follows:

$$\rho_{2(V_1)} \;=\; \frac{a_{2(V_1)} \;\cos(\theta_i)}{2} \tag{3.57}$$

The spreading factor $SF_{W11(V_2)}$ of wave 11 up to the reflection point V_2 is given by:

$$SF_{W11(V_2)} \;=\; \sqrt{\frac{\rho_{2(V_1)}}{\rho_{2(V_1)} \;+\; V_1V2}} \tag{3.58}$$

Referring next to wave 12, the spreading factor $SF_{W12(S)}$ at the point S is deduced. The plane incident wave 12 gets after its first interaction with the cylinder at P the following curvature:

$$\rho_{2(P)} \;=\; \frac{a_{2(P)} \;\cos(\theta_i)}{2}$$

The propagation up to Q yields the radius $\rho_{2(P)}$:

$$\rho_{2(Q)} \;=\; \rho_{2(P)} \;+\; PT \;+\; TQ$$

The incident radius of curvature at Q is given by $\rho_{2(Q)}$. Hence, after the reflection at Q, the radius changes:

$$\rho'_{2(Q)} \;=\; \frac{1}{\frac{1}{\rho_{2(Q)}} \;+\; \frac{2}{a_{2(Q)} \;\cos(\theta_i)}}$$

Finally, up to S the divergence is calculated as:

$$SF_{W12(S)} \;=\; \sqrt{\frac{\rho'_{2(Q)}}{\rho'_{2(Q)} \;+\; QS}} \tag{3.59}$$

Identically to the first discussed transition zone, the way back to the antenna is calculated for two different segments according to the Approximate Method and the classical UTD formalism. Generally, the field received at the antenna is given with the start values $\vec{E}_{11(V_2)}$ and $\vec{E}_{12(S)}$ by:

$$\begin{aligned}\vec{E}_{11,12(M)} = &\vec{E}_{11(V_2)} \cdot \underline{f}_{(V_2)} \cdot \underline{R}_{0(V_1)} \cdot \underline{f}_{(U)} \;\; SF_{W11(V_1)} \;\; e^{-i\left[\vec{k}_1^r \cdot 0\vec{U} + k_1(\,V_2V_1+V_1U)\right]} \\ &+ \;\vec{E}_{12(S)} \cdot \underline{f}_{(S)} \cdot \underline{R}_{0(Q)} \cdot \underline{f}_{(T)} \cdot \underline{R}^b_{(P)} \;\; SF_{W12(P)} \;\; e^{-i\left[\vec{k}_1^r \cdot 0\vec{P} + k_1(SQ+QT+TP)\right]}\end{aligned} \tag{3.60}$$

Where $\underline{f}_{(V_2)}$, $\underline{f}_{(U)}$, $\underline{f}_{(S)}$ and $\underline{f}_{(T)}$ signify the corresponding Fresnel coefficients. The quantities $\underline{R}_{0(V_1)}$, $\underline{R}_{0(Q)}$ and $\underline{R}^{b}_{(P)}$ refer to the UTD reflection coefficients. The two exponents define the phase of the waves 11 and 12. The numerical calculation and the related spreading factors $SF_{W11(V_1)}$ and $SF_{W12(P)}$ in accordance to the two segments is discussed now. Referring to the Approximate Method, a plane incident field is considered at the reflection points V_1 and Q for the way back and marked as segment 1. The Approximate Method is applied in the range: $\varphi_{SSB2} < \varphi_L < \varphi_{SSB2} + 5°$. The segment 2 is related to look angles away from the boundary and given in the range $\varphi_{SSB2} + 5° < 90°$. In this field segment the single waves 11 and 12 are calculated after the classical UTD. Here, the modified radii of curvature due to former interactions on the way to the points of return V_2 and S are taken into account.

- **Segment 1**
  In this field segment, a plane incident wave is considered at V_1 for the way back, so that after the reflection it holds for wave 11:

$$\rho'_{2(V_1)} = \frac{a_{2(V_1)} \cos(\theta_i)}{2}$$

  Setting $1 / \sqrt{\rho'_{2(V_1)} + V_1U + UM}$ equal to $1 / \sqrt{0M}$, the spreading factor $SF_{W11(V_1)}$ in (3.60) is given by:

$$SF_{W11(V_1)} = \sqrt{\rho'_{2(V_1)}}$$

  Next, the spreading factor of wave 12 is derived. In accordance with the Approximate Method it follows for the reflection at Q:

$$\rho'_{2(Q)} = \frac{2}{a_{2(Q)} \cos(\theta_i)} \tag{3.61}$$

  The propagation back from Q to P yields:

$$\rho'_{2(P)} = \rho_2\prime_{(Q)} + QT + TP \tag{3.62}$$

  The curvature $\rho'_{2(P)}$ is given after the reflection at P by:

$$\rho''_{2(P)} = \frac{1}{\frac{1}{\rho'_{2(P)}} + \frac{2}{a_{2(P)} \cos(\theta_i)}} \tag{3.63}$$

  Substituting the term $1 / \sqrt{\rho'_{2(P)} + PM}$ by $1 / \sqrt{0M}$. The final divergence term is defined as:

$$SF_{W12(P)} = \sqrt{\rho''_{2(P)}}$$

- **Segment 2**
  In this range no plane wave front is considered at V_1 for the way back of the round trip. The above mentioned expression according to (3.4.2) are valid except that for the way back the radius $\rho_2'_{(V_1)}$ at V_1 of wave 11 is modified here as follows:

$$\rho_2'_{(V_1)} = \frac{1}{\frac{1}{\rho_2''_{(V_1)} + 2V_1V_2} + \frac{2}{a_2(V_1)\cos(\theta_i)}} \tag{3.64}$$

  Thus, the radius of curvature $\rho_2'_{(Q)}$ at Q for the way back of wave 12 must be regarded. The curvature at Q is given therefore by:

$$\rho_2''(Q) = \frac{1}{\frac{1}{\rho_2'(Q) + 2QS} + \frac{2}{a_2(Q)\cos(\theta_i)}} \tag{3.65}$$

Shadow Region

The third segment corresponds to the shadow region in the range $\varphi_L < \varphi_{SSB2}$. In the shadowed region the wave 11 and 12 are replaced by the wave 13 which creeps on a small arc length on the surface. Similarly to the wave 4 at the first investigated transition zone, wave 13 is first computed up to its point of return V_5 as follows:

$$\vec{E}_{13(V_5)} = \vec{E}_0 \cdot \underline{T}^a_{(V_1,V_2)} \cdot \underline{f}_{(V_3)} \cdot \underline{R}_{0(V_4)} \; SF_{W13(V_5)} \; e^{-i\left[\vec{k}_1^i \cdot 0\vec{V}_1 + k_1 (V_2V_3 + V_3V_4 + V_4V_5)\right]} \tag{3.66}$$

Straightforward the reflection at V_4 is given by $R_H = 1 \;\; R_S = -1$ for the perfect conducting cylinder. In the field expression (3.66) the divergence of wave 13 is given at V_5 by:

$$\rho_{2(V_4)} = \frac{1}{\frac{1}{V_2V_3 + V_3V_4} + \frac{2}{a_2(V_4)\cos(\theta_i)}} \tag{3.67}$$

The propagation up to point V_5 yields the spreading factor $SF_{W13(V_5)}$:

$$SF_{W13(V_5)} = \sqrt{\frac{\rho_{2(V_4)}}{\rho_{2(V_4)} + V_4V_5}} \tag{3.68}$$

Considering $\vec{E}_{13(V_5)}$ as start value for the way back, the received wave 13 is of the following form:

$$\begin{aligned}\vec{E}_{13(M)} = \vec{E}_{13(V_5)} \cdot \underline{f}_{(V_5)} \cdot \underline{R}_{0(V_4)} \cdot \underline{f}_{(V_3)} \cdot \underline{T}^b_{(V_2,V_1)} \;\; SF_{W13(V_2)} \\ e^{-i\left[\vec{k}_1^r \cdot 0\vec{V}_1 + k_1 (V_5V_4 + V_4V_3 + V_3V_2)\right]}\end{aligned} \tag{3.69}$$

The spreading factor $SF_{W13(V_2)}$ of the diffracted wave 13 is derived next. The radius of curvature after the reflection at V_4 on the way to the point of return V_5 is defined by (3.67). The propagation to V_5 and back to V_4 yields:

$$\rho_2'_{(V_4)} = \rho_{2(V_4)} + 2V_4V_5 \tag{3.70}$$

For the reflection at V_4 it yields:

$$\rho_2''(V_4) \;=\; \frac{1}{\frac{1}{\rho_2'(V_4)} \;+\; \frac{2}{a_2(V_4)\cos(\theta_i)}} \tag{3.71}$$

Refer to latter, the divergence is given up to the attachment point V_2 by:

$$SF_{W13(V_2)} \;=\; \sqrt{\frac{\rho_2''(V_4)}{\rho_2''(V_4) \;+\; V_4V_3 \;+\; V_3V_2}} \tag{3.72}$$

Similarly to the previous waves, the divergence from the cylinder to the antenna $1\,/\,\sqrt{V_1M}$ is again approximately given by $1\,/\,\sqrt{0M}$.

Wave 11, 12 and 13 on the boundary

The field $\vec{E}_{11,12}$ on the shadow boundary is given in a first step at the point $V_2 = S$ by [48]:

$$\begin{aligned}\vec{E}_{11,12(V_2=S)} = \vec{E}_0 \cdot \Big[& \underline{f}_{(U)} \cdot \underline{R}_{0(V_1)} \;\; SF_{W11(V_2)} \;\; e^{-i\left[\,\vec{k}_1^{\,i}\cdot 0\vec{U} \;+\; k(\,UV_1 \;+\; V_1V_2)\right]} \\ & -\; \frac{1}{2}\, \underline{f}_{(T)} \cdot \underline{R}_{0(Q)} \;\; SF^a_{W12(S)} \;\; e^{-i\left[\,\vec{k}_1^{\,i}\; 0\vec{T} \;+\; k_1\,(TQ \;+\; QS)\right]} \\ & -\; \underline{f}_{(T)} \cdot \underline{R}_{0(Q)}\; m_{(Q)}\, \sqrt{\frac{2}{k_1}}\, e^{-i\frac{\pi}{4}} \;\; SF^b_{W12(S)} \;\; e^{-i\left[\,\vec{k}_1^{\,i}\; 0\vec{T} \;+\; k_1\,(TQ \;+\; QS)\right]} \left\{ \begin{array}{c} p^*_{(0)} \\ \\ q^*_{(0)} \end{array} \right\} \Big]\end{aligned} \tag{3.73}$$

The first term on the right hand of (3.73) describes the direct incident wave 11 and the second and third terms correspond to the reflected wave 12. Where $\underline{f}_{(U)}$ and $\underline{f}_{(T)}$ describe the corresponding Fresnel coefficients. The reflection on the cylinder is given by $\underline{R}_{0(V_1)}$ and $\underline{R}_{0(Q)}$. The quantity $m_{(Q)}$ is given in appendix *C*.4. Further, the exponents define the phase of the two waves. Due to fact that the points V_2 and S coincide the divergence for the first and second term is given as follows:

$$\rho_{2(V_1=Q)} \;=\; \frac{a_{2(V_1=Q)}\cos(\theta_i)}{2} \tag{3.74}$$

Hence, due that V_1V_2 is equal to QS the divergence up to the points of return yields:

$$SF_{W11(V_2)} \;=\; SF^a_{W12(S)} \;=\; \sqrt{\frac{\rho_{2(V_1)}}{\rho_{2(V_1)} \;+\; V_1V_2}} \tag{3.75}$$

The spreading factor mentioned in the third term takes the spatial divergence of the propagation from P to Q into account. Where the radius is immediately given by $\rho_2 = PT + TQ$. In consequence the radius of curvature after the reflection at Q is given by:

$$\rho_2'(Q) \;=\; \frac{1}{\frac{1}{PT+TQ} \;+\; \frac{2}{a_2(Q)\cos(\theta_i)}} \tag{3.76}$$

In this way the spreading factor $SF^{b}_{W12(S)}$ at the point of return S, is defined as:

$$SF^{b}_{W12(S)} \;=\; \sqrt{\frac{\rho'_2(Q)}{\rho'_2(Q) \;+\; QS}} \tag{3.77}$$

Considering the value of (3.73) as start quantity for the way back, it follows:

$$\vec{E}^{SSB}_{11,12}(M) = \vec{E}_{11,12(V_2=S)} \cdot \Bigg[\underline{f}(V_2) \cdot \underline{R}_0(V_1) \cdot \underline{f}(U)\; SF_{W11(V_1)}\; e^{-i[\vec{k}^r_1 0\vec{U} \,-\, k_1\,(V_2V_1 \,+\, V_1U)]}$$

$$-\;\frac{1}{2}\;\underline{f}(S) \cdot \underline{R}_0(Q) \cdot \underline{f}(T)\; SF_{W12(Q)}\; e^{-i[\vec{k}^r_1 0\vec{P} \,-\, k\,(SQ \,+\, QT \,+\, TP)]}$$

$$-\;\underline{f}(S) \cdot \underline{R}_0(Q) \cdot \underline{f}(T) \cdot m(P)\; \sqrt{\frac{2}{k_1}}\;\; e^{-i\frac{\pi}{4}}\;\; SF_{W12(P)}\;\; e^{-i[\vec{k}^r_1 0\vec{P} \,-\, k\,(SQ \,+\, QT \,+\, TP)]} \left\{ \begin{array}{c} p^*(0) \\ \\ q^*(0) \end{array} \right\} \Bigg] \tag{3.78}$$

Analog to the firstly discussed transition zone, a plane wave is considered here as incident field at the reflection points V_1 and Q for the way back. Thus, the spreading factors $SF_{W11(V_1)}$, $SF_{W12(Q)}$ and $SF_{W12(P)}$ in (3.78) are given by:

$$\rho_{2(V_1=Q)} \;=\; \frac{a_{2(V_1=Q)}\cos(\theta_i)}{2} \tag{3.79}$$

$$SF_{W11(V_1=Q)} \;=\; SF_{W12(V_1=Q)} \;=\; \sqrt{\rho_{2(V_1=Q)}} \tag{3.80}$$

The divergence back to the point P is described by:

$$SF_{W12(P)} \;=\; \sqrt{\frac{\rho_2(Q)}{\rho_2(Q) \;+\; QT \;+\; TP}} \tag{3.81}$$

For numerical purpose the expression $1\,/\,\sqrt{\rho_2(Q) \;+\; V_1U \;+\; UM}$ and $1\,/\,\sqrt{PM}$ were substituted by $1\,/\,\sqrt{0M}$.

3.4.3 Surface Shadow Boundary 3

Waves 5, 6 and 9 near the transition zone

The third and last shadow boundary SSB 3 which occur in the ray field is pointed out in fig. 3.18. Here the wave 5 and 9 are replaced by the wave 6. Due to the fact that all related waves propagate on a long arc length around the target as creeping waves, the backscattered field is powerless compared to the previous discussed shadow boundaries. Nevertheless this boundary also contains information about the target.

Lit region

Straightforward the field $\vec{E}_{5,9}$ at the attachment point Q and T_2 is given through the sum of the direct and reflected field here corresponding to the waves 5 and 9. The sum of both waves

assures the continuity at the transition into the shadow region. On the boundary the points Q and T_2 coincide, yielding:

$$\begin{aligned}\vec{E}_{5,9(Q,T_2)} = & \underbrace{\vec{E}_0 \cdot \underline{f}_{(P)}\, e^{-i\left[\vec{k}_1^i \cdot 0\vec{P} + k_1 PQ\right]}}_{\vec{E}_5(Q)} \\ & + \underbrace{\vec{E}_0 \cdot \underline{R}_{(T_1)} \cdot \underline{f}_{(S)}\ \ SF_{W9(T_2)}\ \ e^{-i\left[\vec{k}_1^i \cdot 0\vec{T}_1 + k_1(T_1S+ST_2)\right]}}_{\vec{E}_9(T_2)}\end{aligned} \tag{3.82}$$

Where $\underline{f}_{(P)}$ and $\underline{f}_{(S)}$ refer to the Fresnel coefficients at the interaction points at the interface. The quantity $\underline{R}_{(T_1)}$ mentions the UTD reflection dyad $\underline{R}_{(T_1)}$ given in appendix $C.3$. Similar to the previous discussed wave the above mentioned exponents define the phase of the waves. The energy loss $SF_{W9(T_2)}$ due to the reflection on the cylinder is presented next. First the wave front of the incidence plane wave 9 at T_2 is giving after the reflection as:

$$\rho_{2(T_1)} \ = \ \frac{a_{2(T_1)}}{2} \tag{3.83}$$

The propagation up to the attachment point T_2 on the cylinder takes then the form:

$$SF_{W9(T_2)} \ = \ \sqrt{\frac{\rho_{2(T_1)}}{\rho_{2(T_1)} \ + \ T_1S \ + \ ST_2}} \tag{3.84}$$

After its propagation around the cylinder, the creeping wave 9 is radiated tangentially away from the target into the space. The propagation of the creeping wave is calculated using the dyadic diffraction coefficient $\underline{T}$ relating the incident space wave at point T_2 with the diffracted wave at point Q'. At the point of observation the field $\vec{E}_{5,9(M)}$ is given by:

$$\vec{E}_{5,9(M)} \ = \ \vec{E}_{5(Q)} \cdot \underline{T}_{(Q,Q')}\, e^{-i\left[\vec{k}_1^r \cdot 0\vec{Q}'\right]} \vec{E}_{9(T_2)} \cdot \underline{T}_{(T_2,Q')}\, e^{-i\left[\vec{k}_1^r \cdot 0\vec{Q}'\right]} \tag{3.85}$$

In the same manner as the previous transition zones, the UTD field over the entire look angle range is divided into three segments.

Segment 1

Close to the shadow boundary $\varphi_{SSB3} < \varphi_L < \varphi_{SSB3} + 5°$, the field is calculated according to the Approximate Method. In this case a plane incident wave is considered at the attachment point $Q = T_2$. Where the distance parameter L_d of $(C.10)$ and the argument of the transition function X_d are infinite. Hence, the transition function reduces to $F(\infty) = 1$ as seen in fig. C.1.

Segment 2

Refer to the lit region $\varphi_{SSB3} + 5° < 90°$, the sum of wave 5 and 9 is computed in accordance to (3.92). The diffraction dyad $\underline{T}_{(T_2,Q')}$ of the arc T_2 to Q' is performed in agreement to the formulas given in appendix $C.4$. According to (3.83) the distance parameter L_d in $(C.11)$ is defined at the attachment point T_2 as follows:

$$L_{d(T_2)} \ = \ \rho_{2(T_1)} + T_1S + ST_2 \tag{3.86}$$

Shadow region

In the third segment $\varphi_L < \varphi_{SSB3}$, the diffracted creeping wave 6 is outlined in fig. 3.8. Here wave 6 propagates additionally as a creeping wave along the arc QE . The wave 6 is expressed as:

$$\vec{E}_{6(M)}\big) \;=\; \vec{E}_0 \cdot \underline{T}_{(Q,\,E)} \cdot \underline{f}_{(T)} \cdot \underline{T}_{(F,\,Q')} \;\; SF_{W6(F)} \;\; e^{-i\,k_1\,(ES\,+\,SF)} \tag{3.87}$$

Its radiation as a space wave from the detachment point E to the attachment point F leads to the divergence:

$$SF_{W6(F)} \;=\; \frac{1}{\sqrt{ET\,+\,TF}} \tag{3.88}$$

The two diffraction dyads $\underline{T}_{(Q,\,E)}\;\underline{T}_{(F,\,Q')}$ have the same distance parameter L_d as the antenna is positioned in the far-field. Where the distance parameter is determined through:

$$L_d \;=\; ET\,+\,TF \tag{3.89}$$

Here the propagation to the cylinder and back to the antenna is interchangeable. Therefore, the double value of $\vec{E}_{5,9}$ and $\vec{E}_6$ must be computed.

Waves 5, 6 and 9 on the boundary

At the look angle corresponding to third shadow boundary (SSB3) the geometrical points of the waves 5 and 9 coincide. Their geometrical attachment and detachment points as spatial and creeping waves are shown in fig. 3.7 and 3.11. In a first step, the superposition of the waves 5 and 9 is calculated up to their common attachment point $Q = T_2$. The field is given at $Q = T_2$ as follows [48]:

$$\begin{aligned}\vec{E}_{5,9\,(Q\,=\,T_2)} = \vec{E}_0 \cdot \Bigg[& \underline{f}_{(P)}\; e^{-i\left(\vec{k}_1^{\,i}\cdot 0\vec{P}\,+\,k_1\,PQ\right)} \;-\; \frac{1}{2}\;\underline{f}_{(S)}\; e^{-i\left(\vec{k}_1^{\,i}\cdot 0\vec{S}\,+\,k_1\,ST_2\right)} \\ & -\; \underline{f}_{(S)}\; m_{(T_1)}\;\sqrt{\frac{2}{k_1}}\;\; e^{-i\frac{\pi}{4}}\;\; SF_{W9(T_2)}\;\; e^{-i\left(\vec{k}_1^{\,i}\cdot 0\vec{S}\,+\,k_1\,ST_2\right)} \left\{ \begin{array}{c} p^*{}_{(0)} \\ \\ q^*{}_{(0)} \end{array} \right\} \Bigg]\end{aligned} \tag{3.90}$$

Here the first term on the right side (3.90) describes the direct incident wave 5, where the second and last term refer to the reflected wave 9. The divergence of the last term yields:

$$SF_{W9(T_2)} \;=\; \frac{1}{\sqrt{T_1S\,+\,ST}} \tag{3.91}$$

On the boundary itself a local plane wave is considered. Hence, the propagation as a creeping wave around the object and the diffraction as a spatial waves at Q' is calculated as follows:

$$\vec{E}_{5,9\,(M)} \;=\; \vec{E}_{5,9\,(Q\,=\,T_2)} \cdot \underline{T}_{(Q\,=\,T_2,\,Q')}\; e^{\,i\left(\vec{k}_1^{\,r}\cdot 0\vec{Q}'\right)} \tag{3.92}$$

The energy spread due to the propagation way back to the receiver $1\,/\,\sqrt{Q'M}$ is set equal to

$1 \,/\, \sqrt{0M}1$ and neglected in the computation. The geometrical parameters for the shadow boundary (SSB3) is determined in the case of a circle of radius R at the height h above the ground by:

$$\sin(\varphi_{lim}) \;=\; \frac{R}{b+h} \tag{3.93}$$

3.5 Transition at a Surface Shadow Boundary

In this work a special emphasis is attributed to the transition regions near the shadow boundaries. Due to the strong attenuation of waves creeping along the surface of an object, the polarization behavior undergo a significant variation near such a transition zone. As mentioned in the introduction of section 3.4, the field in the lit region is calculated after the UTD-GTD for look angles away from the shadow boundary. The approached method is solely applied in the vicinity of the shadow boundary and finally on the shadow boundary itself. In accordance with section 3.4 the field is calculated after the Approximate Method and constrained in the segment $\varphi_{SSB} < \varphi_L < \varphi_{SSB} + 5^\circ$. In the lit region away from the boundary and in the shadow region the field is given by the classical UTD formalism. Thus, three segments have to be combined in order to have a continuous field over the entire look angle range. Therefore, a polynomial fitting near transition zones was carried out. In the following the fit of the UTD field across the first investigated boundary is exemplarily shown here in details. Concerning the second transition zone, one additional reflection at the interface is given here. Otherwise it has the same formal structure as the first one. Due to the strong attenuation of the creeping waves related to the third transition zone, the main focus is on the first two boundaries. In this section the single wave contributions of the implemented ray system are presented once for a perfect conducting interface $\epsilon_2 = PC$ and once for a dielectric soil $\epsilon_2 = 9.6$. Exemplarily, the field is calculated over the entire look angle range as follows:

- **GTD-UTD**
  Away from the boundary in the lit region, the general reflection coefficients $R(UTD)$ and diffraction coefficients $T(UTD)$ are used according to appendix $C.3$ and $C.4$. The waves 3+8 and 4 are calculated up to the shadow boundary after the classical GTD-UTD. In spite of, that after the reflection on the cylinder the superposition of wave 3 and 8 represents no plane wave anymore, the UTD formulas are again applied for the way back. Hence, approaching the boundary from the lit side, the numerical results are not accurate and discontinuity of the field across the shadow boundary is given in consequence.

- **The Approximate Method**
  After the Approximate Method the field is calculated near the boundary in such a way, that the incident wave 3 and 8 at the points of return Q_1 and Q_2 are considered as plane waves for the way back.

- **GO**
  In the deep lit region the GO and UTD fields must again coincide. In order to check this, the reflection at the cylinder is calculated by $R = \pm 1$ for the wave 8 in the lit region.

According to above mentioned notation, the three segments over the whole look angle range are shown for the real and imaginary part of the parallel field component in fig. 3.19 to fig. 3.20. A larger scale is chosen where near the shadow boundary. Correspondingly, the real and imaginary part of the perpendicular component is pointed out in fig. 3.21 and fig. 3.22. The presented results were calculated for a linear field $\vec{E}^0_{||} = 1$ and $\vec{E}^0_{\perp} = 1$. From the figures one recognizes that in the deep lit region the GTD-UTD and the GO fall together as expected. In order to make the field over the three segments continuous, a polynomial fit was chosen for the points in the range $\varphi_{SSB1} - 10° < \varphi_L < \varphi_{SSB1} + 10°$. Such a polynomial fit is nowadays readily given in technical computing language like the software package Matlab. Here, degrees of $6 \leq n \leq 10$ were chosen for the polynomial fit depending on the best match, specially in view of the exact value on the boundary. The corresponding fits of the real and imaginary part are presented once for a perfect conducting interface and a lossless dielectric half-space $\epsilon_2 = 9.6$ in the fig. 3.24 to fig. 3.32.

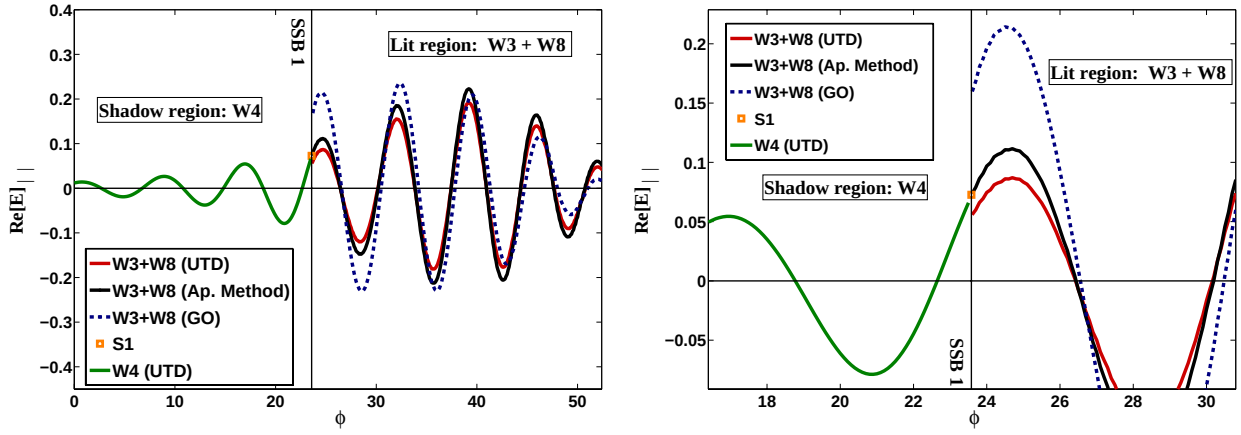

(a) Range ϕ (b) Section SSB

Figure 3.19: Real part of the $\vec{E}_{||}$ component. $[\vec{E}^0_{||} = 1, \vec{E}^0_{\perp} = 1, f = 500MHz, \epsilon_2 = 9.6]$

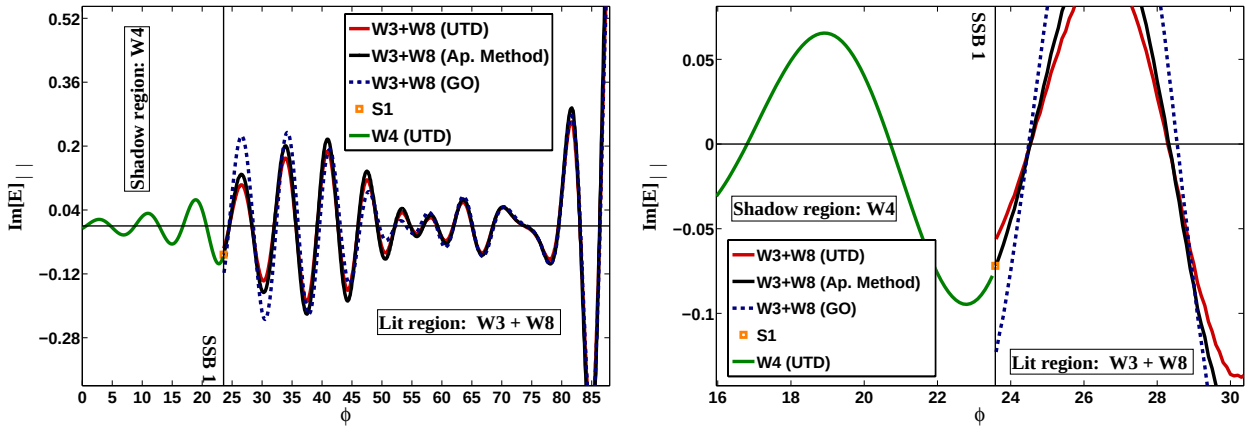

(a) Range ϕ (b) Section SSB

Figure 3.20: Imaginary part of the $\vec{E}_{||}$ component.$[\vec{E}^0_{||} = 1, \vec{E}^0_{\perp} = 1, f = 500MHz, \epsilon_2 = 9.6]$

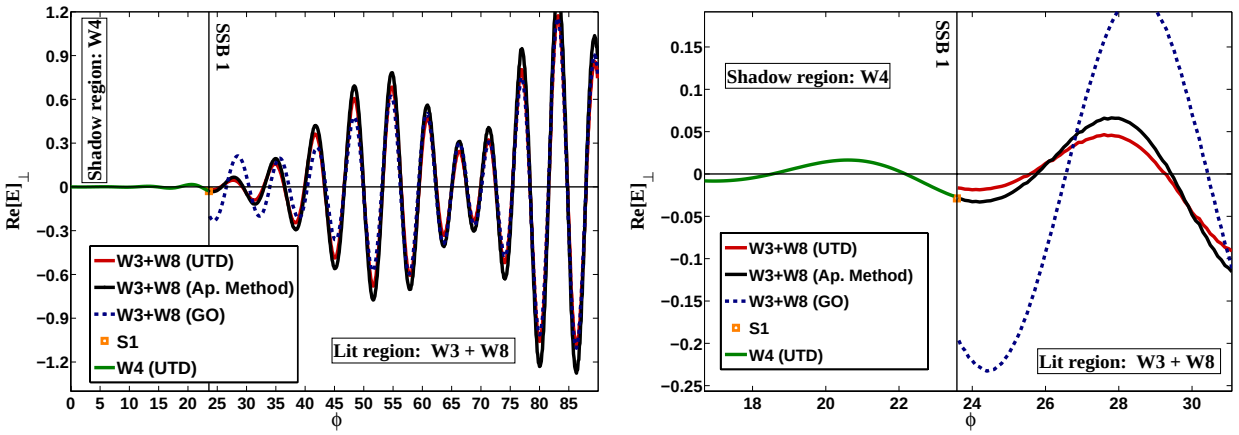

(a) Range ϕ (b) Section SSB

Figure 3.21: Real part of the $\vec{E}_{\perp}$ component. $[\vec{E}^0_{||} = 1, \vec{E}^0_{\perp} = 1, f = 500MHz, \epsilon_2 = 9.6]$

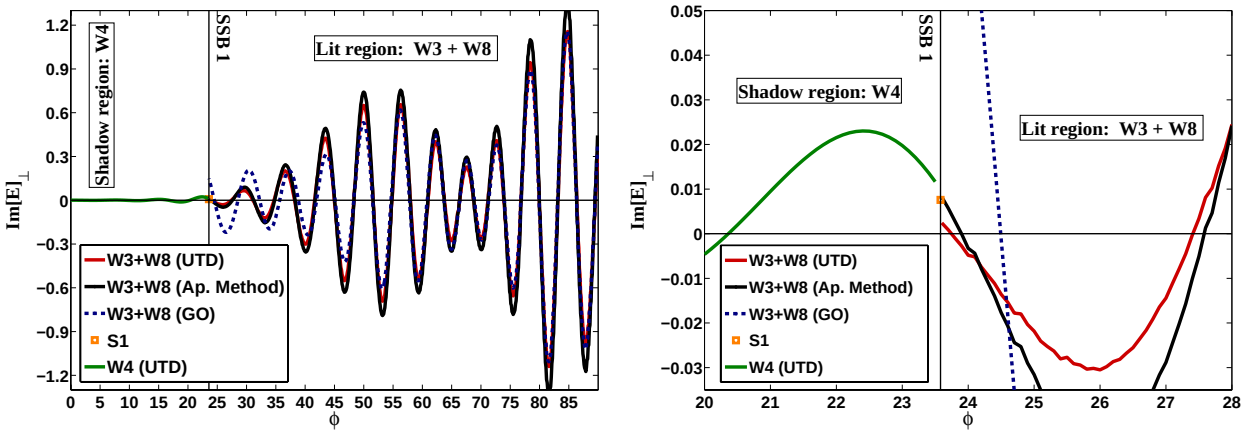

(a) Range ϕ (b) Section SSB

Figure 3.22: Imaginary part of the $\vec{E}_{\perp}$ component. $[\vec{E}^0_{||} = 1, \vec{E}^0_{\perp} = 1, f = 500MHz, \epsilon_2 = 9.6]$

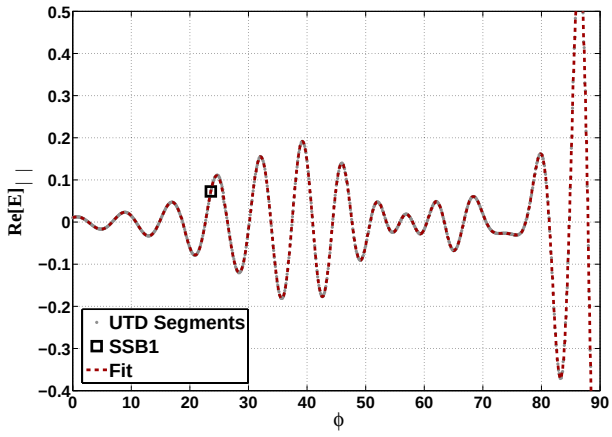

Figure 3.23: Fit of the $\Re(E_{||})$ component. $[\vec{E}^0_{||} = 1, \vec{E}^0_{\perp} = 1, f = 500MHz, \epsilon_2 = 9.6]$

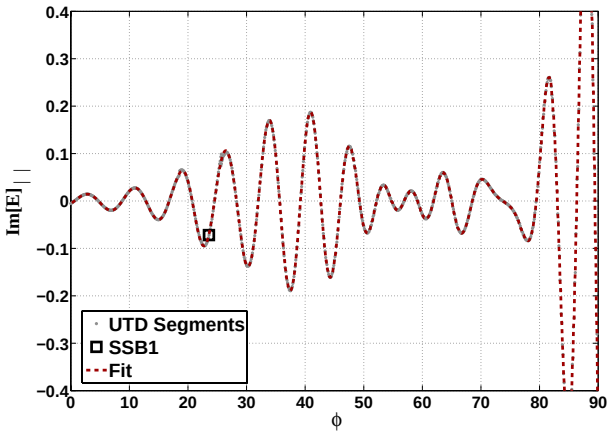

Figure 3.24: Fit of the $\Im(E_{||})$ component. $[\vec{E}^0_{||} = 1, \vec{E}^0_{\perp} = 1, f = 500MHz, \epsilon_2 = 9.6]$

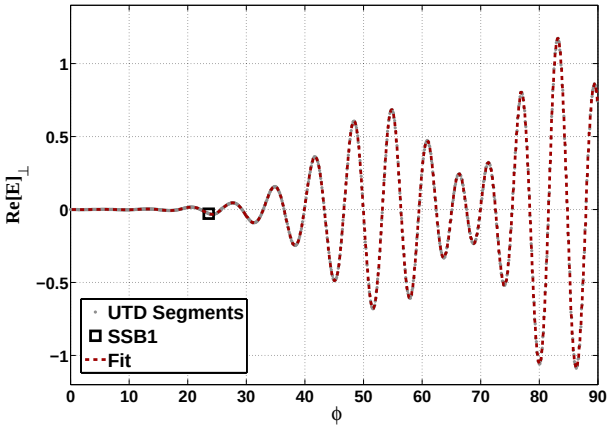

Figure 3.25: Fit of the $\Re(E_\perp)$ component. $[\vec{E}^0_\perp = 1, \vec{E}^0_\perp = 1, f = 500MHz, \epsilon_2 = 9.6]$

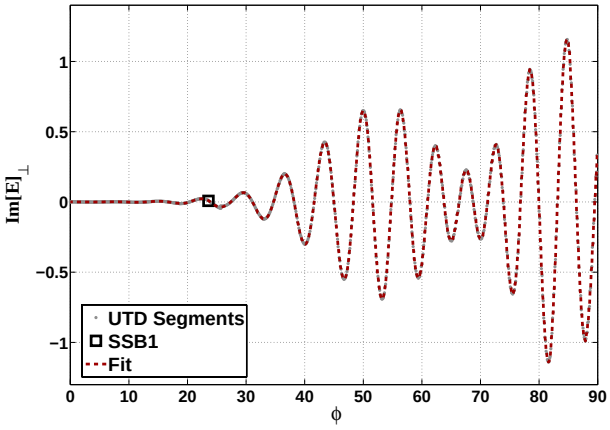

Figure 3.26: Fit of the $\Im(E_\perp)$ component. $[\vec{E}^0_\perp = 1, \vec{E}^0_\perp = 1, f = 500MHz, \epsilon_2 = 9.6]$

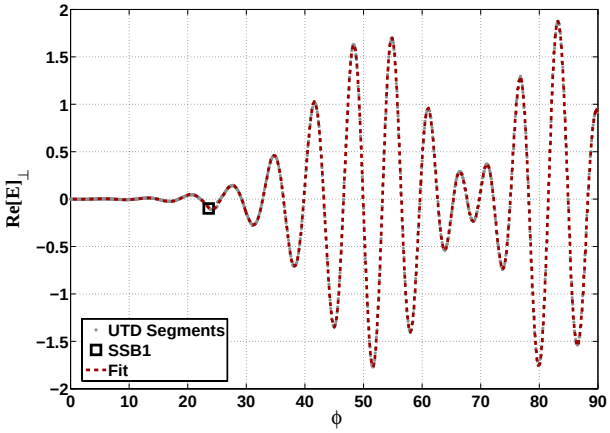

Figure 3.27: Fit of the $\Re(E_\perp)$ component. $[\vec{E}^0_\perp = 1, \vec{E}^0_\perp = 1, f = 500MHz, \epsilon_2 = PC]$

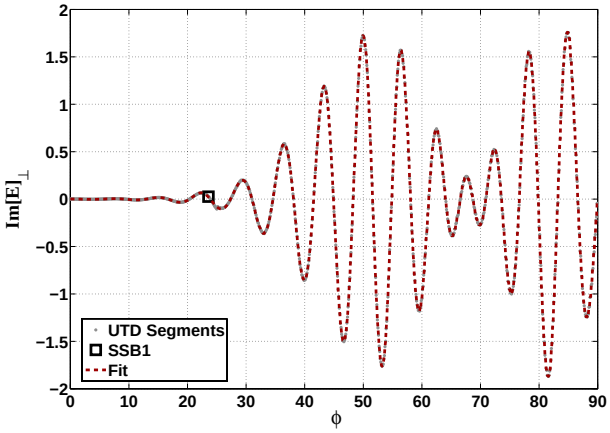

Figure 3.28: Fit of the $\Im(E_\perp)$ component. $[\vec{E}^0_\perp = 1, \vec{E}^0_\perp = 1, f = 500MHz, \epsilon_2 = PC]$

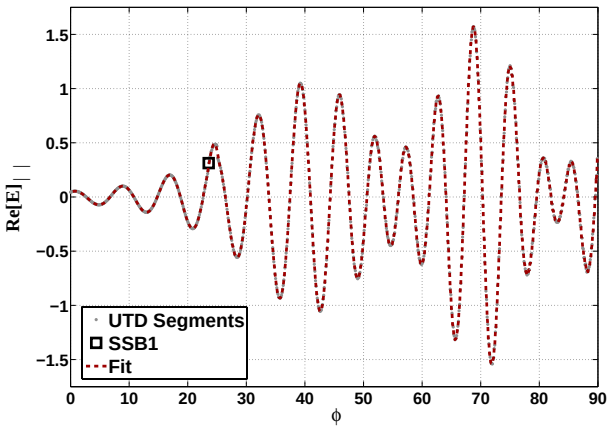

Figure 3.29: Fit of the $\Re(E_{||})$ component. $[\vec{E}^0_{||} = 1, \vec{E}^0_\perp = 1, f = 500MHz, \epsilon_2 = PC]$

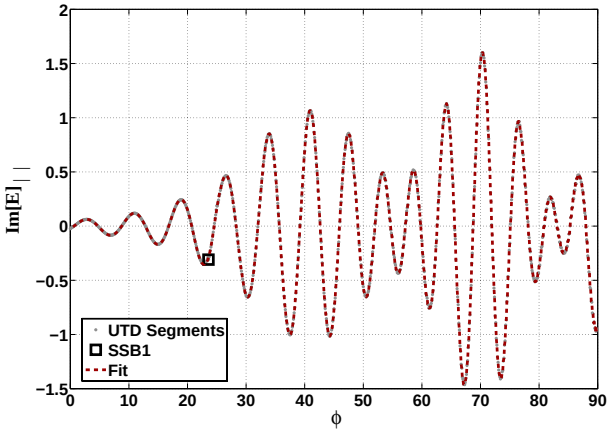

Figure 3.30: Fit of the $\Im(E_{||})$ component. $[\vec{E}^0_{||} = 1, \vec{E}^0_\perp = 1, f = 500MHz, \epsilon_2 = PC]$

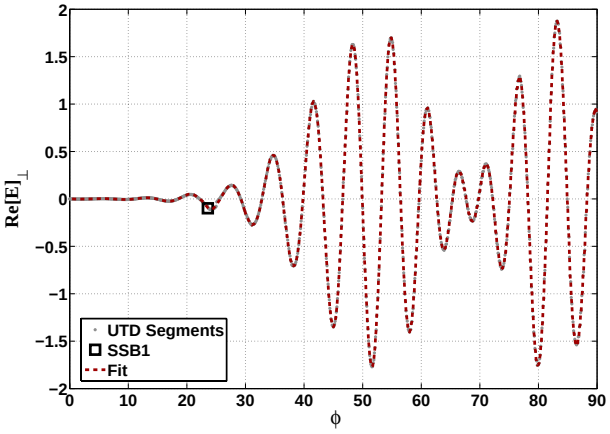

Figure 3.31: Fit of the $\Re(E_\perp)$ component. $[\vec{E}^0_\perp = 1, \vec{E}^0_\perp = 1, f = 500MHz, \epsilon_2 = PC]$

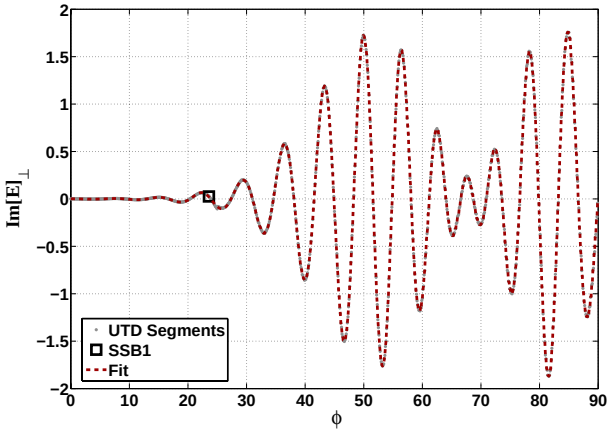

Figure 3.32: Fit of the $\Im(E_\perp)$ component. $[\vec{E}^0_\perp = 1, \vec{E}^0_\perp = 1, f = 500MHz, \epsilon_2 = PC]$

Contributions of the Single Waves

Here the numerical results of the different waves contributions are shown according to the implemented GTD/UTD ray system. The perpendicular field component is illustrated over the look angle range $0° \leq \varphi_L \leq 90°$ once for a perfect conducting (PC) interface and once for dielectric soil $(\epsilon_2 = 9.6)$. Where a linear polarized incident field $\vec{E}^0_\perp = 1, \vec{E}^0_{||} = 1, f = 500MHz, h = 0.5m$ was calculated (fig. 3.33 and 3.34).

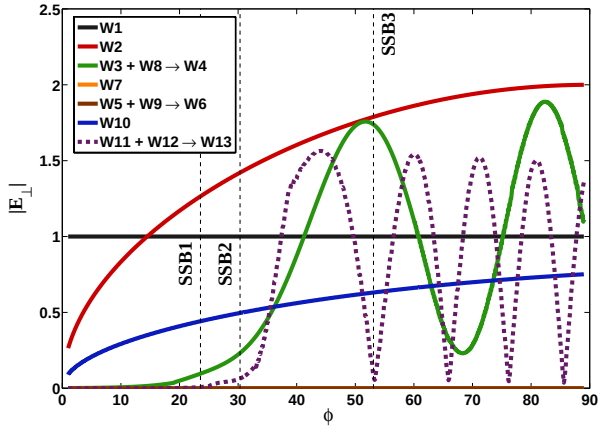

Figure 3.33: PC

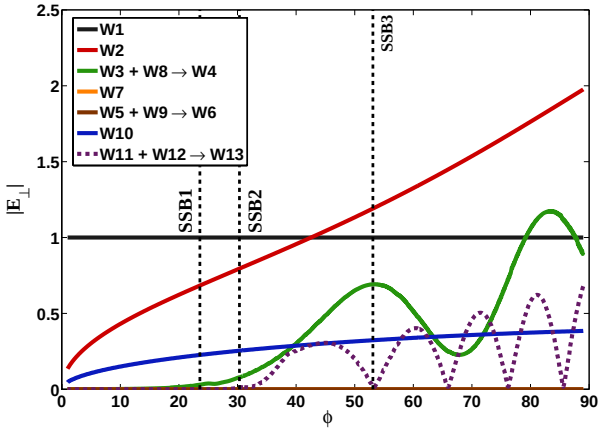

Figure 3.34: $\epsilon_2 = 9.6$

The single waves in the system were normalized with the specular reflection wave 1 for the relating look angle φ. The three transition zone angle are plotted as dashed lines. One recognize the strong attenuation of the field by the transit into the shadow region. Further, the contribution of the creeping wave 5 and 9 and in the shadow region by the wave 6 is very low compared to the other waves in the implemented ray system, except for the creeping wave 7. Thus, the polarimetric behavior of the total ray system is in view of the investigation near transition zones mainly determined by the wave 3, 8 and 4 relating to the SSB1 and wave 11, 12 and 13 for the second transition zone SSB2.

3.6 Ray System Validation

The Mixed Potential Integral Equation (MPIE) of section 2.5 is solved by an extended Method of Moments (MoM) technique as presented in appendix B. In order to validate the ray system, the results achieved by the exact numerical MoM are confronted with those obtained by the GTD. The solution of the MPIE via the MoM is done by finding the elements of the impedance matrix $[Z_{pq}]$. Due to the fact that its elements must be of finite size, and so the basis and test functions, an object with a closed surface has to be considered. Therefore, the scattered field from a perfect conducting sphere situated above and close to the soil is evaluated.
Hence, according to a sphere the waves 1, 2, 3, 10 and 11 from the GTD ray system are taken into account. Whereas the corresponding spreading factors of the waves are modified for the sphere as the perpendicular radius of curvature relative to the plane of incidence is not infinite ($\rho_1 \neq \infty$) in comparison to the cylinder. The wave 3 and 11 are computed for the lit region, respectively up to their shadow boundaries. The Radar Cross Section of both numerical techniques for the parallel and perpendicular field component at the observation point M are presented in fig. 3.35 and fig. 3.36. Neglecting the numerical boundary effects, it is can be seen that a good agreement between the two methods is obtained and so the geometrical étalon solution represents a good approximation for the given problem.

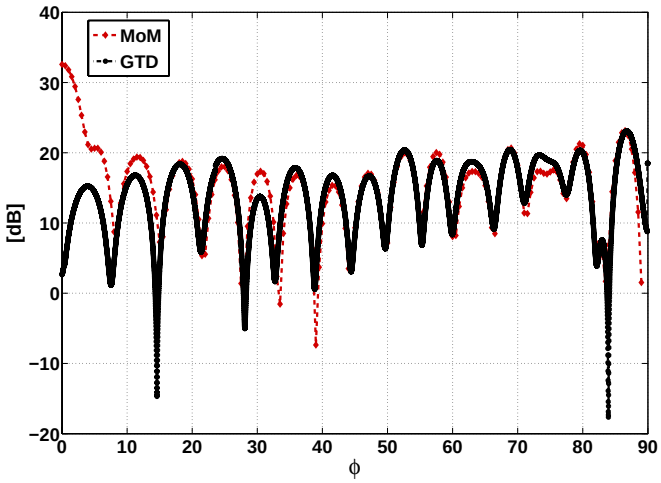

Figure 3.35: RCS of a sphere for $\vec{E}_{\perp}$ component after the MoM and GTD
$[k = 10, r = 2, h = 0.5, \epsilon_2 = 9.6]$

3.7 Radar Cross Section and Representation on the Poincaré Sphere

The UTD ray system with of a cylinder above the interface is considered in the following in order to investigate the behavior of the scattered em-field close to the transition zones. The corresponding spreading factor for $\rho_2 = \infty$ is modified in the numerical code. Further, the polarimetric behavior of the scattered UTD field is investigated in a first step on the Poincaré sphere. The benefit of introducing a UTD ray system consists in the fact that the scattering

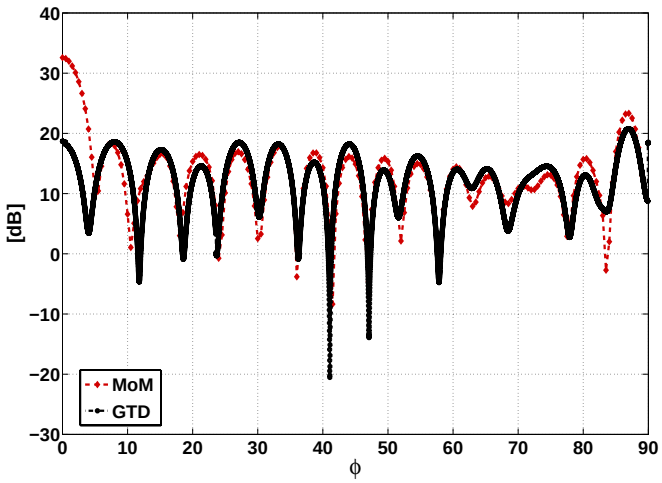

Figure 3.36: RCS of a sphere for $\vec{E}_{||}$ component after the MoM and GTD $[k = 10, r = 2, h = 0.5, \epsilon_2 = 9.6]$

process can be related to single rays. As a result, a decomposition of the general scattering matrix $[S]$ into different mechanism can be made and so leading to a better understanding of the polarimetric behavior.

According to the definition of the Stokes vector in section 1.3.3, the upper hemisphere describes a left handed polarized field. Where the upper pole $g_3 = 1$ signifies a left handed circular polarization LHC. The antipole corresponds to a right handed polarization state, respectively the lower pole $g_3 = -1$ to a right handed circular polarization RHC. As a consequence, the equator line characterizes a linear polarization.

The composition of the Sinclair matrix

Respective to the line of sight LOS the introduced UTD cylinder model is symmetrical and no cross polarization occurs in consequence. Hence, the scattered field E^S is solely given by the diagonal elements of the scattering matrix $[S]$ and the incident field E^0 as follows:

$$\begin{pmatrix} E^S_{\perp} \\ E^S_{||} \end{pmatrix} = \begin{bmatrix} S_{11} & 0 \\ 0 & S_{22} \end{bmatrix} \begin{pmatrix} E^0_{\perp} \\ E^0_{||} \end{pmatrix} \tag{3.94}$$

The scattered UTD field from the cylinder is the sum of the single waves $E^S_{\perp,||} = \sum_{j=1}^{11} w^j_{\perp,||}$. The main elements are directly computed with the unitary incident field $E^0_{\perp,||} = 1$ as follows:

$$S_{11} = \frac{E^S_{\perp}}{E^0_{\perp}} \qquad S_{22} = \frac{E^S_{||}}{E^0_{||}} \tag{3.95}$$

A linear polarized incident field is given at the cylinder of the form $\vec{E}^0_{||} = 1, \vec{E}^0_{\perp} = 1$. The ray system allows now to get a more detailed physical insight the scattering process as the exact MoM program. According to the ray system the decomposition of the scattering matrix $[S]$ is discussed next.

Decomposition of $[S]$

$$W1 \longrightarrow \quad \begin{pmatrix} 1 & 0 \\ 0 & 1 \end{pmatrix}$$

$$+W2 \longrightarrow \quad \begin{pmatrix} 1+DB & 0 \\ 0 & 1-DB \end{pmatrix}$$

$$+W3 \longrightarrow \quad \begin{pmatrix} 1+DB+W3 & 0 \\ 0 & 1-DB+W3 \end{pmatrix}$$

$$+W8 \longrightarrow \quad \begin{pmatrix} 1+DB+W3 & 0 \\ 0 & 1-DB+W3+W8 \end{pmatrix}$$

$$+W10 \longrightarrow \quad \begin{pmatrix} 1+DB+W3+W8+W10 & 0 \\ 0 & 1-DB+W3+W8+W10 \end{pmatrix}$$

$$+W11 \longrightarrow \quad \begin{pmatrix} 1+DB+W3+W8+W10+W11 & 0 \\ 0 & 1-DB+W3+W8+W10+W11 \end{pmatrix}$$

Where only the parallel component of double bounced wave 2 changes its sign.

3.7.1 H - V Polarization

First, the ray field is investigated for a perfect conducting interface, where a purely horizontal or vertical polarized incident field is considered. The h or v polarization states correspond to the perpendicular and parallel polarization of the UTD cylinder model. As a result, no cross polarization occurs during the scattering process. This property is pointed out on the Poincaré sphere (fig 3.37).

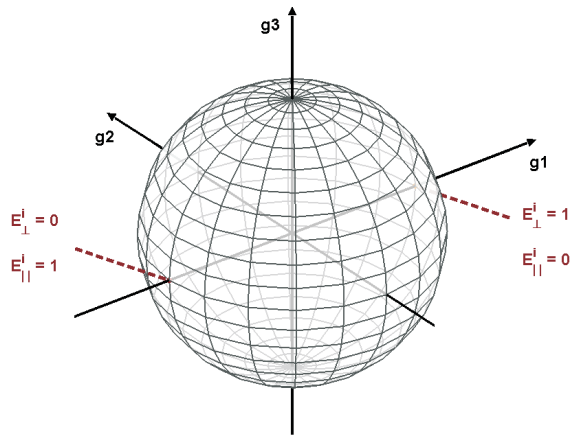

Figure 3.37: GTD-field polarization for $E_v^i = 1$ or $E_h^i = 1$.

Here the backscattered field is again a horizontal polarized field $g_1 = 1, g_2 = 0, g_3 = 0$ for a purely horizontal transmission (h). The same comment for a purely v polarized field. The corresponding point on the sphere is given here by $g_1 = -1, g_2 = 0, g_3 = 0$.

3.7.2 Linear Polarization

The next step consists in regarding a linear polarized field having a tilt orientation angle of $\Phi = \frac{\pi}{4}$ which implies that two field components are equal ($E_\perp = 1$ and $E_{||} = 1$). The polarization states of the backscattered single waves 1, 2, 3, 4, 8, 10 and 11 are checked. According to the law of reflection the tilt orientation angle Φ of an emitted linear polarized wave remains the same after odd reflections, written as:

$$VH(\Phi) \longrightarrow VH(\Phi) \quad odd \ \ (e.g.\ sphere) \tag{3.96}$$

In contrast the orientation angle Φ changes its sign after even reflections. The wave plane is rotated anticlockwise by $\pi - \Phi$

$$VH(\Phi) \longrightarrow VH(-\Phi) \quad even \ \ (e.g.\ dihedral) \tag{3.97}$$

The reflection coefficients at the perfect conducting interface are constant ($f_{||} = 1 \ f_\perp = -1$) over the entire look angle range φ_L. In consequence the amplitudes of both field components are equal after the interaction with the ground. Hence, the tilt angle Φ remains constant over the whole horizon. The individual backscattered polarization states are pointed out on the Poincaré sphere in fig 3.38 to 3.41. Here, for even reflections, like the double bounced wave 2, the corresponding point on the Poincaré sphere lies on the opposite side of the equator (fig 3.38). The field vectors of wave 10 and 11 keep their orientation due to the odd numbered reflections. Both waves are located at $g_1 = 0, g_2 = 1, g_3 = 0$ on the sphere (fig 3.39).

In the same manner the field vectors of wave 3 and 8 keep their orientation as a result of the odd interactions and their location lies also on the equator line $g_1 = 0, g_2 = 1, g_3 = 0$. Recapitulating, no cross polarization occurs if the single waves of the ray system are considered. An

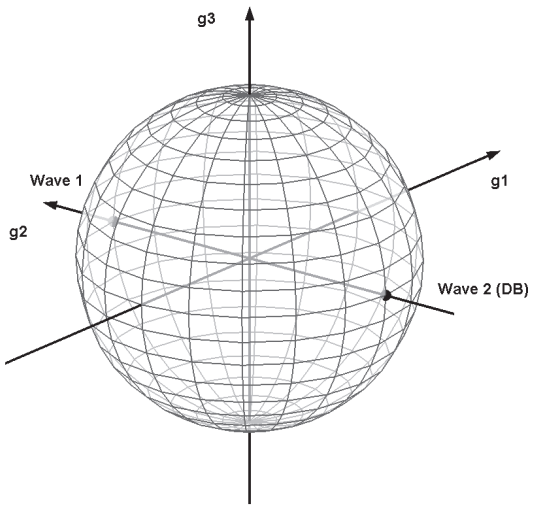

Figure 3.38: Wave 1 and Wave 2
$\vec{E}_{||} = 1\ \vec{E}_{\perp} = 1[\epsilon_2 = PC]$

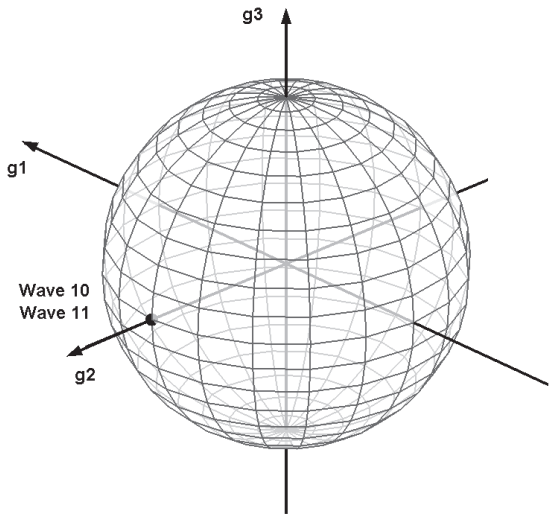

Figure 3.39: Wave 10 and Wave 11
$\vec{E}_{||} = 1\ \vec{E}_{\perp} = 1[\epsilon_2 = PC]$

exception here, represents the creeping wave 4, where a small smearing occurs on the Poincaré sphere.

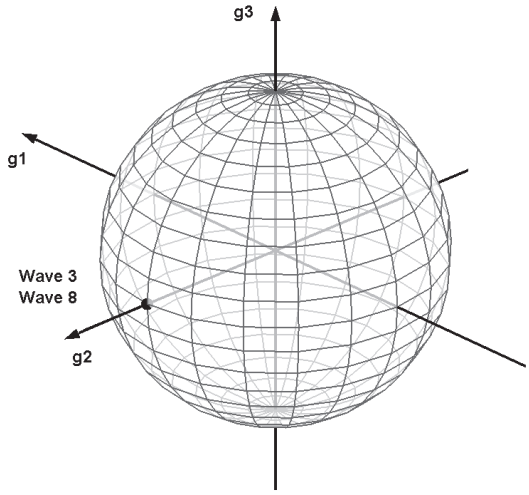

Figure 3.40: Wave 3 and Wave 8
$\vec{E}_{||} = 1\ \vec{E}_{\perp} = 1[\epsilon_2 = PC]$

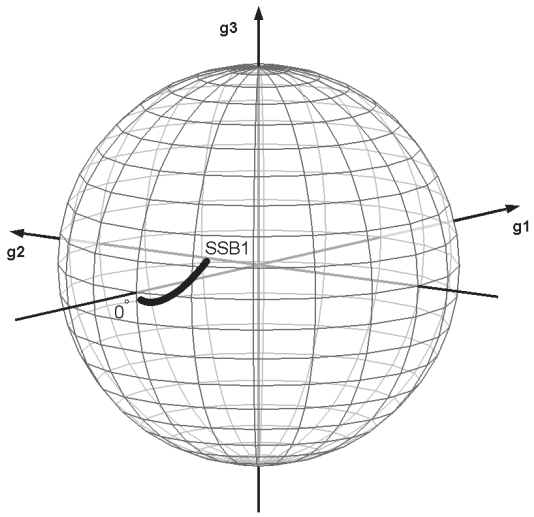

Figure 3.41: Wave 4
$\vec{E}_{||} = 1\ \vec{E}_{\perp} = 1[\epsilon_2 = PC]$

The $E_{\perp}$ (soft) component of wave 4 related to the shadow region is stronger attenuated than its $E_{||}$ (soft) component. Finally, for long arc lengths on the surface only the significant $E_{||}$ component remains. Hence, wave 4 is found near the vertical (hard) polarization state given by $g_1 = -1, g_2 = 0, g_3 = 0$. Here, with decreasing look angle, the arc length along surface is increasing. From this, it follows that the $E_{\perp}$ component is stronger attenuated than the $E_{||}$ component. This different attenuation of the two components leads finally to a smearing on the Poincaré sphere.

Considering now the complex summation of the single waves, the linear polarization is lost.

This is e.g. shown for the superposition of the wave 3 and 8 in fig 3.42 for the look angle range $SSB1 < \phi < 90°$. Where wave 3 and 8 are replaced by wave 4 in the shadow region $0° < \phi < SSB1$. The ray paths of the single wave 3 and 8 between the cylinder and interface depends from the incident angle. Hence, the summation of their fields takes place out of phase. The same holds for the superposition off all the considered waves in the system. The summation of all waves is shown in fig 3.43. Hence, for a varying look angle the total field migrates on the Poincaré sphere even though in the scattering matrix $[S]$ no cross elements occurs. The look angles for the two dominant transition zone SSB1 and SSB2 are situated near the equator line. At the transition zones the ray path of the corresponding waves 3 + 8 and 11 + 12 are almost equal. Here, the summation of the wave twosomes takes place in phase. Away from the boundaries the waves are out of phase and their superposition leads to a depolarization of the backscattered field. Hence, both transition zones, due to the geometrical setup, have characteristic locations on the Poincaré sphere. This behavior was additionally checked for the height h=0.3m. Thus, by exploiting these two characteristic locations on the Poincaré sphere, the height and the radius of a general circular cylinder or a sphere can be clearly determined. In the case of an elliptical object, where three unknowns are present, local minimums may be found in the fit if information is given a priori or for global maximum the third shadow boundary must be determined. According to fig. 3.16 and 3.17, the corresponding geometrical parameters has to fulfilled the two shadow boundary conditions.

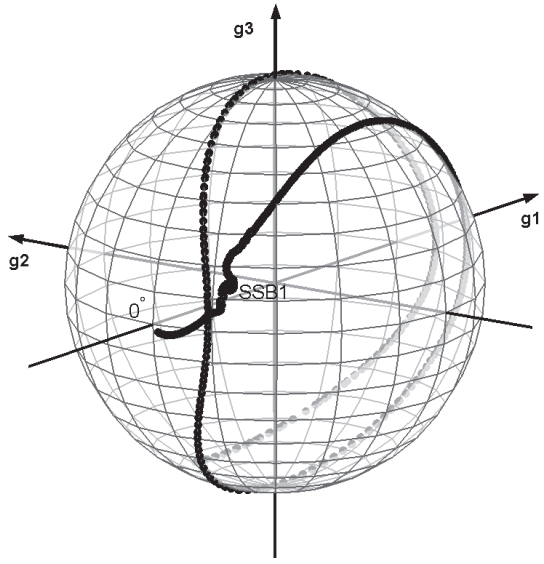

Figure 3.42: SSB1: Wave 3, 4 and 8 $\vec{E}_{||} = 1\ \vec{E}_{\perp} = 1[\epsilon_2 = PC]$

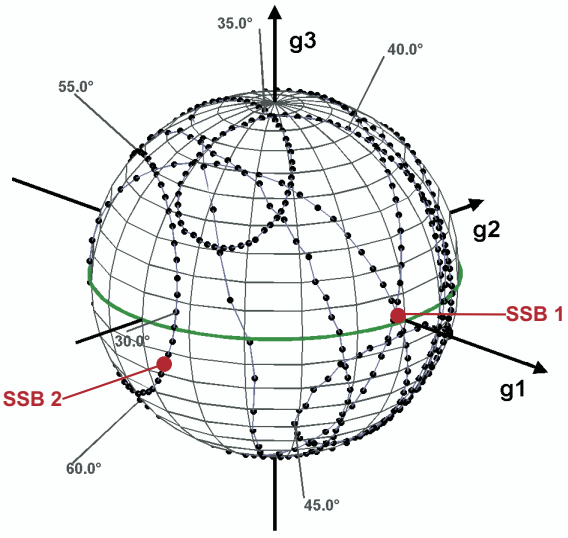

Figure 3.43: Wave 1-13 $\vec{E}_{||} = 1\,\vec{E}_{\perp} = 1$ $[k = 10\frac{1}{m}, r = 2m, h = 0.5m, \epsilon_2 = PC]$

3.7.3 Circular Polarized Incident Field

Here an incident LHC polarized field, given by the phase shift $E_\perp = i$ and $E_{||} = 1$, is discussed. In the same manner the polarization of the single backscattered waves is checked at first. In general, following the IEEE convention, an emitted RHC polarized wave keeps its polarization after odd reflections. This circumstance is written in the form:

$$RHC \longrightarrow RHC \quad odd \ (e.g.\ sphere) \tag{3.98}$$

In contrast, a RHC wave changes its rotation sense after even reflections, described by:

$$RHC \longrightarrow LHC \quad even \ (e.g.\ dihedral) \tag{3.99}$$

On the Poincaé sphere the odd and even reflected waves must therefore lie on opposite hemispheres. This antipode is represented in the the fig 3.44 for the both principle waves 1 and 2. Also the odd reflections of the waves 3, 8, 10 and 11 are pointed out in the figure. The smearing of wave 4 on the Poincaré sphere is shown in fig. 3.45. Similar to the first considered

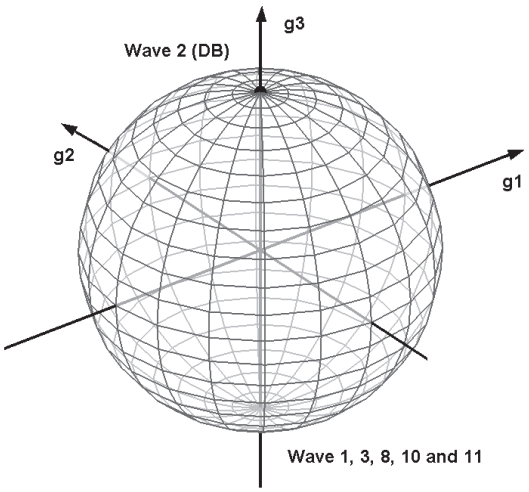

Figure 3.44: Wave 1, 2, 3, 4, 8, 10 and 11 $[\epsilon_2 = PC]$

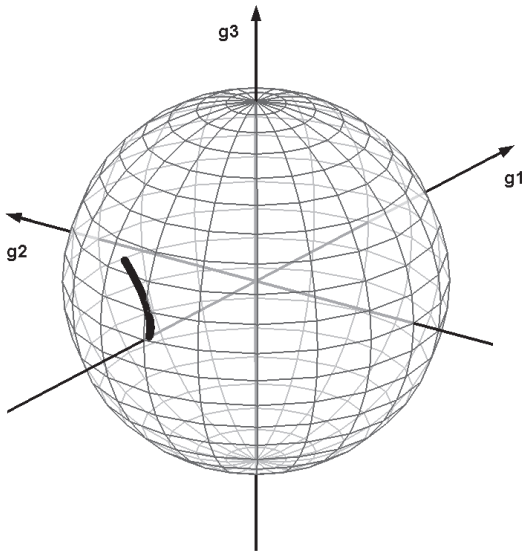

Figure 3.45: Wave 4 $[\epsilon_2 = PC]$

case, the backscattered field is near the shadow boundaries barely depolarized. From fig. 3.46 it is seen, that once the backscattered field is circular and once linear polarized at the shadow boundary. Away from the transition zone the field is strongly depolarized and circles on the Poincaé sphere. In contrast, near the shadow boundaries the corresponding waves are in phase, so that the backscattered field at the transition zones has significant locations on the Poincaé sphere. The same behavior is given for the height h=0.3m.

3.7.4 Elliptical Polarized Incident Field

The diffraction for a general elliptical polarized incident field is considered given by the phase shift $\vec{E}_{||} = 1\ \vec{E}_\perp = 0.5i$. Similar to the circular case, the odd and even reflected waves lie on opposite hemispheres on the Poincaé sphere. The opposite locations on the sphere are outlined

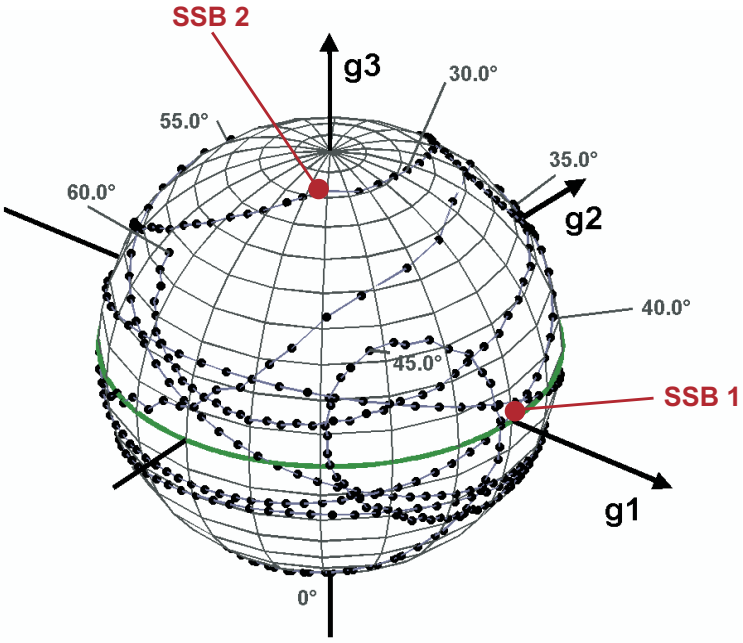

Figure 3.46: Wave 1-13 $\vec{E}_{||} = 1\,\vec{E}_{\perp} = i$ $[k = 10, r = 2, h = 0.5, \epsilon_2 = PC]$

in fig. 3.47. The creeping wave 4 is shown in fig. 3.48. The summation of the wave 1 - 13 and the resulting depolarization is pointed out in fig 3.49. According to the linear and circular polarized field, the transition zones have again significant locations on the Poincaé sphere.

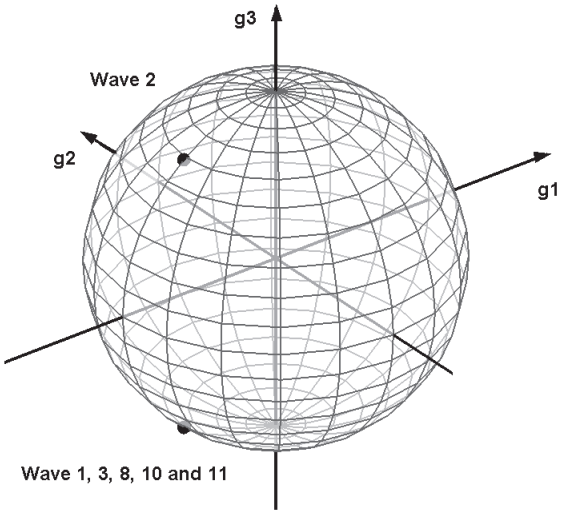

Figure 3.47: Wave 1, 2, 3, 4, 8, 10 and 11 $\vec{E}_{||} = 1\,\vec{E}_{\perp} = 0.5i$ $[\epsilon_2 = PC]$

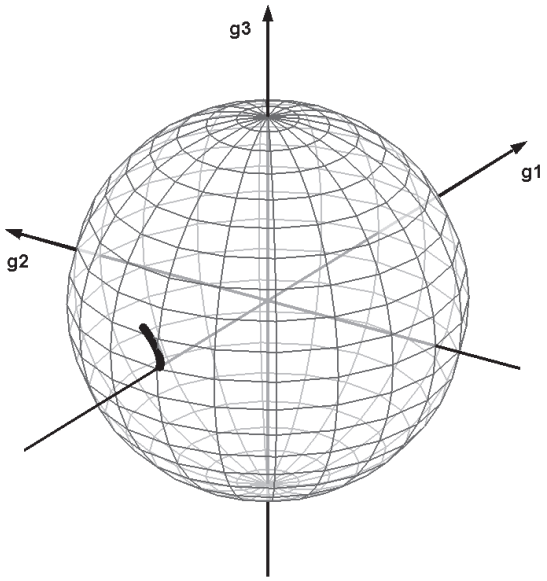

Figure 3.48: Wave 4 $\vec{E}_{||} = 1\,\vec{E}_{\perp} = 0.5i$ $[\epsilon_1 = PC]$

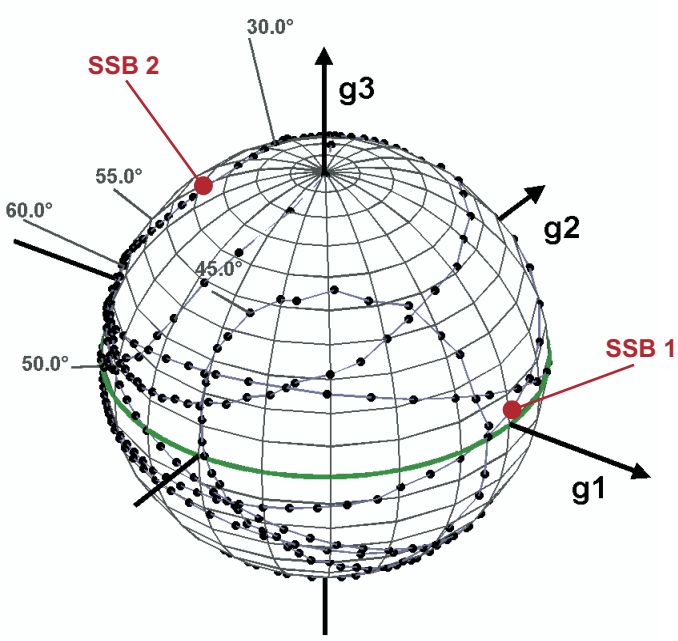

Figure 3.49: Wave 1-13 $\vec{E}_{||} = 1\, \vec{E}_{\perp} = 0.5i$ $[k = 10, r = 2, h = 0.5, \epsilon_2 = PC]$

3.7.5 Dielectric Soil

In the previous sections, a perfect conducting soil was considered in order to get a first insight at the polarimetric behavior. In the following the more general case of a dielectric soil is calculated. Here, the lower dielectric half-space is characterize by the relative permittivity $\epsilon_2 = 9.6$. For

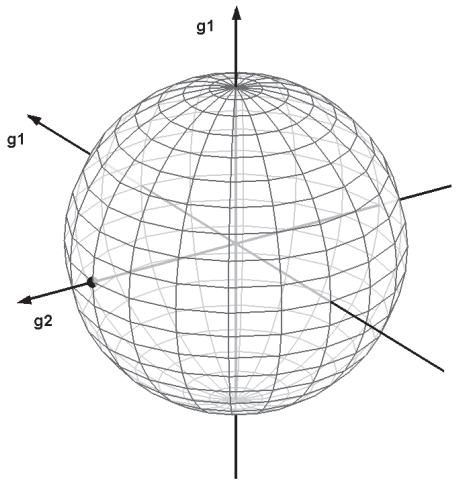

Figure 3.50: Specular Wave 1
$\vec{E}_{||} = 1\, \vec{E}_{\perp} = 1$ $[\epsilon_2 = 9.6\ ]$

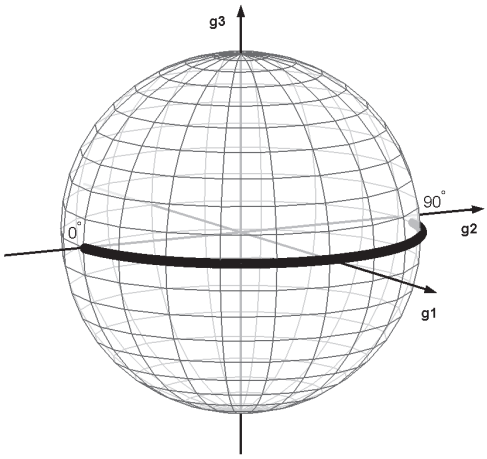

Figure 3.51: Double bounced wave 2
$\vec{E}_{||} = 1\, \vec{E}_{\perp} = 1$ $[\epsilon_2 = 9.6]$

the reason of comparability the geometrical setup and the wave number stay the same as in the previous case of a perfect conducting interface ($k = 10, r = 2, h = 0.5$). A linear polarization given by $E_{\perp} = 1$ and $E_{||} = 1$ with the tilt angle $\Phi = \frac{\pi}{4}$ is regarded as incoming field. In contrast to the perfect conducting interface, the Fresnel coefficients describing the reflections on the interface, depend now from the local incidence angle. Hence, the reflection coefficients vary over

the look angle range and in consequence also the amplitudes. The resulting alteration on the Poincaré sphere according to the single waves of the GTD system is shown in fig. 3.50 to 3.55. An exception is here the specular wave 1 and and wave 10, where normal incidence is always given at the object respectively on the ground. Similarly, the characteristic angles related to the boundaries SSB1 and SSB 2 are located in the vicinity of the equator (fig. 3.56).

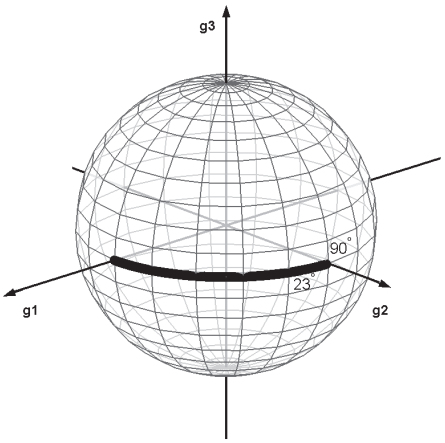

Figure 3.52: Wave 3 $\vec{E}_{||} = 1\ \vec{E}_{\perp} = 1$ $[\epsilon_2 = 9.6]$

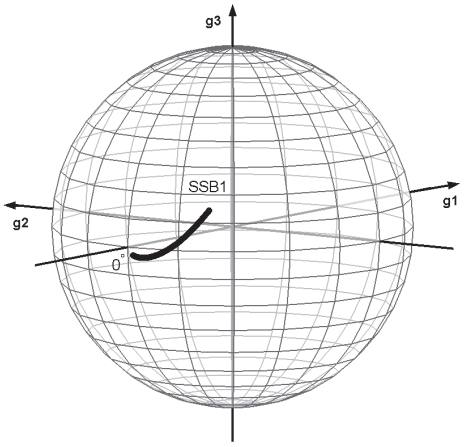

Figure 3.53: Wave 4 $\vec{E}_{||} = 1\ \vec{E}_{\perp} = 1$ $[\epsilon_2 = 9.6]$

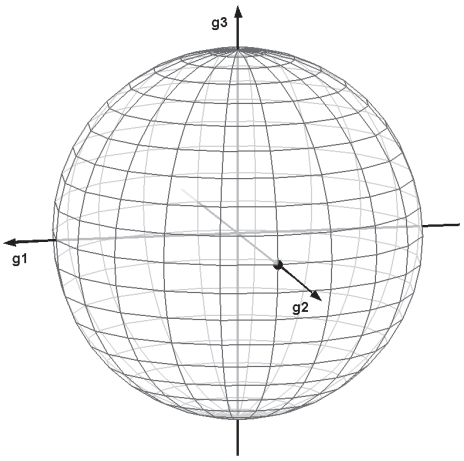

Figure 3.54: Wave 10 $\vec{E}_{||} = 1\ \vec{E}_{\perp} = 1$ $[\epsilon_2 = 9.6]$

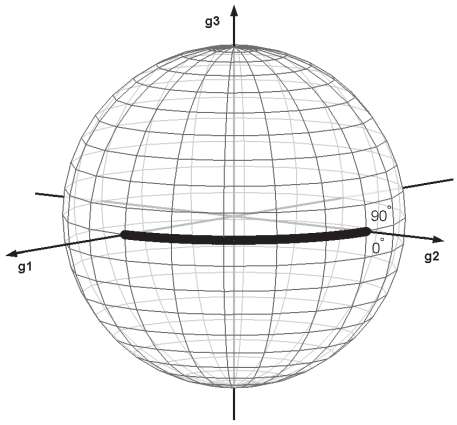

Figure 3.55: Wave 11 $\vec{E}_{||} = 1\ \vec{E}_{\perp} = 1$ $[\epsilon_2 = 9.6]$

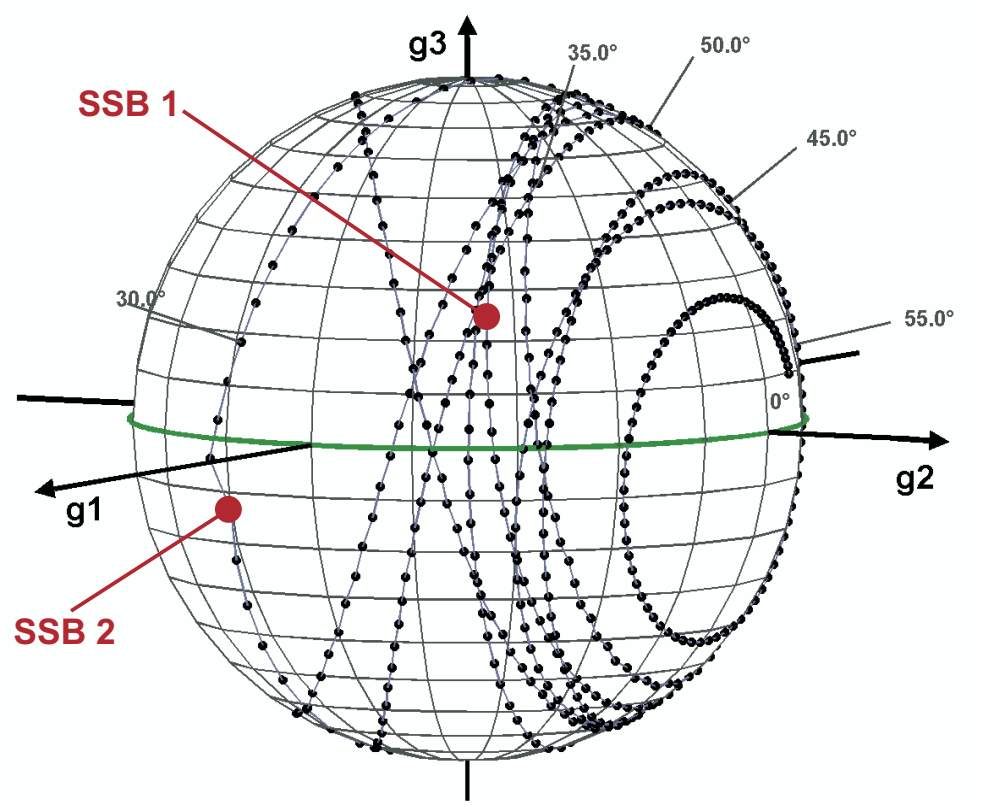

Figure 3.56: Wave 1-13 $\vec{E}_{||} = 1\ \vec{E}_{\perp} = 1\ [k = 10, r = 2, h = 0.5, \epsilon_2 = 9.6]$

CHAPTER 4

Anechoic Chamber Measurements

In order to validate the implemented UTD ray system full polarimetric monostatic measurements (hh, hv and vv) were performed at the European Microwave Signature Laboratory (EMSL) at the Joint Research Centre (JRC) of the European Commission in Ispra-Italy. The EMSL provides a 20m diameter microwave anechoic chamber, where objects can be scanned over a full hemisphere in a monostatic or bistatic alignment as shown in fig 4.1. Thus, the EMSL provides controlled investigations of microwave scattering under stable conditions. The results of the EMSL measurements and the interpretation according to the implemented ray system are discussed in the following.

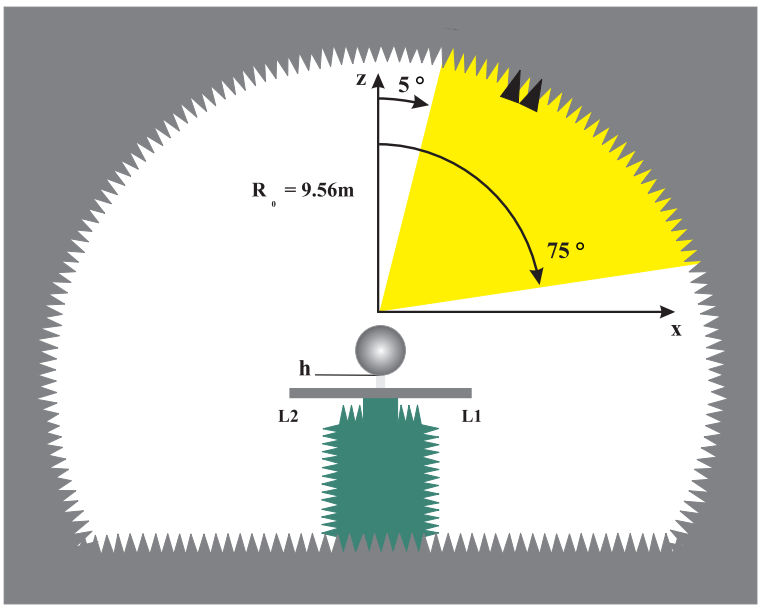

Figure 4.1: Anechoic chamber

4.1 Experimental Setup

In the anechoic chamber the backscattered field of a metallic sphere of 30.5cm in diameter situated above a perfect conducting plate with the dimension 2m×2m was measured at five different heights: h=3.75cm, 5cm, 7.5cm, 10cm and 15cm. Where a monostatic alignment of the transmitting and receiving antenna was chosen and a linear polarized field ($E_h = E_v$) was emitted. The sphere was placed above the center of the plate. The look angle range was fixed from 5° to 75° with breakpoints every half degree $\Delta\varphi_L = 0.5°$. At each of the single 140 breakpoints a frequency sweep over the range $1.5\,GHz - 9.5\,GHz$ with a step of $\Delta f = 10\,MHz$ was performed in order to get a corresponding pulse in the time domain (TD). Hence, 800 different frequencies were measured for each incident angle. The setup of the measurements is shown in fig. 4.1. The different heights were realized by supports made of polystyrene. As polystyrene consists mainly of air, the influence of the supports on the measurements are not significant. Exemplarily, the setup for the measurement corresponding to the height h=10cm is shown in fig. 4.2. The geometrical shadow boundaries SSB 1 and SSB 1 of the transition zones are pointed out for the different heights in table D.1. The report of the measurements are listed in the table D in appendix D.

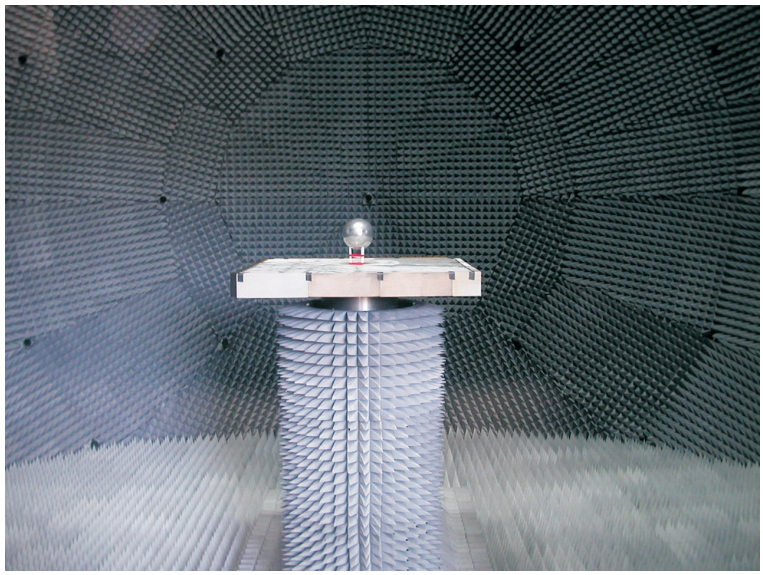

Figure 4.2: Support of the sphere in the EMSL for $h = 10.0cm$

Some restriction in analyzing the data are given due to the geometry of the ground plate. Considering the reflection point C of the double bounced wave 2 outlined in fig. 3.4, C will lie as from a certain angle ϕ_L outside the ground plate. This look angle ϕ_L where the reflection point C lies beyond the plate is listed for the different heights in table D.1. As a result of it, look angles over 75° were not measured. Furthermore, despite the fact that the edges of the ground plate were covered with absorbers, diffractions from the plate edges occur. The geometry of the route from the near edge L_1 relative to the antenna is outlined in fig. 4.4. From this, one see that for small incident angles the distance edge - antenna is greater than the distance phase origin - antenna r_0. Hence, the diffracted waves from the edge L_1 wave have positive arrival

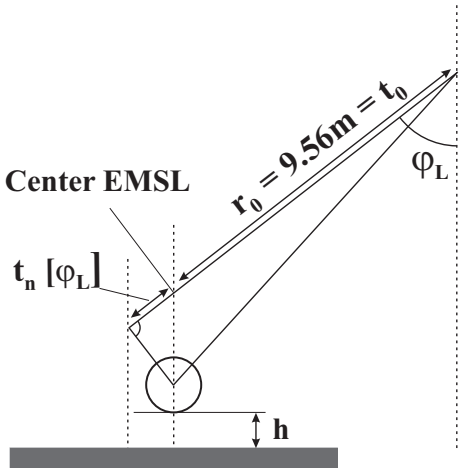

Figure 4.3: Positioning of the measured sphere in the Chamber Origin = Phase Origin

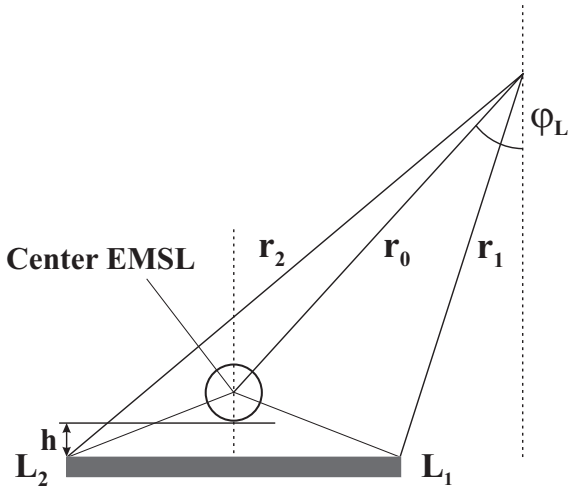

Figure 4.4: Diffraction Geometry from the Plate Edges

times $t_n > 0$. In consequence, for steep incident angles the diffraction from L_1 will superposed with the other waves of the GTD ray system. In contrast, by increasing the incident angle the distance edge-antenna will get smaller as the distance phase origin - antenna r_0. In this case the arrival times are negative $t_n < 0$. The incident angle where the arrivals from the edge L_1 are zero are listed in the table 4.1 for the different measured heights. As a result, look angles under 15° must be interpreted carefully due to the significant diffraction from the edge L_1.

$\phi_{lim} < \phi_L$					
h	$3.75cm$	$5cm$	$7.5cm$	$10cm$	$15cm$
ϕ_{lim}	14°	14.5°	16°	17.5°	20°

Table 4.1: Limiting values for the look angle ϕ_L

Calibration of the Raw Data

A correction of the raw data is required as systematic errors like the coupling between the h and v channel, hardware effects (cables, switches, synthesizer etc.) and residual reflections in the anechoic chamber are given during the measurements. In order to neglect this amplitude and phase noise, a three target calibration and error correction for the monostatic alignment, according to Wiesbeck [66], was carried out. Therefore, an isolation calibration (empty room) and measurements of three different canonical targets were performed, where the scattering matrices are exactly known. Here, the backscattered field of a circular metallic disk and of a dihedral corner with the two rotation angles $\vartheta = 0°$ and $\vartheta = 45°$ around the line of sight were considered. After the correction of the raw data every response is normalized with the direct reflected wave from the sphere. The corresponding files of the calibration measurements are given in the table $D.2$. Additionally, as the center of the sphere did not coincide with the center of the chamber, a geometrical respectively a time correction of the calibrated data had to be carried out. The additional propagation time $t_n(\varphi_L)$ is pointed out in fig. 4.3. The

corresponding off time $t_n(\varphi_L)$ for the single heights h and look angle φ_L was performed in the frequency domain as follows [9]:

$$h(t + t_n) \circ\!\!-\!\!\bullet\ H(f) \exp(\jmath\omega\, t_n(\varphi_L)) \tag{4.1}$$

4.2 UTD Ray System Validation

4.2.1 Kinematic and dynamic aspects

The objective of this section is the validation of the implemented GTD ray system via measurements performed in the EMSL at the JRC. Therefore, in order to recover the single waves of the ray set, the kinematic behavior of the backscattered field is investigated in the time domain over the entire look angle range $5° - 75°$. Here the reel part of the E_{hh} component is considered. The investigation of the transition zones introduced in section 3.4 is realized in the power domain, where the Reflectivity over the look angle range is discussed. The Reflectivity is regarded at the frequency 6.7GHz. Hence, the same term ka=21 is present as in the numerical calculation discussed in chapter 3. Without the present of the ground plate the Radar Cross Section (RCS) of the sphere with the geometrical parameters $r_0 = 15.25cm$ is given by $\sigma = -11.36dB$ ($\sigma = 10 \log \pi r_0^2$) and drawn as a green dashed line in the figures. (In the case that the incident field is normalized the RCS is called Reflectivity)

h1=3.75cm

At the beginning, the sphere was placed 3.75cm above the ground plate. Thus, for the first measurement the same ratio $r_0/h = 4$ is on hand according to the numerical calculation after the MoM. In fig. 4.5 the Reflectivity of the channels E_{hh}, E_{hv} and E_{hh} is shown over the look angle range. According to fig. 4.5 the contribution of the cross polarization is negligible compared to the hh and vv-polarization. In fig. 4.5 the single pulse arrivals for the ray system are plotted versus the look angle. Referring to fig. 4.5 the different waves of the ray system are identified in fig. 4.8, 4.9, 4.9 and 4.10. Additionally, the diffraction from the plate edges L_1 and L_2 get closer at steeper incidence angles in the time domain. In contrast, for flat incidence angles the diffractions of the two edges diverge. As the phase origin is placed in the middle of the sphere the arrival time of the direct reflected wave 1 in free space is given here by t= -1ns. This corresponds two times the radius r_0 of the sphere. The phase terms for the de- and attachment points of the creeping wave 7 neglect each other and therefore the arrival time of the creeping wave 7 is equal to zero. Due to its strong attenuation by traveling around the sphere, wave 7 is negligible. In comparison the spatial waves 3, 8, 10 and 11 related to the shadow boundaries SSB1 and SSB2 and the double bounced wave 2 are clearly identified. The measured arrival times agree here with the numerical results in accordance to the implemented ray system. Additionally, by using the Reflectivity of the E_{hh} and E_{vv} channels the single waves of the ray system are found (fig. 4.11, 4.12, 4.13 and 4.14).

h2=5.0cm

The arrival times of the wave 1 and 7, where no interactions with the plate is present, remain the same. The strong contribution of the waves 1, 2, 3+8 and 10+11 are well distinguished in the fig. 4.16 and 4.17. At steep look angle the diffraction from L_1 and the double bounced wave 2 coincide. According to table 4.1 the edge diffraction L_1 diverge with increasing look angle and can be separated from the single waves.

h3=7.5cm

The backscattered field is investigated here at the height h3=7.5cm. Considering the wiggle representation in fig. 4.21 of the reel part of E_{hh} the double bounced wave 2 from the edge diffraction L_1 is hardly separated. Nevertheless, this is possible according to the power domain as outlined in fig. 4.22.

h4=10.0cm and **h5=15.0cm**

Finally, the distance h4=10.0cm and h5=15.0cm are discussed. In the same manner as the previous heights the kinematic and dynamic behavior of the ray system is pointed out in the fig 4.23 to 4.30. Referring to fig 4.24 and 4.28 the spread of wave 2 and 10 is getting wider with an increasing distance to the ground plate. The same behavior is given for the waves 3+8 and the waves 5+9.

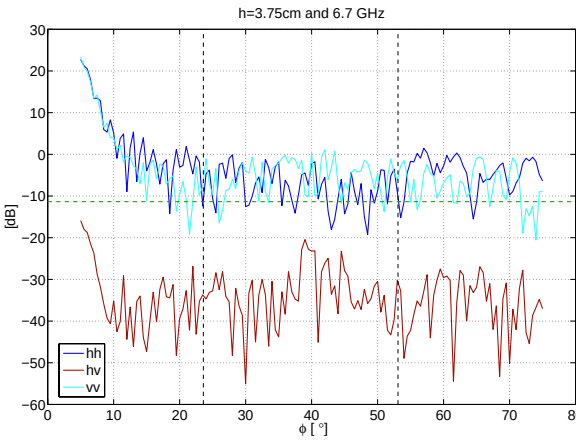

Figure 4.5: RCS of single field components $h1 = 3.75cm$

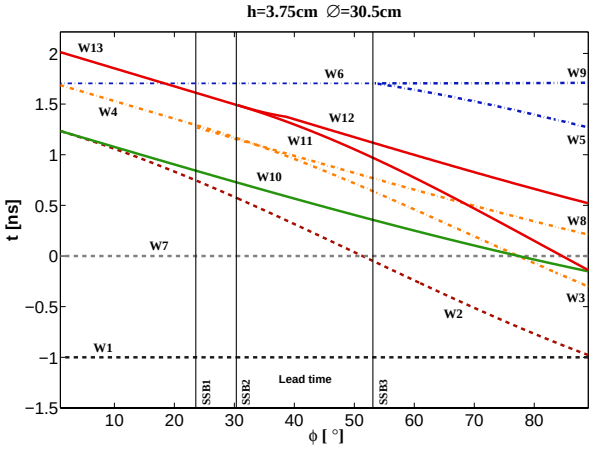

Figure 4.6: Arrivals $h1 = 3.75cm$

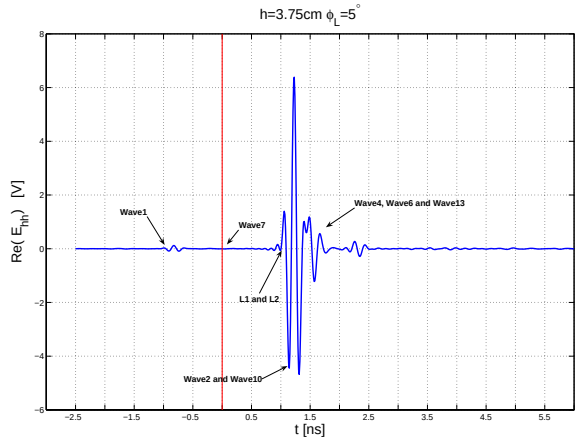

Figure 4.7: Arrivals $\phi_L = 5°$

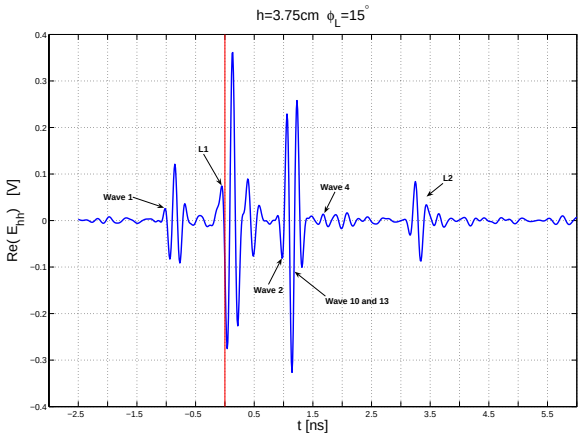

Figure 4.8: Arrivals $\phi_L = 15°$

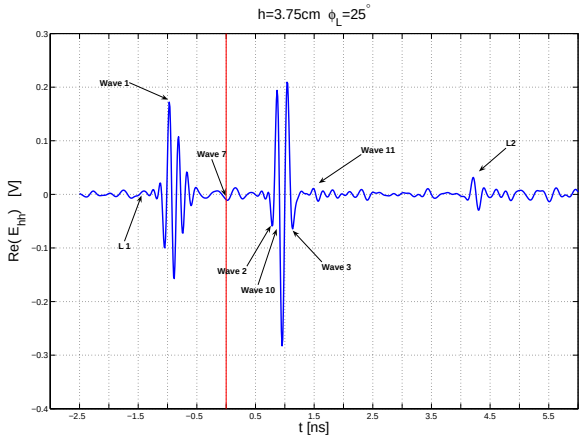

Figure 4.9: Arrivals $\phi_L = 25°$

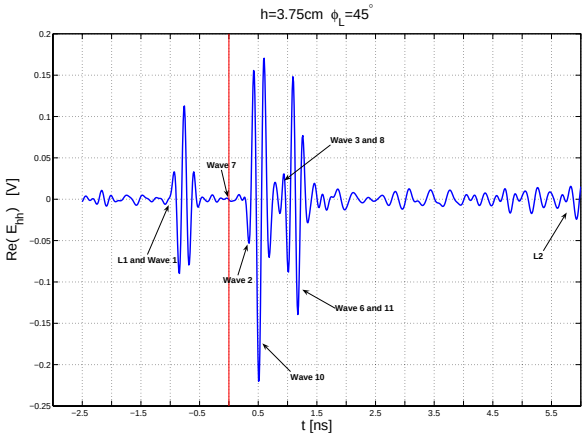

Figure 4.10: Arrivals $\phi_L = 45°$

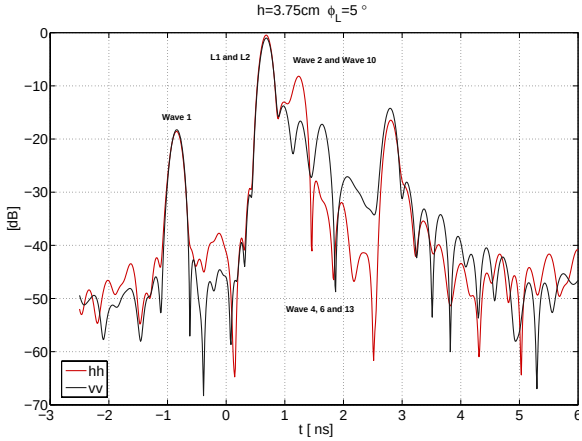

Figure 4.11: RCS $h1 = 3.75cm$, $\phi_L = 5°$

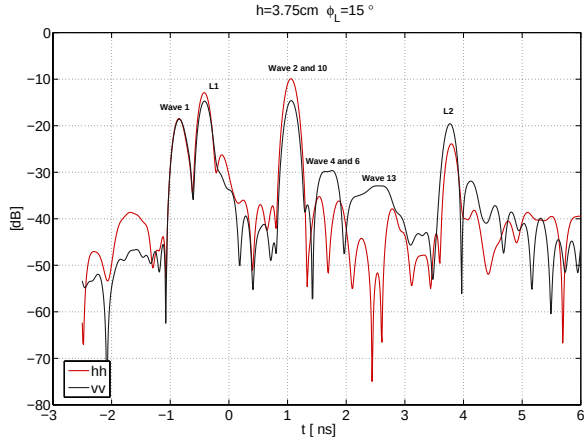

Figure 4.12: RCS $h1 = 3.75cm$, $\phi_L = 15°$

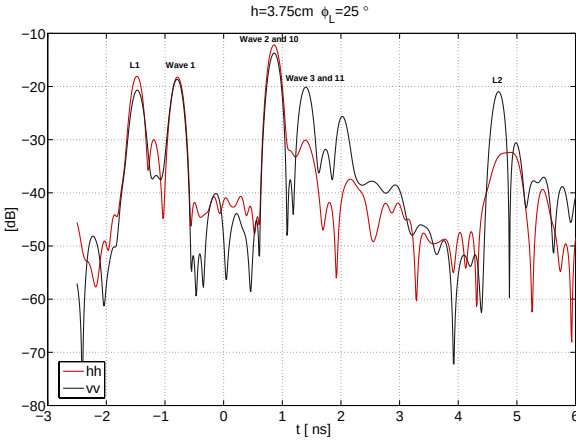

Figure 4.13: RCS $h1 = 3.75cm$, $\phi_L = 25°$

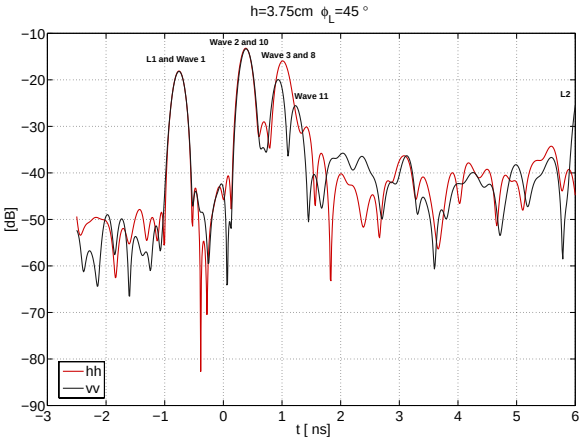

Figure 4.14: RCS $h1 = 3.75cm$, $\phi_L = 45°$

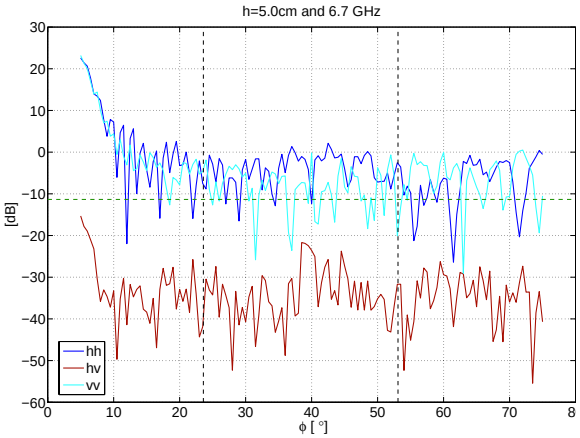

Figure 4.15: RCS $h2 = 5.0cm$

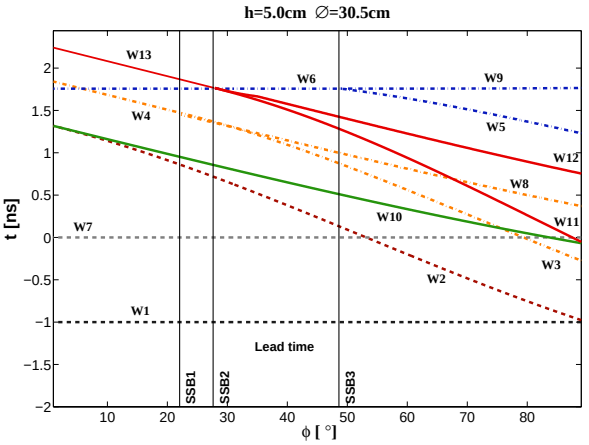

Figure 4.16: Arrivals $h2 = 5.0cm$

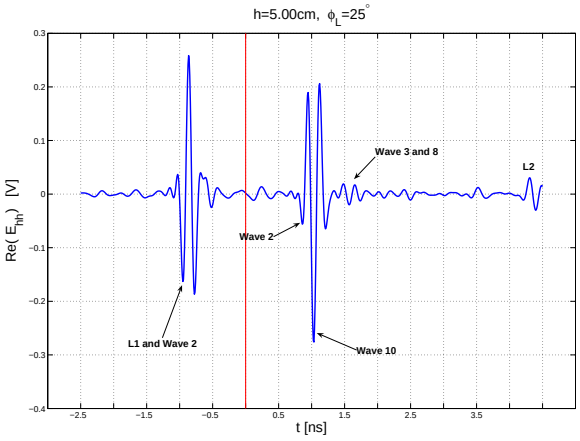

Figure 4.17: Arrivals $h2 = 5.0cm$, $\phi_L = 25°$

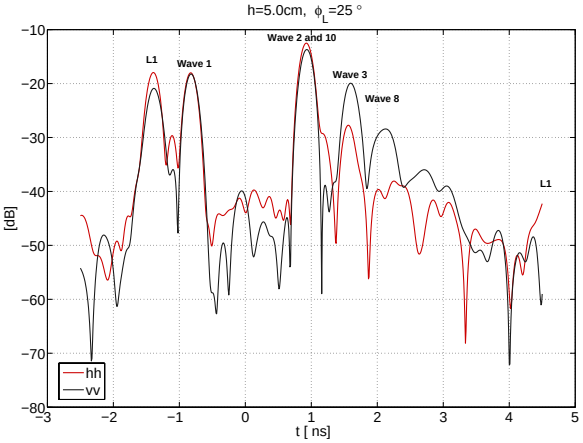

Figure 4.18: RCS $h2 = 5.0cm$, $\phi_L = 25°$

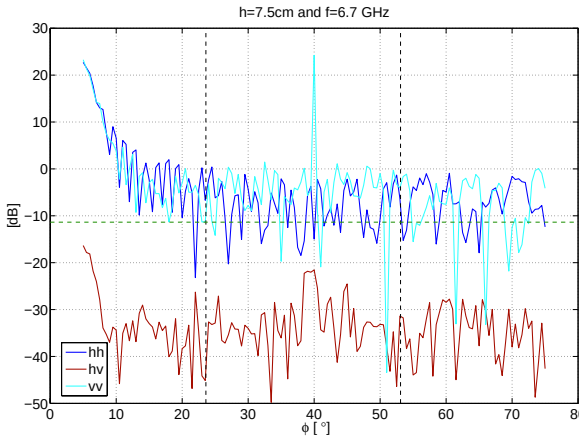

Figure 4.19: RCS of single field components $h3 = 7.5cm$

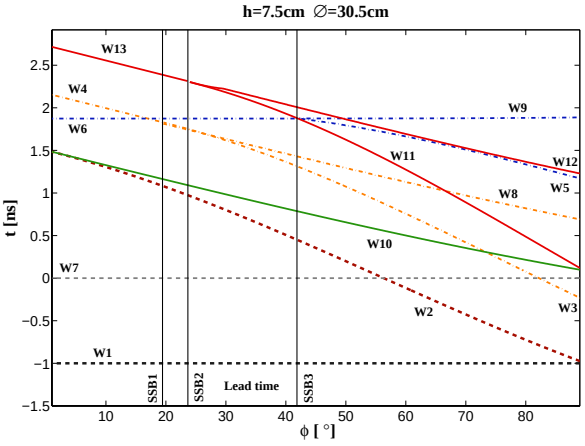

Figure 4.20: Arrivals $h3 = 7.5cm$

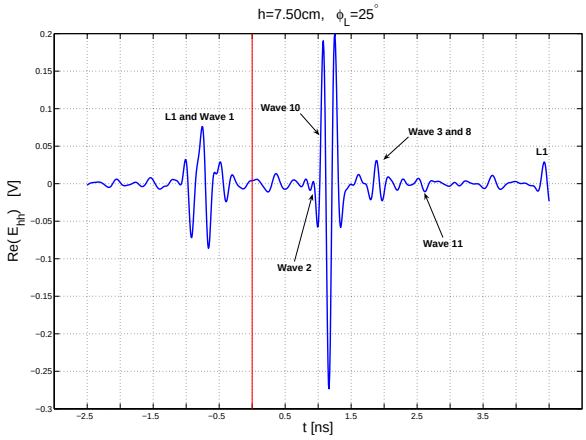

Figure 4.21: Arrivals $h3 = 7.5cm$, $\phi_L = 25°$

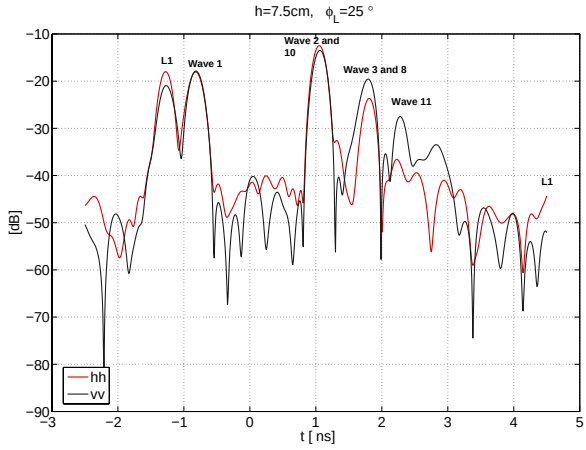

Figure 4.22: RCS $h3 = 7.5cm$, $\phi_L = 25°$

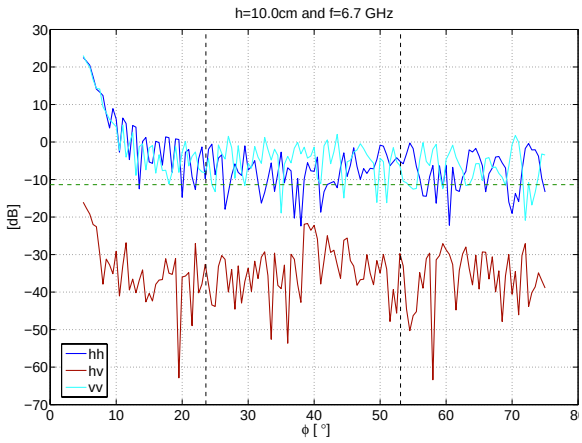

Figure 4.23: RCS of single field components $h4 = 10.0cm$

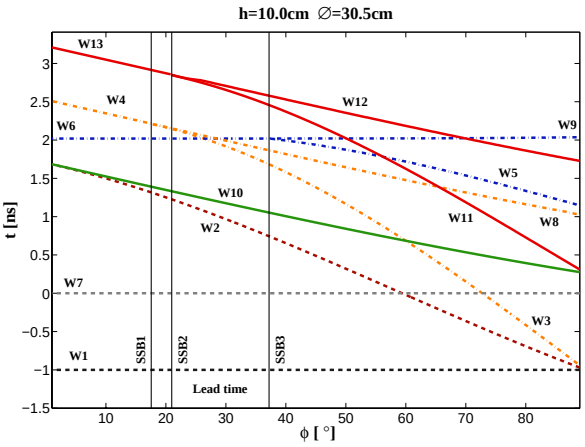

Figure 4.24: Arrivals $h4 = 10.0cm$

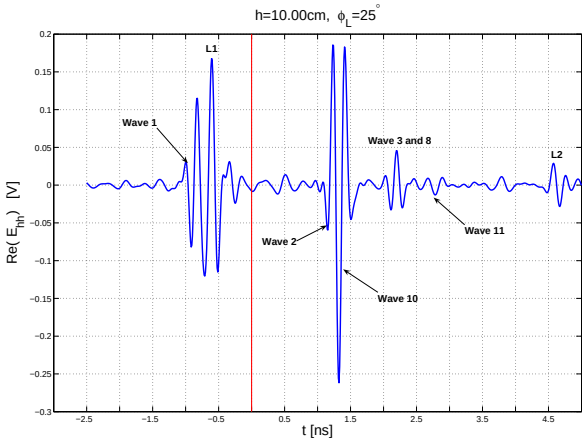

Figure 4.25: Arrivals $h4 = 10.0cm$, $\phi_L = 25°$

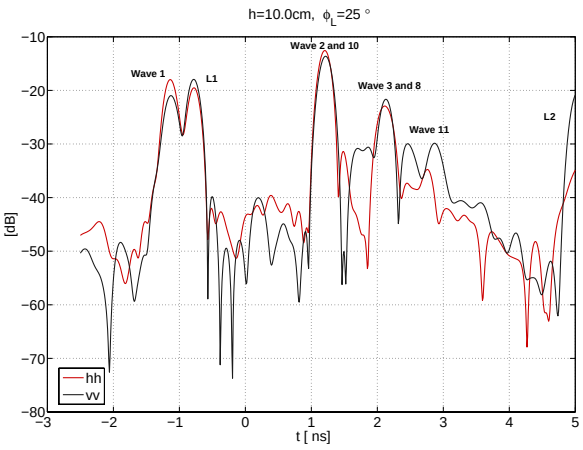

Figure 4.26: RCS $h4 = 10.0cm$, $\phi_L = 25°$

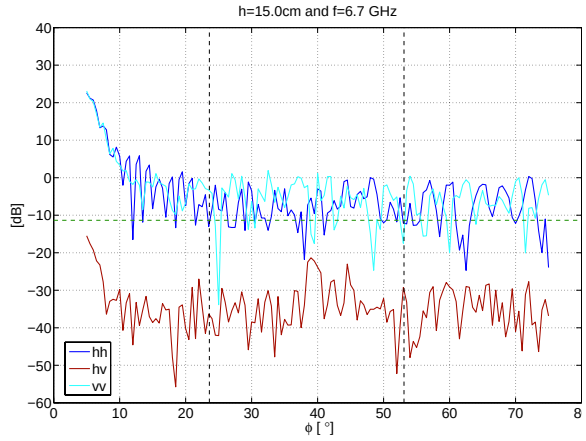

Figure 4.27: RCS of single field components $h5 = 15.0cm$

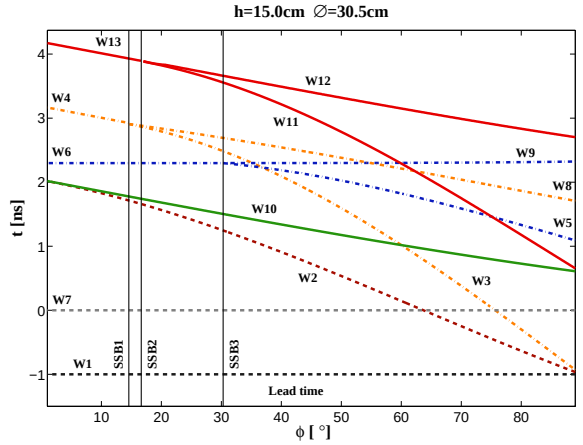

Figure 4.28: Arrivals $h5 = 15.0cm$

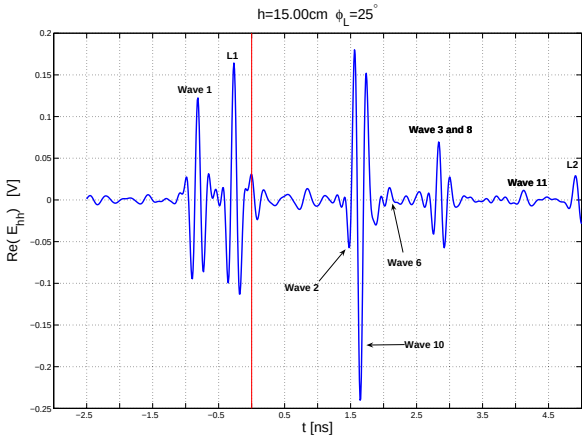

Figure 4.29: Arrivals $h5 = 15.0cm$, $\phi_L = 25°$

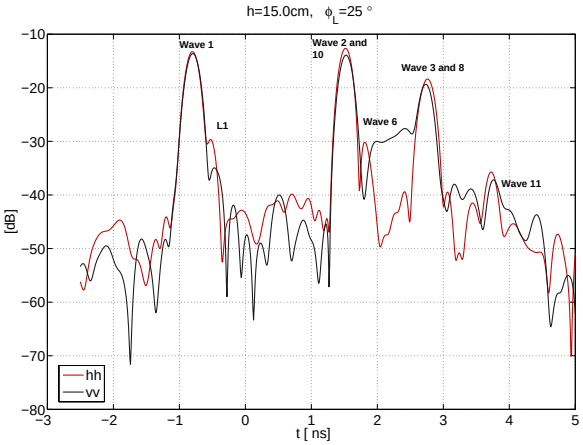

Figure 4.30: RCS $h5 = 15.0cm$, $\phi_L = 25°$

4.2.2 Time Windowed Data

In the previous section the implemented GTD ray system was validated by the measurements performed in a anechoic chamber. The objective here, is to validate the shadow boundaries predicted by the ray model. One outcome of the previous section is that the diffraction from the edges are significant and cannot be neglected. Therefore, as the horizontal aligned edges have a stronger contribution to the hh-component than the vv-component the latter is considered next. In fact, the edges act like horizontal oriented dipoles. Hence, the vv-component is investigated in order to find the transition lit-shadow region. At the shadow boundaries the spatial waves disappear and transform into creeping waves which are strongly attenuated on the shadowed side, leading at the end to a rapid power depression. As one field component is treated a basic representation on the Poincaré sphere is not carried out. According to section 3.7 the direct reflected wave 1 from the sphere is not restricted by a shadow boundary. Hence, the wave 1 gives no information about the geometrical setup like the height and the geometrical properties of the sphere and therefore neglected. This is easily realized in the time domain by a box function as the arrival time of wave 1 is constantly given by t= -1ns. Here, the width of the window is determined by wave 13 at normal incidence which corresponds to the maximal arrival time in the ray system. The Reflectivity of the backscattered vertical component is shown in fig. 4.31 to 4.35 for five different heights at the frequency f=6.7GHz. Further, look angles smaller than the critical angles according to table 4.1 for the different heights are not considered due to the strong contribution of edge L_1 here. As a result of the contributions of the creeping waves 5 and 9, the SSB3 can not be clearly identified. Instead, a good agreement between the transition zones according to the SSB1 and SSB2 and the significant attenuations of the backscattered fields are seen. Hence, the two characteristic angles related to a drop of energy determine the geometrical parameters of the conditions mentioned in fig. 3.16 and 3.17. Additionally to the polarimetric behavior, the two energy minimums can be exploited to get information about the geometrical properties of the target and its height above the ground.

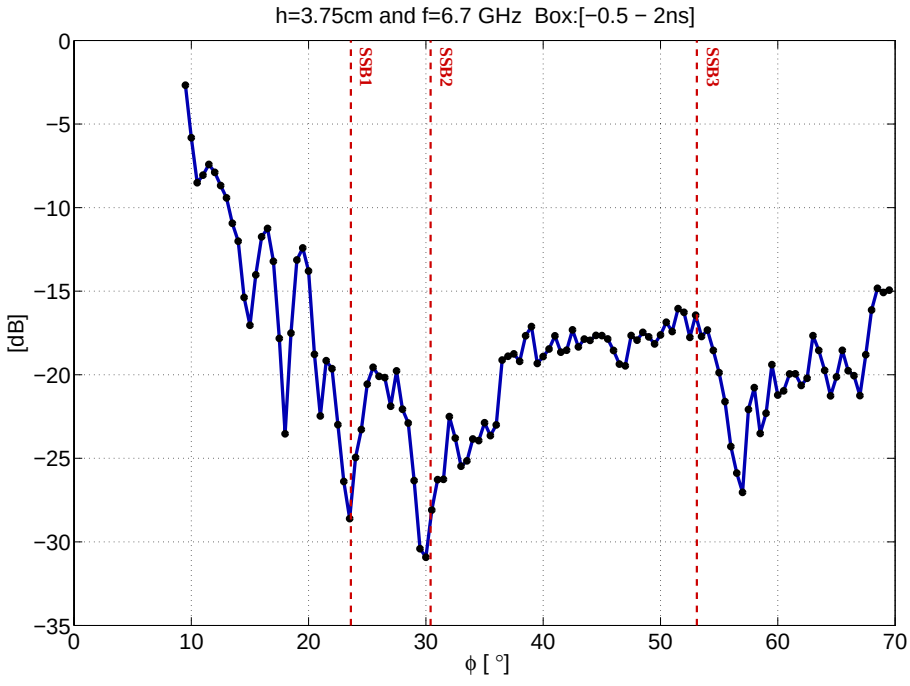

Figure 4.31: Windowed data for h=3.75cm: Boxwidth [-0.5ns - 2ns]

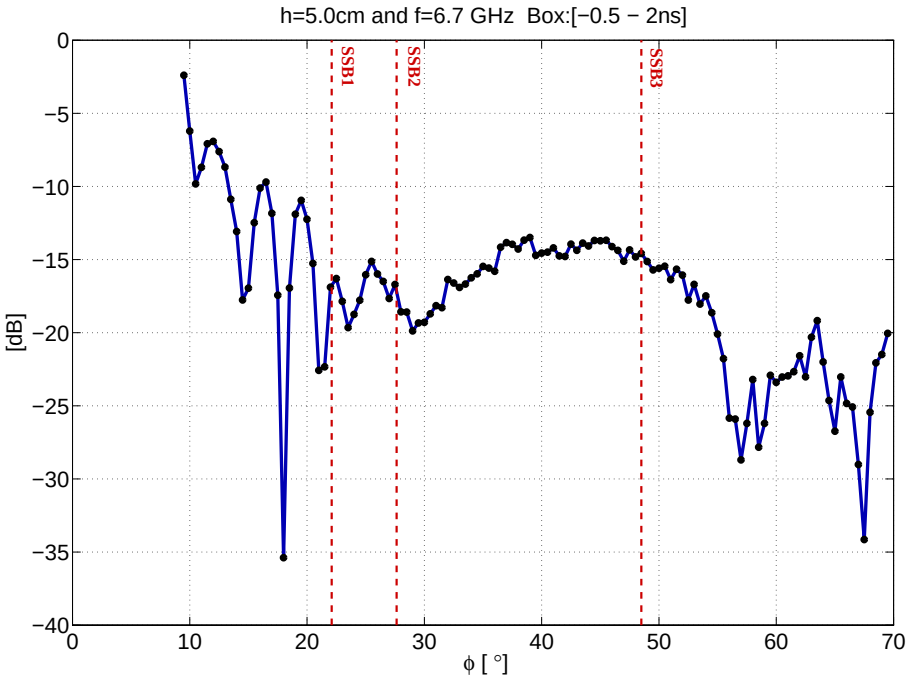

Figure 4.32: Windowed data for h=5.0cm: Boxwidth [-0.5ns - 2.1ns]

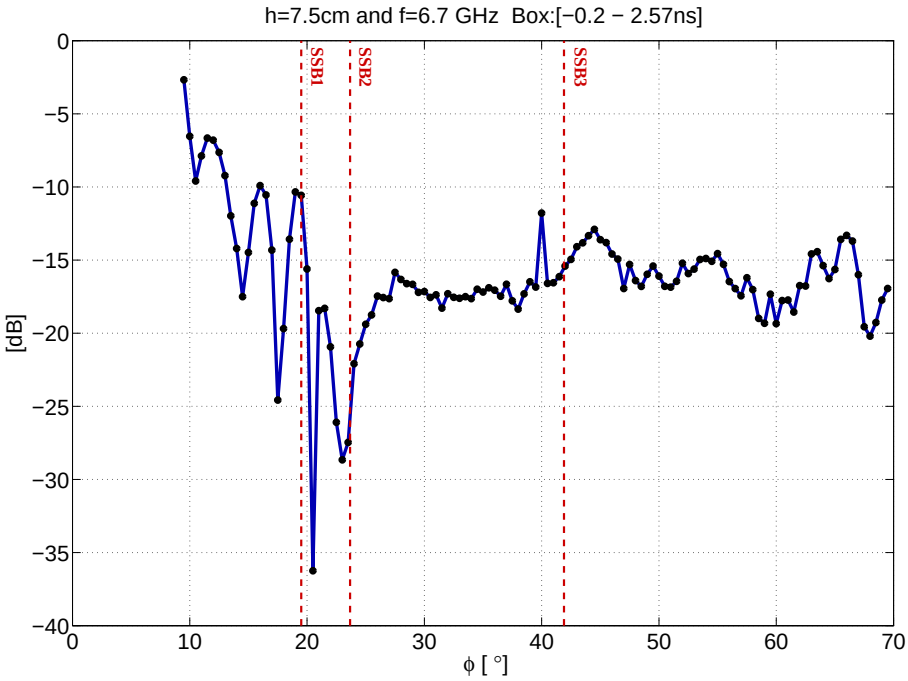

Figure 4.33: Windowed data for h=7.5cm: Boxwidth [-0.2ns - 2.7ns]

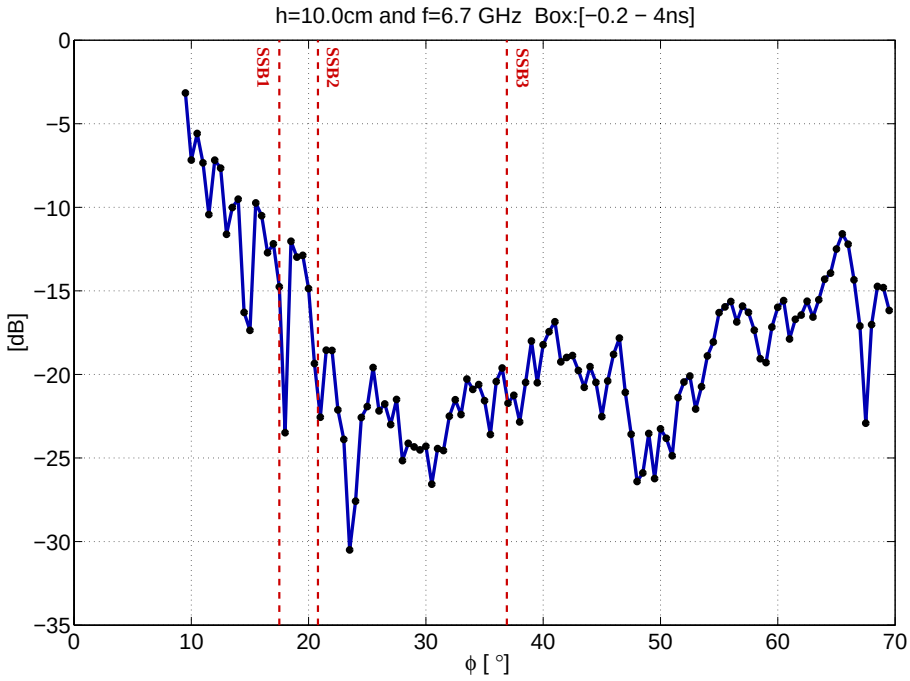

Figure 4.34: Windowed data for h=10.0cm: Boxwidth [-0.2ns - 3.3ns]

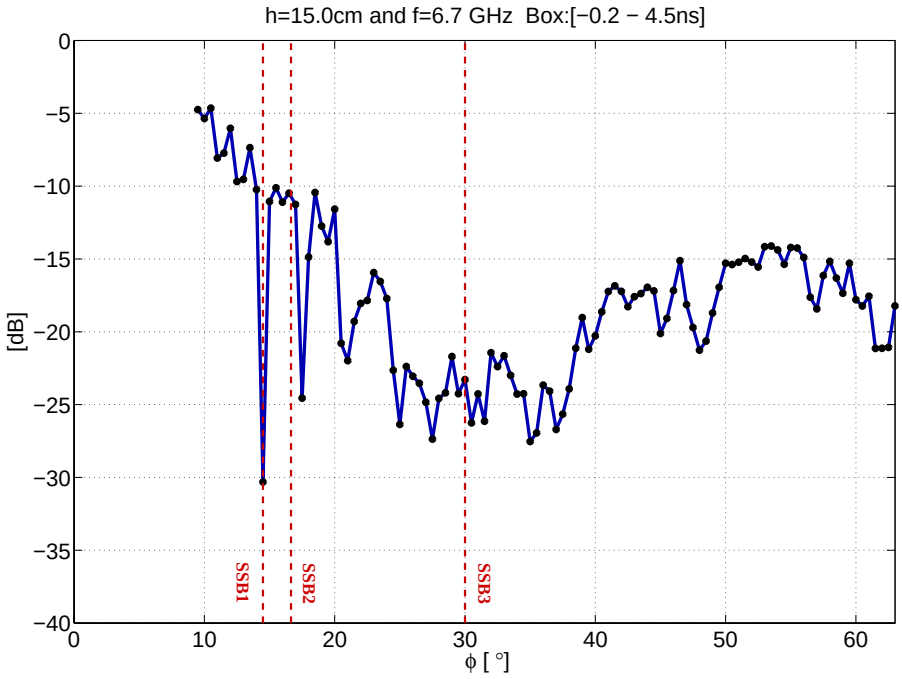

Figure 4.35: Windowed data for h=15.0cm: Boxwidth [-0.2ns - 3.5ns]

CHAPTER 5

Target Situated in the Soil

The cylinder is placed next in the upper dielectric half-space: soil. As the antenna is located in air at point M the field has to transit two times the interface on its round trip, once on its way to the target and once for its way back on. The transitions at the interface air-soil represents a lossy process. Specially, the transition on the way back to the antenna, where the most energy is reflected back into the soil. Further, due to the law of Snellius the transition from the soil into the air modifies the tube of rays as pointed out in fig. 5.1. At the transition into the air the tube of ray is spread. Therefore, at the beginning of this chapter the modification of the ray tube is derived. In accordance to the first investigated case where the cylinder was located in the air a time-dependence $\exp(i\omega t)$ is considered in the following.

5.1 Divergence at the Transition: Soil $\rightarrow$ Air

Due to the different permittivities of the two half-spaces the radii of curvature of the wave front change at the transition soil $\rightarrow$ air. Here, the tube of rays is spread at the transition. Considering a 2D problem, the corresponding radii of curvature $\rho_{(T_1)}$ at T_1 is modified to $\rho'_{2(T_1)}$ (fig. 5.1). The new radius of curvature $\rho'_{2(T_1)}$ is given by the incidence angle φ_i and the refractive index n of the soil as shown in the following. The modification coefficient $\mathcal{D}_{(n,\varphi)}$ is derived next. Considering the two ray tubes with their origin points C_1 and C_2, one looks for the new radius $\rho'_{2(T_1)}$ at T_1. Refer to fig. 5.1 the following segments are given:

$$\overline{C_1T_1} - \overline{C_1M'} = \overline{T_1M'}\,\sin(\varphi_r) \tag{5.1}$$

$$\overline{C_2T_1} - \overline{C_2M'} = \overline{T_1M'}\,\sin(\varphi_i) \tag{5.2}$$

Where in (5.1) and (5.2) the approximation $\cos(\Delta\varphi_i) \approx \cos(\Delta\varphi_r) \approx 1$ was set due to a small variation of $\Delta\varphi_i$ and $\Delta\varphi_r$. According to the law of sines it yields for the triangles $\overline{T_1C_1M'}$ and

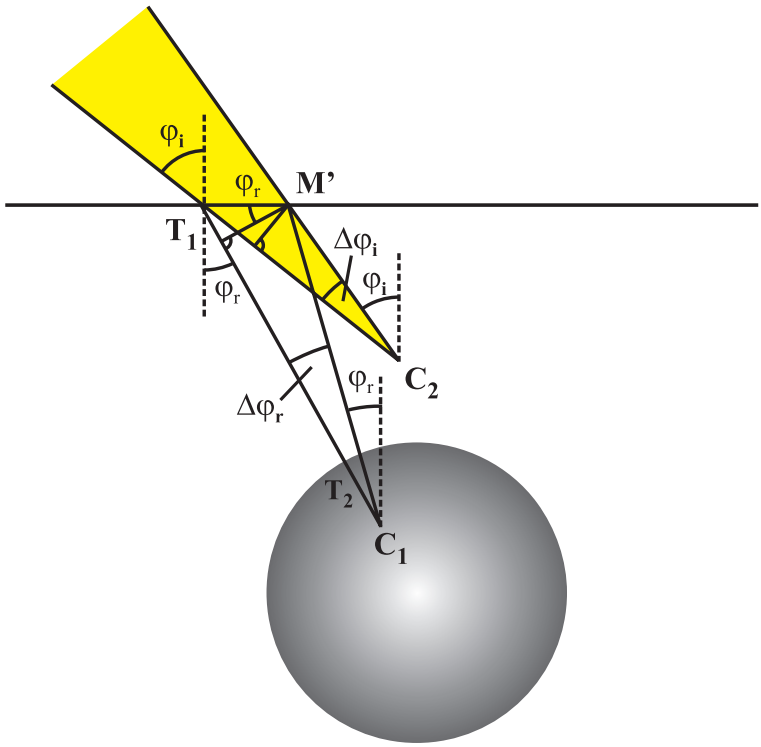

Figure 5.1: Transmission of a tube of rays

$\overline{T_1 C_2 M'}$:

$$\frac{T_1 M'}{\sin \Delta\varphi_r} = \frac{C_1 M'}{\cos \varphi_r} \tag{5.3}$$

$$\frac{T_1 M'}{\sin \Delta\varphi_i} = \frac{C_2 M'}{\cos \varphi_i} \tag{5.4}$$

Substituting (5.3) in (5.1) and (5.4) in (5.2) it leads:

$$\overline{C_1 T_1} = \overline{T_1 M'} \left[\frac{\sin(\varphi_r)\, \sin(\Delta\varphi_r) + \cos(\varphi_r)}{\sin(\Delta\varphi_r)} \right] \tag{5.5}$$

$$\overline{C_2 T_1} = \overline{T_1 M'} \left[\frac{\sin(\varphi_i)\, \sin(\Delta\varphi_i) + \cos(\varphi_i)}{\sin(\Delta\varphi_i)} \right] \tag{5.6}$$

Dividing (5.6) by (5.5) one gets:

$$\frac{\overline{C_2 T_1}}{\overline{C_1 T_1}} = \frac{\rho_2'(T_1)}{\rho_2(T_1)} = \left[\frac{\sin(\varphi_i)\, \sin(\Delta\varphi_i) + \cos(\varphi_i)}{\sin(\varphi_r)\, \sin(\Delta\varphi_r) + \cos(\varphi_r)} \right] \left[\frac{\sin(\Delta\varphi_r)}{\sin(\Delta\varphi_i)} \right] \tag{5.7}$$

The variation of the angles φ_r and φ_i is related via the law of reflection. Here, the transition between the soil and the free air is given by:

$$\sin(\varphi_i) = n \sin \varphi_r \tag{5.8}$$

$$\sin(\varphi_i + \Delta\varphi_i) = n \sin(\varphi_r + \Delta\varphi_r) \tag{5.9}$$

The latter expression (5.9) is rewritten as:

$$\sin(\varphi_i)\cos(\Delta\varphi_i) \;+\; \sin(\varphi_i)\cos(\Delta\varphi_i) \;=\; n\,[\sin(\varphi_r)\cos(\Delta\varphi_r) \;+\; \cos(\varphi_r)\sin(\Delta\varphi_r)\,] \tag{5.10}$$

From (5.10) it follows:

$$\frac{\sin(\Delta\varphi_r)}{\sin(\Delta\varphi_i)} \;=\; \frac{1}{n}\,\frac{\cos(\Delta\varphi_i)}{\cos(\Delta\varphi_r)} \tag{5.11}$$

Considering small variation $\Delta\varphi_i \approx \Delta\varphi_r \approx 0$ and considering (5.11), one gets from (5.7) the modified curvature $\rho_{2(T_1)}'$ as follows:

$$\rho_{2(T_1)}' \;=\; \mathcal{D}_{(n,\,\varphi)}\;\rho_{2(T_1)} \tag{5.12}$$

Where the modification coefficient $\mathcal{D}_{(n,\varphi)}$ is defined by:

$$\boxed{\mathcal{D}_{(n,\,\varphi)} \;=\; \frac{1}{n}\,\left[\frac{\cos^2\varphi_i}{\cos^2\varphi_r}\right]} \tag{5.13}$$

5.2 Ray System

In the first considered case where the object was situated in the air surface shadow boundaries occurred for the backscattered field. The interface acts here as a mirror. Here in contrast, where the target is located under the interface most energy is spread in the upper half-space and is not mirrored back to the antenna. In consequence no shadow boundaries are given in the ray field. The ray field consists of five different waves and their ray paths are presented at the beginning. Afterwards their corresponding asymptotic formulas for the numerical calculation are presented.

5.2.1 List of the Waves

The backscattered GTD-UTD field from a cylinder embedded in the lower half-space soil was built up by five different waves. Their path geometries and interactions with the object and interface are pointed out in fig. 5.2 to 5.6. Where the location of the antenna is given at point M. Similar to the first case, the wave 1 here is reflected perpendicular from the cylinder as shown in fig. 5.2. The first interaction between the cylinder and the interface is pointed out in fig. 5.3.

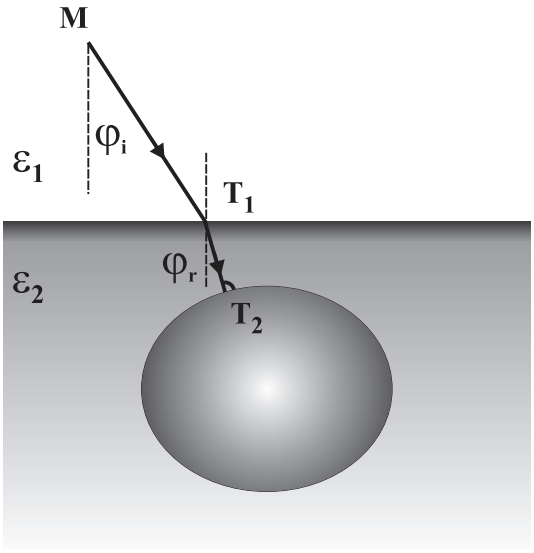

Figure 5.2: Wave 1

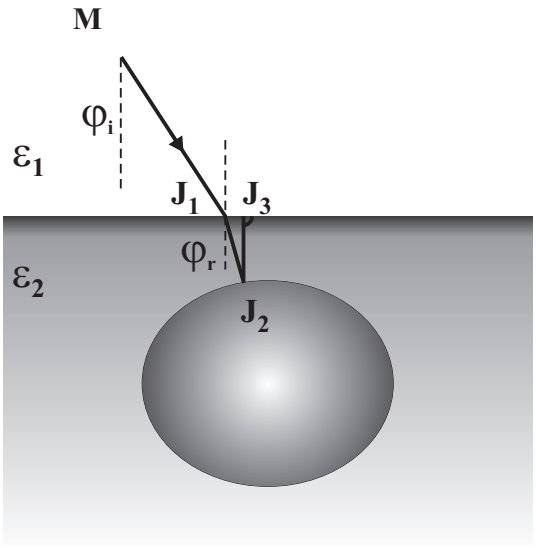

Figure 5.3: Wave 2

The third considered wave in the system is the creeping wave presented in fig. 5.4.
Furthermore, due to the transition from the soil into the free air refracted waves occur along the interface. This type of wave is outlined in fig. 5.3. Here, the wave 4 propagates around the cylinder as a creeping wave and detaches tangentially at U_3 from the cylinder. From there the wave 4 propagates towards the interface. Where for incident angles greater than $\varphi_{crit.}$ wave 4 is refracted as a lateral wave propagating along the interface. Its velocity of propagation is given by c_0 according to the upper layer air. On its way from U_4 to U_5 wave 4 radiates elementary waves into the lower half-space with the angle $\varphi_{crit.}$ and is exponentially attenuated in the $\hat{z}$-direction according to Bouche and Molinet [8].

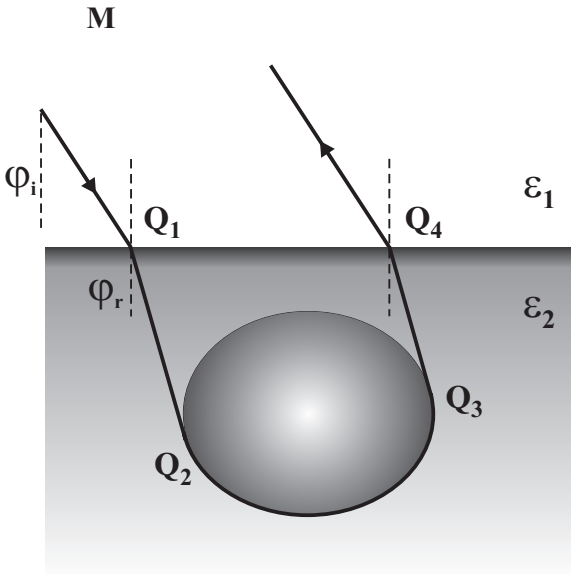

Figure 5.4: Wave 3

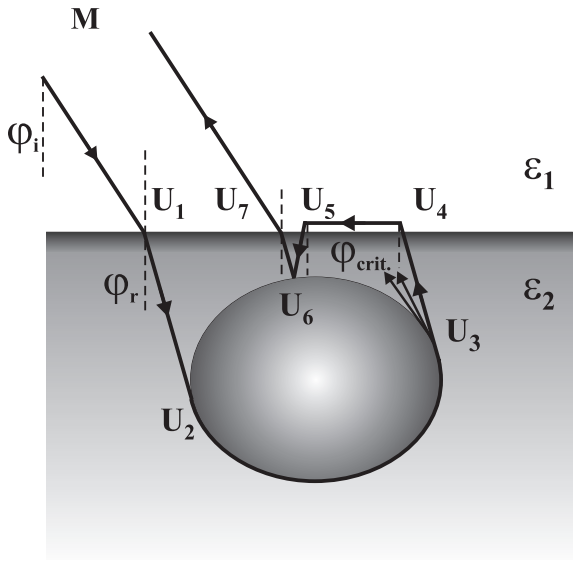

Figure 5.5: Wave 4

Note that the lateral wave 4 is one special wave of a bundle of lateral waves propagating along the interface. Wave 4 is reflected on the cylinder at point U_5 and after its transition at U_6 propagates back to the antenna. The critical angle $\varphi_{crit.}$, where lateral waves are generated at

the transition soil → air, is defined by the refraction angle $\varphi_i = \pi/2$. According to the law of reflection (5.8) it follows:

$$\varphi_{crit.} = \arcsin(\frac{1}{n}) = \arcsin\left(\frac{c_2}{c_1}\right) \tag{5.14}$$

Where c_1 correspond to the free space velocity c_0. According to the homogeneous soil properties ϵ_{eff} introduced in (1.4) one rewrites (5.14) as follows:

$$\varphi_{crit.} = \arcsin\left(\sqrt{\frac{\epsilon^1_{eff}}{\epsilon^2_{eff}}}\right) \tag{5.15}$$

Where for the upper half-space air it turns out $\epsilon^1_{eff} = 1$. Finally, wave 5 detaches from the cylinder (Z_3) and interacts withe the interface and cylinder at (Z_4) and (Z_5) (fig. 5.6).

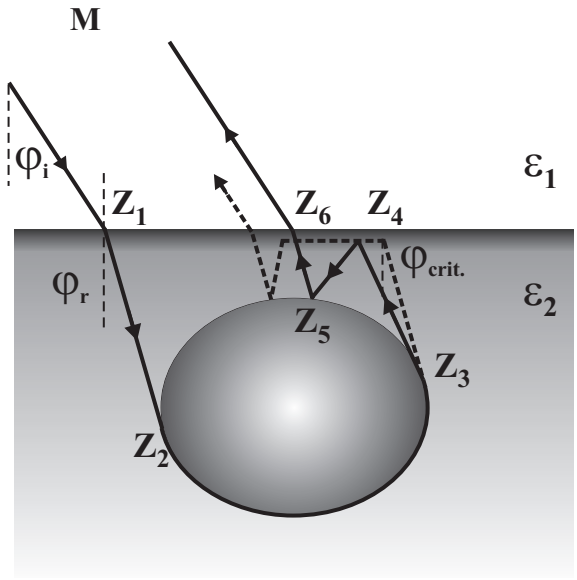

Figure 5.6: Wave 5

5.2.2 Numerical Implementation of the Ray System

Wave 1

In general the different interactions between the cylinder and interface represents a loss of energy. Additionally the creeping waves considered here are very strong attenuated. Hence, the wave 1 having only one single reflection at the cylinder is the main contributor of the ray system. Like the case where the cylinder was situated in the air, the phase origin is placed in the center of the target. Also, the spreading factor $\frac{1}{\sqrt{OM}}$ and the propagation term $\exp(-2\,i\,k_1\,0M)$ are neglected for the numerical calculation. The wave 1 is given as follows:

$$\vec{E}_{(M)} = \vec{E}_0 \cdot \underline{T}^i{}_{(T_1)} \cdot \underline{R}_{0(T_2)} \cdot \underline{T}^r{}_{(T_1)} \; SF_{W1(T_1)} \; e^{-2i\left[\vec{k}^i_1 \cdot \overrightarrow{0T_1} + k_2\, T_1 T_2,\right]} \tag{5.16}$$

Where the dyads $\underline{T}^i$ and $\underline{T}^r$ describe the two transition of wave 1 across at the interface. The dyad $\underline{R}_0$ signifies the reflection at T_2 for the perfect conducting surface. Straightforward, according to (5.12) the spatial divergence of wave 1 is given after its transition at the interface

by:

$$SF_{W1(T_1)} \;=\; \sqrt{\rho'_{2(T_1)}} \tag{5.17}$$

In agreement with (5.12) the radius of curvature is modified here as follows:

$$\rho'_{2(T_1)} \;=\; \mathcal{D}_{(n,\varphi)} \left(\frac{ao_{(T_2)}}{2} \;+\; T1T2 \right) \tag{5.18}$$

For numerical purpose one set the term $1 \,/\, \sqrt{\rho'_{2(T_1)} \,+\, T_1 M}$ for the way back equal to $1 \,/\, \sqrt{0M}$.

Wave 2

Wave 2 describes the first interaction between the target and the interface. The backscattered field received at the antenna is given by:

$$\vec{E}_{(M)} \;=\; \vec{E}_0 \cdot \underline{T}^i{}_{(J_1)} \cdot \underline{R}^2_{0(J_2)} \cdot \underline{f}_{(J_3)} \cdot \underline{T}^r{}_{(J_1)} \;\; SF_{W2(J_1)} \;\; e^{-2i\left[\vec{k}^i_1 \cdot 0\overrightarrow{J_1} \,+\, k_2\,(J_1 J_2 \,+\, J_2 J_3) \right]} \tag{5.19}$$

Where the Fresnel dyad $\underline{f}$ takes the reflection at the interface into account. In (5.19) the modified radii of curvature at the reflection points J_1, J_2 and J_3 are calculated similar as in chapter 3. The resulting radius of curvature at the transition point J_1 after this procedure is when modified with the factor $\mathcal{D}$ for the way back according to (5.12). As for five and more reflections the received energy at the antenna is negligible, other multiple waves are useless.

Wave 3 (Creeping wave)

According to fig. 5.4 the wave 3 is conducted around the cylinder as a creeping wave and when radiated back to the antenna. Its field is given here by:

$$\vec{E}_{(M)} \;=\; 2\vec{E}_0 \cdot \underline{T}(Q_1) \cdot \underline{D}(Q_2) \cdot \underline{D}(Q_3) \cdot \underline{T}(Q_4) \; e^{i\,att^s_h} \; e^{-i\left[\vec{k}^i_1 \cdot 0\overrightarrow{Q_1} + \vec{k}^i_1 \cdot 0\overrightarrow{Q_4} + k_2\, Q_2 Q_3 \right]} \tag{5.20}$$

As a long arc length is on hand for wave 3 the asymptotic approximation of the attachment and detachment coefficients according to the work of Bouche and Molinet [8] are considered. The formulas after [8] are presented in appendix (C.4.2). Where in (5.20) the attenuation coefficients for the hard (h) and soft(s) component corresponding to the $||$ and $\perp$ component are given by:

$$e^{i\,att^s_h} \;=\; e^{i\gamma \frac{l_c}{a}} \tag{5.21}$$

One notes that the way to the cylinder and back is interchangeable. Thus, the double value has to be computed. In the same manner as the previous two waves the divergence term $1 \,/\, \sqrt{Q_3 Q_4 \cdot \mathcal{D} \,+\, Q_4 M}$ for the way back is substituted by $1 \,/\, \sqrt{0M}$.

Wave 4 (Lateral wave)

According to fig. 5.5 one recognizes that all the detachment points U_3 along the cylinder represent a line source. The problem in calculating the wave 4 consists here in finding a solution of a line source radiating near the interface of two dielectric half-spaces, where lateral waves are

generated at the interface. A solution for a source in the presence of a semi-infinite dielectric medium is given in the work of Felsen [23]. According to the notation used in fig. 5.5 and considering equation (57c) in section 5.5 and fig. 5.5.2(b) in [23], the field of a wave radiating from the point U_3 and propagating as lateral wave to the point U_6 is given after some manipulation as follows:

$$I_b \;=\; \frac{1}{\sqrt{2\pi}} \;\frac{e^{i\,[k_2\,(L_1+L_3)\,+\,k_1 L_2]}\;\;\epsilon^{\frac{1}{4}}\;\;e^{-i\frac{\pi}{4}}}{(1\;-\;\epsilon)\;\;(k_2 L_2)^{\frac{3}{2}}} \tag{5.22}$$

In the work of Felsen a normalized source rate ($|E_0| \;=\; 1$) is considered at U_3. In contrast the source rate after Bouche and Molinet [8] in appendix 1 on page 467 is defined as:

$$E_{0\,(U_3)} \;=\; \underbrace{\frac{e^{i\frac{\pi}{4}}}{\sqrt{8\pi k}}}_{D_s}\;\frac{e^{ikr}}{\sqrt{r}} \tag{5.23}$$

Hence, in order to compute the field up to the point U_6 after the formulas specified in [23], the field value at U_3 has to be divided by D_s. This yields:

$$\vec{E}_{(M)} \;=\; \vec{E}_0 \cdot \underline{T}^i{}_{(U_1)} \cdot \underline{D}_{(U_2)} \left(\frac{I_b}{D_s}\right) \underline{T}^r{}_{(U_7)}\; SF_{W4} \;\;\; e^{-i\left[\,\vec{k}_1^{\,i}\cdot\overrightarrow{0U_1}\,+\,\vec{k}_1^{\,r}\cdot\overrightarrow{0U_7}\,+\,k_2\,(U_1U_2\,+\,U_2U_3\,+\,U_6U_7)\right]} \tag{5.24}$$

In the expression (5.24) the spatial divergence up to U_6 is considered. After the reflection at U_6 the radius of curvature is modified as:

$$\rho_{2\,(U_6)} \;=\; \frac{a_{2\,(U_6)}\cos(\theta_i)}{2} \tag{5.25}$$

The propagation to the transition point U_7 yields:

$$\rho_{2\,(U_7)} \;=\; \rho_{2\,(U_6)} \;+\; U_6U_7 \tag{5.26}$$

At U_7 the radius is spread after the transition as follows:

$$\rho'_{2\,(U_7)} \;=\; \mathcal{D}_{(n,\,\varphi)}\,\rho_{2\,(U_7)} \tag{5.27}$$

Finally, the divergence for the way back is given by:

$$SF_{W4} \;=\; \sqrt{\rho'_{2\,(U_7)}} \tag{5.28}$$

Where $1/\sqrt{\rho'_{2\,(U_7)} \;+\; U_7M}$ was substituted by $1\,/\,\sqrt{0M}$.

Wave 5

The last considered wave of the ray system has, after being radiated as a space wave from the

cylinder, an interaction at the interface and cylinder before propagating back to the antenna. According to the UTD, the wave 5 takes the form:

$$\vec{E}(M) \;=\; \vec{E}_0 \cdot \underline{T}^i(Z_1) \cdot \underline{D}(Z_2) \cdot \underline{D}(Z_3) \cdot \underline{f}(Z_4) \cdot \underline{R}_0(Z_5) \cdot \underline{T}^r(Z_6)\; SF_{W5}\; e^{-i\left[\,\vec{k}_1^i \cdot \vec{0Z_1} \,+\, k_2\, Z_1 Z_6\,\right]} \tag{5.29}$$

Where the term $Z_1 Z_6$ corresponds to the entire ray path $Z_1 Z_2 + Z_2 Z_3 + Z_3 Z_4 + Z_4 Z_5 + Z_5 Z_6$. The spreading factor is computed similarly as the previous discussed waves. Here, the radius of curvature $\rho_{2(Z_5)}'$ after the reflection at Z_5 is given by:

$$\rho_{2(Z_5)}' \;=\; \frac{1}{\frac{1}{Z_3 Z_4 + Z_4 Z_5} \;+\; \frac{2}{a_{2(Z_4)} \cos(\theta_i)}} \tag{5.30}$$

This gives the modified curvature $\rho_{2(Z_6)}'$ after the transition:

$$\rho_{2(Z_6)}' \;=\; \mathcal{D}_{(n,\,\varphi)\varphi)}\; \left(\rho_{2(Z_5)}' \;+\; Z_5 Z6\right) \tag{5.31}$$

Hence, it follows the spreading factor:

$$SF_{W5} \;=\; \sqrt{\rho_{2(Z_6)}'} \tag{5.32}$$

In latter expression the term $1/\sqrt{\rho_{2(Z_6)}' \;+\; Z_6 M}$ was set equal to $1\,/\,\sqrt{0M}$.

5.3 Numerical Results

5.3.1 Single Wave Contributions

The ray system is computed first for a linear polarized incident field where $\vec{E}_{\perp}^{0} = 1$, $\vec{E}_{||}^{0} = 1$, $f = 500\,MHz$, $\epsilon_2 = 9.6$, $d = 0.5$. The numerical results of the absolute amplitude values for a lossless soil are presented in fig. 5.7. Due to the strong attenuation of the creeping waves in the considered ray system the backscattered field is finally given by the spatial waves 1 and wave 2. Then, a incident field with the complex permittivity $\epsilon_2 = 9.6 - 0.2i$ is considered. Refer to [34] and [47] this corresponds to a slight lossy soil. The numerical results are shown in fig. 5.8. Subsequently the lost of the soil is increased by setting $\epsilon_2 = 9.6 - i$. This correspond e.g. to a sandy soil with a poor moisture. The corresponding curves are shown in fig. 5.9. The field components for a permittivity $\epsilon_2 = 9.6 - 5i$ is presented in fig. 5.10. It is apparent that if the attenuation is strong only the main reflection from wave 1 remains as a significant signal. An effective permittivity with an imaginary part between $\epsilon_{eff}'' = 5 - 8$ corresponds here to e.g. clayey soils or soils with a high salinity.

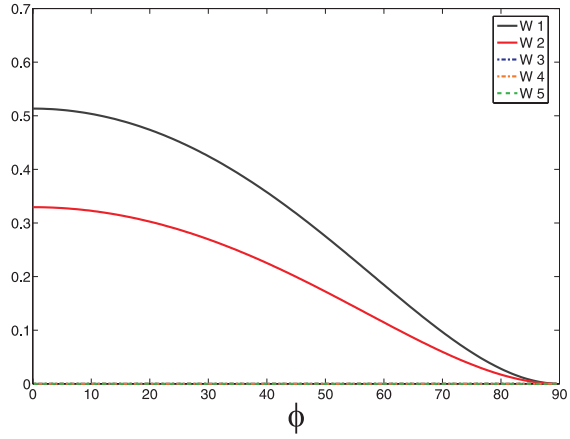

(a) $|\vec{E}_{\perp}|$

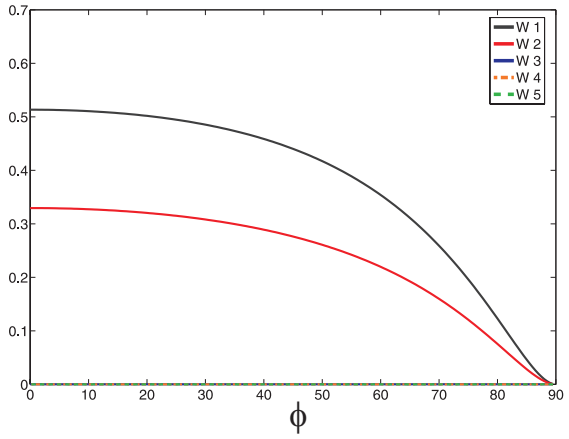

(b) $|\vec{E}_{||}|$

Figure 5.7: Ray contributions
$[\vec{E}^0_{\perp} = 1, \vec{E}^0_{||} = 1, f = 500MHz, \epsilon_2 = 9.6\, d = 0.5]$

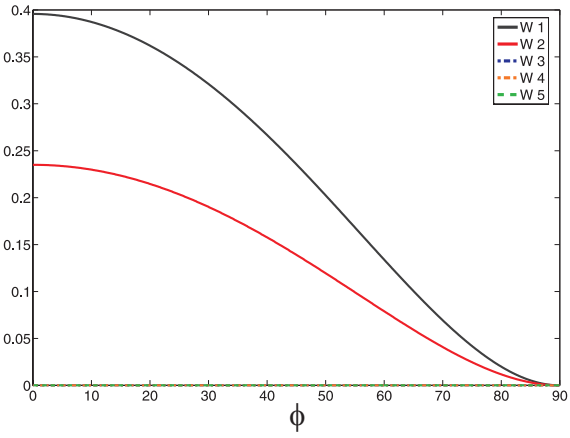

(a) $|\vec{E}_{\perp}|$

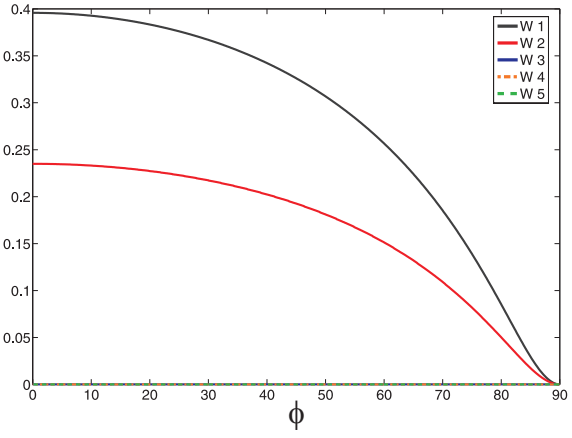

(b) $|\vec{E}_{||}|$

Figure 5.8: Ray contributions
$\vec{E}^0_{\perp} = 1,\ \vec{E}^0_{||} = 1,\ f = 500MHz,\ \epsilon_2 = 9.6 - 0.2i,\ d = 0.5m$

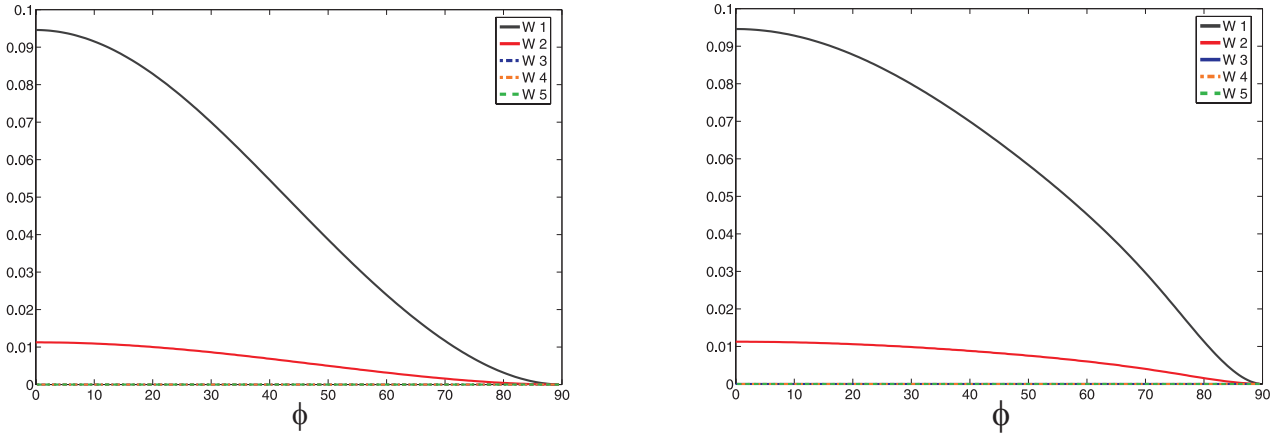

(a) $|\vec{E}_{\perp}|$ (b) $|\vec{E}_{||}|$

Figure 5.9: Ray contributions
$\vec{E}^0_{\perp} = 1$, $\vec{E}^0_{||} = 1$, $f = 500MHz$, $\epsilon_2 = 9.6 - i$, $d = 0.5m$

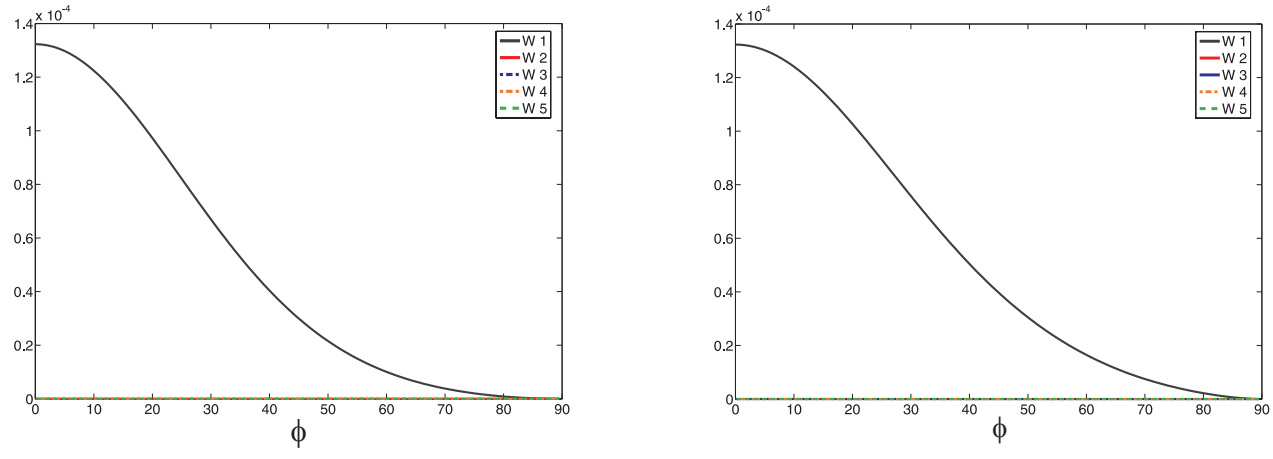

(a) $|\vec{E}_{\perp}|$ (b) $|\vec{E}_{||}|$

Figure 5.10: Ray contributions
$\vec{E}^0_{\perp} = 1$, $\vec{E}^0_{||} = 1$, $f = 500MHz$, $\epsilon_2 = 9.6 - 5i$, $d = 0.5m$

5.3.2 Representation on the Poincaré sphere

According to the results of the previous section the polarization of the two principal wave 1 and 2 and of the ray system is presented on the Poincaré sphere for different lossy soils described by $\epsilon_2 = \epsilon_2' - i\epsilon_2''$. The single polarization states of the wave 1 and 2 are shown for a linear polarized incident field in fig. 5.11 and fig. 5.12 where $\vec{E}_{\perp}^{0} = 1$, $\vec{E}_{||}^{0} = 1$, $f = 500MHz$, $d = 0.5$ are constant. When a circular polarized field is considered and the corresponding results of wave 1 and 2 are outlined in fig. 5.13 and fig. 5.14. In order to investigate the effect of the

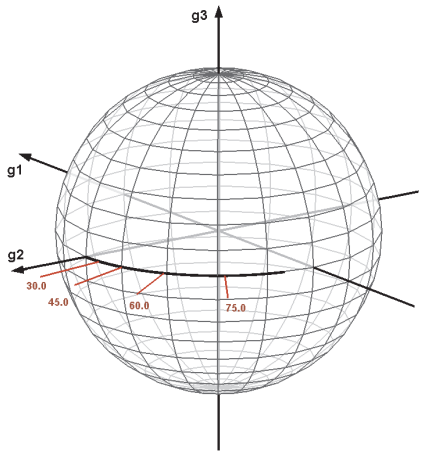

Figure 5.11: Wave 1
$[\vec{E}_{\perp}^{0} = 1, \vec{E}_{||}^{0} = 1, f = 500MHz, \epsilon_2 = 9.6]$

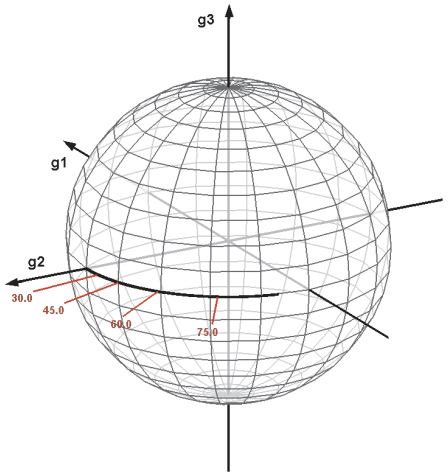

Figure 5.12: Wave 2
$[\vec{E}_{\perp}^{0} = i, \vec{E}_{||}^{0} = 1, f = 500MHz, \epsilon_2 = 9.6]$

distance target - interface the cylinder was positioned at the two different distances h=0.3m and h=0.5m. The polarization of the backscattered ray system for the different losses is shown in fig. 5.17 and fig. 5.18. With increasing loss the locations on the Poincaré sphere move away from the equator line leading to a polarization ladder. Of particular interest is the fact that the superposition of the two main contributors wave 1 and 2 gives virtually a linear polarization for both computed heights in a loss-free soil. Further, comparing both figures one see immediately that the distance from the interface has no influence on the location on the Poincaré sphere.

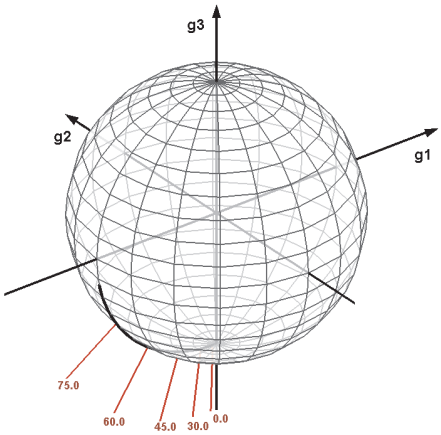

Figure 5.13: Wave 1
$[\vec{E}_{\perp}^{0} = i, \vec{E}_{||}^{0} = 1, f = 500MHz, \epsilon_2 = 9.6]$

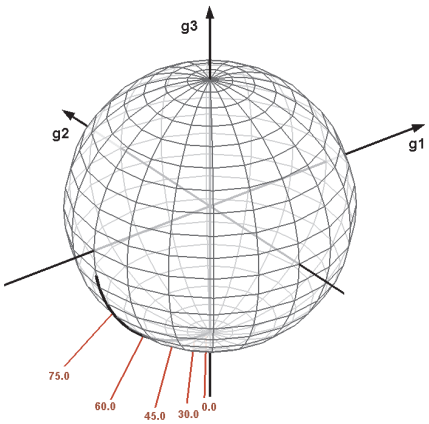

Figure 5.14: Wave 2
$[\vec{E}_{\perp}^{0} = i, \vec{E}_{||}^{0} = 1, f = 500MHz, \epsilon_2 = 9.6]$

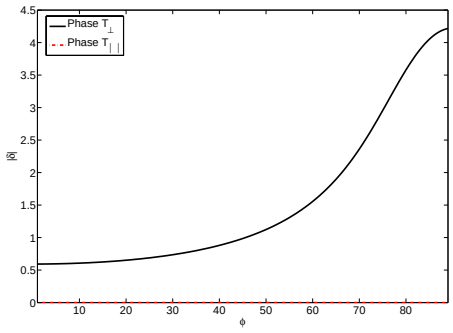

Figure 5.15: $\epsilon_2 = 9.6 - i$

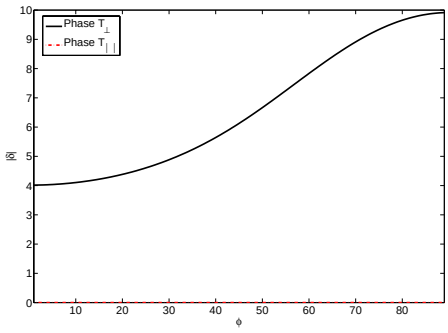

Figure 5.16: $\epsilon_2 = 9.6 - 8i$

The distance from the equator line is solely due to the soil's loss. This result is surprising as one may think that due to different ray paths the superposition of the two principles waves takes place out of phase. This is not the case as due to the geometrical setup and refraction index of the lossy soil the path length $J_1J_2 + J2J_3$ of wave 2 is over the entire look angle range nearly twice as long as the distance sphere $\rightarrow$ interface (T_1T_2) according to wave 1. Hence, the single steps of the polarization ladder can be directly related to the loss of the soil. The small phase shift is given here at the transition soil $\rightarrow$ air. According to the transition coefficient introduced in appendix $A.1$ a phase shift occurs at the transition lossy soil $\rightarrow$ free space. The phase of the perpendicular and parallel transmission coefficient are shown in fig. 5.15 and fig. 5.16 for a complex permittivity $\epsilon_2 = 9.6 - i$ and $\epsilon_2 = 9.6 - 8i$. With increasing loss the phase different also increase which leads finally to the polarization ladder on the Poincaré sphere.

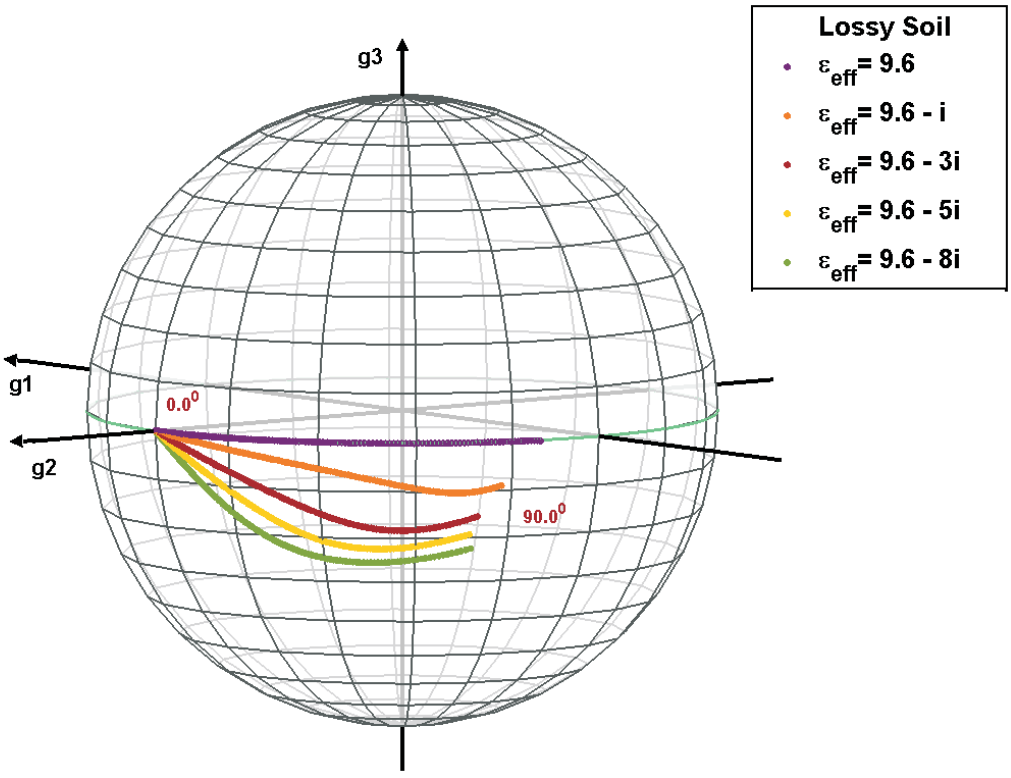

Figure 5.17: d = 0.3m

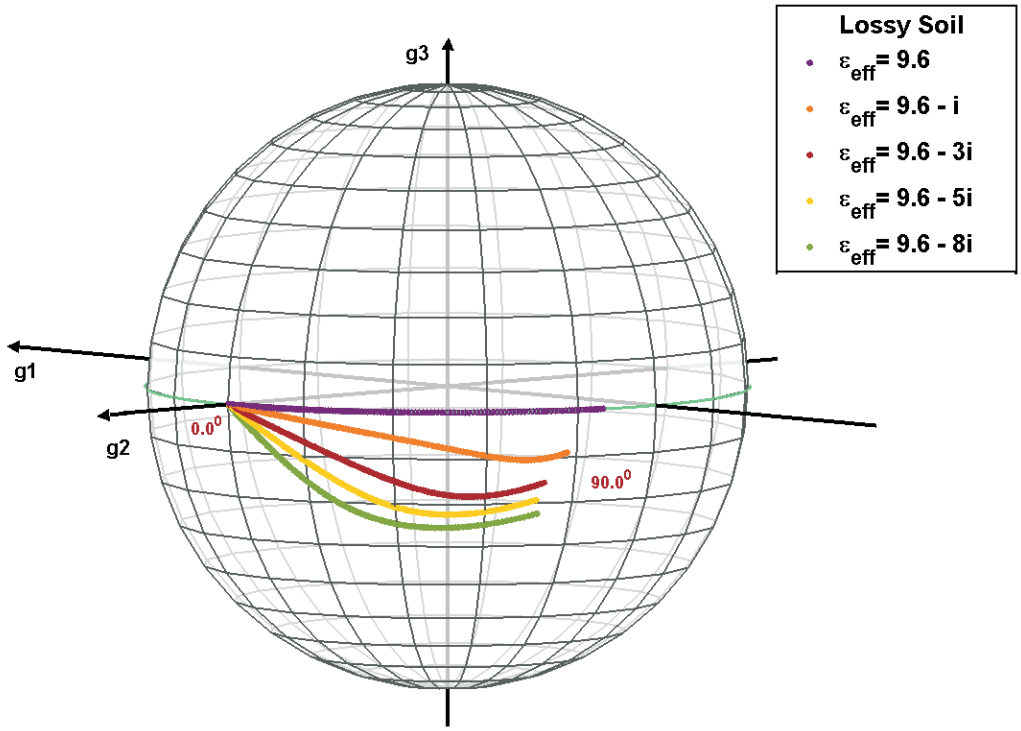

Figure 5.18: d = 0.5m

RADAR Polarimetry Decomposition

During the scattering process, the superposition of the different occurring interactions can be done either in a coherent or incoherent way. One can directly measure the voltage components of the backscattered field over time as long as the assembly emitter, target and receiver is deterministic and time invariant. If incoherent scattering processes are on hand, one cannot measure the voltage over time as due to the statistical averaging the voltage would vanish e.g. monochromatic waves. In this case, a power measurement is considered. A power measurement is based on averaging the incoming energy over a certain time interval. Therefore, the information about the relative phase between the elements of the scattering matrix $[S]$ is lost. Hence, a voltage measurement is related to scattering processes of statistical first order, where the power measurements describes scattering mechanisms of second order. The different common decomposition theorems are based on these two types of measurement.

Huynen [35] was the first to extract information about the scattering mechanism directly from a power measurement. In his classical work of 1970, the decomposition of the Müller/Kennaugh Matrix $[M]$ is done in a more intuitive way as it was "Phenomenological". From that time on, a number of decomposition theorems were introduced in Radar polarimetry. Therefore, a general historical overview of the existing decomposition theorems in radar polarimetry are presented in the block diagram according to Pottier [54].

In chapter 6, the decomposition of the Sinclair matrix $[S]$ after the theorems of Krogager [43] and Cameron [11] is presented. Both theorems are based on a voltage measurement, useful for coherent scattering processes.

The classical target decomposition after Huynen [35], based on a power measurement is presented at he beginning of the following chapter 7. According to incoherent scattering mechanisms, an analysis of the eigenvalues based decomposition after Cloude and Pottier [18] [19] is treated.

The four different decomposition theorems discussed in this thesis, were applied on the EMSL measurements which were investigated in chapter 4. The results are presented in the chapter 6 and chapter 7.

The following overview over the different ways of extracting information nowadays from the backscattered field is respectfully quoted from a lecture course held by Professor E. Pottier [56]:

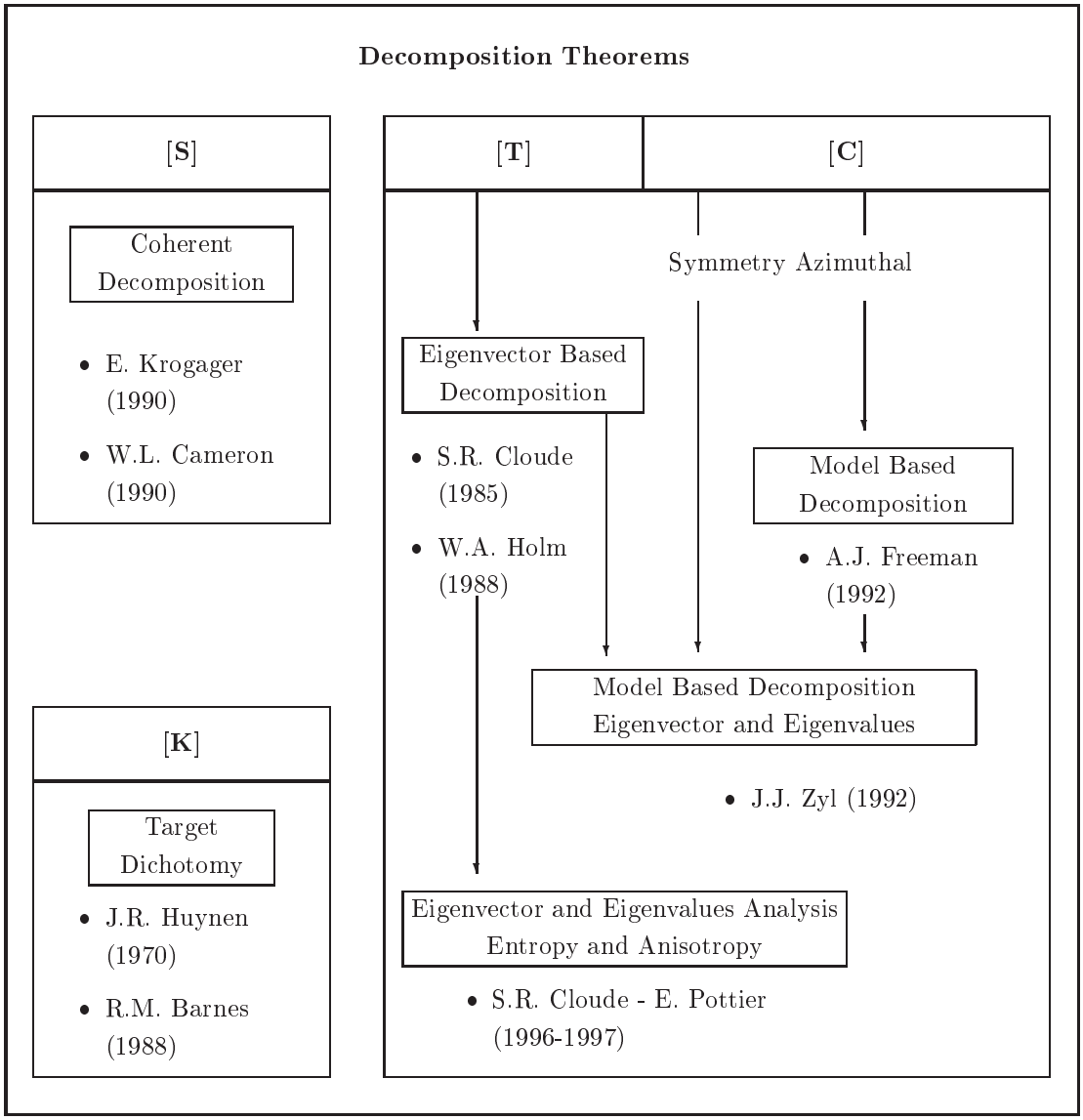

CHAPTER 6

Coherent Decomposition Theorems

In this chapter two different decomposition theorems according to a coherent scattering process are presented and applied on the data measured in the EMSL. The first presented decomposition theorem here was introduced by Krogager [43]. Then the decomposition reported by Cameron [11] is considered and its results obtained from the measured data are discussed .

6.1 Krogager Decomposition and Code Implementation

Based on observation, Krogager [43] presumed that the backscattered fields from an illuminated area could be mostly split up into three different scatterer types. The first type describes odd reflections at the scattering process, where the second type is related to even interactions at the target. The corresponding canonical targets are a sphere and a dihedral. Both canonical targets describe a single and a double interaction with the target. The last and third type describes the circular polarization that may occur at the scattering process. Hence, the Krogager formula consists in a coherent decomposition of the general scatter matrix $[S]$ into a series of three canonical scatterer, namely a sphere, a diplane and a circular dipole (helix) either with a left or right-handed circulation. In order to split the scattering matrix $[S]$ into these three scatterer types the Sinclair matrix $[S]$ is rewritten as follows:

$$[S] \;=\; \begin{bmatrix} a+b & c \\ \\ c & a-b \end{bmatrix} \tag{6.1}$$

According to the three Pauli Spin matrices, (6.1) is decomposed as:

$$[S] \;=\; |a|\, e^{i\phi_a} \begin{bmatrix} 1 & 0 \\ 0 & 1 \end{bmatrix} \;+\; |b|\, e^{i\phi_b} \begin{bmatrix} 1 & 0 \\ 0 & -1 \end{bmatrix} \;+\; |c|\, e^{i\phi_c} \begin{bmatrix} 0 & 1 \\ 1 & 0 \end{bmatrix} \tag{6.2}$$

The first term describes odd-bounced reflections and may be interpreted as the reflection from

a surface, sphere or corner reflector. The second term describes even-bounce reflections e.g. dihedral. Depending from its orientation around the LOS the dihedral gives contribution to the cross elements of $[S]$. For example, the last term may also be related to a reflection of a $\pi/4$ tilted dihedral. Thus, this ambiguity due to the dependence of the two last terms in (6.2) must be clarified. Their coupling is described in [43] by:

$$[S] \;=\; e^{i\phi_a} \left\{ |a| \begin{bmatrix} 1 & 0 \\ 0 & 1 \end{bmatrix} \;+\; |b|\, e^{i(\phi_b - \phi_a)} \left(\begin{bmatrix} 1 & 0 \\ 0 & -1 \end{bmatrix} \;+\; c' \begin{bmatrix} 0 & 1 \\ 1 & 0 \end{bmatrix} \right) \right\} \tag{6.3}$$

Where per definition it holds:

$$c' \;=\; \frac{|c|}{|b|}\, e^{i(\phi_c - \phi_b)} \;=\; c'_{re} \;+\; i\, c'_{im} \tag{6.4}$$

In order to recover the expressions of a diplane and helix, Krogager decomposed (6.3) in the following way:

$$\begin{aligned} [S] = e^{i\phi_a} \Bigg\{ \; |a| \begin{bmatrix} 1 & 0 \\ 0 & 1 \end{bmatrix} \quad + \quad |b|\, e^{i(\phi_b - \phi_a)} \Bigg(\begin{bmatrix} 1 - |c'_{im}| & c'_{re} \\ c'_{re} & -(1 + |c'_{im}|) \end{bmatrix} \\ + \;\; |c'_{im}| \begin{bmatrix} 1 & sgn(c'_{im})\; i \\ sgn(c'_{im})\; i & -1 \end{bmatrix} \Bigg) \Bigg\} \end{aligned} \tag{6.5}$$

The rotational direction of the helix term is given by the sign of $\Im(c')$. Finally, the general scattering matrix $[S]$ is decomposed into a coherent addition of three scatterer types which correspond to a sphere (s), a diplane (d) and a helix (h). Whereas, the single terms are weighted with their related complex coefficients k_s, k_d and k_h. Hence:

$$[S] \;=\; e^{i\phi_s} \Big\{ k_s [S]_{sphere} \;+\; e^{i\phi_r} \left[\, k_d [S]_{diplane} \;+\; k_h [S]_{helix} \,\right] \Big\} \tag{6.6}$$

The absolute reel values of the complex coefficients k_s, k_d and k_h are given by:

$$k_s \;=\; |a| \tag{6.7}$$

$$k_d \;=\; |b| \sqrt{(1 - |c'_{im}|)^2 \;+\; |c'_{re}|^2} \tag{6.8}$$

$$k_h \;=\; |b||c'_{im}| \tag{6.9}$$

The rotation of the helix is fixed by:

$$\begin{aligned} c'_{im} \;&>\; 0 \quad left - handed \\ c'_{im} \;&<\; 0 \quad right - handed \end{aligned} \tag{6.10}$$

The skip angle Θ between the normal of the polarization plane and the normal of the diplane is determined by:

$$\Theta_d \;=\; \frac{1}{2}\arctan\left(\frac{c'_{re}}{1-|c'_{im}|}\right) \tag{6.11}$$

In general, the "absolute" phase is not given and therefor the sphere is taken as reference. Substituting the phase terms in (6.5) with the relative phase θ_r, given by :

$$\theta_r \;=\; \begin{cases} \theta_r \;=\; 0 & , \quad a \;=\; 0 \\ \theta_r \;=\; \theta_c \;-\; \theta_a & , \quad b \;=\; 0 \\ \theta_r \;=\; \theta_b \;-\; \theta_a & , \quad else \end{cases} \tag{6.12}$$

Finally, it follows:

$$[S] \;=\; k_s[S]_{sphere} \;+\; e^{i\phi_r}\,[\,k_d[S]_{diplane} \;+\; k_h[S]_{helix}\,] \tag{6.13}$$

The scattering mechanisms of the three terms are summarized as :

- **Sphere**
  The odd interactions at the scattering process.

- **Diplane**
  The even interactions at the scattering process..

- **Helix**
  This term demonstrate the capability of the target to transform a incident linear polarized wave into a circular polarized wave.

A priori, the coefficients k_s, k_d and k_h are given with the Huynen parameters as:

$$k_s \;=\; \sqrt{2A_0} \tag{6.14}$$

$$k_d \;=\; \sqrt{2(B_0-|F|)} \tag{6.15}$$

$$k_h \;=\; \frac{2F}{\sqrt{B_0+B}} \tag{6.16}$$

For sphere-cylinder model considered here no cross elements are given in $[S]$. Hence, the helix coefficient k_h is equal to zero.

Results after the Krogager Theorem

The Krogager decomposition of the scattering matrix $[S]$, measured in the anechoic chamber, is presented and discussed next. The coefficients k_s and k_d over the look angles is shown in the fig. 6.1 to 6.4 according to the heights 5.0cm, 7.5cm, 10.0cm and 15.0cm. From the Krogager decomposition, it follows that the scattering matrix correspond at the transition zones more to a sphere. The waves related to the shadow boundary are strongly attenuated at the transition zones, so that the reflection contribution of the sphere becomes more significant. According to the strong edge diffraction, look angles below 14° should not be considered in the data set, see table (4.1).

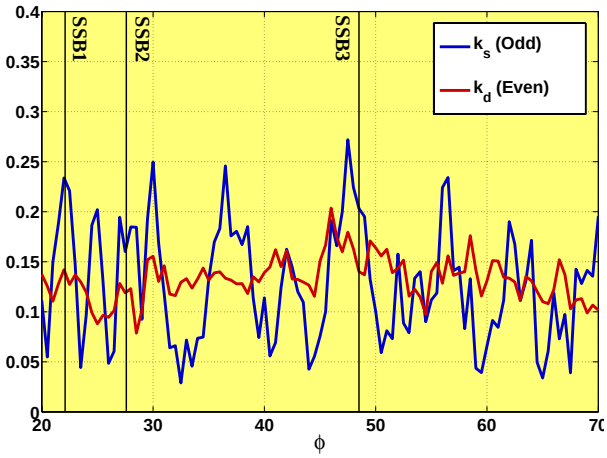

Figure 6.1: EMSL: $h = 5.0cm$, $f = 6.7GHz$

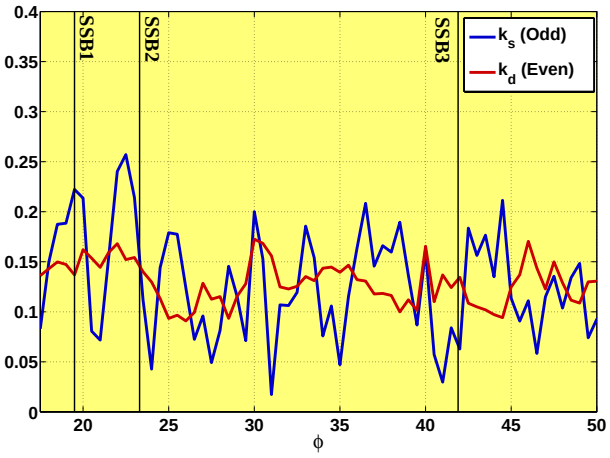

Figure 6.2: EMSL: $h = 7.5cm$, $f = 6.7GHz$

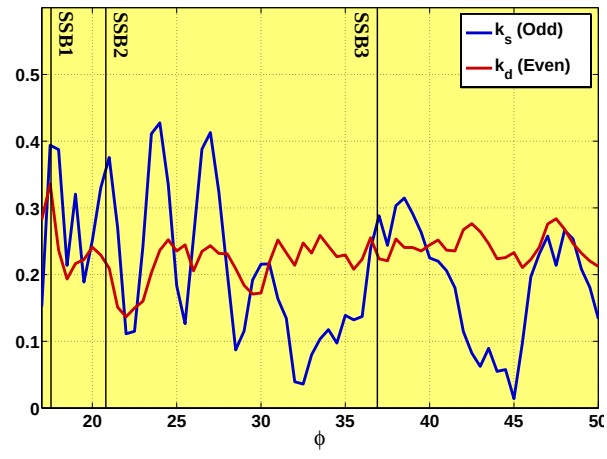

Figure 6.3: EMSL: $h = 10.0cm$, $f = 6.7GHz$

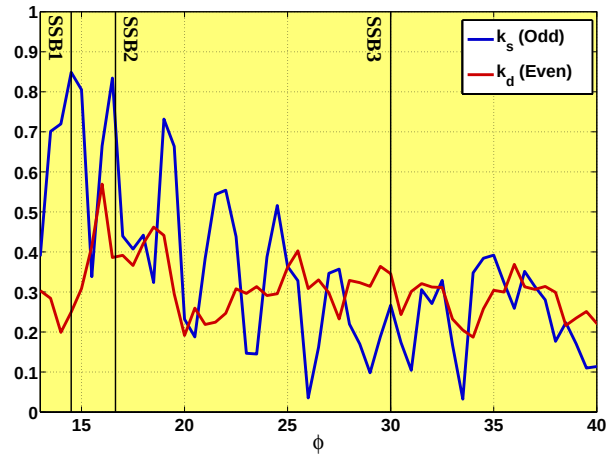

Figure 6.4: EMSL: $h = 15.0cm$, $f = 6.7GHz$

6.2 Cameron Decomposition

6.2.1 Reciprocity Angle

Generally, every quadratic scattering matrix e.g. $[S]$ can be decomposed in a coherent sum of a symmetric and asymmetric matrix. It holds [67]:

$$[S] \;=\; [S]_{Sym.} \;+\; [S]_{Asym.} \tag{6.17}$$

Where the symmetric component $[S]_{Sym.}$ obeys the principle of reciprocity. The appearance of an asymmetric term violating the reciprocity rule is due to non-linear interactions of the field with the target, propagation effects or incoherent superposition of waves. Both matrices are given by:

$$[S]_{Sym.} \;=\; \frac{1}{2}\left([S] \;+\; [S]^T\right) \tag{6.18}$$

$$[S]_{Asym.} \;=\; \frac{1}{2}\left([S] \;-\; [S]^T\right) \tag{6.19}$$

In the work of Cameron [11] a vector representation is introduce as follows:

$$\vec{S}_{Sym.} \;=\; [P_{Sym.}]\,\vec{S} \tag{6.20}$$

$$\vec{S}_{Asym.} \;=\; ([I] \;-\; [P_{Sym.}])\,\vec{S} \tag{6.21}$$

Where the operator $P_{Sym.}$ is defined as:

$$[P_{sym.}] = \begin{bmatrix} 1 & 0 & 0 & 0 \\ 0 & \frac{1}{2} & \frac{1}{2} & 0 \\ 0 & \frac{1}{2} & \frac{1}{2} & 0 \\ 0 & 0 & 0 & 1 \end{bmatrix} \tag{6.22}$$

The two matrices $[S]_{Sym.}$ and $[S]_{Asym}$ describe two subspaces in the C^4 space. Their basis are perpendicular to each other as the inner product is equal to zero. Hence:

$$\left\langle \vec{S}_{Sym}, \vec{S}_{Asym} \right\rangle \;=\; 0 \tag{6.23}$$

The "degree of reciprocity" of a measured scattering matrix $[S]$ is related through the rotation angle Θ_{rec} between the matrix $[S]$ and its symmetric part $[S_{Sym}]$. For an absolute symmetric scattering matrix it follows $\Theta_{rec} = 0$ as no rotation is present. The reciprocity angle Θ_{rec} is defined by:

$$\cos(\Theta_{rec}) \;=\; \frac{\left\langle \vec{S}, \vec{S}_{Sym.} \right\rangle}{\|\vec{S}\|\,\|\vec{S}_{Sym.}\|} \;=\; \frac{\vec{S} \cdot \vec{S}^*_{Sym.}}{\|\vec{S}\|\,\|\vec{S}_{Sym.}\|} \tag{6.24}$$

The magnitude of the measured scattering matrix $[S]$ is normalized $\hat{S}$ and according to (6.20),

the angle Θ_{rec} is calculated by:

$$\cos(\Theta_{rec}) \;=\; \| \, [P_{sym.}] \, \hat{S}_{sym} \| \tag{6.25}$$

Where the range of the reciprocity angle Θ_{rec} is given by

$$0 \leq \cos(\Theta_{rec}) \leq \frac{\pi}{2} \, , \tag{6.26}$$

varying from an absolute reciprocal scatterer to a non reciprocal scatterer.

6.2.2 Target Symmetry

For the given case where a measured scattering matrix $[S]$ is subject to reciprocity, the notation $[S]_{rec}$ is used. According to Cameron a scattering matrix $[S]_{rec}$ can be decomposed into components which correspond to the symmetric and asymmetric properties of the target. Here, the angle τ describes the deviation of the matrix from an absolute symmetric matrix $[S]_{sym}$. The angle τ is given through the operator $[D]$ as follows:

$$\cos(\tau) \;=\; \left| \frac{\left(\vec{S}_{sym}, \; [D] \, \vec{S}_{sym} \right)}{|| \; \vec{S}_{sym} \; || \;\; || \; [D] \, \vec{S}_{sym} \; ||} \right| \tag{6.27}$$

6.2.3 Match Angle

In order to classify the target in different scatterer types, the measured matrix $[S]_{rec}$ is tested with canonical scattering matrices $[S_t]$. The deviation angle Θ_t is given here by:

$$\cos(\Theta_t) \;=\; \left| \frac{\left(\vec{S}_{rec}, \; \vec{S}_t \right)}{|| \; \vec{S}_{rec} \; ||} \right| \tag{6.28}$$

Cameron took different canonical scatterer for the test procedure. The corresponding test matrices are listed below:

$$Sphere = \frac{1}{\sqrt{2}}\begin{bmatrix} 1 & 0 \\ 0 & 1 \end{bmatrix} \qquad Diplane = \frac{1}{\sqrt{2}}\begin{bmatrix} 1 & 0 \\ 0 & -1 \end{bmatrix}$$

$$Dipole = \begin{bmatrix} 1 & 0 \\ 0 & 0 \end{bmatrix} \qquad Cylinder = \frac{1}{\sqrt{5}}\begin{bmatrix} 2 & 0 \\ 0 & 1 \end{bmatrix}$$

$$Narrow\ Diplane = \frac{1}{\sqrt{5}}\begin{bmatrix} 2 & 0 \\ 0 & -1 \end{bmatrix} \qquad \frac{1}{4}\,Wave\ Device = \frac{1}{\sqrt{2}}\begin{bmatrix} 1 & 0 \\ 0 & j \end{bmatrix}$$

$$Helix_{(HL)} = \frac{1}{2}\begin{bmatrix} 1 & j \\ j & -1 \end{bmatrix} \qquad Helix_{(HR)} = \frac{1}{2}\begin{bmatrix} 1 & -j \\ -j & -1 \end{bmatrix}$$

6.2.4 Results after the Cameron Theorem

According to the theorem of Cameron, the measured scattering matrices were tested with a diplane, dipole and cylinder. It can be assumed that the polarimetric behavior of the cylinder class after Cameron is similarly to the one corresponding to a sphere. The two matrices are in the same equivalence class if for the match scatter angle it holds $\theta_t = 0°$. A mismatch is present if both are orthogonal $\theta_t = 90°$. The match angle θ_t is presented in the fig. 6.5 to fig. 6.8 for the different measured heights from the plate. After the Cameron theorem, the scattering matrix at the transition zones corresponds a dipole and cylinder.

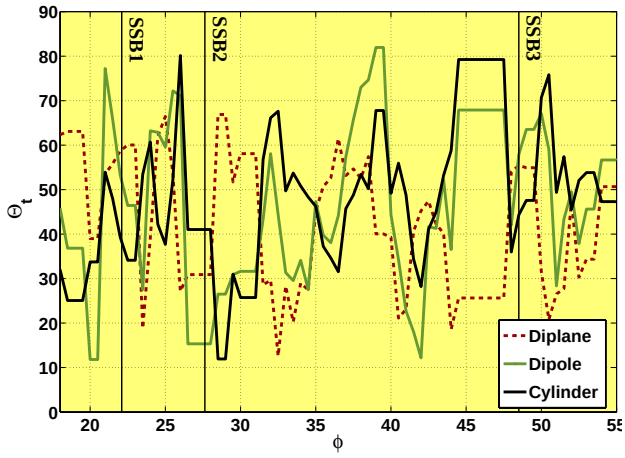

Figure 6.5: EMSL
$h = 5.0cm,\ \ f = 6.7GHz$

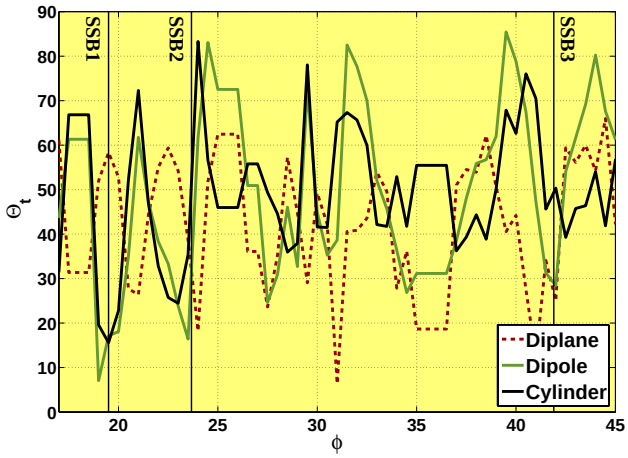

Figure 6.6: EMSL
$h = 7.5cm,\ \ f = 6.7GHz$

The match angle in contrast for a diplane has its maximum values at such shadow boundaries.

According to the UTD ray system this polarimetric behavior is explained as follows: The superposition of the odd bounced wave 3, 8 and 11, 12 is done in a incoherent way as the look angle varies. This is due to the fact that the single ray paths don't change linearly with the look angle variation.

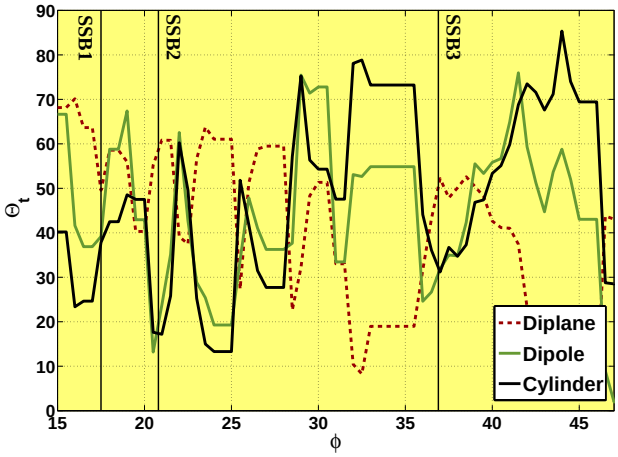

Figure 6.7: EMSL
$h = 10.0cm, \quad f = 6.7GHz$

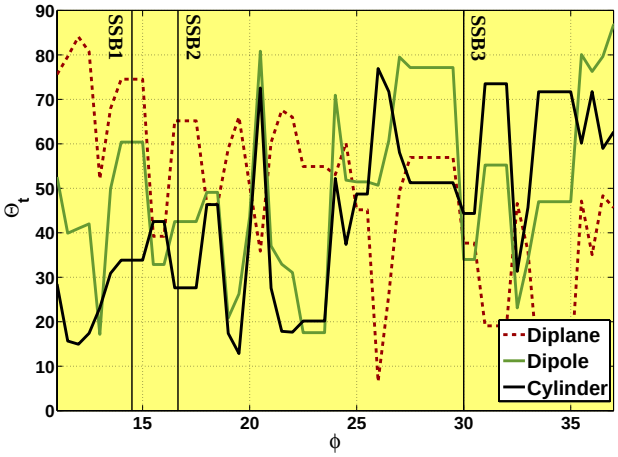

Figure 6.8: EMSL
$h = 15.0cm, \quad f = 6.7GHz$

Hence, the reflected field represents a sum of many scattering centers leading to a incoherent superposition. In such transition zones the odd bounced wave 3, 8 and 11, are strong attenuated and replaced by creeping waves in the shadow region. So, due the strong attenuation of the odd bounced wave, the contribution of the direct reflected wave 1 becomes more important. Nevertheless, the results show that the projection onto subspaces is very sensitive for a varying look angle leading to a fast up and down of the match angles.

CHAPTER 7

Incoherent Decomposition Theorems

After discussing the decomposition of the voltage matrix $[S]$ for deterministic targets, two decomposition methods based on power measurements for incoherent scattering mechanisms will be described in the following. In RADAR polarimetry, the first scattering matrices considered in the power domain were the Müller matrix $[M]$ used in the the forward scatter alignment (FSA) convention and the Kennaugh matrix $[K]$ for the back scatter alignment (BSA) convention. The trace or span of the Kennaugh matrix expresses the total power, whereas the span of the Müller matrix does not. Alternative matrices in the power domain that have been introduced in the last two decades are the covariance matrix $[C]$ and the coherency matrix $[T]$. Both matrices are generated by a inner product of the so-called target vector. Here, the target vector is a general vectorization of the scattering matrix $[S]$. In the case of the coherency matrix $[T]$, the Pauli spin elements are used for the vectorization. The covariance matrix $[C]$ is convenient in the RADAR engineering sector due to the fact that its diagonal elements express the total power of the corresponding channel.

The first attempt in RADAR polarimetry to extract physical insight of the scattering process using measurements in the power domain was reported in the innovative work of Huynen [35]. His empirical decomposition of the Müller matrix $[M]$ is based on the interpretation of polarimetric data sets acquired from several canonical targets. Hence, Huynen's decomposition was made up in an empirical approach. Starting from his measurements, Huynen postulated to decompose the entire scattering process, described by the operator $[M]$, into a sum of simpler canonical scattering mechanism. By decomposing the Müller matrix $[M]$ in this way, it is possible to get information about the properties of the target itself.

Finally, a eigenvalue based decomposition of $[M]$ introduced by Cloude and Pottier [18] is briefly presented. The polarimetric entropy H and the target scattering parameter α, calculated by this method are discussed.

7.1 Graves Matrix [G]

An alternative to the 4×4 Müller matrix $[M]$ for describing the backscattered power from a target is represented by the 2×2 Graves power matrix $[G]$ [25]. It will be useful to deal with the Huynen parameters. A detailed investigation of it is done in the work of Pottier [53] and Krogager [43]. Using the the Graves matrix the backscattered power is given by [45]:

$$P_s \;=\; \frac{1}{8\pi Z_0 R^2}\, \vec{E}_i^{*}[G]\vec{E}_i \tag{7.1}$$

Where the quantity R indicates the distance between the target and the antenna. Expression (7.1) is valid in the far field approximation. The Graves matrix $[G]$ is defined as:

$$[G] \;=\; [S]^{*}\,[S] \tag{7.2}$$

The elements of the main diagonal of $[G]$ are reel and the cross elements are complex quantities, according to:

$$[G] = \begin{bmatrix} G_{11} & G_{12} \\ G_{21} & G_{22} \end{bmatrix} = \begin{bmatrix} |S_{11}|^2 \;+\; |S_{12}|^2 & S_{11}^{*}S_{12} \;+\; S_{12}^{*}S_{22} \\ S_{11}S_{12}^{*} \;+\; S_{12}S_{22}^{*} & |S_{12}|^2 \;+\; |S_{22}|^2 \end{bmatrix} \tag{7.3}$$

The Graves matrix $[G]$ fulfills the condition $[G] = [G]^{T^{*}}$, thus $[G]$ is hermitian and the three following properties are valid:

- The eigenvalues of $[G]$ are real numbers
- The eigenvectors of $[G]$ define an orthogonal vector space
- The normalized eigenvectors of $[G]$ can be used to define a unitary transformation matrix $[U]$

The last point implies that the rows of the unitary transformation matrix $[U]$ may be generated by means of the normalized eigenvectors of $[G]$. The eigenvector analysis of $[G]$ implies that:

$$[G]\vec{e}_i \;=\; \Lambda_i\vec{e}_i \tag{7.4}$$

$$[\,[G] - \Lambda_i[I]\,]\,\vec{e}_i \;=\; \vec{0} \tag{7.5}$$

The solution of the eigenvalue problem is immediately given by the condition $Det(\,[G]-\Lambda_i[I]\,) = 0$, where $[I]$ is the unit matrix. It follows the eigenvalues in the form:

$$\Lambda_{1,2} \;=\; \frac{Tr[G] \pm \sqrt{Tr([G])^2 \;-\; 4Det([G])}}{2} \tag{7.6}$$

The corresponding eigenvectors $\vec{e}_i \;=\; (x_i, y_i)$ are obtained by substituting the solutions of (7.6)

in (7.5). Setting the component x_i of the eigenvector $\vec{e}_i$ equal to 1, it turns out:

$$x_i \;=\; 1, \quad y_i \;=\; \frac{\Lambda_i - G_{11}}{G_{12}} \tag{7.7}$$

Hence, the normalized eigenvectors $\vec{e}_{1,2}$ are defined by:

$$\begin{aligned} \vec{e}_{1,2} &= \frac{|G_{12}|}{\sqrt{|G_{12}| \;+\; |\Lambda_{1,2} - G_{12}|^2}} \begin{bmatrix} 1 \\ \frac{\Lambda_{1,2}-G_{11}}{G_{12}} \end{bmatrix} \\ \vec{e}_{1,2} &= \frac{1}{\sqrt{1 \;+\; |\rho_{1,2}|^2}} \begin{bmatrix} 1 \\ \rho_{1,2} \end{bmatrix} \end{aligned} \tag{7.8}$$

Where $\rho_{1,2} \;=\; \frac{\Lambda_{1,2}-G_{11}}{G_{12}}$ has been set. The special case where the determinant of $[G]$ is equal to zero is presented next.

Non Deterministic Case Det[G] = 0
From (7.3) it follows that:

$$S_{11}^* S_{12} \;+\; S_{12}^* S_{22} \;=\; 0 \tag{7.9}$$

and the eigenvalues and the eigenvectors cannot be uniquely determined anymore. Two relevant cases have to be considered, discussed next.

1. $\mathbf{S_{12} \neq 0}$

The characteristic polynomial of the eigenvalue problem reduces to:

$$\Lambda_i(\Lambda_i - Tr[G]) \;=\; 0 \tag{7.10}$$

The first trivial solution $\Lambda_1 = 0$ leads to the zero vector as eigenvector. Considering the second, non trivial solution $\Lambda_2 = Tr[G]$, one rewrites the condition in (7.9) for the non deterministic case in the following manner:

$$|S_{12}| \left[|S_{11}| e^{i(\phi_{12} - \phi_{11})} \;+\; |S_{22}| e^{i(\phi_{22} - \phi_{12})} \right] \;=\; 0 \tag{7.11}$$

Since $S_{12} \neq 0$ is assumed here, it follows from (7.11) that the sum of the two terms in the bracket must equal to zero. Hence, it results for the magnitude and phase difference of the complex sum:

$$|S_{11}| \;=\; |S_{22}| \tag{7.12}$$

$$\phi_{22} - \phi_{11} \;=\; (2n-1)\pi \tag{7.13}$$

Considering (7.10) this means that the trace of $[G]$ can be expressed either by S_{11} or S_{22}. Both complex quantities have the same magnitude but differ in the phase by π. Therefore, the second eigenvalue Λ_2 related to the non-trivial solution can now be expressed in two ways fitting (7.10):

$$\Lambda_{2a} = 2(|S_{11}|^2 + |S_{12}|^2) \tag{7.14}$$

$$\Lambda_{2b} = 2(|S_{22}|^2 + |S_{12}|^2) \tag{7.15}$$

Expression (7.10) may be rewritten as follows [53]:

$$\left[S_0 - \sqrt{Tr(G)}\right] \left[S_0 + \sqrt{Tr(G)}\right] = 0, \tag{7.16}$$

Where S_0 is set equal to $\sqrt{\Lambda_2}$. According to the solution Λ_2 only the eigenvector

$$\vec{e}_2 = \begin{pmatrix} e_{21} \\ e_{22} \end{pmatrix}$$

is clearly determined. In addition the eigenvalue must verify the condition $[S]\vec{e}_2 = S_0\vec{e}_2^*$.
It turns out:

$$e_{21} = \in \mathbb{C} \tag{7.17}$$

$$e_{22} = \frac{S_0\, e_{11}^* - S_{11}\, e_{11}}{S_{12}} \tag{7.18}$$

Choosing $e_{21} = 1$ it follows from (7.8) for the second component:

$$\rho = \frac{\sqrt{\Lambda_0}e^{i\Theta} - S_{11}}{S_{12}}, \tag{7.19}$$

Where the range of Θ is given by $[0, 2\pi]$. The second eigenvector $\vec{e}_1$ is performed through the unitary condition $\vec{e}_1^{\,T*} \cdot \vec{e}_2 = 0$.

2. $S_{12} = 0$

Here the cross elements of the Graves matrix $[G]$ are equal to zero $G_{12} = G_{21} = 0$ and reduces to:

$$[G] = \begin{bmatrix} G_{11} & 0 \\ 0 & G_{22} \end{bmatrix} = \begin{bmatrix} |S_{11}|^2 & 0 \\ 0 & |S_{22}|^2 \end{bmatrix} \tag{7.20}$$

This degenerated case provides immediately the eigenvalues $\Lambda_1 = |S_{11}|^2$ and $\Lambda_2 = |S_{22}|^2$. In view of getting the diagonal scattering matrix $[S]_D$ ordered by $|S_{11}| > |S_{22}|$ the unitary matrix are defined as follow [53]:

$$|S_{11}| > |S_{22} \implies [U] = \begin{bmatrix} 1 & 0 \\ 0 & 1 \end{bmatrix} \tag{7.21}$$

$$|S_{11}| < |S_{22} \implies [U] = \begin{bmatrix} 0 & 1 \\ 1 & 0 \end{bmatrix} \tag{7.22}$$

Diagonalization of the Graves matrix [G]

The hermitian matrix $[G]$ is diagonalized via the 2×2 unitary transformation matrix $[U]$ by:

$$[G_D] \;=\; [U]^{*T}[G][U] \tag{7.23}$$

Where the normalized eigenvectors of $[G]$ represent the two rows of $[U]$ and $[U]^{*T}[U] \;=\; [I]$. Further, the diagonal form of $[G]$ is also given by the the scattering matrix $[S]$ as follows:

$$[G_D] \;=\; [S_D]^* \, [S_D] \tag{7.24}$$

and the diagonal of $[G_D]$ are the eigenvalues of $[G]$:

$$[G_D] \;=\; \begin{bmatrix} \Lambda_1 & 0 \\ 0 & \Lambda_2 \end{bmatrix} \tag{7.25}$$

Next the diagonalization of $[S]$ by the unitary matrix $[U]$ is discussed. The general diagonalization procedure of $[S]$ is given by:

$$[S_D] \;=\; [A]^{-1}[S][A] \tag{7.26}$$

Comparing (7.23) and (7.24) it follows for the substitution $[A] = [U]$ in 7.26 the relation:

$$[A]^{-1} \;=\; [U]^T \tag{7.27}$$

Hence, $[S_D]$ is expressed in terms of the unitary matrix $[U]$ as follows:

$$[S_D] \;=\; [U]^T[S][U] \tag{7.28}$$

The unitary matrix $[U]$ defined by the eigenvectors of [G] will be used in the following section for calculating $[S_D]$. For the sake of completeness the unitary matrix $[U]$ is defined by the eigenvectors (7.8) in the following manner:

$$[U] \;=\; \frac{1}{\sqrt{1 \,+\, |\rho|^2}} \begin{bmatrix} 1 & -\rho^* \\ \rho & 1 \end{bmatrix} \tag{7.29}$$

In the latter ρ is substituted by $\rho = |\rho| e^{i\phi} \in \mathbb{C}$. The eigenvectors of $[G]$ do not change their direction in space with a change of basis. Only their length will be multiplied with the corresponding eigenvalues. The maximum possible backscattered power will be received, if the eigenvectors are taken as polarization state for the antenna in the BSA convention. Therefore, this polarization is called the "co-polarization maximum". For its orthogonal polarization, the minimal power will be received. It is therefore called the "xpoll zero polarization" (cp. optical polarization filters).

7.2 Huynen's Target Decomposition

Next, the Müller matrix $[M]$ is expressed in terms of the elements S_{ij} of the scattering matrix $[S]$, by introducing the coherency vector $\vec{J} = \vec{E} \otimes \vec{E}^*$. Where $\otimes$ indicates the Kronecker product and $\langle \cdots \rangle$ the time averaging of the power measurement. It holds [6]:

$$[M] \;=\; \Big\langle [A]\,([S] \otimes [S]^*)\,[A]^{-1} \Big\rangle \tag{7.30}$$

Where $[A]$ is the so-called Kronecker product matrix, given by:

$$[A] = \begin{bmatrix} 1 & 0 & 0 & 1 \\ 1 & 0 & 0 & -1 \\ 0 & 1 & 1 & 0 \\ 0 & i & -i & 0 \end{bmatrix} \qquad [A]^{-1} = \frac{1}{2} \begin{bmatrix} 1 & 1 & 0 & 0 \\ 0 & 0 & 1 & -i \\ 1 & -1 & 0 & 0 \\ 0 & i & -i & 0 \end{bmatrix} \tag{7.31}$$

Hence, the Müller matrix $[M]$ can be expressed in terms of the scattering matrix $[S]$ elements as follows:

$$[M] = \begin{bmatrix} \left\langle \frac{|S_{11}|^2+2|S_{12}|^2+|S_{22}|^2}{2} \right\rangle & \left\langle \frac{|S_{11}|^2-|S_{22}|^2}{2} \right\rangle & \left\langle \Re\left(S_{11}+S_{22}\right) S_{12}^* \right\rangle & \left\langle \Im\left(S_{22}-S_{11}\right) S_{12}^* \right\rangle \\ \left\langle \frac{|S_{11}|^2-|S_{22}|^2}{2} \right\rangle & \left\langle \frac{|S_{11}|^2-2|S_{12}|^2+|S_{22}|^2}{2} \right\rangle & \left\langle \Re\left(S_{11}-S_{22}\right) S_{12}^* \right\rangle & \left\langle -\Im\left(S_{11}+S_{22}\right) S_{12}^* \right\rangle \\ \left\langle \Re\left(S_{11}+S_{22}\right) S_{12}^* \right\rangle & \left\langle \Re\left(S_{11}-S_{22}\right) S_{12}^* \right\rangle & \left\langle |S_{12}|^2 + \Re\left(S_{11} S_{22}^*\right) \right\rangle & \left\langle -\Im\left(S_{11} S_{22}\right) \right\rangle \\ \left\langle \Im\left(S_{22}-S_{11}\right) S_{12}^* \right\rangle & \left\langle -\Im\left(S_{11}+S_{22}\right) S_{12}^* \right\rangle & \left\langle -\Im\left(S_{11} S_{22}\right) \right\rangle & \left\langle |S_{12}|^2 - \Re(S_{11} S_{22}^*) \right\rangle \end{bmatrix} \tag{7.32}$$

Huynen's Dichotomy

In his work of 1970 Huynen renamed the elements of the Müller matrix as follows:

$$[M] = \begin{bmatrix} A_0 + B_0 & C & H & F \\ C & A_0 + B & E & G \\ H & E & A_0 - B & D \\ F & G & D & -A_0 + B_0 \end{bmatrix} \tag{7.33}$$

As $[M]$ is subject to the associative law, it can be decomposed into a series of single matrices. The reason for decomposing the operator $[M]$ here, is to find simpler scattering mechanisms in form of submatrices which give more physical insight on the single mechanisms of the entire scattering process. The Huynen decomposition of the Müller matrix is based on the assumption that a partially polarized wave can be split in two well separated parts, namely in a totally polarized wave and in one which is totally unpolarized. This is known as "Dichotomy" and led Huynen to the search of a particular matrix N representing target fluctuation to be extracted from the Müller matrix $[M]$. The remaining matrix M_S represents a fixed target and is directly associated to the geometrical symmetry of the scatterer. The unpolarized part results from the asymmetric shape of the object and is rotational independent. The different reflection points on the asymmetric shape lead to an incoherent superposition of the different reflected waves. The Huynen's dichotomy is pointed out in fig. 7.1.

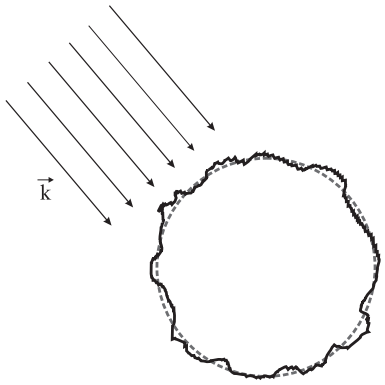

Figure 7.1: Scattering of an object

According to the dichotomy, the matrix $[M]$ is separated into the submatrix $[M_S]$ and $[N]$, where the term $[M_S]$ is related to the symmetrical properties of the target and $[N]$ can be interpreted as a disturbance term of the symmetry. Thus, the Huynen decomposition of the Müller matrix $[M]$ yields:

$$[M] = [M_S] + [N] \tag{7.34}$$

Not all of the 9 Huynen parameters contribute to the asymmetric perturbation term $[N]$. Indeed, after [53] it holds:

$$[M] = \begin{bmatrix} A_0 + B_0^S & C & H & F^S \\ C & A_0 + B^S & E^S & G \\ H & E^S & A_0 - B^S & D \\ F^S & G & D & -A_0 + B_0^S \end{bmatrix} + \begin{bmatrix} B_0^N & 0 & 0 & F^N \\ 0 & B^N & E^N & 0 \\ 0 & E^N & -B^N & 0 \\ F^N & 0 & 0 & B_0^N \end{bmatrix} \quad (7.35)$$

7.2.1 Huynen-Euler Parameters

According to Huynen the physical meaning of the Euler parameters is given by:

- **m** $(m \geq 0)$
  The parameter m denotes the maximal receivable power from the target for the optimum polarization and related to the largest eigenvalue of the scattering matrix $[S]$.

- γ $(0° \leq 45°)$
  The parameter γ corresponds to canonical scattering mechanism and was denoted by Huynen as characteristic angle. Objects with an angle $\gamma = 45°$ have no influence on the polarization of the incident field. In contrast, for a given angle $\gamma = 0°$, the polarization of the scattered wave is completely defined by the object [33].

- ν $(-45° \leq 45°)$
  Rewriting eqn.(10.15) in the Ph.D. of Huynen [35] with the notation λ for the eigenvalues in the following way:

$$\begin{aligned} \lambda_1 &= 1 \\ \lambda_2 &= \tan^2 \gamma \; e^{-i\,4\nu}, \end{aligned}$$

  The quantity 4ν describes the phase difference between the two eigenvalues λ_1 and λ_2. Considering odd bounced reflections a small amplitude A_0 may be given where $\nu = 0°$. Superposing a single double bounced wave with an amplitude A_{DB} which is much greater than A_0, it follows a phase difference of $\nu = \pm 45°$. Thus, ν must be interpreted very carefully and cannot be related directly to major or minor odd (e.g. sphere) and even bounced (e.g. dihedral) mechanisms.

- $\tau_{\mathbf{m}}$ $(-45° \leq 45°)$
  The parameter τ_m is related to the ellipticity for getting the optimal polarization state in order to get the maximum backscattered power from the target.

7.2.2 Numerical Implementation

The elements of the measured $[S]$ matrix were used for defining the corresponding Graves matrix $[G]$. The eigenvalues and eigenvectors analysis of $[G]$ determines the Euler parameter discussed in the previous section. For the sake of readability, the row vectors of $[U]$ are renamed as follows:

$$[U] = \begin{bmatrix} m_x & m_{x_\perp} \\ m_y & m_{y_\perp} \end{bmatrix} \quad (7.36)$$

The scattering matrix $[S]$ can be diagonalized into the matrix $[S]_D$ according to (7.28). Where the eigenvalues of $[S]_D$ are the elements λ_1 and λ_2, given by:

$$[S]_D = \begin{bmatrix} \lambda_1 & 0 \\ 0 & \lambda_2 \end{bmatrix} = \begin{bmatrix} S_{11}m_x^2 + 2S_{12}m_x m_y + S_{22}m_y^2 & 0 \\ 0 & S_{11}m_{x_\perp}^2 + 2S_{12}m_{x_\perp}m_{y_\perp} + S_{22}m_{y_\perp}^2 \end{bmatrix} \tag{7.37}$$

In the work of [35], the two eigenvalues of $[S]_D$ are related to the Euler parameter ν and γ as follows:

$$\lambda_1 = e^{i(2\nu+\xi)} \tag{7.38}$$

$$\lambda_2 = \tan\gamma^2 e^{-i(2\nu-\xi)} \tag{7.39}$$

The determinant of a matrix is given by the multiplication of its eigenvalues [10]:

$$Det([S]) = \prod_{i=1}^{n} \lambda_i \tag{7.40}$$

As a result, a simple relation between the eigenvalues of $[G]$ and $[S]$ is confirmed in the following manner:

$$Det([G]) = Det([S])\ Det([S]^*) \tag{7.41}$$

$$\Lambda_1\ \Lambda_2 = \lambda_1^2\ \lambda_2^2 \tag{7.42}$$

Considering the ratio of (7.38) and (7.39) and according to (7.42), it turns out for the Euler parameter ν and γ:

$$\frac{\lambda_1}{\lambda_2} = \sqrt{\frac{\Lambda_1}{\Lambda_2}} = \left|\frac{1}{\tan^2\gamma}\right| e^{i4\nu} \tag{7.43}$$

By rearranging the eigenvalues according to their size ($\Lambda_1 > \Lambda_2$), the Euler parameter m is given by:

$$m = \sqrt{\Lambda_1} \tag{7.44}$$

The Euler parameter τ_m can be appointed by means of the field component ratio ρ [43]:

$$\sin 2\tau_m = \frac{2\ Im(\rho)}{1\ +\ |\rho|^2} \tag{7.45}$$

7.2.3 Results after the Huynen Theorem

According to the Huynen's target decomposition the scattering matrix $[S]$ for the heights 5.0cm, 7.5cm, 10.0cm and 15.0cm is investigated in the following. The Euler-Huynen target size parameter m and the even reflection parameter ν are shown in the fig. 7.2 to 7.9. The eigenvalue analysis of the Graves matrix $[G]$ shows that for all measured heights the two principals shadow boundaries SSB1 and SSB2 lies on a local maximum of the target size parameter m. Due to the strong attenuation of the spatial waves at the transition, the contribution of the specular wave 1 is reinforced, signifying a bigger object. This polarimetric behavior is emphasized by the parameter γ at the shadow boundaries. Here, the transition regions fall together with local minimum values denoting that the scattering mechanism includes a odd number of reflections, here the direct wave 1.

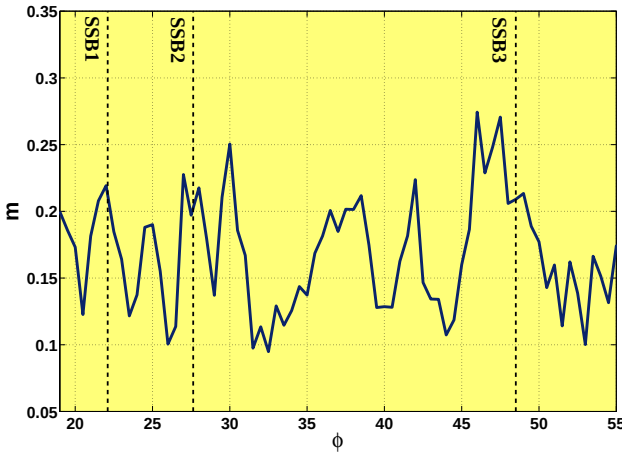

Figure 7.2: Target size parameter m:
$h = 5.0cm, \quad f = 6.7GHz$

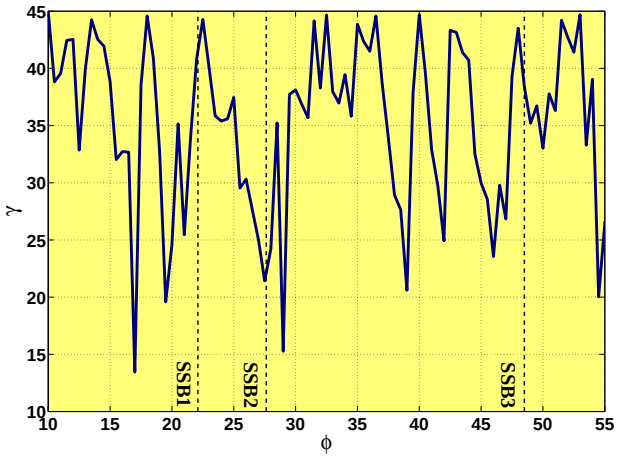

Figure 7.3: Euler parameter γ:
$h = 5.0cm, \quad f = 6.7GHz$

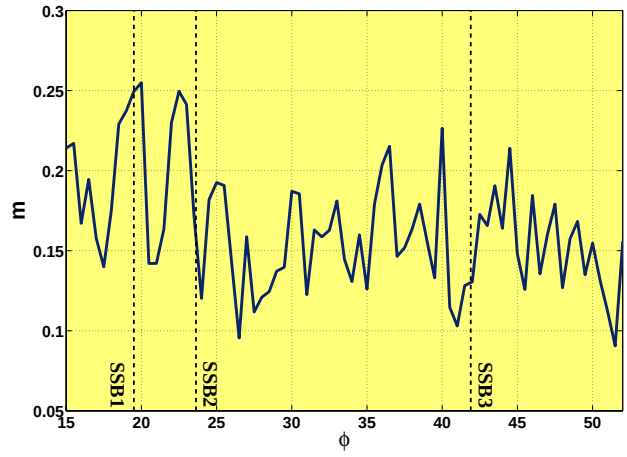

Figure 7.4: Target size parameter m:
$h = 7.5cm, \quad f = 6.7GHz$

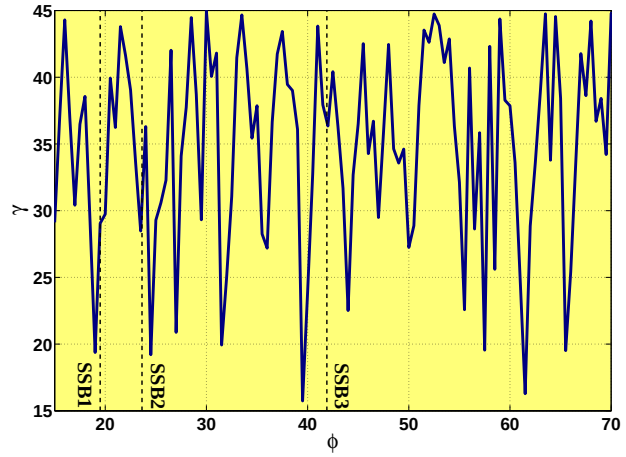

Figure 7.5: Euler parameter γ:
$h = 7.5cm, \quad f = 6.7GHz$

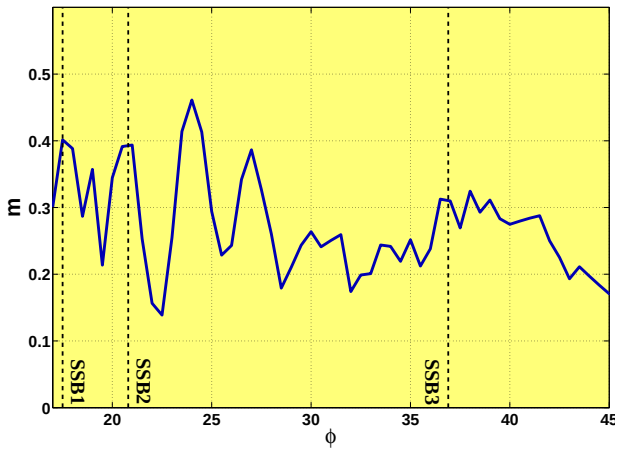

Figure 7.6: Target size parameter m:
$h = 10.0cm, \quad f = 6.7GHz$

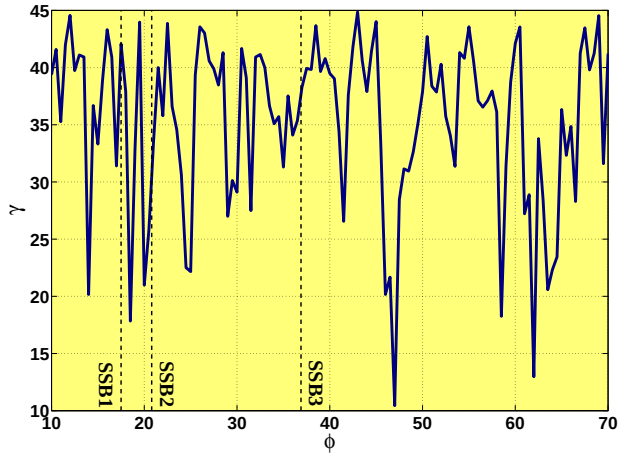

Figure 7.7: Euler parameter γ:
$h = 10.0cm, \quad f = 6.7GHz$

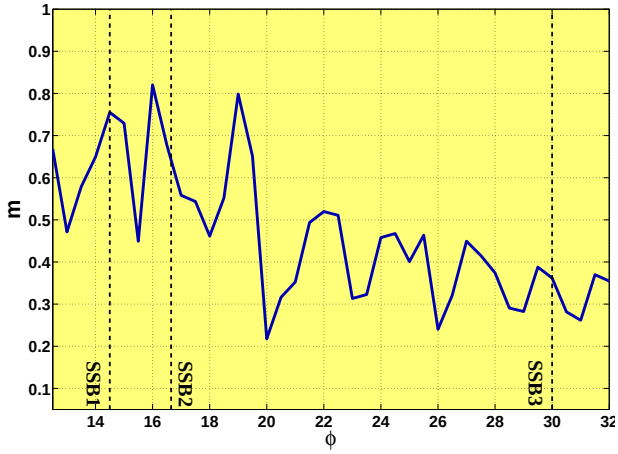

Figure 7.8: Target size parameter m:
$h = 15.0cm, \quad f = 6.7GHz$

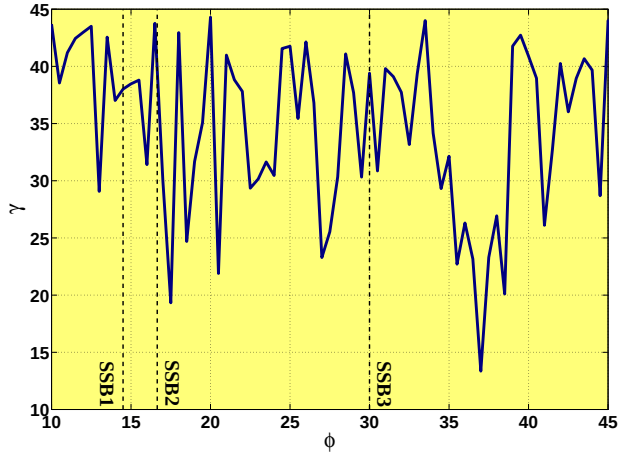

Figure 7.9: Euler parameter γ:
$h = 15.0cm, \quad f = 6.7GHz$

7.3 Eigenvalue Decomposition

The coherence matrix $\langle[T]\rangle$ and covariance matrix $\langle[C]\rangle$ based on power measurements are introduced. Both matrices $\langle[T]\rangle$ and $\langle[C]\rangle$ contain the same polarimetric information about the scattering process but have a different notation. The elements of $\langle[T]$ and $\rangle[C]$ represents power quantities and therefore describe the scattering process by a second order statistic. The emphasis is attributed in this section to the coherence matrix $\langle[T]\rangle$. Here, the eigenvalue analysis of $\langle[T]\rangle$ is carried out. According to the deterministic cylinder model without averaging, the entropy-anisotropy decomposition theorem is presented for this special case by one eigenvalue. In general, the eigenvalue based decomposition theorem has the important features:

- The eigenvalue analysis is invariant for a unitary basis transformation. It is not based on models and in consequence a quantitative data inversion is possible.
- Statistical effects (Speckle) can be better investigated. An important property for improving the Signal to Noise Ratio (SNR).
- Besides single targets, the backscattering from volumetric areas like forests or human agriculture can be better distinguished.
- The derived quantity entropy H gives a prediction about the limits of radar measurements in view of the decomposition in significant scatterer mechanisms.

7.3.1 Vectorization

The complex scattering matrix $[S]$ encloses at leat all the different scattering mechanisms. Instead of using the 2×2 matrix notation, the whole information of $[S]$ can be put in a 4×1 so-called target vector k. This vectorization, is given by:

$$\vec{k} = V([S]) \tag{7.46}$$

$$= \frac{1}{2} Tr\ ([S]\ \Psi) \tag{7.47}$$

$$= (k_0\ k_1\ k_2\ k_3)^T \tag{7.48}$$

Where the operator Ψ is a set of 2×2 complex matrices with orthogonal basis. Generally two orthogonal standard sets are used for the vectorization of $[S]$:

- Ψ_L **Lexicographic**

$$\Psi_L = \begin{bmatrix} 2 & 0 \\ 0 & 0 \end{bmatrix} \begin{bmatrix} 0 & 2 \\ 0 & 0 \end{bmatrix} \begin{bmatrix} 0 & 0 \\ 2 & 0 \end{bmatrix} \begin{bmatrix} 0 & 0 \\ 0 & 2 \end{bmatrix} \tag{7.49}$$

- Ψ_P **Pauli**

$$\Psi_P = \sqrt{2}\begin{bmatrix} 1 & 0 \\ 0 & 1 \end{bmatrix}\sqrt{2}\begin{bmatrix} 1 & 0 \\ 0 & -1 \end{bmatrix}\sqrt{2}\begin{bmatrix} 0 & 1 \\ 1 & 0 \end{bmatrix}\sqrt{2}\begin{bmatrix} 0 & -i \\ i & 0 \end{bmatrix} \tag{7.50}$$

Hence, two target vectors are given as follows:

$$\vec{k}_p = \frac{1}{\sqrt{2}}\begin{pmatrix} S_{xx}+S_{yy} \\ S_{xx}-S_{yy} \\ S_{xy}+S_{yx} \\ i(S_{xy}-S_{yx}) \end{pmatrix} \tag{7.51}$$

$$\vec{k}_L = \begin{pmatrix} S_{xx} \\ S_{xy} \\ S_{yx} \\ S_{yy} \end{pmatrix} \tag{7.52}$$

In the case of a monostatic BSA setup the scattering matrix $[S]$ is symmetric. In consequence the target vectors reduce to 3×1 vectors.

$$\vec{k}_p = \frac{1}{\sqrt{2}}\begin{pmatrix} S_{xx}+S_{yy} \\ S_{xx}-S_{yy} \\ 2S_{xy} \end{pmatrix} \tag{7.53}$$

$$\vec{k}_L = \begin{pmatrix} S_{xx} \\ \sqrt{2}S_{xy} \\ S_{yy} \end{pmatrix} \tag{7.54}$$

7.3.2 Coherency Matrix

The coherency matrix $\langle[T]\rangle$ is given by the Kronecker product $\otimes$ as follows:

$$\langle[T]\rangle = \langle\vec{k}_P \otimes \vec{k}_P^{*T}\rangle \tag{7.55}$$

In a similar manner the covariance matrix $\langle[C]\rangle$ is calculated with the target vector $\vec{k}_L$ by:

$$\langle[C]\rangle = \langle\vec{k}_L \otimes \vec{k}_L^{*T}\rangle \tag{7.56}$$

According to (7.53) and (7.54) it yields for the matrices $[T]$ and $[C]$:

$$\langle[C]\rangle = \left\langle\begin{bmatrix} |S_{xx}|^2 & \sqrt{2}S_{xx}S_{xy}^* & S_{xx}S_{yy}^* \\ \sqrt{2}S_{xy}S_{xx}^* & 2|S_{xy}|^2 & \sqrt{2}S_{xy}S_{yy}^* \\ S_{xx}^*S_{yy}) & \sqrt{2}S_{xy}^*S_{yy} & |S_{yy}|^2 \end{bmatrix}\right\rangle \tag{7.57}$$

$$\langle[T]\rangle = \frac{1}{2}\left\langle\begin{bmatrix} |S_{xx}+S_{yy}|^2 & (S_{xx}+S_{yy})(S_{xx}-S_{yy})^* & 2S_{xy}^*(S_{xx}+S_{yy}) \\ (S_{xx}+S_{yy})^*(S_{xx}-S_{yy}) & |S_{xx}-S_{yy}|^2 & 2S_{xy}^*(S_{xx}-S_{yy}) \\ 2S_{xy}(S_{xx}+S_{yy})^* & 2S_{xy}(S_{xx}-S_{yy})^* & 4|S_{xy}|^2 \end{bmatrix}\right\rangle \tag{7.58}$$

In the diagonal of $\langle[C]\rangle$ appears exclusively the square of the horizontal xx and vertical yy components representing the power of the channels. Whereas in $[T]$ mixed terms are given. Due to latter $\langle[C]\rangle$ is preferred in radar engineering, where $\langle[T]\rangle$ is generally considered in the Radar

polarimetry community. The coherency matrix $\langle[T]\rangle$ is given in terms of the Huynen parameters [53] [55]:

$$\langle[T]\rangle = \begin{bmatrix} 2A_0 & C-iD & H+iG \\ C+iD & B_0+B & E+iF \\ H-iG & E-iF & B_0-B \end{bmatrix} \tag{7.59}$$

Refereing to (7.58) or (7.59) it follows that $\langle[T]\rangle$ is hermitian. This property involves the following important features:

- **Diagonalisable**
  The coherence matrix $\langle[T]\rangle$ can by means of its eigenvalues always be diagonalized by:

$$[T_D] = \begin{bmatrix} \lambda_1 & 0 & 0 \\ 0 & \lambda_2 & 0 \\ 0 & 0 & \lambda_3 \end{bmatrix} = [U_3]^{*T} \langle[T]\rangle [U_3] \tag{7.60}$$

  The unitary transformation matrix U is given by [18]:

$$[U_3] = \begin{bmatrix} \cos(\alpha_1) & \cos(\alpha_2) & \cos(\alpha_3) \\ \sin(\alpha_1)\cos(\beta_1)e^{i\delta_1} & \sin(\alpha_2)\cos(\beta_2)e^{i\delta_2} & \sin(\alpha_3)\cos(\beta_3)e^{i\delta_3} \\ \sin(\alpha_1)\cos(\beta_1)e^{i\gamma_1} & \sin(\alpha_2)\cos(\beta_2)e^{i\gamma_2} & \sin(\alpha_3)\cos(\beta_3)e^{i\gamma_3} \end{bmatrix} \tag{7.61}$$

- **Decomposition**
  A regular hermitian matrix has the property $[U_3]^{*T}[U_3] = [I]$. In view of decomposing the coherency matrix $\langle[T]\rangle$, expression (7.60) is rewritten in the following way:

$$\langle[T]\rangle = [U_3] \begin{bmatrix} \lambda_1 & 0 & 0 \\ 0 & \lambda_2 & 0 \\ 0 & 0 & \lambda_3 \end{bmatrix} [U_3]^{*T} \tag{7.62}$$

  Hence, $\langle[T]\rangle$ can be decomposed into a series of three orthogonal sub-matrices, each weighted with its corresponding eigenvalue. Here, the row vectors of the unitary matrix $[U_3]$ represents the three complex basis. $\langle[T]\rangle$ is rewritten in terms of three linearly independent matrices $[T_1], [T_2]$ and $[T_3]$ as:

$$\langle[T]\rangle = \lambda_1 \left[\hat{e}_1\hat{e}_1^{*T}\right] + \lambda_2 \left[\hat{e}_2\hat{e}_2^{*T}\right] + \lambda_3 \left[\hat{e}_3\hat{e}_3^{*T}\right]$$

$$\langle[T]\rangle = \lambda_1 [T_1] + \lambda_2 [T_2] + \lambda_3 [T_3]$$

  With the properties:

- **Eigenvalues**
  The eigenvalues of $\langle[T]\rangle$ are reel and nonnegative.
- **Basis Invariant**
  The eigenvalues are independent of the chosen basis.

The average values of the parameter α, β, γ and δ for the entire scattering process are given by the eigenvalues. Their values change with an altering of basis contrary to the eigenvalues.

$$\begin{aligned}
\bar{\alpha} &= \frac{\alpha_1\lambda_1 + \alpha_2\lambda_2 + \alpha_3\lambda_3}{\lambda_1 + \lambda_2 + \lambda_3} \\
\bar{\beta} &= \frac{\beta_1\lambda_1 + \beta_2\lambda_2 + \beta_3\lambda_3}{\lambda_1 + \lambda_2 + \lambda_3} \\
\bar{\gamma} &= \frac{\gamma_1\lambda_1 + \gamma_2\lambda_2 + \gamma_3\lambda_3}{\lambda_1 + \lambda_2 + \lambda_3} \\
\bar{\delta} &= \frac{\delta_1\lambda_1 + \delta_2\lambda_2 + \delta_3\lambda_3}{\lambda_1 + \lambda_2 + \lambda_3}
\end{aligned}$$

The physical interpretation of the different angles is given by [18]:

- α [0° 90°]
  The parameter α_i of the eigenvector is roll invariant and describes the internal degree of freedom of the scatterer. Hence, it can be related to a type of scattering mechanism or if $\bar{\alpha}$ is considered, to an average mechanism. The range of α corresponds to: surface scattering $\alpha = 0°$, encompassing a dipole scattering $\alpha = 45°$ and moves into a double bounced scattering $\alpha = 90°$.
- β [−180° 180°]
  Represents the physical orientation of the scatterer relative to the LOS.
- γ and δ
  Referred as scatterer phase angles.

7.3.3 Entropy and α-Parameter

As discussed in the previous section, the parameter α_i is related to a type of scattering, weighted by its eigenvalue λ_i. Cloude and Pottier demonstrated that the information about scattering mechanisms is limited by the three eigenvalues. For example, if the three eigenvalues are equal, the corresponding three eigenvectors have the same importance. Hence, three deterministic scattering contributors are present and no information about a scattering type can be outlined. The scattered field includes no useful polarimetric information. This mixed up is described with the polarimetric entropy H as follows [19]:

$$H = -\sum_{i=1}^{n} P_i \log_n P_i \tag{7.63}$$

Where the relative intensity quantity P_i is given by:

$$P_i = \frac{\lambda_i}{\sum_{i=1}^{n} \lambda_i} , \tag{7.64}$$

According to the above mentioned, maximal three possible eigenvalues can be given $n = 3$. Finally, the entropy H is given as:

$$H = \frac{1}{\lambda_{tot} \ln 3} \left[-\lambda_1 \ln\left(\frac{\lambda_1}{\lambda_{tot}}\right) - \lambda_2 \ln\left(\frac{\lambda_2}{\lambda_{tot}}\right) - \lambda_3 \ln\left(\frac{\lambda_3}{\lambda_{tot}}\right) \right] \tag{7.65}$$

Here, $\log_3 A = \frac{\ln A}{\ln 3}$ and $\lambda_{tot} = \lambda_1 + \lambda_2 + \lambda_3$ was set. The average parameter $\bar{\alpha}$ is defined by:

$$\bar{\alpha} = \alpha_1 P_1 + \alpha_2 P_2 + \alpha_3 P_3 \tag{7.66}$$

7.3.4 Eigenvalue Analysis

First, the formalism for calculating the eigenvalues and the corresponding eigenvectors of $[T]$ is presented for the general case where $S_{xy}, S_{yx} \neq 0$. According to the property that $[T]$ is a hermetic matrix, one rewrites $[T]$:

$$\langle [T] \rangle = \frac{1}{2} \left\langle \begin{bmatrix} t_1 & t_4 & t_5 \\ t_4^* & t_2 & t_6 \\ t_5^* & t_6^* & t_3 \end{bmatrix} \right\rangle \tag{7.67}$$

The eigenvalue problem $det\left(\langle [T] \rangle - \lambda [I]\right) = 0$ leads to a polynomial term of order three:

$$\lambda^3 - a_2 \lambda^2 - a_1 \lambda - a_0 = 0 \tag{7.68}$$

Where the coefficients a_i are defined by:

$$\begin{aligned} a_0 &= t_1 t_2 t_3 + 2 t_4 t_5 t_6 - t_2 |t_5|^2 - t_1 |t_6|^2 - t_3 |t_4|^2 \\ a_1 &= -t_1 t_2 - t_1 t_3 - t_2 t_3 + |t_4|^2 + |t_5|^2 + |t_6|^2 \\ a_2 &= t_1 + t_2 + t_3 \end{aligned}$$

According to (7.67), the reel quantities t_1, t_2 and t_3 and the complex quantities t_4, t_5 and t_6 are given. Hence, a complex equation of the form $z^3 + a_2 z^2 + a_1 z + a_0 = 0 \;\; z \in \mathbb{C}$ must be solved. According to (3.8.2) in Abramowitz and Stegun [1], the following substitution is performed:

$$q = -\frac{1}{3} a_1 - \frac{1}{9} a_2^2 \tag{7.69}$$

Additionally one sets:

$$r \;=\; \frac{1}{6}a_1 a_2 \;+\; \frac{1}{2}a_0 \;+\; \frac{1}{27}a_2^3 \tag{7.70}$$

In order to get three possible reel eigenvalues, the irreducible case must be considered:

$$q^3 \;+\; r \leq 0 \tag{7.71}$$

As a result, the complex variables s_1 and s_2 are resumed as follows:

$$\begin{aligned} s_1 &= [r \;+\; i\sqrt{-q^3 \;-\; r^2}]^{\frac{1}{3}} \\ s_2 &= [r \;-\; i\sqrt{-q^3 \;-\; r^2}]^{\frac{1}{3}} \end{aligned}$$

The parameters S_1 and S_2 are rewritten in the form:

$$\begin{aligned} s_1 &= \sqrt{-q}\, e^{i\frac{\phi}{3}} \\ s_2 &= \sqrt{-q}\, e^{-i\frac{\phi}{3}} \end{aligned}$$

The argument of the complex quantities S_1 and S_2 is given by the following tangent:

$$\tan\phi \;=\; \frac{\sqrt{|-q^3 \;-\; r^2|}}{r} \tag{7.72}$$

The reel eigenvalues are given by [1]:

$$\begin{aligned} (s_1 \;+\; s_2) &= 2\sqrt{-q}\cos\frac{\phi}{3} \\ (s_1 \;-\; s_2) &= 2i\sqrt{-q}\sin\frac{\phi}{3} \end{aligned}$$

Finally, the three possible eigenvalues are determined by:

$$\begin{aligned} \lambda_1 &= (s_1 \;+\; s_2) \;+\; \frac{a_2}{3} \\ \lambda_2 &= -\frac{1}{2}(s_1 \;+\; s_2) \;+\; \frac{a_2}{3} \;-\; \frac{\sqrt{3}}{2}(s_1 \;-\; s_2) \\ \lambda_3 &= -\frac{1}{2}(s_1 \;+\; s_2) \;+\; \frac{a_2}{3} \;-\; \frac{\sqrt{3}}{2}(s_1 \;-\; s_2) \end{aligned}$$

The corresponding three eigenvectors are given through:

$$(\,\langle [T]\rangle \;-\; \lambda_i [I]\,)\,\vec{e}_i \;=\; \vec{0} \tag{7.73}$$

written out as follows:

$$\begin{pmatrix} t_1 - \lambda_i & t_4 & t_5 \\ t_4^* & t_2 - \lambda_i & t_6 \\ t_5^* & t_6^* & t_3 - \lambda_i \end{pmatrix} \begin{pmatrix} e_{1i} \\ e_{2i} \\ e_{3i} \end{pmatrix} = \vec{0} \tag{7.74}$$

Written out, it yields:

$$\begin{aligned} t_1 - \lambda_i e_{1i} + \quad t_4 e_{2i} \quad + \quad t_5 e_{3i} \quad &= 0 \\ t_4^* e_{1i} \quad + t_2 - \lambda_i e_{2i} + \quad t_6 e_{3i} \quad &= 0 \\ t_5^* e_{1i} \quad + \quad t_6^* e_{2i} \quad + t_3 - \lambda_i e_{3i} &= 0 \end{aligned}$$

Where the solution is given by its minors:

$$\frac{e_{1i}}{D_{e_{1i}}} = \frac{e_{2i}}{D_{e_{2i}}} = \frac{e_{3i}}{D_{e_{3i}}} = \frac{1}{D} = const. \tag{7.75}$$

According to the last row it holds for the three components:

$$\frac{e_{11}}{t_4 t_6 - a_2 t_5} = \frac{e_{21}}{-[a_1 t_6 - t_4^* t_5]} = \frac{e_{31}}{a_1 a_2 - |t_4|^2} \tag{7.76}$$

Whereas the substitutions $a_1 = t_1 - \lambda_i$ and $a_2 = t_2 - \lambda_i$ have been performed. Hence, the two components may be expressed in terms of the component e_{11} as:

$$\begin{aligned} e_{31} &= f_3 e_{11} \\ e_{21} &= f_2 e_{11} \end{aligned}$$

$$f3 = \frac{|t_4|^2 - a_1 a_2}{a_2 t_5 - t_4 t_6} \tag{7.77}$$

$$\begin{aligned} f2 &= \frac{t_4^* t_5 - a_1 t_6}{t_4 t_6 - t_5 a_2} \\ &= -\frac{1}{t_4}[a_1 + t_5 f_3] \end{aligned} \tag{7.78}$$

By setting the component e_{11} equal to 1, one gets:

$$\begin{pmatrix} e_{1i} \\ e_{2i} \\ e_{3i} \end{pmatrix} = \frac{1}{\sqrt{1 + |f_2|^2 + |f_3|^2}} \begin{pmatrix} 1 \\ f_2 \\ f_3 \end{pmatrix} \tag{7.79}$$

Further, every single row in (7.61) corresponds to one of the three normalized eigenvectors.

Comparing the eigenvectors with the row of (7.61) the appropriate parameters α, β, δ and γ are calculated as follows:

$$\begin{pmatrix} |e_{1i}| \\ |e_{2i}|e^{i\delta_i} \\ |e_{3i}|e^{i\gamma_i} \end{pmatrix} = \begin{pmatrix} \cos\alpha_i \\ \sin\alpha_i \cos\beta_i e^{i\delta_i} \\ \sin\alpha_i \cos\beta_i e^{i\gamma_i} \end{pmatrix} \tag{7.80}$$

Deterministic Targets

In the case that a deterministic and symmetrical object is measured the terms t_4, t_5 and t_6 are vanishing and the coherency matrix $\langle[T]\rangle$ is reduced to the 2×2 matrix:

$$\langle[T]\rangle = \frac{1}{2}\left\langle \begin{bmatrix} |S_{xx} + S_{yy}|^2 & (S_{xx} + S_{yy})(S_{xx} - S_{yy})^* \\ (S_{xx} + S_{yy})^*(S_{xx} - S_{yy}) & |S_{xx} - S_{yy}|^2 \end{bmatrix} \right\rangle \tag{7.81}$$

Yielding to a decomposition into two eigenvalues:

$$\langle[T]\rangle = [U_2] \begin{bmatrix} \lambda_1 & 0 \\ 0 & \lambda_2 \end{bmatrix} [U_2]^{*T} \tag{7.82}$$

In (7.81) averaging processes are present at the scatterer. If no statistical processes are given, only one single eigenvalue remains, yielding:

$$[T] = [U_2] \begin{bmatrix} \lambda_1 & 0 \\ 0 & 0 \end{bmatrix} [U_2]^{*T} \tag{7.83}$$

In consequence one single eigenvector remains, giving in the form:

$$\begin{pmatrix} |e_{1i}| \\ |e_{2i}|e^{i\delta_i} \end{pmatrix} = \begin{pmatrix} \cos\alpha_i \\ \sin\alpha_i e^{i\delta_i} \end{pmatrix} \tag{7.84}$$

7.3.5 Results after the Eigenvalue Analysis

According to the eigenvalue based decomposition only a non-zero eigenvalue occur due to the symmetry and absolute deterministic setup in the anechoic chamber ($H = 0$). The single target angle α is outlined for the different heights in fig. 7.10 to 7.13. At the transition zones SSB1 and SSB2 α lies between $15° < \alpha < 35°$, whereas α is related to a local minimum. This signifies that near the transition regions the scattering type corresponds more to an odd bounce mechanism (sphere) than to an even bounce mechanism (diplane). What is the reason for such a polarimetric behavior?

As a perfect conducting interface was taken for the measurements, the contribution of the double bounced wave 2 is the strongest one in the backscattered field. It is not affected by any shadow boundary so that its significant contribution is given over the whole look angle range φ_L for α. According to section 3.7, the superposition of the odd bounced wave 3, 8 and 11, 12 takes place in a incoherent way due to the variation of the look angle. Additionally, at the transition

region the odd bounced wave 3, 8 and 11, 12 are strong attenuated and replaced by creeping waves. Hence, at the transition zones the contribution of the odd bounced wave 1 is fortified. This behavior is reflected in a local minimum of α.

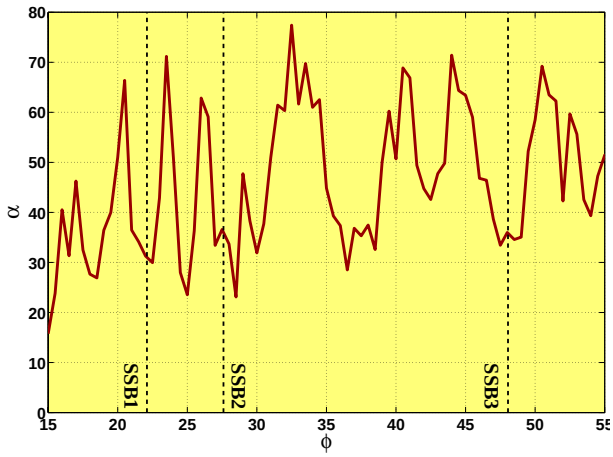

Figure 7.10: Mechanism Parameter α: $h = 5.0cm, \quad f = 6.7GHz$

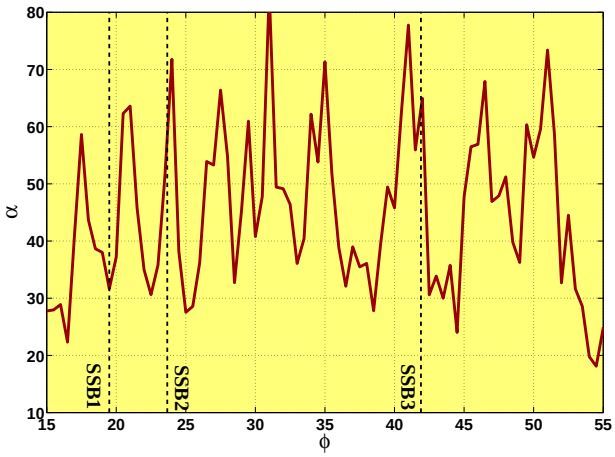

Figure 7.11: Mechanism Parameter α: $h = 7.5cm, \quad f = 6.7GHz$

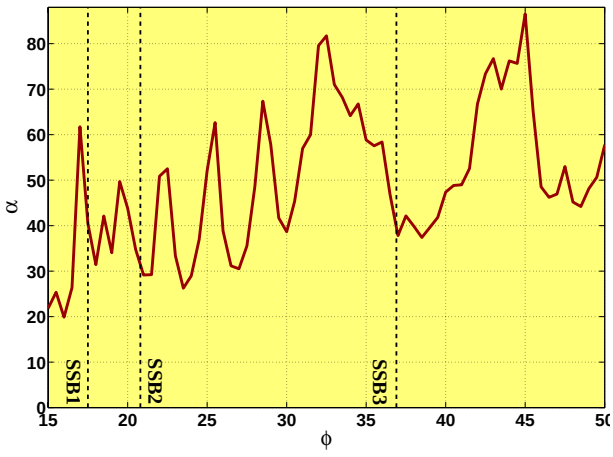

Figure 7.12: Mechanism Parameter α: $h = 10.0cm, \quad f = 6.7GHz$

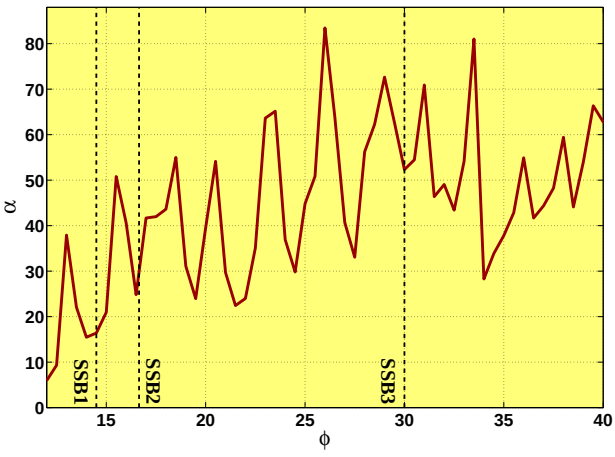

Figure 7.13: Mechanism Parameter α: $h = 15.0cm, \quad f = 6.7GHz$

Summary and Outlook

In the preceding chapters, the polarimetric behavior of the field diffracted by a target in front of the air-soil interface was investigated for an incident field varying from perpendicular to grazing incidence. The backscattered field for the monostatic alignment considered here was analyzed by the Geometrical Theory of Diffraction (GTD) or étalon method. In this work, a refined ray model was implemented where, besides the multiple reflections between the target and the interface, also creeping waves were considered giving a better understanding of the physical scattering mechanisms. For the first investigated case, where the target was situated in the air, 13 different waves were considered according to the Fermat principle. The accuracy of the implemented ray model was checked by an exact integral equation method. Here, the exact numerical method is founded on an extended Method of Moments technique. An existing algorithm calculating the scattering of an illuminated object in free space was modified for the given case where the air and the soil form a two layer media. Here, the corresponding Green dyad was modified after the Michalski method for transforming the Electric Field Integral Equation (EIFE) into the less singular Mixed Potential Integral Equation (MPIE). The related Sommerfeld integrals in the Green dyad were replaced by a more rapid and robust series according to the Discrete Complex Image method. A good agreement between the GTD ray system and the exact Method of Moments has been obtained.

In the treatment where the target was situated above the ground, a special emphasis was attributed to the transition regions. Near the shadow boundaries, the reflected spatial waves disappear and transform into creeping waves on the target which are strongly attenuated on the shadowed side. The investigations proved that the elements of the Sinclair matrix $[S]$ and the corresponding polarization state undergo a rapid variation which was visualized on the Poincaré sphere. At the shadow boundaries, the path length of the related waves are similar. Thus, the concerned waves are in phase. In consequence, the superposition of the waves in the transition regions leads to a slight depolarization of the field. Depending on the incident polarization, either linear or circular the backscattered field is situated near the equator line on Poincaré sphere representing a linear polarization, or at one pole corresponding to a circular polarization. Hence, as the shadow boundaries depend here on the geometrical properties, the angular location of the transition regions can be exploited in order to get information on the geometrical parameters. For the case where the target was embedded in the soil, no surface shadow boundaries are given. Here, on the way back from the target lateral waves are generated at the interface. As a result of

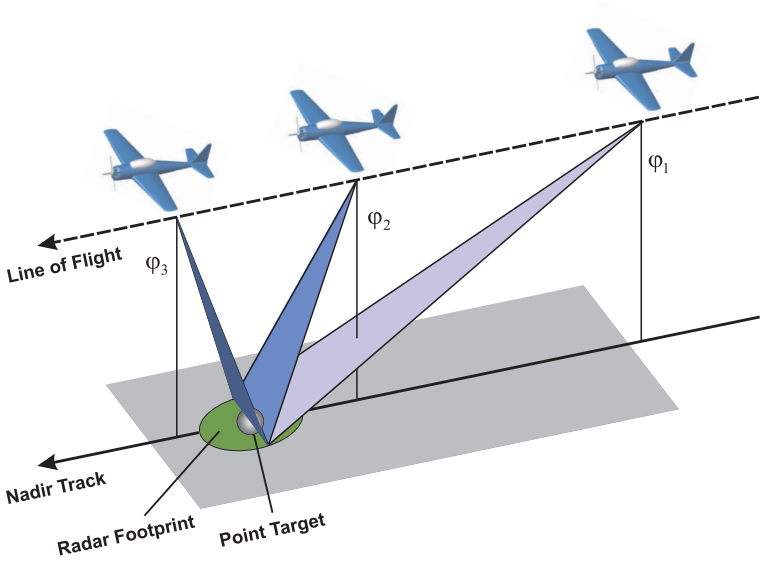

Figure 7.14: "Pseudo Spot-light modus"

the lossy soil and the strong attenuation of the creeping waves the direct and first reflected wave between the target and the interface remain as utilizable signals compared to the other waves of the ray system. It was pointed out that over the entire look angle range the ray path between the sphere and the interface of the second contributor is nearly twice as long as the single one of the direct wave. Consequently the superposition of the principal waves doesn't not lead to a depolarization. In contrast, at the transition from a lossy soil into the air, a phase shift occurs for the perpendicular field component. The resulting location on the Poincaré sphere gives a one to one relation to the soil loss.

Measurements were performed at the European Microwave Signature Laboratory (EMSL) at the Joint Research Centre (JRC) of the European Commission, for a sphere above a perfect conducting interface. Despite the fact that the interface was given by a 2m $\times$ 2m plate and diffraction from the edge was present, the implemented GTD ray model was validated and the predicted transition zones according to the different heights were found.

The anechoic chamber data were applied to different decomposition theorems commonly used in Radar polarimetry. The coherent decomposition theorem after Krogager into a sphere, dihedral and helix showed that at the SSB the object appears as a sphere corresponding to local maxima values of k_S. A comparable behavior is predicted by the Cameron theorem. Here, a good match with a cylinder and dipole near shadow boundaries are given, where the match scatterer angle Θ_t corresponds to local minima. In contrast Θ_t, related to a diplane, corresponds to local maxima. For incoherent decomposition theorems, the target decomposition after Huynen showd that at the boundaries the target size m corresponds to local maxima. This agrees with the strong attenuation of the space waves in the shadow region. In contrast the even reflection parameter ν is related to local maxima near such boundaries. As the interactions between the target and interface are strongly attenuated, this denotes that the target itself defines the polarization of the backscattered field. Finally, according to the eigenvalue decomposition after Cloude and Pottier for the deterministic situation here, an entropy $H = 0$ and a non zero eigenvalue

follows. The parameter α lies for the different measured heights in the range of $30° < \alpha < 40°$ at the boundaries. This corresponds rather to a dipole than to a odd bounced reflected wave. Although the transition zone occurs together with local maxima or minima, it was demonstrated here that the different decomposition theorems are not suitable for getting information about the geometrical parameters for a target near the interface. Due to the strong diffraction of the horizontal aligned edge a representation on the Poincaré sphere was not investigated.

Since the time frame of a thesis is limited not all ideas could be realized within the frame of this work. Therefore this treatment is only one small step on a long way. In this work, due to the introduced GTD ray system where spatial and creeping are considered, it was demonstrated that the angular location of the transition zones on the Poincaré sphere are significant according to the geometrical properties of the target and its distance from the interface. Further measurements for e.g. more complex targets should be realized additionally for a varying azimuth angle $0° - 360°$ besides the look angle variation $0° - 90°$ and the significant diffraction points of investigated. In the near future the variation of the incidence angle at a target may be realized by illuminating an area in the spot-light modus as outlined in fig. 7.14. Hence, the additional information according to the transition zones could be exploited.

Bibliography

[1] "*Handbook of Mathematical Functions*", Abramowitz and Stegun, Dover Publications, Inc., New York, 1970.

[2] "*Asymptotic methods in short-wave diffraction theory*",Babič V.M, Buldyrev V.S., Springer Verlag, 1991.

[3] "*Dipole Radiation in the Presence of a Conducting Half-Space*", *Baños, A, Jr.*, Pergamon Press, Oxford, London, Edinburgh, New York, Paris, Frankfurt, 1966.

[4] "*Target vectors: Spinorial concepts*", Bebbington D.H.O., 2nd Int. Workshop on Radar Polarimetry, IRESTE, Nantes, France, Sept. 1992, pp.26-36.

[5] "*Electromagnetic Fields*", J. van Bladel, McGrawHill

[6] "*Journées Internationales de la Polarimétrie Radar*", Recueil des communications des Journées Internationales de la Polarimétrie Radar à Nantes le 20,21 et 22 Mars 1990, Chapter: Indroduction du concept de la Polarimetrie, edité par J.I.P.R Ireste Universite de Rennes France, Boerner W.M., 1990.

[7] "*Principles of Optics*", Born M. and Wolf E., Pergamon Press, New York (1986).

[8] "*Asymptotic Methods in Electromagnetics*", Bouche D., Molinet F. and Mittra R., Springer Verlag, Berlin, Heidelberg, New York, 1997.

[9] "*FFT Schnelle Fourier-Transformation*", Brigham Oran E., Verlag R. Oldenbourg , 1992.

[10] "*Taschenbuch der Mathematik*",Bronstein I.N. and Semendjajew K.A., Verlag Nauka Moskau B.G. Teubner Verlagsgesellschaft Stuttgart-Leipzig Verlag Harri Deutsch Thun und Frankfurt/Main, 1991.

[11] "*Feature motivated polarization scattering matrix decomposition*", Cameron W.L., Leung L.K., IEEE International Radar Conference 1990, Record of the IEEE 1990 International, Pages:549-557, 7-10 May 1990.

[12] "*A mathematical formulation of the Equivalence Principle*", Chen Kun-Mu, IEEE Transactions on Microwave Theory and Techniques, Vol. 37, No. 10, March 1989.

[13] "*Electromagnetic Scattering by three-dimensional arbitrary complex/conducting bodies*",Chen Q., Wilton D. R., Antennas and Propagation Society International Symposium, Vol.2, Pages:590-593, May 1990.

[14] "*Current induced on a conducting cylinder located near the planar interface between two semi-infinite half-spaces*", Butler C. M., Xiao-Bang Xu and Glisson A., IEEE Transactions on Antennas and Propagation, Vol.33, No. 6, March 1985.

[15] "*A closed-form spatial Green's function for the thick Microstrip Substrate*", Chow Y.L., Yang J.J., D.G. Fang and Howard G.E., IEEE Transactions on Microwave Theory and Techniques, Vol. 39, No. 3, March 1991.

[16] "*Group theory and polarization algebra*, Cloude S.R., OPTIK, Vol 75, No.1, pp. 26-36, 1986.

[17] Cloude S.R.and Pottier E.: "*Concept of polarization entropy in optical scattering*", Optical Engineering, Vol 34, No.6, June 1995.

[18] Cloude S.R.and Pottier E.: "*A Review of Target Decomposition Theorems in Radar Polarimetry*",IEEE Transactions on Geoscience and Remote Sensing, Vol 34, No.2, March 1996.

[19] "*An Entropy Based Classification Scheme for Land Applications of Polarimetric SAR*", Cloude S.R. and Pottier E., IEEE Transactions on Geoscience and Remote Sensing, Vol 35, No.1, January 1997.

[20] Cloude S.R.and Pottier E.: "*Polarimetric SAR Interferometry*", IEEE Transactions on Geoscience and Remote Sensing, Vol 36, No.5, January 1997.

[21] "*Application of Decomposition Theories to experimental scattering data from dielectric rough surfaces*", Cucurachi A., TMR Report, Mothesim May 1999.

[22] "*Discrete image theory for horizontal electric dipoles in a multilayered medium*", Fang D.G., Yang J.J. and Delisle G.Y., IEEE Proceedings, Vol. 135, No. 5, Oct. 1988.

[23] "*Radiation and Scattering of Waves*", Felsen, L. and Marcuvitz N., Prentice-Hall, Inc., 1973.

[24] "*Fast Multipole Method for Scattering from an arbitrary PEC target above or buried in a lossy half space*", Geng N., IEEE Transactions on Antennas and Propagation, Vol. 49, No. 5, May 2001.

[25] Graves C.D.: "*Radar Polarization Power Matrix*", Graves C.D., Proceeding of the IRE, Vol.44, No.5, pp.248-252, 1956

[26] "*Theoretische Physik*", Greiner, W., Verlag Harri Deutsch, 1986.

[27] "*Recherches sur les solutions fondamentales et l'intégration des équations linéaires aux dérives partielles (premier mémoire).*", Hadamard J, Annales Scientifiques de l'École Normale Supérieure Sér. 3, 21 (1904), p. 535-556

[28] "*Recherches sur les solutions fondamentales et l'intégration des équations linéaires aux dérives partielles (deuxième mémoire).*", Hadamard J, Annales Scientifiques de l' École Normale Supérieure Sér. 3, 22 (1905), p. 101-141

[29] "*Time Harmonic Electromagnetic Fields*", Harrington Roger F., McGraw-Hill, New York, Toronto, London 1961.

[30] "*Field Computation by Moment Methods*", Harrington Roger F., Mcmillan, New York, 1968.

[31] "*Origin and Development of the Method of Moments*", Harrington Roger F., Electrical and Computer Engineering Department, Syracuse University, NY 13210.

[32] "*Optik*", Hecht Eugene, Addison-Wesley Verlag, 1989.

[33] "*Principles and Applications of Millimeter-Wave Radar*", Holm W.A., Artech House, 1987.

[34] "*Entwicklung hochfrequenter Meßverfahren zur Boden- und Schneefeuchtebestimmung*", Hübner C. , Ph.D. 1999, Wissenschaftliche Berichte FZKA 6329, Institut für Meteorologie und Klimaforschung, Forschungszentrum Karlsruhe.

[35] "*Phenomenological Theory of Radar Targets*", Huynen J. R., Ph.D. 1970.

[36] "*Effect Of Target Size And Tilt On Target Identification Based Upon Full Polarimetric Radar*", Huynen J. R., Geoscience and Remote Sensing Symposium, 1989. IGARSS'89. 12th Canadian Symposium on Remote Sensing. 1989 International, Vol.2, pp.937 - 940, July 10 -14th 1989.

[37] "*Journées Internationales de la Polarimétrie Radar*", Recueil des communications des Journées Internationales de la Polarimétrie Radar à Nantes le 20,21 et 22 Mars 1990, Chapter: La matrice de Stokes et sa relation avec les proprietes physique de la cible, edité par J.I.P.R Ireste Universite de Rennes France, Huynen J.R., 1990.

[38] Huynen J. R.: "*Physical reality and mathematical process in radar polarimetry*", Antennas and Propagation, 1991. ICAP 91., Seventh International Conference on (IEE) , Pages:257 - 261, Vol.1, 15-18 Apr 1991.

[39] "*Klassische Elektromechanik*", Jackson, J.D., Walter de Gruyter, 1982.

[40] "*Decay exponents and diffraction coefficients for surface waves on surfaces of nonconstant curvature* ", J.B. Keller et B.R. Levy, IRE Trans. Ant. Prop., AP-7, p. 52-61, Dec. 1959

[41] "*A Geometrical Theory of Diffraction*", J.B. Keller, J. Calculus of Variations and its Applications, Mc Graw Hill, New York, 1958

[42] "*Geometrical Theory of Diffraction*", J.B. Keller, J. Opt. Soc. Amer., 52, p. 116-130, 1962

[43] "*Aspects of Polarimetric Radar Imaging*", Krogager E., Ph.D., Danish Defence Research Establishment, 1993.

[44] "*Approximate boundary conditions for electromagnetic field on the surface of conducting bodies*", Leontovich M. A., Collection book investigation of radio waves propagation, Moscow, Academy of sciences, 1948, pp. 512.

[45] "*Principles and Application of Imaging Radar*", Lewis A.J., Manual of Remote Sensing, 3rd Edition, Vol.2, John Wiley and Sons, Inc., 1998

[46] "*On the Huynen's target characteristic parameters*", Lin S.M., Antennas and Propagation Society International Symposium, 1990. AP-S. Merging Technologies for the 90's. Digest. , Pages:566 - 568, Vol.1, 7-11 May 1990.

[47] "*Vergleich der Finiten-Differenzen-Methode mit der Split-Step-Methode zur Erstellung synthetischer Radargramme unter Berücksichtigung der frequenzabhängigen effektiven Permittivität des Bodens*", Marquart, N.P., Master Thesis,Geophysical Institute of Karlsruhe Germany, 2000.

[48] "*Indroduction to the Uniform Geometrical Theory of Diffraction*", McNamara, D.A., Pistorius, C.W.I., and Malherbe J.A.G., Artech Kouse, Boston, London, 1990.

[49] "*Electromagnetic Scattering and Radiation by surfaces of arbitrary shape in layered media, Part I: Theory* ", Michalski K.A., Zheng D., IEEE Transactions on Antennas and Propagation, Vol. 38, No. 3, March 1990.

[50] "*Discrete complex image mixed-potential integral equation analysis of microstrip patch antennas with vertical probe feeds*", Michalski K.A., Mosig J.R., Electromagnetics, No. 17, pp.377-392, 1995.

[51] "*Modelisation d'un reseau fini large bande*", Molinet F. and Tort S., Rapport Final D'Etude, Marche N^o085/714/$CNES$/97/6766/00, Document MOTHESIM N^o609 18. March 1999.

[52] "*Journées Internationales de la Polarimétrie Radar*", Recueil des communications des Journées Internationales de la Polarimétrie Radar à Nantes le 20,21 et 22 Mars 1990, edité par J.I.P.R Ireste Universite de Rennes France.

[53] "*Contribution de la Polarimétrie dans la Discrimination de Cibles Radar. Application a l'Imagerie Électromagnétique Haute Résolution.*", Pottier E., These a l'Universite de Rennes1, 1990.

[54] "*A Review of Polarimetric Target Decomposition Theorems*", Pottier E., T.M.R Training Workshop, DLR Oberpfaffenhofen, Germany, December 1st 1990.

[55] "*Habillitationsschrift*", Pottier E., hab. a l'Universite de Rennes1, 1999.

[56] "*Radar Polarimetry - From Basics to Applications*", Pottier E., Lecture Course at the UPC, Barcelona, Spain, 19-23 April 2004.

[57] "*Modelisation d'un reseau fini large bande*", Molinet F., Tort S., Rapport Final D'Etude, Marche N^o085/714/$CNES$/97/6766/00, Document MOTHESIM N^o609 18. Mai 1999.

[58] "*Application of the Method of Moments to electromagnetic scattering by surfaces-arbitrary shape*", Rao Sadasiva M., Séminaires sur les méthodes de calcul modernes en électromagnétisme, 3-7 September 1984 at SUPELEC - Gif-sur-Yvette.

[59] "*Radar Cross Section Handbook Volume 1*", Ruck T. George, Barrick E. Donald, Stuart D. William and Krichbaum K. Clarence,Plenum Press New York, 1970.

[60] "*Über die Ausbreitung der Wellen in der drahtlosen Telegraphie*", Sommerfeld A., Annalen der Physik, Bd. 28, 1909, S. 665-736, 1909.

[61] "*Applications of the Method of Moments to electromagnetic fields*", Strait B.J.,The Scee Press.

[62] "*Polarization in Electromagnetic Systems*", Stutzman W. L., Artech House Inc., Boston-London, 1993.

[63] "*Computational Electrodynamics*", Taflove A., Artech House Inc., Boston-London, 1995.

[64] "*Microwave Remote Sensing, Active and Passive, Volume I-III, From Theory to Applications*", Ulaby, F., Moore, R., Fung, A., Artech House, 1986.

[65] "*Signaturuntersuchungen an einem polarimetrischen Pulsradar*", Wanielik G., Dissertation, Reihe 10 Informatik/Kommunikationstechnik Nr. 97, VDI Verlag, 1988.

[66] "*Single reference, three target calibration and error correction for monostatic, polarimetric free space measurements*, Wiebeck W. and Khny D., Proceedings of the IEEE, Vol. 79, No. 10, October 1991.

[67] "*Matrizen und ihre Anwendungen 1 - Grundlagen*", Zurmühl R. and Falk S., 7.Auflage, Springer Verlag, 1997.

APPENDIX A

At the Boundary

Along this work, the reflection of an electromagnetic wave and at the interface of two dielectrics is given. Furthermore, the polarization of the waves in the considered GTD ray system is related to the plane of incidence at the reflection points. Therefore, the Fresnel coefficients for the reflection and transition at an interface are introduced in the following. Additionally, the image theory is briefly outlined. The image theory was used to determine the geometrical parameters of the waves related to the shadow boundaries, needed for the numerical implementation of the GTD model considered in this work.

A.1 Fresnel Coefficients

The reflection coefficient is given by the ratio of the reflected and incident wave amplitude. In the same manner, the transmission coefficient is described by the ratio of the transmitted and incident wave amplitude. In the following an object is considered, which is large enough in the direction transversal to the direction of the wave propagation so that no diffraction occurs. The obstacle is of a different electrical material than the surrounding space.
From the boundary conditions, it follows that the normal component of the field must be continuous at the interface. Thus, the boundary conditions for the normal component of the magnetic induction and electrical displacement at the interface are defined as:

$$\left[\epsilon\left[\vec{E}_i(\vec{r},\omega)+\vec{E}_r(\vec{r},\omega)\right]-\epsilon\,\vec{E}_t(\vec{r},\omega)\right]\cdot\hat{n} \;=\; 0 \tag{A.1}$$

$$\left[\vec{k}_1\times\vec{E}_i(\vec{r},\omega)+\vec{k}_1\times\vec{E}_r(\vec{r},\omega)-\vec{k}_2\times\vec{E}_t(\vec{r},\omega)\right]\cdot\hat{n} \;=\; 0 \tag{A.2}$$

On the surface the free charges can displace. Hence, the parallel tangential component of the total field is equal to zero, given in the form:

$$\left[\epsilon\left[\vec{E}_i(\vec{r},\omega)+\vec{E}_r(\vec{r},\omega)\right]-\epsilon\vec{E}_t(\vec{r},\omega)\right]\times\hat{n} \;=\; 0 \tag{A.3}$$

$$\left[\frac{1}{\mu_1}(\vec{k}_1\times\vec{E}_i(\vec{r},\omega)+\vec{k}_1\times\vec{E}_r(\vec{r},\omega))-\frac{1}{\mu_2}(\vec{k}_2\times\vec{E}_t(\vec{r},\omega))\right]\times\hat{n} \;=\; 0 \tag{A.4}$$

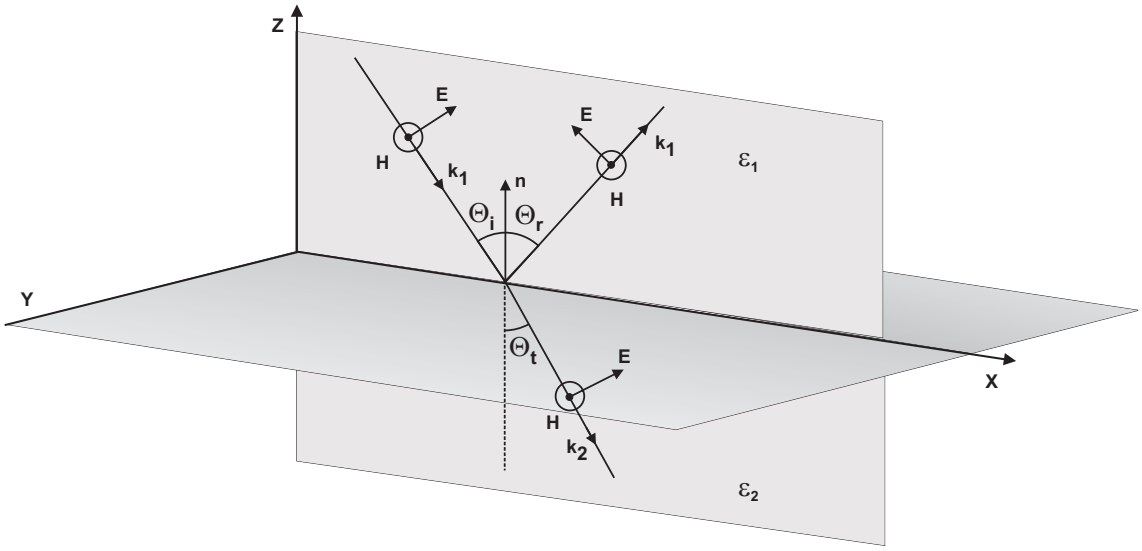

Figure A.1: Parallel E-field component

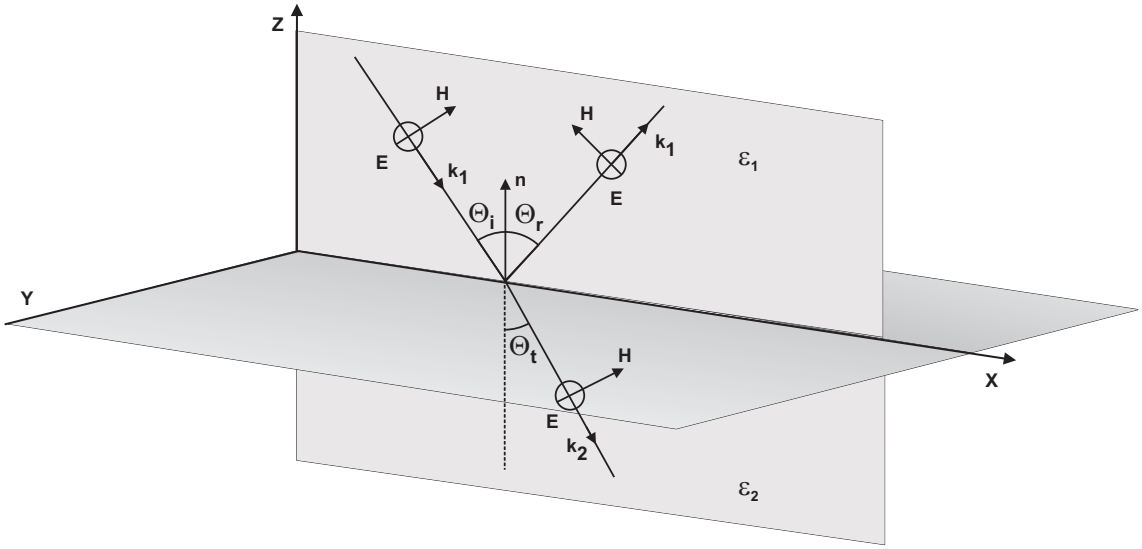

Figure A.2: Perpendicular E-field component

$$\vec{E}_1^{tot} = \vec{E}_i + \vec{E}_r \tag{A.5}$$
$$\vec{E}_2^{tot} = \vec{E}_t \tag{A.6}$$

Every arbitrary polarization state can be described by a perpendicular and parallel component, here related to the plane of incidence. Depending from the given polarization, the transversal electrical (TE) or transversal magnetic (TM) is considered. Additionally, the normal component of the impedance Z is also continuous across the interface. Finally, the reflection and transmission coefficients are defined by:

$$R_{TE} = \frac{n_1 \cos\theta^i - \frac{\mu_1}{\mu_2} n_2 \cos\theta^t}{n_1 \cos\theta^i + \frac{\mu_1}{\mu_2} n_2 \cos\theta^t} \tag{A.7}$$

$$T_{TE} = \frac{2n_1 \cos\theta^i}{n_1 \cos\theta^i + \frac{\mu_1}{\mu_2} n_2 \cos\theta^t} \tag{A.8}$$

$$R_{TM} = \frac{\frac{\mu_1}{\mu_2} n_2^2 \cos\theta^i - n_1 n_2 \cos\theta^t}{\frac{\mu_1}{\mu_2} n_2^2 \cos\theta^i + n_1 n_2 \cos\theta^t} \tag{A.9}$$

$$T_{TM} = \frac{2n_1 n_2 \cos\theta^i}{\frac{\mu_1}{\mu_2} n_2^2 \cos\theta^i - n_1 n_2 \cos\theta^t} \tag{A.10}$$

A.2 Image Theory

Image theory

To figure out how the geometrical problem was solved for finding the different ray paths with variation of the incidence angle it should be mentioned that the wave 3,11 and 5 are the incident field and the wave 8,12 and 9 the ones reflected from the object. The total field is given by the sum of the incident and reflected field in the lit region. That's more comprehensible if one recalls the image theory for a perfect conducting soil and look at the reflection point on the image object as presented in fig. A.3 and fig. A.4.

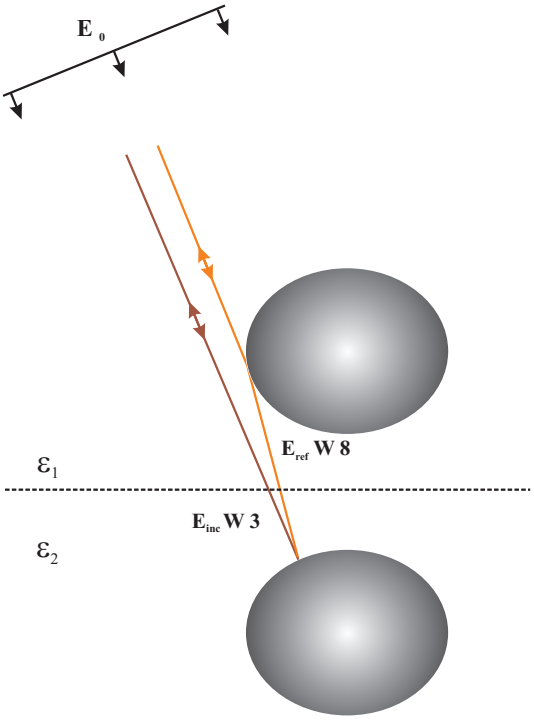

Figure A.3: Image for transition region 1

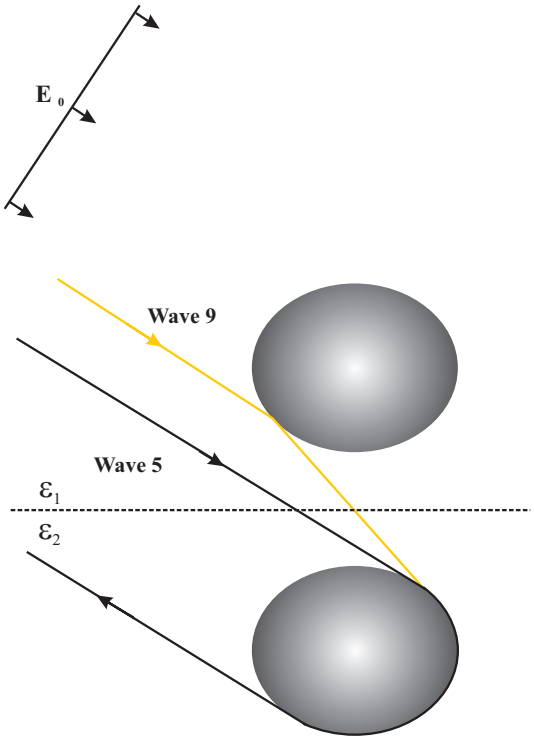

Figure A.4: Image for transition region 3

APPENDIX B

Method of Moments

Here, the numerical implementation of the extended Method of Moment technique for solving the Mixed Potential Integral Equation according to chapter 2 is discussed in greater details.

B.1 Current Basis Functions

The given surface integral of the MPIE is performed in such a way that the surface of the object is approximated by plane triangular patches. The first step in the numerical calculation consists in fixing the apexes and edges of these triangular patches. Every edge l_q on the patched surface is related here to its triangles twosome $\vec{T}_q^{\,n+}(\vec{r}')$ and $\vec{T}_q^{\,n-}(\vec{r}')$ as shown in fig. B.1. Thus, every point on the patch $\vec{T}_q^{\,n+}(\vec{r}')$ may be given by the vector $\vec{r}\,'$ or through the local vector $\vec{\rho}_q^{\,+}$ defined by the apex of the triangle $\vec{T}_q^{\,n+}$. In the same manner, a point on the triangle $\vec{T}_q^{\,n-}$ is fixed. Where the vector $\vec{\rho}_q^{\,-}$ is pointed toward the apex of the triangle $\vec{T}_q^{\,n-}$. According to Rao [58], the basis functions are given by:

$$\vec{f}_{\,q}(\vec{r}\,') \;=\; \begin{cases} \frac{l_q}{2A_q^+}\,\vec{\rho}_q^{\,+} & , \quad \vec{r}\;in\;T_q^+ \\ \frac{l_q}{2A_q^-}\,\vec{\rho}_q^{\,-} & , \quad \vec{r}\;in\;T_q^- \\ 0 & , \quad else \end{cases} \tag{B.1}$$

Where the length of the edge is given by l_q and the area of the triangle by $A_q^{\pm}$. It follows for the divergence at an edge:

$$\nabla_{\vec{r}\,'} \cdot \vec{f}_{\,q}(\vec{r}\,') \;=\; \begin{cases} \frac{l_q}{A_q^+} & , \quad \vec{r}\;in\;T_q^+ \\ \frac{l_q}{A_q^-} & , \quad \vec{r}\;in\;T_q^- \\ 0 & , \quad else \end{cases} \tag{B.2}$$

The current distribution on the surface is described by the basis functions. For a given number N of apexes the currents are given by:

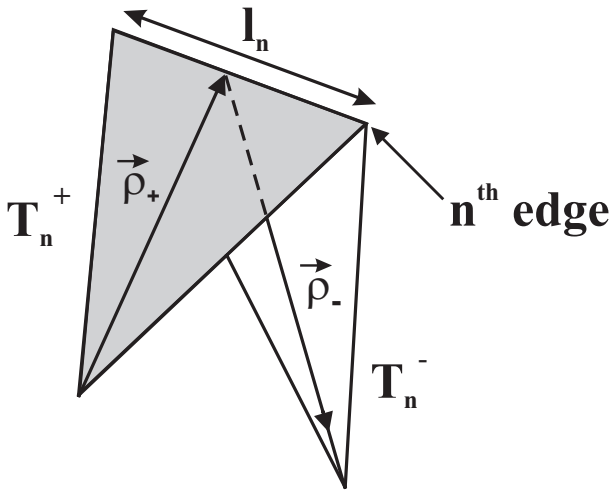

Figure B.1: Base function for the triangular patches $T_n^{\pm}$ at the edge l_n

$$\vec{J}_{(\vec{r}\,')} \;=\; \sum_{q=1}^{N} I_q \; \vec{f}^{\,n}_{q\,(\vec{r}\,')} \tag{B.3}$$

According to $(B.1)$ and $(B.2)$ it follows:

- The basis functions have only a normal component through the common edge l_q of the triangle twosome $T_q^{\pm}$. In consequence only a current flow through the common edge remains.
- The divergence of the currents over a closed surface is equal to zero.
- The normal component of $\vec{\rho}_q^{\pm}$ at the edge l_q corresponds to the height of a triangle. The height is given by $2\,\frac{A_q^{\pm}}{l_q}$. Hence, according to $(B.1)$ it follows that the flux through an edge l_q is unitary. This assures the continuity of the normal current component through an edge. Thus, every single edge is directly related to a current coefficient I_q.

B.2 Numerical Implementation of the MoM for solving the MPIE

As a perfect conducting surface is considered, the incident field $\vec{E}_{i(\vec{r})}$ is related to the scattered field by the boundary condition at the surface: $\hat{n} \times \left[\vec{E}_i \;+\; \vec{E}_s\right] \;=\; 0$. According to chapter 2 the incident field is given in terms of the scalar and vector potential Φ and $\vec{A}$ by:

$$\vec{E}_{i(\vec{r})} \;=\; i\omega\vec{A}_{(\vec{r})} \;-\; \nabla_r \Phi_{(\vec{r})} \tag{B.4}$$

Where for the current distribution on the entire surface S' the potential Φ and $\vec{A}$ are given by:

$$\vec{A}_{(\vec{r})} \;=\; \iint\limits_{S'} \overline{\overline{K}}_A \; \vec{J}_{(\vec{r}\,')} \, dS' \tag{B.5}$$

$$\Phi_{(\vec{r})} \;=\; \iint\limits_{S'} K_\Phi \; q_{(\vec{r}')} \; dS' \tag{B.6}$$

Considering first a single edge l_n of a triangle $T_n^{\pm}$ twosome its area is denoted by Δ_q. According to (2.107) and substituting (2.111) in (B.4) the incident field is given by:

$$\begin{aligned}\vec{E}_{i(\vec{r})} = \; i\omega \iint\limits_{\Delta_q} \Bigg\{ & \Big[\; \hat{x}(\vec{J}\cdot\hat{x}) \;+\; \hat{y}(\vec{J}\cdot\hat{y})\Big] \;\; K_A^1 \;+\; \hat{z}\left[(\nabla'\cdot\vec{J})K_A^{2a} \;+\; (\vec{J}\cdot\hat{z})K_A^{2b}\right] \\ & +\; \nabla\,\frac{\partial}{\partial z}(\vec{J}\cdot\hat{z})K_A^3 \Bigg\}\, d\Delta l_q \;+\; \nabla \iint\limits_{\Delta_q} (\nabla'\cdot\vec{J})K_\Phi\, d\Delta l_q\end{aligned}$$

The current distribution in B.2 is substituted by the basis functions and the corresponding current coefficient. According to (B.3) it follows for all triangle patches:

$$\begin{aligned}\vec{E}_{i(\vec{r})} = \sum_{q=1}^{n} I_q \Bigg\{ & i\omega \iint\limits_{\Delta_q} \Big\{ \left[\; \hat{x}(\vec{f}_q^{\,n}\cdot\hat{x}) \;+\; \hat{y}(\vec{f}_q^{\,n}\cdot\hat{y})\right] \;\; K_A^1 \\ & +\; \hat{z}\left[(\nabla'\cdot\vec{f}_q^{\,n})K_A^{2a} \;+(\vec{f}_q^{\,n}\cdot\hat{z})K_A^{2b}\right] \\ & +\; \nabla\,\frac{\partial}{\partial z}(\vec{f}_q^{\,n}\cdot\hat{z})K_A^3 \Big\}\, d\Delta l_q \\ & +\; \nabla \iint\limits_{\Delta_q} (\nabla'\cdot\vec{f}_q^{\,n})K_\Phi\, d\Delta l_q \Bigg\}\end{aligned} \tag{B.7}$$

Up to now, expression (B.7) cannot be solved as for one equation n unknowns exist. According to the Gauss elimination an equation system of dimension $n \times n$ has to be set. This is done by a inner product of (B.7) with a set of test functions Δ_p, also called testing procedure. For computation reasons the basis functions Δ_q considered here are also used as test functions Δ_p in the MoM algorithm DIFFRA[1]. Extracting the derivations operators outside of the integration sign the inner product of (B.7) is given by a set of test functions as follows:

$$\begin{aligned}\iint\limits_{\Delta_p} \vec{E}_{i(\vec{r})}\cdot\vec{f}_{p\,(\vec{r})}\; dl_p = \sum_{q=1}^{N} I_q \Bigg\{ & i\omega \iint\limits_{\Delta_p} \vec{f}_{p\,(\vec{r})}\; dl_p \iint\limits_{\Delta_q} \Big\{ \left[\; \hat{x}(\vec{f}_q^{\,n}\cdot\hat{x}) \;+\; \hat{y}(\vec{f}_q^{\,n}\cdot\hat{y})\right] \;\; K_A^1\; dl_q \\ & +\iint\limits_{\Delta_p} \vec{f}_{p\,(\vec{r})}\; dl_p \hat{z} \iint\limits_{\Delta_q} \left[(\nabla'\cdot\vec{f}_q^{\,n})K_A^{2a} \;+(\vec{f}_q^{\,n}\cdot\hat{z})K_A^{2b}\right]\; dl_q \\ & +\iint\limits_{\Delta_p} \vec{f}_{p\,(\vec{r})}\; dl_p\; \nabla \underbrace{\frac{\partial}{\partial z} \iint\limits_{\Delta_q} (\vec{f}_q^{\,n}\cdot\hat{z})K_A^3 \Big\}\; dl_q}_{F_1} \\ & +\iint\limits_{\Delta_p} \vec{f}_{p\,(\vec{r})}\; dl_p\; \nabla \underbrace{\iint\limits_{\Delta_q} (\nabla'\cdot\vec{f}_q^{\,n})K_\Phi\; dl_q}_{F_2} \Bigg\}\end{aligned}$$

[1]Program for computing the scattered field from a perfect conducting obstacle. The surface of the obstacle can be close or either open with joined wires. The electric field integral equation is solved by using the MoM.

The numerical calculation of $B.2$ is simplified by applying the derivations operators directly on the basis functions. According to $B.2$ and using the following relation:

$$\underbrace{\iint\limits_{\Delta_p} \nabla \cdot \left[\vec{f}_p \, F_i \right]}_{0} = \iint\limits_{\Delta_p} \left[\nabla \cdot \vec{f}_p \, F_i + \vec{f}_p \cdot \nabla F_i \right] dl_p \tag{B.8}$$

it yields:

$$\begin{aligned} \iint\limits_{\Delta_p} \vec{E}_i(\vec{r}) \cdot \vec{f}_p(\vec{r}) \, dl_p = \sum_{q=1}^{N} I_q \Bigg\{ & i\omega \iint\limits_{\Delta_p} \vec{f}_p(\vec{r}) \, dl_p \iint\limits_{\Delta_q} \Big\{ \left[\hat{x}(\vec{f}_q^{\,n} \cdot \hat{x}) + \hat{y}(\vec{f}_q^{\,n} \cdot \hat{y}) \right] K_A^1 \, dl_q \\ & + \iint\limits_{\Delta_p} \vec{f}_p(\vec{r}) \, dl_p \hat{z} \iint\limits_{\Delta_q} \left[(\nabla' \cdot \vec{f}_q^{\,n}) K_A^{2a} + (\vec{f}_q^{\,n} \cdot \hat{z}) K_A^{2b} \right] dl_q \\ & - \iint\limits_{\Delta_p} \left(\nabla \cdot \vec{f}_p(\vec{r}) \right) dl_p \frac{\partial}{\partial z} \iint\limits_{\Delta_q} (\vec{f} \cdot \hat{z}) K_A^3 \Big\} \, dl_q \\ & - \iint\limits_{\Delta_p} \left(\nabla \cdot \vec{f}_p(\vec{r}) \right) dl_p \iint\limits_{\Delta_q} (\nabla' \cdot \vec{f}_q^{\,n}) K_\Phi \, dl_q \Bigg\} \end{aligned} \tag{B.9}$$

Finally, the implementation of the MPIE in the DIFFRA program is given by:

$$\begin{aligned} \iint\limits_{\Delta_p} \vec{E}_i(\vec{r}) \cdot \vec{f}_p(\vec{r}) \, dl_p = \Bigg[& i\omega \iint\limits_{\Delta_p} \left\{ \vec{f}_p(\vec{r}) \left(A_1^{pq} + A_2^{pq} \right) + \left(\nabla \cdot \vec{f}_q^{\,n} \right) A_3^{pq} \right\} dl_p \\ & - \iint\limits_{\Delta_p} \left(\nabla \cdot \vec{f}_q^{\,n} \right) A_\Phi^{pq} \, dl_p \Bigg] \sum_{q=1}^{N} I_q \end{aligned} \tag{B.10}$$

The single terms of the vector potential are given as follows:

$$\begin{aligned} A_1^{pq} &= \iint\limits_{\Delta_q} \left[\hat{x}(\vec{f}_q^{\,n} \cdot \hat{x}) + \hat{y}(\vec{f}_q^{\,n} \cdot \hat{y}) \right] K_A^1 \, dl_q \\ A_2^{pq} &= \iint\limits_{\Delta_q} \left[(\nabla' \cdot \vec{f}_q^{\,n}) K_A^{2a} + (\vec{f}_q^{\,n} \cdot \hat{z}) K_A^{2b} \right] dl_q \\ A_3^{pq} &= \frac{\partial}{\partial z} \iint\limits_{\Delta_q} (\vec{f}_q^{\,n} \cdot \hat{z}) K_A^3 \, dl_q \end{aligned} \tag{B.11}$$

and the scalar potential is calculated in the form:

$$A_\Phi^{pq} = \iint\limits_{\Delta_q} (\nabla' \cdot \vec{f}_q^{\,n}) \, K_\Phi \, dl_q \tag{B.12}$$

B.3 Code Implementation

One may rewrite $(B.10)$ in matrix form, where the left side corresponds to the voltage vector. The summation on the right side is replaced by a column vector of coefficients corresponding to the surface currents. The relation of the scattered field and the induced currents on the surface are given through the quadratic $p \times q$ impedance matrix $[Z_{pq}]$ as follows:

$$\vec{V}_p \;=\; [Z_{pq}]\;\vec{I}_q \tag{B.13}$$

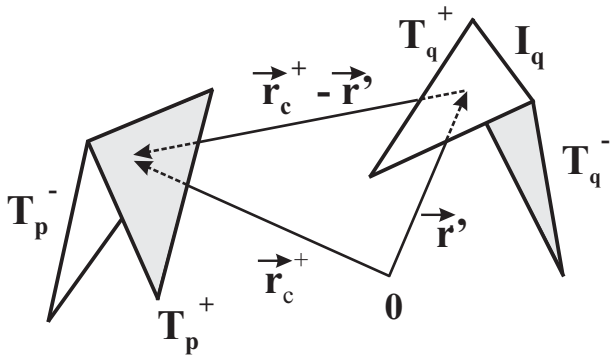

Figure B.2: Basis function T_q' and test function T_p

B.3.1 Voltage Vector

The voltage vector $\vec{V}_p$ in $(B.13)$ is given for the triangles $+\Delta_p$ and $-\Delta_p$ as:

$$\begin{aligned}\vec{V}_p \;=\; \iint\limits_{\Delta_p} \vec{E}_{i(\vec{r})} \cdot \vec{f}_{p\,(\vec{r})}\; dl_p \;&=\; \iint\limits_{+\Delta_p} \vec{E}_{i(\vec{r})} \cdot \vec{f}_p{}^{+}{}_{(\vec{r})}\; dl_p \;+\; \iint\limits_{-\Delta_p} \vec{E}_{i(\vec{r})} \cdot \vec{f}_p{}^{-}{}_{(\vec{r})}\; dl_p \\ &=\; \iint\limits_{+\Delta_p} \vec{E}_i \frac{l_p}{2A_p^+}\, \vec{\rho}_p{}^{+}\; dl_p \;+\; \iint\limits_{-\Delta_p} \vec{E}_i \frac{l_p}{2A_p^-}\, \vec{\rho}_p{}^{-}\; dl_p\end{aligned}$$

The numerical calculation can be simplified by the following approximation. For long distances between the triangles $T_q^{\pm}$ and the observation point $\vec{r}$, the value of a test triangle twosome $T_p^{\pm}$ is considered to be constant. Hence:

$$\vec{E}_{i(\vec{r}_p^{\pm})} \;\approx\; \vec{E}_{i(\vec{r}_p^{c\pm})} \;\approx\; const.$$

Considering the value at the centroid of every single test triangle twosome, one CPU time consuming surface integration is dropped. Where the voltage vector $\vec{V}_{(\vec{r})}$ of a common edge l_p is simplified as follows:

$$\vec{V}_{(\vec{r})} \;=\; l_p \;\left[\; \vec{E}_{i(\vec{r}_{c+})} \cdot \frac{\vec{\rho}_p{}^{+}}{2} \;+\; \vec{E}_{i(\vec{r}_{c-})} \cdot \frac{\vec{\rho}_p{}^{-}}{2} \;\right]$$

B.3.2 Impedance Matrix

According to $(B.10)$ the impedance matrix $[Z]$ given in the form:

$$[Z]_{pq} \;=\; i\omega \iint\limits_{\Delta_p} \Big[\vec{f}_p(\vec{r}\,)\,(\,A_1^{pq} \,+\, A_2^{pq}) \,+\, (\nabla\cdot\vec{f}_q^{\,n})\,A_3^{pq} \;-\; (\nabla\cdot\vec{f}_q^{\,n})\,A_\Phi^{pq} \Big]\; dl_p \tag{B.14}$$

Once more, the integration over the test triangles can be approximated by their centroid values. The impedance matrix $[Z]$ is rewritten as follows:

$$\begin{aligned}
[Z]_{pq} = l_p \Bigg\{ i\omega \;\Big[\; & \vec{A}_{1(\vec{r}_p^{\,c+})}\,\frac{\vec{\rho}_p^{\,c+}}{2} \;+\; \vec{A}_{1(\vec{r}_p^{\,c-})}\,\frac{\vec{\rho}_p^{\,c-}}{2} \\
& +\; \vec{A}_{2(\vec{r}_p^{\,c+})}\,\frac{\vec{\rho}_p^{\,c+}}{2} \;+\; \vec{A}_{2(\vec{r}_p^{\,c-})}\,\frac{\vec{\rho}_p^{\,c-}}{2} \\
& -\; \vec{A}_{3(\vec{r}_p^{\,c+})} \;+\; \vec{A}_{3(\vec{r}_p^{\,c-})} \;\Big] \\
& -\; A_{\Phi(\vec{r}_p^{\,c+})} \;+\; A_{\Phi(\vec{r}_p^{\,c-})} \Bigg\}
\end{aligned} \tag{B.15}$$

Surface Co-Ordinates

The apexes of a single triangle $T_q^{n\pm}$ are described by $\vec{r}_1$, $\vec{r}_2$ and $\vec{r}_3$. The edges opposite of the corresponding apexes are indicated with l_1, l_2 and l_3 as shown in fig. B.3. In a single triangle three possible bases may be defined by using the same index as their corresponding apex. The basis vector can here point in or out of the triangle. Its direction is related to the sign of the current coefficient I_q at the edge l_q. Hence, the basis vectors are given by:

$$\vec{\rho}_i \;=\; \pm(\,\vec{r}\,' \,+\, \vec{r}_i\,) \qquad\qquad i \;=\; 1,2,3 \tag{B.16}$$

Where the vector $\vec{r}'$ points to the triangle T_q. The three possible vectors $\vec{\rho}_i$ split the area of T_q

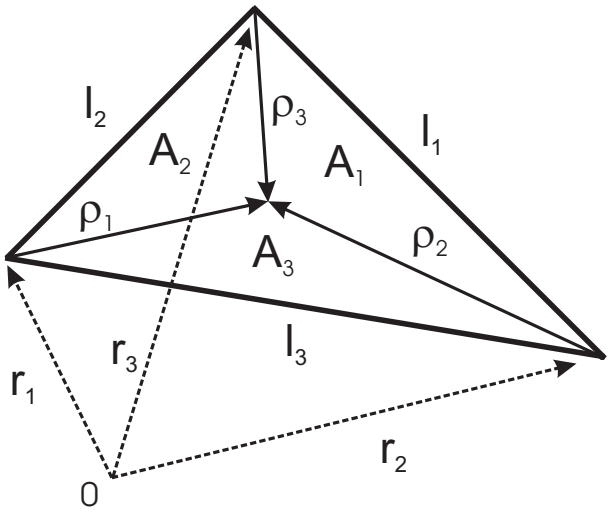

Figure B.3: Surface co-ordinates

into three subareas A_1, A_2 and A_3. It holds:

$$A_q \;=\; A_1 \,+\, A_2 \,+\, A_3 \tag{B.17}$$

The relative three area parts are given by:

$$\xi = \frac{A_1^{\pm}}{A_q^{\pm}} \quad \eta = \frac{A_2^{\pm}}{A_q^{\pm}} \quad \zeta = \frac{A_3^{\pm}}{A_q^{\pm}}$$

Where it holds in turn

$$\xi + \eta + \zeta = 1 \tag{B.18}$$

According to $(B.17)$ and $(B.18)$ the surface co-ordinates at triangle T_q is given in terms of:

$$\vec{r}\,' = \xi\vec{r}_1 + \eta\vec{r}_2 + \zeta\vec{r}_3 \tag{B.19}$$

Considering the surface co-ordinates according to $(B.19)$, the implementation of the single potential terms in the DIFFRA program mentioned in chapter 2 is given by:

- $\vec{\boldsymbol{A}}_{\mathbf{1}}(\vec{\boldsymbol{r}}_{\boldsymbol{p}}^{\,c\pm}) = \boldsymbol{A}_{\mathbf{1}ix}^{pq}(\vec{\boldsymbol{r}}_{\boldsymbol{p}}^{\,c\pm}) \cdot \hat{\boldsymbol{x}} + \boldsymbol{A}_{\mathbf{1}iy}^{pq}(\vec{\boldsymbol{r}}_{\boldsymbol{p}}^{\,c\pm}) \cdot \hat{\boldsymbol{y}}$

$$A_{1ix}^{pq} = \pm l_i \left[r_{1x} I_{\xi}^{K_A^1} + r_{2x} I_{\eta}^{K_A^1} + r_{3x} I_{\zeta}^{K_A^1} - r_{ix} I^{K_A^1} \right]$$

$$A_{1iy}^{pq} = \pm l_i \left[r_{1y} I_{\xi}^{K_A^1} + r_{2y} I_{\eta}^{K_A^1} + r_{3y} I_{\zeta}^{K_A^1} - r_{iy} I^{K_A^1} \right]$$

$$I_{\xi}^{K_A^1} = \int_0^1 \int_0^{1-\eta} K_A^1(\vec{r}^{\,c}_{p\pm}, \vec{r}\,'_{\pm})\, \xi \, d\xi \, d\eta$$

$$I_{\eta}^{K_A^1} = \int_0^1 \int_0^{1-\eta} K_A^1(\vec{r}^{\,c}_{p\pm}, \vec{r}\,'_{\pm})\, \eta \, d\xi \, d\eta$$

$$I^{K_A^1} = \int_0^1 \int_0^{1-\eta} K_A^1(\vec{r}^{\,c}_{p\pm}, \vec{r}\,'_{\pm})\, d\xi \, d\eta$$

$$I_{\zeta}^{K_A^1} = I^{K_A^1} - I_{\xi}^{K_A^1} - I_{\eta}^{K_A^1}$$

- $\vec{\boldsymbol{A}}_{\mathbf{2}}(\vec{\boldsymbol{r}}_{\boldsymbol{p}}^{\,c\pm}) = \boldsymbol{A}_{\mathbf{2}iz}^{pq}(\vec{\boldsymbol{r}}_{\boldsymbol{p}}^{\,c\pm}) \cdot \hat{\boldsymbol{z}}$

$$A_{2iz}^{pq} = \pm \left(2 l_i I^{K_A^{2a}} + l_i \left[r_{1z} I_{\xi}^{K_A^{2b}} + r_{2z} I_{\eta}^{K_A^{2b}} + r_{3z} I_{\zeta}^{K_A^{2b}} - r_{iz} I^{K_A^{2b}} \right] \right)$$

$$I^{K_A^{2a}} = \int_0^1 \int_0^{1-\eta} K_A^{2a}(\vec{r}^{\,c}_{p\pm}, \vec{r}\,'_{\pm})\, d\xi \, d\eta$$

$$I_{\xi}^{K_A^{2b}} = \int_0^1 \int_0^{1-\eta} K_A^{2b}(\vec{r}^{\,c}_{p\pm}, \vec{r}\,'_{\pm})\, \xi \, d\xi \, d\eta$$

$$I_{\eta}^{K_A^{2b}} = \int_0^1 \int_0^{1-\eta} K_A^{2b}(\vec{r}^{\,c}_{p\pm}, \vec{r}^{\,\prime}_{\pm})\, \eta \, d\xi \; d\eta$$

$$I^{K_A^{2b}} = \int_0^1 \int_0^{1-\eta} K_A^{2b}(\vec{r}^{\,c}_{p\pm}, \vec{r}^{\,\prime}_{\pm})\, d\xi \; d\eta$$

$$I_{\zeta}^{K_A^{2b}} = I^{K_A^{2b}} - I_{\xi}^{K_A^{2b}} - I_{\eta}^{K_A^{2b}}$$

- $\boldsymbol{A_{3i}^{pq} = l_i \frac{\partial}{\partial z} \left[r_{1z} I_{\xi}^{K_A^3} + r_{2z} I_{\eta}^{K_A^3} + r_{3z} I_{\zeta}^{K_A^3} - r_{iz} I^{K_A^3} \right]}$

$$I_{\xi}^{K_A^3} = \int_0^1 \int_0^{1-\eta} K_A^3(\vec{r}^{\,c}_{p\pm}, \vec{r}^{\,\prime}_{\pm})\, \xi \, d\xi \; d\eta$$

$$I_{\eta}^{K_A^3} = \int_0^1 \int_0^{1-\eta} K_A^3(\vec{r}^{\,c}_{p\pm}, \vec{r}^{\,\prime}_{\pm})\, \eta \, d\xi \; d\eta$$

$$I^{K_A^3} = \int_0^1 \int_0^{1-\eta} K_A^3(\vec{r}^{\,c}_{p\pm}, \vec{r}^{\,\prime}_{\pm})\, d\xi \; d\eta$$

$$I_{\zeta}^{K_A^3} = I^{K_A^3} - I_{\xi}^{K_A^3} - I_{\eta}^{K_A^3}$$

- $\boldsymbol{A_{\Phi i}^{pq} = \pm 2 l_i I_{K_\Phi}}$

$$I_{K_\Phi} = \int_0^1 \int_0^{1-\eta} K_\Phi(\vec{r}^{\,c}_{p\pm}, \vec{r}^{\,\prime}_{\pm})\, d\xi \; d\eta$$

APPENDIX C

Uniform Reflection and Diffraction Theory

In this section, a short overview of the reflection and diffraction coefficients according to McNamara [48] and Bouche and Molinet [8] is given.

C.1 Transition Function

A special function introduced in the UTD formalism is the transition function $F(x)$. Its large and small argument behavior is briefly shown in fig. C.1 according to McNamara [48]. The complex transition function $F(x)$ is given for a $e^{i\,\omega t}$ time-dependence as:

$$F(x) \;=\; 2\,i\,\sqrt{x}\,e^{ix}\int_{\sqrt{x}}^{\infty} e^{-iu^2}\,du \tag{C.1}$$

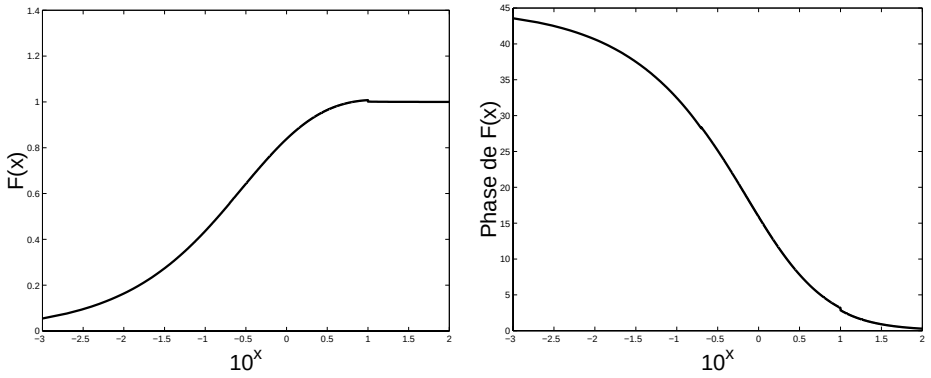

(a) Modul (b) Phase

Figure C.1: The transition function F(x)

C.2 Pekeris Function

The Pekeris caret functions $\hat{P}_{s,h}(x)$ are given by the Fock scattering functions $p(x)$ and $q(x)$ for a $e^{i\omega t}$ time-dependence in the form:

$$\hat{P}_s(x) \;=\; p(x)\, e^{-i\frac{\pi}{4}} \;-\; \frac{e^{-i\frac{\pi}{4}}}{2x\sqrt{\pi}} \tag{C.2}$$

$$\hat{P}_h(x) \;=\; q(x)\, e^{-i\frac{\pi}{4}} \;-\; \frac{e^{-i\frac{\pi}{4}}}{2x\sqrt{\pi}} \tag{C.3}$$

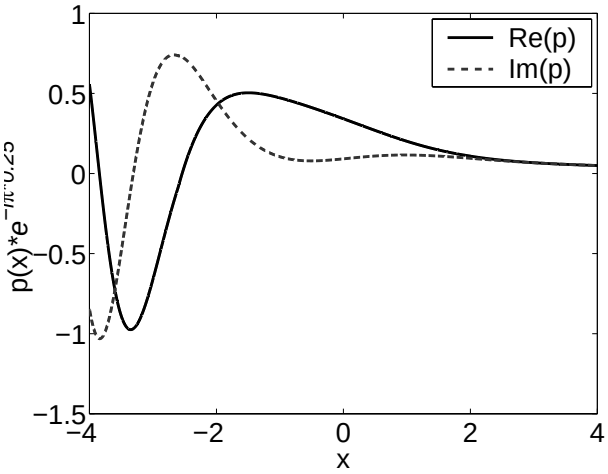

Figure C.2: Fock scattering function p

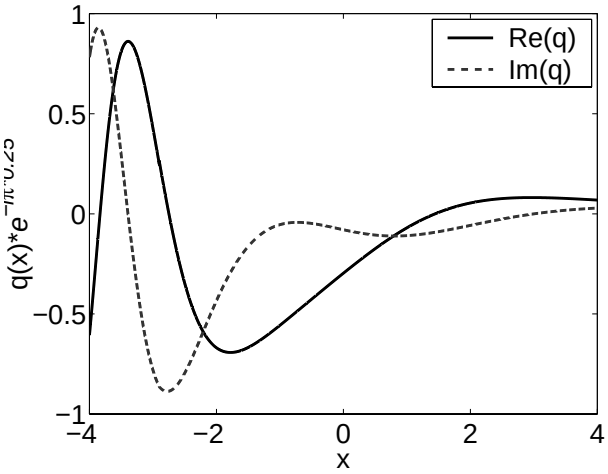

Figure C.3: Fock scattering function q

C.3 Uniform Reflection Coefficients

The general reflection coefficients for the perpendicular (soft) and parallel (hard) component, relative to the plane of incidence, is given as [48]:

$$R_S^H \;=\; -\sqrt{\frac{-4}{\xi_p}}\; e^{-i\frac{\xi_p^3}{12}}\; e^{-i\frac{\pi}{4}} \left[-\frac{F(X_p)}{2\xi_p\sqrt{\pi}} + \left\{ \begin{array}{c} p^*(\xi_p) \\ q^*(\xi_p) \end{array} \right. \right] \tag{C.4}$$

Where p^* and q^* are the Fock scattering functions and have to be considered for the corresponding soft and hard component. The asterisk in $C.4$ implies here that the complex conjugate has to be taken in the case of a $\exp(-i\omega t)$ time-dependance. The argument X_p for the transition function $F(X_p)$ is given in the form:

$$X_p \;=\; 2\,k\,L_p\,cos^2(\theta^i)$$

The quantity ξ_p is the Fock parameter and given by:

$$\xi_p \;=\; -2\,m(Q_r)\;cos\theta^i$$

The quantity $m(Q_r)$ is calculated via:

$$m(Q_r) \;=\; \left[\frac{k\,a_0(Q_r)}{2}\right]^{\frac{1}{3}}$$

Where parameter L_P is defined as:

$$L_p \;=\; \frac{s^r s^i}{s^r + s^i}$$

The length s^i is the distance from the source to the reflection point and s^r describes the way to the point of observation. For the monostatic case $s^i = s^r$ considered along the thesis it yields:

$$L_p \;=\; s^{i,r}$$

C.4 Uniform Diffraction Coefficients

C.4.1 General Formulation

The uniform surface diffraction coefficient is given by [48]:

$$T_S^H \;=\; -\sqrt{m(Q)\;\;m(B)}\;\sqrt{\frac{2}{k}}\;\; e^{-ikt}\;\; e^{-i\frac{\pi}{4}} \left\{ -\frac{F(X_d)}{2\xi_d\sqrt{\pi}} + \left[\begin{array}{c} p^*(\xi_d) \\ q^*(\xi_d) \end{array} \right] \right\} \tag{C.5}$$

Where properties of the surface are included in the Fock parameter ξ_d. For a given arc length ξ_d is calculated as:

$$\xi_d \;=\; \int_{\tau(Q')}^{\tau(Q)} \frac{m(\tau)}{a_0(\tau)}\,d\tau \tag{C.6}$$

Further, the curvature parameter $m(\tau)$ is defined by:

$$m(\tau) \;=\; \left[\frac{k\,a_0(\tau)}{2}\right]^{\frac{1}{3}} \tag{C.7}$$

The arc length t along the surface is given as follows:

$$t \;=\; \int_{\tau(Q')}^{\tau(Q)} d\tau \tag{C.8}$$

The argument of the transition function $F(X_d)$ and distance parameter L_d are given by:

$$X_d \;=\; \frac{kL_d\xi_d^2}{2m_{(Q')}\,m_{(Q)}} \tag{C.9}$$

$$L_d \;=\; \frac{s^d s'}{s^d + s'} \tag{C.10}$$

Hence, according to the monostatic case $s' = s^d$ and a plane field $s^{d,\prime} \to \infty$, $(C.10)$ reduces to:

$$L_d \;=\; s^{d,\prime} \tag{C.11}$$

C.4.2 Asymptotic Solution for the Cylinder

The diffracted field from a perfect conducting cylinder is given after the n-th rotation according to Bouche and Molinet [8] by $(A1.12)$ for a time dependence $exp\,(i\omega t)$ as follows:

$$E(M) \;=\; \frac{e^{i\,k\,l_1}}{\sqrt{l_1}} \left[\sum_{n=1}^{\infty} -i\,e^{i\,\nu_n\,\frac{l_c}{a}}\;\frac{R_n}{2k}\right] \frac{e^{i\,k\,l_2}}{\sqrt{l_2}} \tag{C.12}$$

The quantity l_1 and l_2 are the path lengths to and back from the cylinder. Where R_n is defined as:

$$R_n \;=\; \frac{\Omega H_\nu^2\,[ka]}{\frac{\partial}{\partial\nu}\Omega H_{\nu_n}^1\,[ka]} \tag{C.13}$$

Written out Ω is given by:

$$\Omega \;=\; \frac{\partial}{\partial r} \;+\; i\zeta$$

Expression $C.13$ is simplified by replacing the Hankel function by its asymptotic approximation. For the cylinder (2D) the following approximation is made:

$$R_n \;=\; -\frac{2i}{\pi 2^{\frac{7}{3}}}\;\;(ka)^{\frac{1}{3}}\;\;e^{-2\,i\,\frac{\pi}{3}}\;\;\frac{1}{\left[A_i'(y_n)\right]^2 \;-\; y_n\left[A_i(y_n)\right]^2}$$

where

$$y_n \;=\; 2^{\frac{1}{3}}\,e^{-i\frac{\pi}{3}}\,(ka)^{-\frac{1}{3}}\,(\nu_n - ka)$$

and ν_n are the zeros of order n. Hence, one gets:

$$\frac{\partial H_{\nu_n}^1(ka)}{\partial r} \;+\; i\zeta H_{\nu_n}^1(ka) \;=\; 0$$

The formula ($C.12$) is rewritten with the relation:

$$D_s \;=\; \frac{e^{i\frac{\pi}{4}}}{\sqrt{8\pi k}}$$

and

$$D_s^2\, D_{rs}^2 \;=\; -i\,\frac{R_n}{2k}$$

in the following form:

$$E(M) \;=\; D_s\,\frac{e^{i\,k\,l_1}}{\sqrt{l_1}}\;\left[\sum_{n=1}^{\infty} e^{i\,\nu_n\,\frac{l_c}{a}}\;D_{rs}^2\right]\;D_s\,\frac{e^{i\,k\,l_2}}{\sqrt{l_2}} \tag{C.14}$$

Diffraction Coefficients
Three diffraction coefficients are given in ($C.14$). Where the coefficient D_s describes the transition of the 2-D line source into a wave propagating in the 3-D space. In the same way the tangential radiation of the creeping wave from the surface of the cylinder represents a 2-D line source. For a small line source element the asymptotic expression of the Green function for the free space is given by:

$$\frac{i}{4}H_0^1\,[kR] \;\sim\; \frac{e^{i\frac{\pi}{4}}}{\sqrt{8\pi k}}\;\frac{e^{ikR}}{\sqrt{R}} \;=\; D_s\;\frac{e^{ikR}}{\sqrt{R}}$$

The term D_{rs} can be interpreted as the de-and attachment coefficient at the cylinder. It describes the transition from a space wave in a creeping wave at the attachment point Q and vice versa at the detachment point Q'. The quantity D_{rs} depends strongly from the surface geometry at the points Q and Q' and of the wave polarization. For a cylinder it remains:

$$D_{rs}^2 \;=\; D_{rs}(Q)\;D_{rs}(Q')$$

The parameter ν_n belongs to the phase term of the creeping wave. Thus, ν_n describes the phase change and the attenuation of the creeping wave on its way along the arc $\overline{QQ'}$. According to Keller and Levy [40] the diffraction coefficient D_n is of the form:

$$D_n^2 \;=\; D_s\;D_{rs}^2$$

Numerical Implementation
According to ($C.14$) it follows for a plane wave:

$$E(Q) \;=\; \frac{D_s}{\sqrt{l_1}} \;=\; E_0^i$$

The backdasattered field at the observation point M is given by:

$$E(M) \;=\; \underbrace{E_0^i\;e^{i\,k\,l_1}}_{Way\ there}\underbrace{\left[\sum_{n=1}^{\infty} e^{i\,\nu_n\,\frac{l_c}{a}}\;D_n^2\right]}_{Cylinder}\;\underbrace{\frac{e^{i\,k\,l_2}}{\sqrt{l_2}}}_{Way\ back} \tag{C.15}$$

$$D_S^2 = \frac{1}{\sqrt{2\pi k}} \left(\frac{ka}{2}\right)^{\frac{1}{3}} \frac{e^{i\frac{\pi}{12}}}{\left[A_i'(-q_n)\right]^2} \qquad (E_\perp) \tag{C.16}$$

$$D_H^2 = \frac{1}{\sqrt{2\pi k}} \left(\frac{ka}{2}\right)^{\frac{1}{3}} \frac{e^{i\frac{\pi}{12}}}{\bar{q}_n \left[A_i(-\bar{q}_n)\right]^2} \qquad (E_{||}) \tag{C.17}$$

$$e^{i\nu_n \frac{l_c}{a}} = \underbrace{e^{ikl_c}}_{Phase} \quad \underbrace{e^{i\gamma\frac{l_c}{a}}}_{Attenuation} \tag{C.18}$$

Where the attenuation factor γ is given by:

$$\gamma = \left(\frac{ka}{2}\right)^{\frac{1}{3}} e^{i\frac{\pi}{3}} \left\{ \begin{array}{c} q_n \\ \bar{q}_n \end{array} \right\} + O\left[\left(\frac{ka}{2}\right)^{-\frac{4}{3}}\right] \tag{C.19}$$

$$\begin{array}{ll} q_1 = 2,33811 & q_2 = 4,08795 \\ \bar{q}_1 = 1,01879 & \bar{q}_2 = 3,24820 \end{array}$$

$$\begin{aligned} A_i'(-q_1) &= 0.70121082 \\ A_i(-\bar{q}_1) &= 0.53565666 \end{aligned}$$

If a time dependence $exp(-i\omega t)$ is given, the complex conjugate of $(C.16)$ and $(C.17)$ has to be considered.

APPENDIX D

EMSL Measurement Reports

$Height$ h $[cm]$	$Ratio$ $\varnothing/h$ [ ]	$SSB1$ ϕ_1 [$^\circ$]	$SSB2$ ϕ_2 [$^\circ$]	$SSB3$ ϕ_3 [$^\circ$]	$0Cx \leq 2m$ ϕ_L [$^\circ$]	$0Cx \leq 1m$ ϕ_L [$^\circ$]
3.75	8	23.60	30.33	53.10	84.20	77.50
5.00	6	22.10	27.63	48.50	83.80	76.70
7.50	4	19.50	23.63	41.90	83.00	75.10
10.00	3	17.50	20.79	36.90	82.30	73.60
15.0	2	14.50	16.65	30.00	80.70	70.50
30.0	1	9.70	10.43	19.50	76.30	62.10
60.0	0.5	5.80	6.03	11.60	67.90	48.50

Table D.1: Shadow boundaries and geometrical limits of the setup

Calibration					
			f $[1.5GHz - 9.5GHz]$	Δf $10MHz$	Polarization H-V
Target	φ	Tilt	Scenario file	Local file	Date
Empty-chamber	35.0°	—	gtd-h0575	L1241433	04.05.2005
Only target support	35.0°	—	gtd-h0575	L1301449	10.05.2005
Disk	35.0°	0°	gtd-h0575	L1301442	10.05.2005
Dihedral	35.0°	0°	gtd-h0575	L1301500	10.05.2005
Dihedral	35.0°	$-45°$	gtd-h0575	L1301507	10.05.2005

Table D.2: Calibration of the raw datas

h=3.75 cm					
SSB1 23.6°	SSB2 53.1°	f $[1.5GHz - 9.5GHz]$	Δf $10MHz$	Polarization H-V	Δh 41.5cm
Range	$\Delta\varphi$	Scenario file	Local name	Date	
$5.0° - 75.0°$	0.5°	gtd-h0375	L1191537	29.04.2005	

h=5.0 cm					
SSB1 22.1°	SSB2 48.5°	f $[1.5GHz - 9.5GHz]$	Δf $10MHz$	Polarization H-V	Δh 40cm
Range	$\Delta\varphi$	Scenario file	Local file	Date	
$5.0° - 75.0°$	0.5°	gtd-h0575	L1221054	02.05.2005	

h=7.5 cm					
SSB1 19.5°	SSB2 41.9°	f $[1.5GHz - 9.5GHz]$	Δf $10MHz$	Polarization H-V	Δh 38cm
Range	$\Delta\varphi$	Scenario file	Local file	Date	
$5.0° - 75.0°$	0.5°	gtd-h0575	L1221600	02.05.2005	

Table D.3: EMSL-measurements I

h=10.0 cm					
SSB1 17.5°	SSB2 36.9°	f $[1.5GHz - 9.5GHz]$	Δf $10MHz$	Polarization H-V	Δh 35.5cm
Range	$\Delta\varphi$	Scenario file	Local file	Date	
$5.0° - 75.0°$	0.5°	gtd-h0575	L1230920	03.05.2005	

h=15.0 cm					
SSB1 14.5°	SSB2 30.0°	f $[1.5GHz - 9.5GHz]$	Δf $10MHz$	Polarization H-V	Δh 30cm
Range	$\Delta\varphi$	Scenario file	Local file	Date	
$5.0° - 75.0°$	0.5°	gtd-h0575	L1231453	03.05.2005	

h=30.0 cm					
SSB1 9.7°	SSB2 19.5°	f $[1.5GHz - 9.5GHz]$	Δf $10MHz$	Polarization H-V	Δh 15cm
Range	$\Delta\varphi$	Scenario file	Local file	Date	
$5.0° - 75.0°$	0.5°	gtd-h0575	L1240829	04.05.2005	

Table D.4: EMSL-Measurements II

SI Derived Units and Abbreviations

SI Derived Units

Symbol		**Quantity**	**SI**
Q	:	Electrical charge	$C = A \cdot s$
J	:	Current density	A/m^2
σ	:	Electric conductance	C/m^2
Φ	:	Magnetic flux	$Wb = V \cdot s$
$\vec{E}$	:	Electrical field vector	V/m
$\vec{H}$	:	Magnetic field vector	A/m
$\vec{D}$	:	Displacement current vector	C/m^2
$\vec{B}$	:	Magnetic flux density vector	$T = Wb/\mathrm{m}^2$
$\vec{P}$	:	Electrical polarisation vector	C/m^2
$\vec{M}$	:	Magnetisation vector	$V \cdot s/\mathrm{m}^2$
ρ	:	Electric charge density	C/m^3
Ω	:	Electric resistance	V/A
ϵ	:	Relative permittivity coefficient	[ ]
ϵ_0	:	Permittivity of vacuum	$C/(V \cdot m)$
μ	:	Relative magnetic permeability	[ ]
μ_0	:	Permeability of vacuum	$V \cdot s/(A \cdot m)$
χ_e	:	Electrical susceptibility	[ ]
χ_m	:	Magnetic susceptibility	[ ]

Abbreviations

CEM	Computational Electromagnetic
CPU	Central Processing Unit
DCIM	Discrete Complex Image Method
EFIE	Electric Field Integral Equation
EMSL	European Microwave Signature Laboratory
FD	Finite Difference frequency domain method
FDTD	Finite Difference Time Domain method
GO	Geometrical Optic
GTD	Geometrical Theory of Diffraction
HF	High Frequency
LHC	Left Handed Circular
MoM	Method of Moments
MPIE	Mixed Potential Integral Equation
QS	Quasi Static
RCS	Radar Cross Section
RHC	Right Handed Circular
SSB	Surface Shadow Boundary
UTD	Uniform Theory of Diffraction

Acknowledgment

First and foremost I would like to thank my thesis advisor Dr. Frédéric Molinet from the company MOTHESIM for his continuing help, being always present for discussions at any time and simple to the fact that he shared his exhaustable knowledge about electromagnetism. His paternal help started from the first day of this thesis and never stopped until the end of the thesis.

I am indebted to my thesis advisor Prof. Eric Pottier for his support in the subject Radar polarimetry and encouragement during the writing and preparation of this thesis.

Also a gratefully acknowledge to Mr. Stéphane Tort from the company MOTHESIM for his efforts and help.

Further, I would like to thank Dr. Laurent Ferro-Famil, Joëelle Drouet and all SA.P.H.I.R. members for their support during my stay in Rennes.

I also highly appreciate the opportunity I had to join the IPSC at the Joint Research Center from the European Commission in Ispra, Italy. For that acknowledge to Dr. Joaquim Fortuny. At the the IPSC I would like to thank Alberto Martinez (The EMSL Master), Marco Basso, Dr. Marco Gemmer and last but not leat Dr. Oliver Müllenhoff.

From the Joint Research Center I ought to mention Marina Hasiwa and family, Sebastian Hoffmann, Lars(e) Hareng and the members of the JRC Dive Club for the good times we shared under and outside the water.

Also thanks to Dr. Thomas Börner and Prof. A. Moreira from the German Aerospace Center (DLR) for the possibility to realize my "PHD Mission" in Rennes.

Sincere thanks to my parents for their support and encouragement during my lifetime.

This site will not be complete unless I thanked Martina Rudisile the most wonderful human being in my life! Thanks for you patience.